Fundamental Studies of Premixed Combustion

by

Md. Zahurul Haq

A thesis submitted in accordance with the requirements for the degree of

Doctor of Philosophy

School of Mechanical Engineering,

The University of Leeds.

September 1998

The candidate confirms that the work submitted is his own and that appropriate credit has been given where reference has been made to the work of others.

To my dear wife

Shilvi

Abstract

The thesis comprises a fundamental study of spherical premixed flame propagation, originating at a point under both laminar and turbulent propagation. Schlieren ciné photography has been employed to study laminar flame propagation, while planar mie scattering (PMS) has elucidated important aspects of turbulent flame propagation. Turbulent flame curvature has also been studied using planar laser induced fluorescence (PLIF) images.

Spherically expanding flames propagating at constant pressure have been employed to determine the unstretched laminar burning velocity and the effect of flame stretch, quantified by the associated Markstein lengths. Methane-air mixtures at initial temperatures between 300 and 400 K, and pressures between 0.1 and 1.0 MPa have been studied at equivalence ratios of 0.8, 1.0 and 1.2. Values of unstretched laminar burning velocity are correlated as functions of pressure, temperature and equivalence ratio. Two definitions of laminar burning velocity and their response to stretch due to curvature and flow strain are explored. Experimental results are compared with two sets of modeled predictions; one model considers the propagation of a spherically expanding flame using a reduced mechanism and the second considers a one dimensional flame using a full kinetic scheme. Data from the present experiments and computations are compared with those reported elsewhere. Comparisons are made with iso-octane-air mixtures and the contrast between fuels lighter and heavier than air is emphasized.

Flame instability in laminar flame propagation become more pronounced at higher pressures, especially for lean and stoichiometric methane-air mixtures. Critical Peclet numbers for the onset of cellularity have been measured and related to the appropriate Markstein number. Analyses using flame photography clearly show the flame to accelerate as the instability develops, giving rise to a cellular flame structure. The underlying laws controlling the flame speed as cellularity develops have been explored.

PMS images have been analysed to obtain the distributions of burned and unburned gas in turbulent flames. These have enabled turbulent burning velocities to be derived for stoichiometric methane-air at different turbulent r.m.s. velocities and initial pressures of 0.1 MPa and 0.5 MPa. A variety of ways of defining the turbulent burning velocity have been fruitfully explored. Relationships between these different burning velocities are deduced and their relationship with the turbulent flame speed derived. The deduced relationships have also been verified experimentally.

Finally, distributions of flame curvature in turbulent flames have been measured experimentally using PMS and PLIF. The variance of the distribution increases with increase in the r.m.s. turbulent velocity and decrease in the Markstein number. Reasons for these effects are suggested.

Acknowledgments

I wish to express my heartfelt thanks to Prof. D. Bradley and Dr. M. Lawes for their encouragement and guidance throughout the period of this research and during the preparation of this thesis.

I would like to thank Dr. R. Woolley for his assistance and stimulating discussions throughout the project. I would also like to thank Mr. I. Suardjaja for his assistance with some experiments.

My thanks are also due to all the staff in the Thermodynamics Laboratory.

I would also like to express my sincere thanks to Mrs. and Dr. Rahin for their friendship and help throughout the period of my stay at Leeds.

Financial assistance of the Commonwealth Association of Universities is gratefully acknowledged.

Finally, I would like to express my thanks to my parents and my wife for their love and encouragement throughout the period of my research.

Publications

The following paper has been submitted for publications:

Laminar burning velocity and Markstein lengths of methane-air mixtures; with X. J. Gu, M. Lawes and R. Woolley

Table of Contents

List of Tables

List of Figures

List of Symbols

a	amplitude of perturbation, defined in Eq. 5.3
a_{o}	initial perturbation amplitude
A	Flame area
A	empirical constant, in § 1.5 and § 5.4
B	empirical constant, defined in Eq. 5.12
B_{e}	empirical constant, defined in Eq. 5.14
$B_{\mathrm{e}\infty}$	empirical constant, defined in § 5.5
$\bar{A}(n)$	logarithmic growth rate, at spherical harmonics n
$(C)_{\mathrm{p}}$	pressure dependent constant, defined in Eq. 4.5
Da	turbulence Damköhler number, defined in § 1.6
D_{ij}	binary mass diffusivity, defined in § 1.2
D_{T}	thermal diffusivity of the mixture, defined in § 1.2
E	activation energy
f	numerical constant, defined in § 5.4

$F(x)$	probability distribution function, defined in Eq. 7.5
H	flame front curvature, given by Eqs. 7.1 and 7.2
k	wave number
Ka	turbulence Karlovitz number, defined in § 1.6
L	integral length scale
$L_{\mathrm{s}}, L_{\mathrm{c}}, L_{\mathrm{sr}}, L_{\mathrm{cr}}$	Markstein lengths, defined in § 1.4
L_{b}	burned gas Markstein length, defined in Eq. 1.5
Le	Lewis number, given by D_{T}/D_{ij}
$\dot{m}$	the mass burning rate of the flame
m_{bi}	mass burned within perimeter of radius R_i
m_{bo}	mass burned outside perimeter of radius R_i
m_{u}	mass unburned outside the perimeter of radius, R_{T}
m_{ui}	mass unburned within perimeter of radius R_i
m_{uo}	mass unburned between perimeters of radii $R_i \leq r < R_{\mathrm{T}}$
$Ma_{\mathrm{s}}Ma_{\mathrm{c}}, Ma_{\mathrm{sr}}, Ma_{\mathrm{cr}}$	Markstein numbers, defined in § 1.4
P_{o}	reference pressure (0.1 MPa)
Pe_{c}	theoretical critical Peclet number for onset of flame instability
Pe_{cl}	experimentally determined critical Peclet number
Pe_{o}	datum Peclet number, defined in Eq. 5.6
Pe_{t}	critical Peclet number for transition to turbulent flame

Pr	Prandtl number, given by ν/D_{T}
P_{u}	initial pressure
r_{cl}	critical radius at the onset of instability
r_{o}	datum flame radius, defined in Eq. 1.12
r_{sch}	schlieren front radius
r_{u}	cold flame front radius, defined in § 3.3
R	universal gas constant
R_i	mean general radius
R_{a}	reference radius, defined in § 6.2
R_{m}	reference radius, defined in § 6.2
R_{r}	reference root radius, defined in § 6.2
R_{T}	reference tip radius, defined in § 6.2
R_{v}	reference radius, defined in § 6.2
R_ξ	reference radius, defined in Eq. 6.2
Re_{L}	Reynolds number, given by by $u'L/\nu$
Re_λ	Reynolds number, given by $u'\lambda/\nu$
s	mean cold gas speed, defined in Eq. 6.28
s	distance measured along the flame front
$\mathcal{S}$	flame speed factor, defined in Eq. 3.15
S_{s}	unstretched laminar flame speed

S_{n}	stretched laminar flame speed
t, t_k	time from ignition
$\bar{t}$	nondimensional time, defined in Eq. 5.15
T_{ad}, T_{b}	adiabatic flame temperature
T_{f}	flame temperature
T^{o}	Inner layer temperature
T_{o}	reference temperature (300 K)
T_{u}	unburned gas reactant temperature
u_{g}	gas velocity ahead of the flame front
u'	r.m.s. turbulence velocity
u'_k	effective r.m.s. turbulence velocity
u_l	unstretched laminar burning velocity
$u_{l,0}$	reference burning velocity
u_{n}	stretched laminar burning velocity, defined in Eq. 1.1
u_{nr}	stretched mass burning velocity, defined in Eq. 1.3
u_{t}	turbulent burning velocity, defined in Eq. 6.6
$u_{\mathrm{t}'}$	turbulent burning velocity, defined in Eq. 6.5
u_{tr}	turbulent burning velocity, defined in Eq. 6.4
Ze	Zeldovich number, defined in Eq. 4.8

Greek letters

α	flame stretch rate
α_{c}	stretch rate due to flame curvature, defined in Eq. 3.7
α_{s}	stretch rate due to flame strain, defined in Eq. 3.8
α_{T}	temperature index, defined in Eq. 4.1
β	Zeldovich number, defined in Eq. 4.7
β_{P}	pressure index, defined in Eq. 4.1
δ_{D}	characteristic laminar flame thickness, given by D_{ij}/u_l
δ_l	characteristic laminar flame thickness, given by ν/u_l
δ_{T}	characteristic laminar flame thickness, given by D_{T}/u_l
η	Kolmogorov length scale
κ	a constant, defined in Eq. 5.7
λ	Taylor microscale of turbulence
Λ	wave length
ν	unburned gas kinetic viscosity
σ	density ratio, given by $\rho_{\mathrm{u}}/\rho_{\mathrm{b}}$
$\sigma(r)$	average volume fraction unburned at radius, r
ρ_{b}	burned gas density
ρ_{u}	unburned gas density
τ_{c}	characteristic chemical time, given by δ_l/u_l

τ_{m}	characteristic flow time, given by L/u'
ϕ	equivalence ratio
ω, Ω	perturbation growth rate parameter

Chapter 1

Introduction

1.1 General Introduction

There is a continuing demand for increased energy efficiency of gas turbines and reciprocating engines, and a deepening concern over problems related to the environment, energy, and hazards. All these have, during the past few decades, stimulated a tremendous burst of interest and research activities in the field of combustion. The simultaneous occurrence of chemical reaction and transport of mass, momentum, and energy makes analyses of these problems extremely complex. Moreover, practical flames are nearly all turbulent because of the requirement to produce high volumetric rates of energy production for efficiency and compactness. This further complicates combustion research even if one addresses the problem at a fundamental level in which practical difficulties might be neglected.

It has become widely accepted that turbulent flames in spark-ignited gasoline engines can be treated as an array of laminar flamelets with no turbulence structure residing within them (Bradley 1992). The concept of laminar flame propagation and the effect of stretch on it forms an integral part of the understanding of turbulent flames. Turbulent burning parameters are usually compared with laminar combustion parameters, by normalizing the former with the latter to produce dimensionless groups.

There is a dearth of reliable laminar burning data, especially at high pressure and temperature. Most of those data that exist for conditions above atmospheric pressure have been deduced from pressure measurements during explosions, with no visual observation of the flame. In consequence, the effects of any flame distortion and developing flame instability, which can enhance the burning rate, have been masked. In addition, pressure measurements yield the rate of mass burning rather than the rate of propagation of the flame into the cold mixture and experiments usually have been undertaken without addressing the effect of flame stretch. A close coupling exists between flame stretch, flame instability and burning velocity, and neglect of these may well explain the wide variation in the magnitudes of reported laminar burning velocities (Rallis and Garforth 1980, Bradley *et al.* 1996, Bradley *et al.* 1998).

In the present study, flame propagation in methane-air premixtures is studied in both laminar and turbulent conditions. In the case of the former the experimental and theoretical studies cover the consequences of the onset of flame instabilities. In the case of the latter it includes a scrutiny of the most appropriate way of defining the turbulent burning velocity. Methane, the major component of natural gas, is the simplest and lightest of the hydrocarbon series. It can provide a useful contrast with the burning characteristics of the heavier hydrocarbons which include propane and octane. Moreover, the methane oxidation mechanism is well understood and its burning characteristics can be accurately modeled. Therefore, methane is well suited for the study of combustion at the fundamental level.

1.2 Structure of a Laminar Planar Flame

With the tremendous advances in both computing power and techniques, it is now possible to solve numerically the steady-state comprehensive mass, species and energy conservation equations with a complete reaction mechanism (Glassman 1996). Using the reaction mechanism and some thermodynamic and transport property data base, the temperature and concentration profiles of all the species considered are estimated

and the mass burning rate of the flame ($\dot{m} = \rho_{\mathrm{u}} u_l$) is calculated as an eigenvalue of the problem and, since the unburned gas mixture density, ρ_{u}, is known, the unstretched laminar burning velocity, u_l, is determined. This is an intrinsic property of a combustible fuel-air mixture, and is defined as 'the velocity, relative to and normal to the flame front, with which the unburned gas moves into the front and is transformed into products under laminar flow conditions' (Heywood 1988).

Shown in Fig. 1.1 is the distribution of some major species and temperature for a freely propagating planar stoichiometric methane-air flame at an initial temperature of 300 K and initial pressure of 0.1 MPa. It is computed using the Sandia PREMIX code (Kee *et al.* 1985) with the reaction mechanism of GRI-Mech (Frenklach *et al.* 1995). The temperature profile, T_{f}, in Fig. 1.1(a) shows the existence of two layers of finite thickness, the preheat zone and the oxidation-layer. In the preheat zone, the temperature of the unburned mixture is raised by heat conduction from the reaction zone without significant energy release; while chemical energy of the mixture is released as heat in the oxidation-layer. Therefore, the curvature of the temperature profile ($\mathrm{d}^2 T_{\mathrm{f}}/\mathrm{d}x^2$) is positive in the preheat zone and negative in the oxidation-layer, with the transition occuring at the inner layer at a characteristic temperature, T^{o} (Göttgens *et al.* 1992). This temperature was interpreted by Göttgens *et al.* (1992) as the critical temperature at which the chemistry is 'turned on', and represents a balance point between radical production and consumption (Seshadri 1996). The value of T^{o} was used by Göttgens *et al.* (1992) and Peters and Williams (1987) to correlate the laminar burning velocity, and by Seshadri (1996) to predict the flammability limits of the reactant mixture.

The laminar flame thickness, δ_l, is a characteristic length for a given fuel-air mixture at a given initial condition. In the early asymptotic analysis of Zeldovich *et al.* (1985), Δx which corresponds to the segment of the tangent spanning the temperature interval between unburned gas temperature, T_{u}, and adiabatic flame temperature, T_{b}, was used to approximate δ_l, and is shown by dotted lines in Fig. 1.1(a). Clearly, this is

not an absolute definition of the flame thickness as the inspection of the concentration profiles in Fig. 1.1(b) suggests that different flame thicknesses might be defined based on the production or consumption of a particular species. Moreover, estimation of such flame thicknesses requires the computation of temperature profile and its derivatives. However, alternative characteristic flame thicknesses have been estimated such as:

- diffusion length, $\delta_{\mathrm{D}} = D_{ij}/u_l$, where D_{ij} is the mass diffusivity of the deficient reactant, i, with respect to the abundant reactant, j;
- thermal length, $\delta_{\mathrm{T}} = D_{\mathrm{T}}/u_l$, where D_{T} is the thermal diffusivity of the mixture;
- hydrodynamic length, $\delta_l = \nu/u_l$, where ν is the kinematic viscosity of the mixture.

These flame thicknesses can be related by the nondimensional Lewis number, Le, and Prandtl number, Pr, by: $\delta_{\mathrm{D}} = Le^{-1}\ \delta_{\mathrm{T}}$ and $\delta_l = Pr\ \delta_{\mathrm{T}}$. Lewis number is defined by D_{T}/D_{ij}, and Prandtl number is defined by ν/D_{T}. The definition $\delta_l = \nu/u_l$ is used throughout the present work.

1.3 Laminar Burning Velocities

For a non-planar flame, the mass rate of entrainment of unburned gas into the flame front, $\mathrm{d}m_{\mathrm{u}}/\mathrm{d}t$, is, in general, not the same as the rate of formation of the burned product, $\mathrm{d}m_{\mathrm{b}}/\mathrm{d}t$, because of the finite flame thickness. Hence, two definitions of laminar burning velocity exist (Bradley *et al.* 1996). One definition is based on the 'entrainment velocity' of unburned mixture into the flame front and has been expressed by Rallis and Garforth (1980) as:

$$u_{\mathrm{n}} = -\frac{1}{A\rho_{\mathrm{u}}}\frac{\mathrm{d}m_{\mathrm{u}}}{\mathrm{d}t} \tag{1.1}$$

where, A is the flame front area. The spatial velocity of the flame front, also known as the flame speed, S_{n}, is readily measurable by observing the flame's spatial temporal development. However, flame speed is not a unique property of a combustible mixture but the sum of u_{n} and the gas expansion velocity, u_{g}, immediately adjacent to the

flame front:

$$S_{\mathrm{n}} = u_{\mathrm{g}} + u_{\mathrm{n}} \tag{1.2}$$

Of the two terms on the right of Eq. 1.2, u_{g} is, in general, the larger and is a function of the densities of burned and unburned gas at any instant, as well as of the presence or absence of any constraining boundary.

The second definition of laminar burning velocity, u_{nr}, based on the appearance of burned products, has been computed for atmospheric methane-air mixtures by Bradley *et al.* (1996) as:

$$u_{\mathrm{nr}} = \frac{1}{A\rho_{\mathrm{u}}}\frac{\mathrm{d}m_{\mathrm{b}}}{\mathrm{d}t} \tag{1.3}$$

Such a burning velocity is determined from measurements of pressure rise in closed vessels, as in the experiments of Metghalchi and Keck (1980), and Ryan and Lestz (1980). It is analogous, under turbulent conditions, to the mass burning velocity, u_{tr}, introduced by Abdel-Gayed *et al.* (1986).

1.4 Flame Stretch and its Effects on Burning Velocities

Practical flames do not conform to the idealized planar steady configuration. Instead they can be wrinkled and unsteady, and can exist in flow fields that are nonuniform and unsteady. Therefore, a propagating flame front is subjected to strain and curvature effects which together constitute flame stretch and change the frontal area. The rate of change of flame area with time constitutes flame stretch. Hence, the flame stretch rate, α, at any point on a flame surface is defined as the Lagrangian time derivative of the logarithm of the area, A, of an infinitesimal element of the surface surrounding the point (Williams 1985),

$$\alpha = \frac{\mathrm{d}\ln A}{\mathrm{d}t} = \frac{1}{A}\frac{\mathrm{d}A}{\mathrm{d}t} \tag{1.4}$$

Flame stretch can increase or decrease the flame speed significantly (Bradley *et al.* 1996, Aung *et al.* 1997). However, a linear relationship between flame speed and

stretch rate has been reported in theoretical analysis (Matalon and Matkowsky 1982, Clavin 1985), numerical computation (Bradley *et al.* 1996) and experiment (Dowdy *et al.* 1990, Aung *et al.* 1997, Bradley *et al.* 1998). A burned gas Markstein length, L_b is defined to account for the sensitivity of flame speed to stretch (Clavin 1985), such that:

$$S_s - S_n = L_b \, \alpha \tag{1.5}$$

where S_s is the unstretched flame speed, and is obtained as the intercept value of S_n at $\alpha = 0$, in the plot of S_n against α.

Expressions of flame stretch rate in terms of the local characteristics of the flow field and flame curvature have been established by Chung and Law (1984), Matalon (1983), Candel and Poinsot (1990), Bradley *et al.* (1992) and Bradley *et al.* (1996). For a constant pressure flame propagation, total stretch rate is the algebraic sum of the stretch due to aerodynamic strain, α_s, and the stretch due to flame curvature, α_c (Candel and Poinsot 1990):

$$\alpha = \alpha_s + \alpha_c \tag{1.6}$$

Hence, strain rate and curvature may be interchangeable in the description of the flame area evolution. However their contributions to the flame structure are not interchangeable (Echekki and Chen 1996). The effect of strain rate and curvature on laminar flame propagation has been reviewed by Law *et al.* (1997).

The variation in burning velocity due to stretch is given by (Bradley *et al.* 1996):

$$u_l - u_n = L_c \, \alpha_c + L_s \, \alpha_s \tag{1.7}$$

in which L_c and L_s are Markstein lengths associated, respectively, with curvature and strain.

In general, the Markstein lengths are different for the two definitions of burning velocity (Bradley *et al.* 1996), hence,

$$u_l - u_{\rm nr} = L_{\rm cr}\ \alpha_{\rm c} + L_{\rm sr}\ \alpha_{\rm s} \tag{1.8}$$

where, $L_{\rm cr}$ and $L_{\rm sr}$ are the Markstein lengths associated, respectively, with curvature and strain for $u_{\rm nr}$.

A Markstein number is the Markstein length normalized by the flame thickness, δ_l. Similarly, stretch rate can be normalized by a chemical stretch rate given by the reciprocal of the chemical life time, $\tau_{\rm c} = \delta_l/u_l$, to give a Karlovitz stretch factor, K (Glassman 1996). Hence, Eqs. 1.7 and 1.8 become:

$$\frac{u_l - u_{\rm n}}{u_l} = K_{\rm c} Ma_{\rm c} + K_{\rm s} Ma_{\rm s} \tag{1.9}$$

and,

$$\frac{u_l - u_{\rm nr}}{u_l} = K_{\rm c} Ma_{\rm cr} + K_{\rm s} Ma_{\rm sr}. \tag{1.10}$$

Hence, $K_{\rm c}$ and $K_{\rm s}$ are the Karlovitz stretch factors due to curvature and strain respectively.

1.5 Evolution of Instabilities

Law *et al.* (1997) have attributed the development of flame instabilities in the form of cells and ridges of characteristic sizes over the flame surface as 'perhaps one of the most beautiful and fascinating phenomena in the flame dynamics'. It has been long observed that the flame on a Bunsen burner may split up into triangular flamelets forming a polyhedral pyramid that sometimes even spins about its vertical axis (Smith and Pickering 1928). It is now well established that the manifestation of spontaneous flame instability is not unique and depends on a series of factors that includes mixture properties and the shape and size of the flame (Markstein 1951, Istratov and Librovich 1969, Groff 1982, Zeldovich *et al.* 1985, Bradley and Harper 1994, Law *et al.* 1997).

1.5.1 Analysis of Instability in Planar Flame

The seminal stability analyses of Darrieus and Landau (Williams 1985) treated the flame as a gasdynamic surface of discontinuity in density that propagates normal to itself at a constant speed and formulated the problem of hydrodynamic instability of a plane flame front. In their analysis, two dimensional quantities: the flame propagation velocity and the wave number, k (or wave length, $\Lambda = 2\pi/k$), were uniquely combined to give a dimensional growth rate, a. The analysis did not consider any characteristic length and hence the flame was unstable to disturbances of all wavelengths for gas expansion ($\sigma > 1$), where σ is the density ratio defined by ρ_u/ρ_b. Moreover, short wavelength perturbations (large k) grow faster than the long wave length perturbations and the growth rate of the perturbations becomes infinite as the wavelength approaches zero. Thus, instability of a flame should be revealed experimentally as small-scale perturbations which grow to large amplitudes. This is not observed experimentally (Zeldovich *et al.* 1985), and the experimentally observed uniformity of cell size rather suggests a maximum instability at a particular wave number (Markstein 1951).

In Landau's analysis, a flame front was viewed as an infinitely thin surface separating burned and unburned gases. When the wavelengths of the perturbations become comparable to the diffusional-thermal thickness of the flame front, the idea of a flame as a surface of gasdynamic discontinuity loses is validity and this finite thickness has to be taken into the account; that is, the changes in its structure under the influence of the gasdynamic perturbations with the resulting change in the propagation velocity of the distorted flame in the premixture both become significant. To include the effect of the perturbations on the flame propagation velocity, Markstein (1951) proposed the effect of distortions of the flame structure be characterized by a phenomenological constant with the dimension of length, now known as the 'Markstein length'. This relates to the curvature of the flame front and the aerodynamic strain rate. The analysis yields an inner cut-off of wavelength, where a planar flame is stable to perturbations of shorter wavelength and unstable to those of long-wave length. This approach results in the

stabilization of short-wave length disturbances only when the phenomenological constant has a certain sign. When the sign is reversed, the short-wave perturbations could provide an additional destabilizing factor (Sivashinsky 1983).

Sivashinsky (1983) has reviewed the recent developments of flame instability, showing that cellular instability in not a hydrodynamic, but a thermo-diffusive instability. The source of this instability has been called 'preferential diffusion'. Simply stated the thermal gradients in the preheat zone in a flame can be stabilizing or destabilizing depending on the curvature of the flame and the Markstein number (Bradley and Harper 1994). A high value of Markstein number is, to some degree, stabilizing and able to counter the underlying Darrieus-Landau instability. A negative Markstein number results in early instabilities. A heavy-fuel lean-flame is more stable than a heavy-fuel rich-flame.

1.5.2 Growth of Instabilities in Spherical Flame Propagation

The development of instability in a spherically expanding flame front is different from that in a planar flame, as the flame size of the former increases with time. The originally smooth spherical surface becomes wrinkled, with consequent increase in flame speed. This is because the growth of the amplitude of the distortions of the flame front surface is faster than the propagation rate of the flame sphere (Istratov and Librovich 1969). If the trough and crests in the flame surface increase slower than the near-linear increase in the radius of the sphere as a whole, then the flame front is smoothed out in time, despite the absolute increase in the amplitude of the distortions (Zeldovich *et al.* 1985, Bechtold and Matalon 1987). Hence, a spherically expanding flame in a premixture is a bifurcation phenomenon, in which the flame becomes unstable at a radius, greater than a critical value, while remaining stable below that critical radius (Matalon and Erneux 1984).

The time dependence of the disturbance during spherical flame propagation follows a power law, rather than one of the exponential growth rate which is inherent to the

planar flame. Zeldovich *et al.* (1985) have shown by dimensional arguments that the rate of growth of the perturbation amplitude, $\frac{da}{dt}$ obeys the relationship :

$$\frac{da}{dt} \sim u_n \frac{a}{\Lambda} \tag{1.11}$$

where, Λ is the disturbance wavelength. For a planar flame, Λ is constant and integration of Eq. 1.11 leads to an exponential law. For the spherical flame, however, the perturbation wavelength should be expanded in a spherical harmonic series, rather than an ordinary Fourier series, and the perturbation wavelength corresponding to a particular spherical harmonic increases in proportion to the radius of the sphere and, therefore, to the time (Zeldovich *et al.* 1985). Hence, integration of Eq. 1.11 leads to a power law. This implies that the perturbations grow more slowly in a spherical flame than in a planar flame (Minaev *et al.* 1996). Istratov and Librovich (1969) used this fact to explain the difference between experimental and theoretical results.

1.5.3 Regimes of Flame Propagation for Spherical Flames

It is well established experimentally that under appropriate conditions, a spherically propagating premixed flame may become aerodynamically and thermo-diffusively unstable as a result of the effects of conduction, diffusion combined with flame stretch at the flame front (Groff 1982, Bradley and Harper 1994, Bradley *et al.* 1998). At higher Lewis numbers it is initially thermo-diffusively stable, but as it propagates and the stretch rate reduces, instabilities eventually give rise to pronounced wrinkling of the flame at the larger radii (Bechtold and Matalon 1987). Such instabilities, which also develop at low Markstein number, Ma, are predominantly hydrodynamic and are initiated at a critical value of Peclet number, Pe_C, the flame radius normalized by the flame thickness, δ_l. Below this critical value of Pe_C, flame stretch rate is sufficiently high to maintain the flame stability and the flame surface is smooth (Bradley and Harper 1994, Bradley 1998). At the critical value, Pe_C, the developing instabilities take the form of cracks propagating across the flame surface (Bradley and Harper 1994). The formation of this instability illustrated by Bradley (1998) is shown in Fig. 1.2. A region of

high negative curvature in the flame surface, typically arising from interaction with a spark electrode, initiates a propagating crack. Such cracks are prone to cross-cracking at corners, until eventually they form a coherent cellular structure covering the entire flame surface.

This first occurrence of a developed cellular structure is observed at a second critical number, Pe_{cl}, which is usually much higher than the first critical number, Pe_{c} (Groff 1982, Bradley *et al.* 1998, Bradley 1998). It is accompanied by an increase in flame speed, as a result of the rapid increase in flame surface area. This observed flame acceleration is used to estimate the value of Pe_{cl}, and is discussed in § 3.3. For values of $Pe \geq Pe_{\mathrm{cl}}$, the flame speed increases continuously as a consequence of the increasing wrinkled flame surface area. Measured values of flame speeds in large unconfined explosions (Lind and Whitson 1977, Makeev *et al.* 1983), when plotted against time, t, suggested to Gostintsev *et al.* (1987) a transition to a turbulent flame propagation at a third critical Peclet number, Pe_{t}. Gostintsev *et al.* (1987) surveyed the results of several experimental measurements of flame propagation in large scale explosions and suggested the value of Pe_{t}, was between about 120,000 and 220,000, for the transition to a turbulent flame. In this regime they related the flame radius, r, to time by a law of the form:

$$r = r_{\mathrm{o}} + A\, t^{3/2} \tag{1.12}$$

in which r_{o} is a datum flame radius and A^2 is an empirical constant that depends upon the mixture. A has the dimensions of rate of energy release per unit mass [J/(Kg.sec)].

1.6 Classification of Turbulent Premixed Flames

Turbulent flames found in practical devices cover a wide spectrum of phenomena which depend on the intensity of the turbulence, the temperature and pressure levels, the reactant air-fuel ratio and the fuel itself (Borman and Ragland 1998). Dimensional analysis reveals a range of premixed combustion modes in these practical devices, progressing from wrinkling laminar flamelets, to well-stirred reactors. These modes corresponds

to different regimes of combustions and require different approaches for understanding and modeling (Matthews *et al.* 1996). Classical premixed combustion diagrams (Borghi 1985, Peters 1986, Poinsot *et al.* 1990) assume that a reacting flow may be characterized in terms of two non-dimensional numbers:

1. The ratio of the turbulence integral length scale, L, to the laminar flame thickness, δ_l, and

2. the ratio of the root-mean-square velocity fluctuation, u', to the unstretched laminar burning velocity, u_l.

In these diagrams, different regime transitions are associated with specific lines corresponding to constant values of some non-dimensional numbers. These non-dimensional numbers are:

1. Turbulence Reynolds number, Re_{L}, defined as:

$$Re_{\mathrm{L}} = \frac{u' L}{\nu} \tag{1.13}$$

2. Turbulence Karlovitz number, Ka, defined as (Poinsot *et al.* 1990):

$$Ka = \tau_{\mathrm{c}} \left(\frac{1}{A} \frac{\mathrm{d}A}{\mathrm{d}t} \right) \simeq \tau_{\mathrm{c}} \left(\frac{u'}{\lambda} \right) = \frac{u'}{u_l} \frac{\delta_l}{\lambda} \tag{1.14}$$

3. Turbulence Damköhler number based on integral length scale, Da, defined as:

$$Da = \frac{\tau_{\mathrm{m}}}{\tau_{\mathrm{c}}} \tag{1.15}$$

, hence, characteristics flow time, τ_{m}, is the life time of larger eddies in the flow (Turns 1996), and is defined as:

$$\tau_{\mathrm{m}} = \frac{L}{u'} \tag{1.16}$$

Shown in Fig. 1.3 is such a diagram where the logarithm of u'/u_l is plotted over the logarithm of L/δ_l. Here the regimes of premixed combustion are identified as:

1. Laminar flame regime, characterized by $Re_{\mathrm{L}} \leq 1$,
2. Wrinkled flamelet regime, characterized by $Re_{\mathrm{L}} > 1$, $Ka < 1$ and $u' \leq u_l$,
3. Corrugated flamelet regime, characterized $Re_{\mathrm{L}} > 1$, $Ka < 1$ and $u' > u_l$,
4. Distributed reaction zone, characterized $Re_{\mathrm{L}} > 1$, $Ka > 1$ and $Da > 1$,
5. Well stirred reactors, characterized by $Re_{\mathrm{L}} > 1$, $Ka > 1$ and $Da \leq 1$.

Originally, it was believed (Peters 1986) that the line, $Ka = 1$, which is the Klimov-Willimas criterion, is the limit between the flamelet regimes and the distributed reaction zones. However, direct numerical studies of Poinsot *et al.* (1990) have suggested higher values of Ka for this boundary, which is shown in Fig. 1.3 by broken lines. In this figure, the regime corresponding to the engine combustion is also shown by dotted lines as suggested by Matthews *et al.* (1996). Hence, it appears that the flame in normally operating spark-ignition engines fall within the flamelet regime.

In the flamelet regime, turbulence does not affect the chemistry significantly because the characteristic residence time within the reaction zone is much smaller than the characteristic turnover time of the turbulent eddies. In this regime, propagating reaction fronts, which are wrinkled and convoluted by turbulence, can be identified. However, within the corrugated flamelet regime, flame peninsulas may become increasingly important as the turbulence intensity increases and/or as the mixture becomes more dilute (Matthews *et al.* 1996). Hence, the effect of strain and curvature are important for the spark-ignition engine combustion simulations. The effect of strain have been widely used to correlate the turbulent burning velocity.

Recently the analyses of turbulent flame in the flamelet regimes have involved the various spatial statistical properties of the flame surface. Hence, the flame surface area, flame curvature and orientation statistics provide a complete geometrical description

of the turbulent flame surface propagation (Lee *et al.* 1993). The flame surface area is important as an indicator of the degree of flame front wrinkling, as well as a means to measure the turbulent burning velocity. Flame stretch due to aerodynamic strain and curvature affects the turbulent flame propagation. Previously, only the effect of strain was used to correlate with the turbulent burning velocity (Bradley *et al.* 1992), probably because the overall effect of the flamelet curvature on the burning rate integrates to zero for the symmetric curvature distribution (Becker *et al.* 1990). However, a non-linear relationship between curvature and stretch is now well recognized and as a result positive and negative curvature cannot be regarded as cancelling each other (Kostiuk and Bray 1994).

1.7 Turbulent Flame Propagation in SI Engines

In a turbulent premixture, the spark energy initiates reaction and a propagating flame front capable of overcoming the high geometric stretch. As the flame kernel grows and the influence of the geometric stretch is superseded by stretch due to aerodynamic strain, the flame is, at first, wrinkled by only the smallest scales of turbulence, whilst the larger scales convect the flame kernel without wrinkling the flame front significantly (Ting *et al.* 1995, Abdel-Gayed *et al.* 1987). Figure 1.4(a) shows schematically, small flame ball interactions. The small flame ball is wrinkled by the small scaled, closely spaced corrugations; while the largest eddies, have been described as 'wandering giants' that occasionally kick the flame around causing the flame convection (Ting *et al.* 1995). The large flame ball / small eddy interaction is shown in Fig 1.4(b). The size of the eddy interacting with the initial flame kernel plays an important role in the early flame development. Early flame growth is of particular interest because it is critical to the complicated transient combustion process in a closed combustion chamber. Although most of the mass in the chamber burns in the later stage of the combustion, a large portion of the total combustion time is occupied by early flame growth (Checkel and Ting 1993). It is now widely accepted that the early flame development is the key factor affecting the cycle-to-cycle variations in the engine (Shen *et al.* 1996).

As the kernel continues to grow it becomes progressively wrinkled by larger length scales with an associated increase in the turbulent burning velocity as a result of the contribution of an increasingly larger portion of the turbulence spectrum (Ting *et al.* 1995), until the size of the kernel is sufficient to be affected by the entire turbulence spectrum. Eventually a fully developed turbulent flame ensues (Abdel-Gayed *et al.* 1987, Ting and Checkel 1997). However, a reverse effect, "de-developing turbulence", might occur as the flame approaches the walls - such that only progressively smaller scales of turbulence affect the flame propagation (Merdjani and Sheppard 1993).

1.8 Turbulent Burning Velocity and their Correlations

Unlike a laminar flame, which has a characteristic burning velocity that depends uniquely on the properties of the mixture and the initial condition, a turbulent flame has a propagation velocity that depends also on the flow field parameters. Turbulent burning velocity, u_t, is defined as 'the velocity at which unburned mixture enters the flame zone in a direction normal to the flame' (Turns 1996). In this definition, the flame surface is represented as some time-mean quantity, recognizing that the instantaneous position of the high-temperature reaction zone may fluctuate widely. Experimentally, the value of u_t is usually measured from two-dimensional photographs of an essentially the three-dimensional phenomenon. Traditionally, turbulent burning velocity has been related to the r.m.s. turbulent velocity and both of these quantities have been normalized by the laminar burning velocity.

In a seminal work, Bradley *et al.* (1992) have presented correlations of turbulent burning velocity from about 1650 experimental values, obtained in burner and stirred bombs. This relationship between u_t/u_l and u'_k/u_l is shown in Fig. 1.5. Here, u'_k is the 'effective' r.m.s. turbulent velocity influencing the flame. As the flame develops this value tends towards u'. The full line curves in the figure show the effects of flame straining by turbulent field in terms of the product of the Karlovitz stretch factor, K, and the Lewis number, Le. Previously (Abdel-Gayed *et al.* 1987), the correlations had

been presented in terms of K for two ranges of Le. However, Bradley *et al.* (1992) found that the experimental data correlated better with the product KLe than solely with K for two separate ranges of Le. The dashed lines represent values of R_L/Le^2, which is the appropriate dimensionless group expressing turbulent Reynolds number effects. These were obtained from a rearrangement of the equation for the Karlovitz stretch factor. These correlations are relevant to both combustion in engines and gaseous explosions hazards, though the latter tend to have larger length scales.

However, problems emerge in the definition of u_t. These are principally associated with definition of the mean flame area, with which the burning velocity must be coupled. Because of this, measured values of turbulent burning velocities deduced from pressure records can be different from those measured from schlieren-based photographs. Abdel-Gayed *et al.* (1986) identified two burning velocities, one, u_t, based on the propagation rate of the flame front and another, u_{tr}, a true burning rate based on the conversion rate to burned products. Further studies of these two definitions are important and form a part of the present work.

1.9 Scope of the Thesis

The thesis reports studies of spherically expanding premixed flames for different initial conditions of pressure, temperature and equivalence ratio under both laminar and isotropic turbulent conditions. Schlieren photography is used predominantly to study the laminar flame propagation, while the planar Mie scattering (PMS) technique is used to study turbulent flame propagation. Flame surface contours of turbulent flames also are obtained using the planar laser induced fluorescence (PLIF) technique. The experimental techniques employed are described in Chapter 2.

Measurements and the computational techniques for developing laminar burning velocities and Markstein numbers are discussed in Chapter 3, while the results thus obtained and comparisons of them with the results of others are presented in Chapter 4. It is found that laminar flames at high pressure more readily become cellular beyond a

a certain critical size. The transition to a cellular flame and the subsequent increase in flame speed is presented in Chapter 5.

After this study of laminar flames and their instabilities the structure of turbulent flames revealed by PMS is reported in Chapter 6. This leads to an examination of different ways of defining the turbulent burning velocity and the presentation of results also in the same chapter.

Analyses of flame fronts using PMS and PLIF techniques are presented in Chapter 7. These yield pdfs of curvature for a number of different condition. These pdfs are related to turbulent r.m.s. velocities and to the earlier work on flame instabilities.

Chapter 8 draws conclusions from the work and makes some suggestions for further researches.

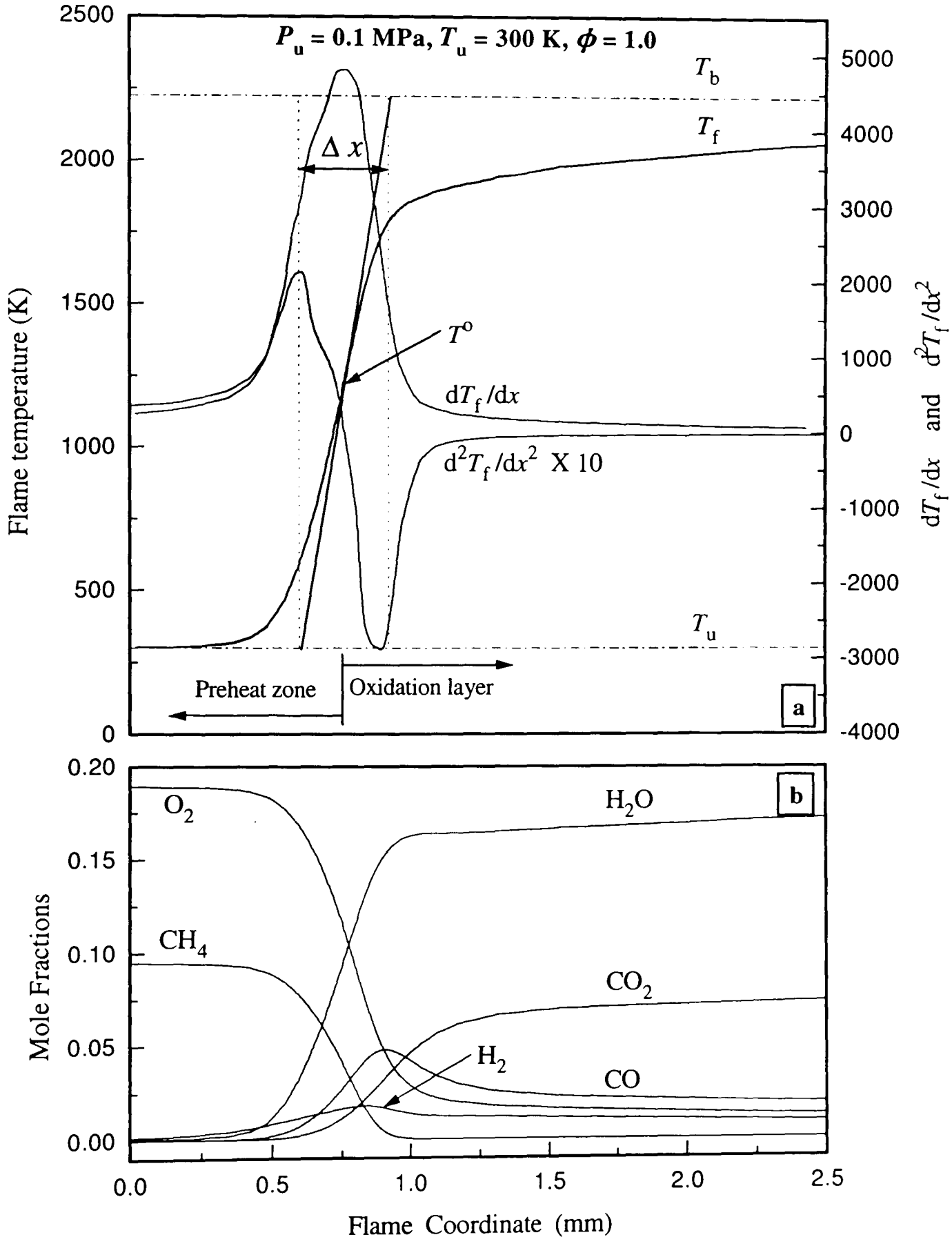

Fig. 1.1. Composition, temperature profiles and their derivatives for a freely propagating, one-dimensional, adiabatic premixed flame in a stoichiometric methane-air mixture at 0.1 MPa and 300 K.

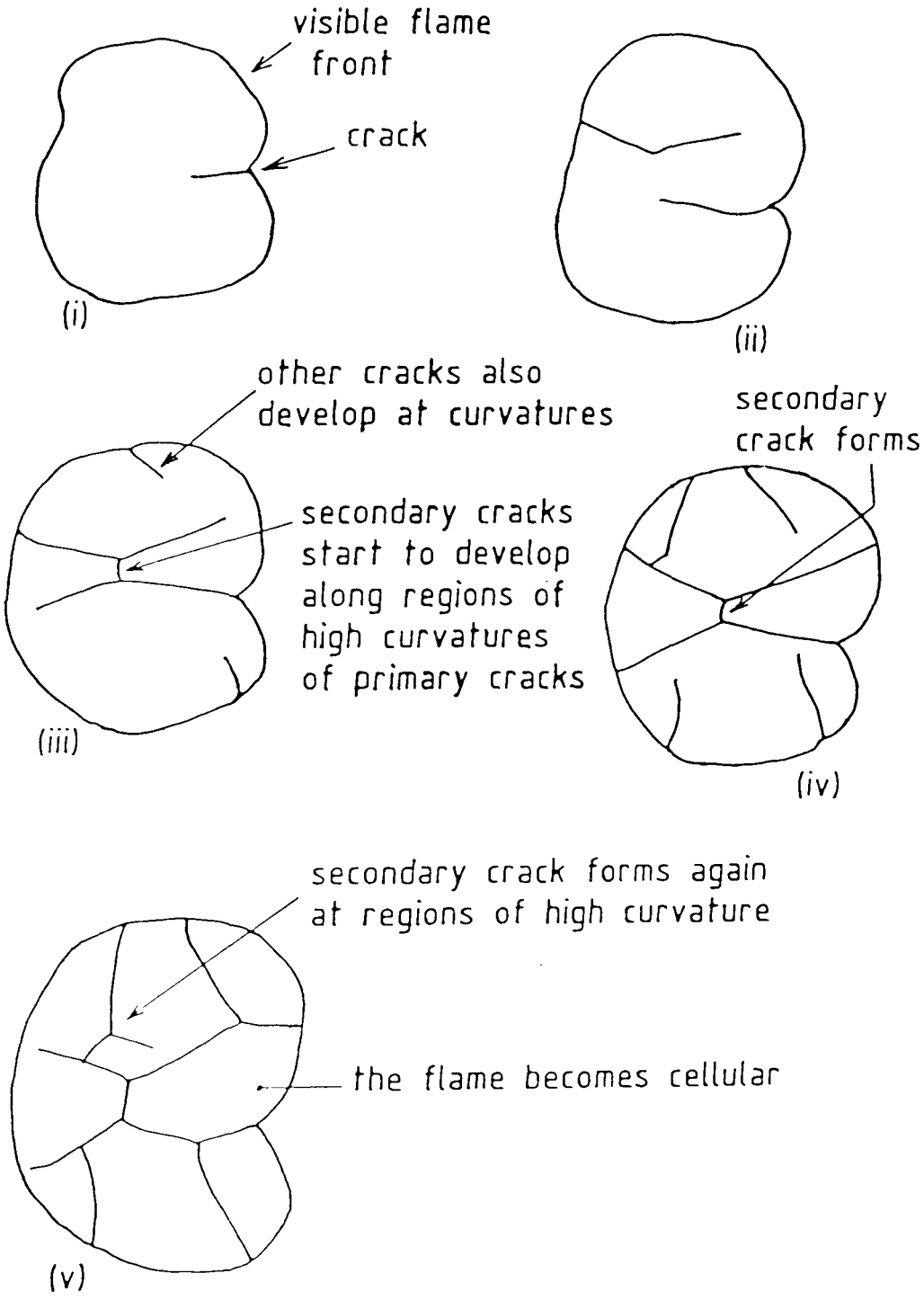

Fig. 1.2. Details of crack development on a flame surface (Bradley 1998).

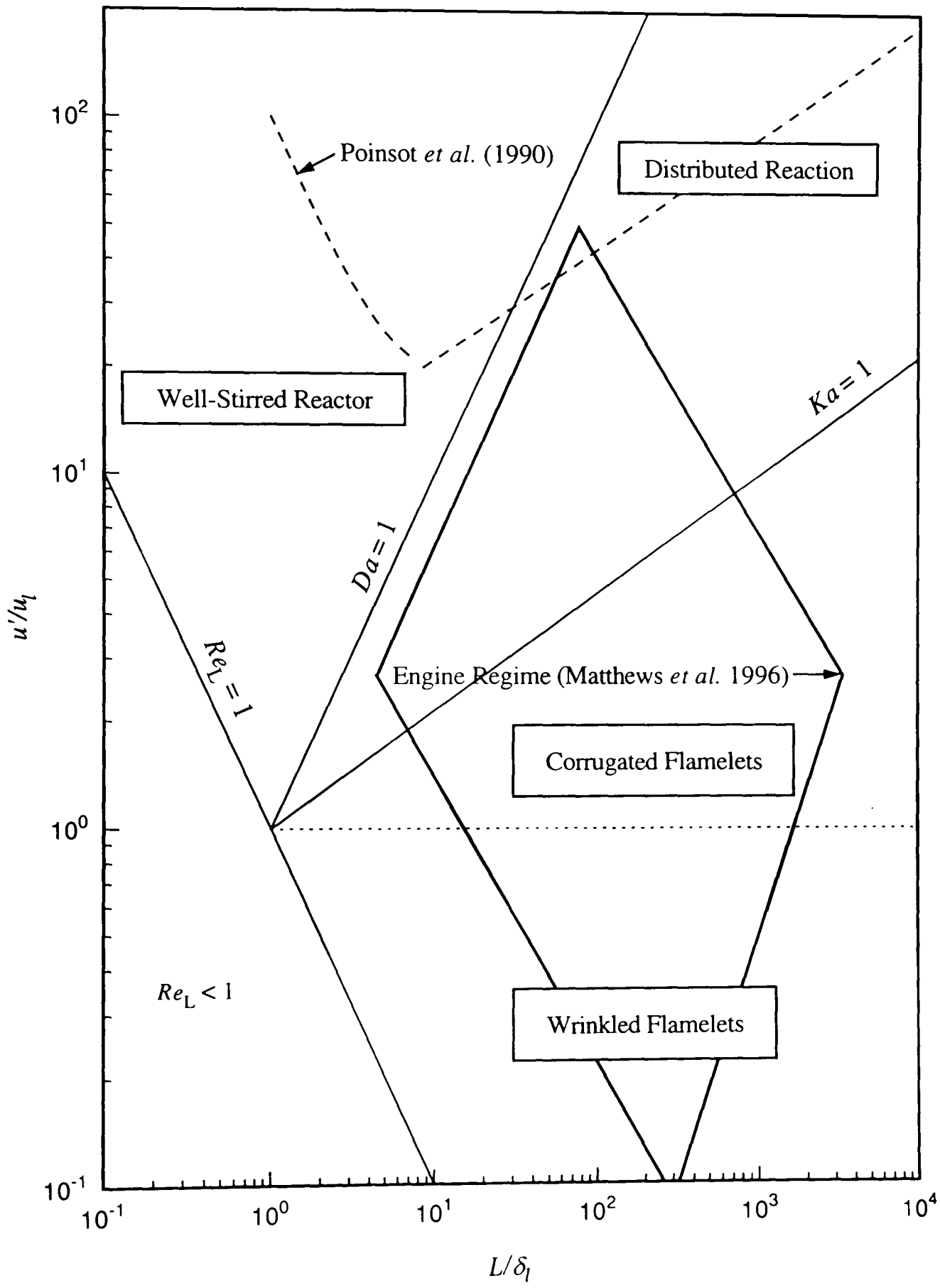

Fig. 1.3. Regimes of turbulent premixed combustion.

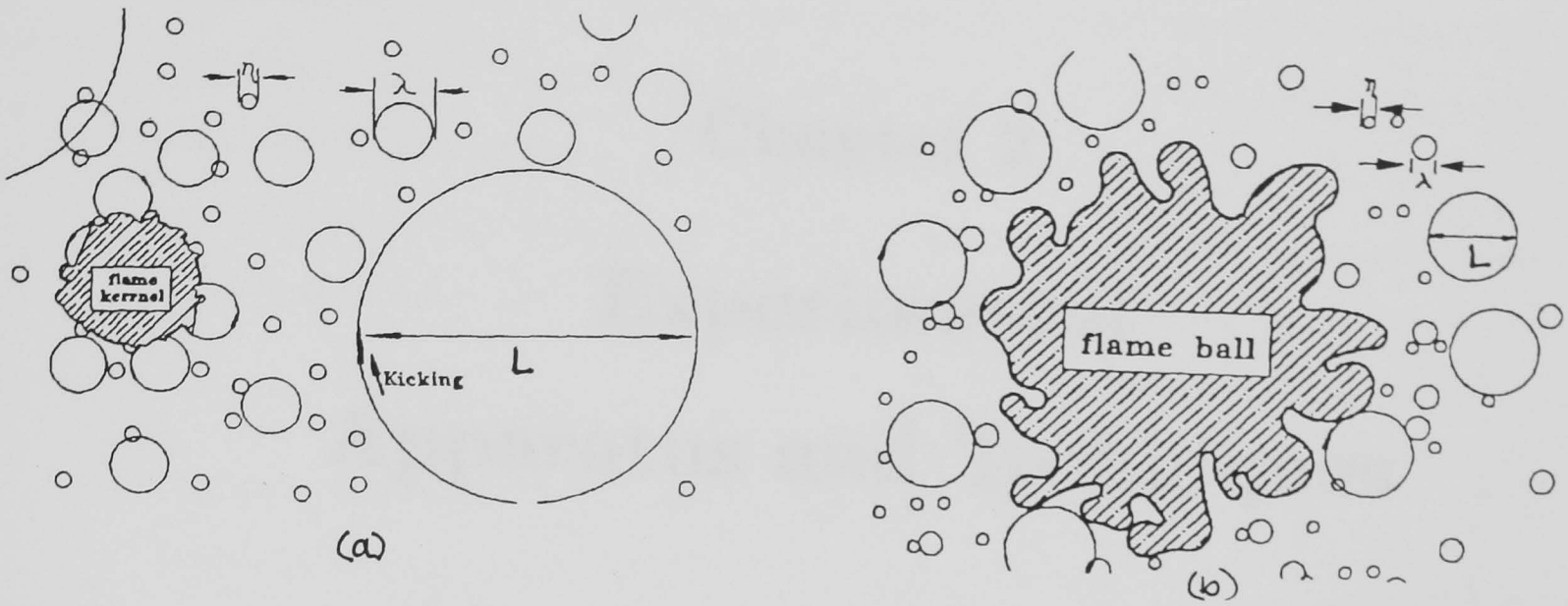

Fig. 1.4. Relative size of the flame kernel (a) a small flame kernel in the midst of relatively large eddies of different sizes, and (b) a large flame kernel in the midst of relatively small eddies of different sizes (Ting *et al.* 1995).

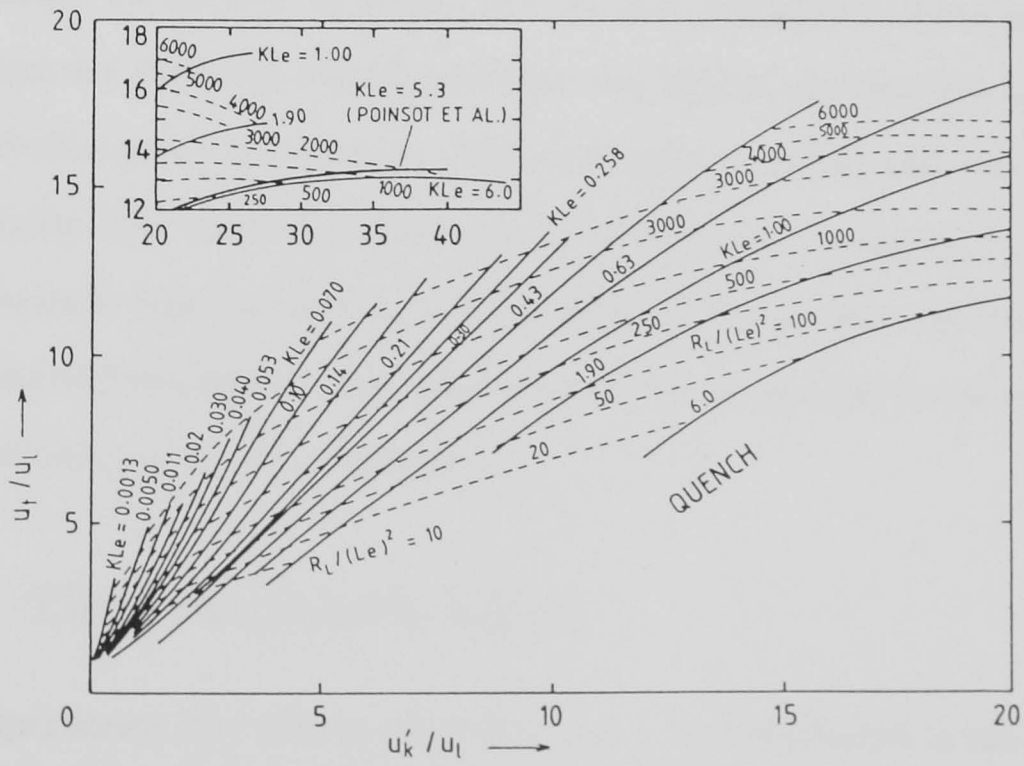

Fig. 1.5. Correlation of turbulent burning velocity by Bradley *et al.* (1992). Broken curves show R_{L}/Le^2.

Chapter 2

Experimental Apparatus and Techniques

2.1 Introduction

Flame propagation in methane-air mixtures was studied at various initial pressures, temperatures and compositions under laminar and turbulent conditions in a combustion vessel. Schlieren photography was used to study laminar flame propagation, while a planar mie scattering (PMS) technique was used to elucidate the important aspects of turbulent flame propagation. Turbulent flame curvature also has been studied using planar laser induced fluorescence (PLIF) images. Apparatus common to these techniques is reported first and this is followed by the more specific apparatus and experimental techniques. Only brief descriptions are reported in those instances where detailed information exists elsewhere.

2.2 The Combustion Vessel

The experiments described in the present study were conducted in the fan-stirred combustion vessel shown in Fig. 2.1. It is a 380 mm diameter spherical stainless steel vessel capable of withstanding the temperatures and pressures generated from explosions at initial pressures of up to 1.5 MPa and initial temperatures of up to 600 K. The vessel

has 3 pairs of orthogonal windows of 150 mm diameter and 100 mm thickness, made with schlieren quality glass. These windows provided the optical access required for the photographic and laser techniques used in the present study. Four identical, eight bladed, separately controlled fans, symmetrically disposed in a regular tetrahedron configuration, created a central region of isotropic turbulence. The speed of each fan was accurately adjustable between 3.3 and 176 Hz (200 and 10000 rpm) via a solid state variable frequency converter unit. Details of the vessel have been described by Ali (1995) and the fan speed control mechanism was described by Scott (1992).

The turbulence parameters within the vessel were calibrated by Bradley *et al.* (1996)(b) using laser doppler velocimetry (LDV). The turbulence within the central region of the vessel was found to be uniform and isotropic with very low mean velocities. The r.m.s. turbulence velocity, u', was found to be represented by

$$u'(\mathrm{m/s}) = 0.00119 f_s(\mathrm{rpm}) \tag{2.1}$$

where f_s is the fan speed. The integral length scale, L, obtained by a two point correlation, was found by Bradley *et al.* (1996)(b) to be 20 mm and was independent of fan speed and pressure.

A quartz pressure transducer, Kistler 701H, was mounted flush with the inner surface of the vessel to record the pressure rise prior and during an explosion. The transducer was connected to a Kistler Charge Amplifier, type 5007, which is then connected to a personal computer via an analogue to digital converter (ADC) board, DAS-50, supplied by Keithley Instruments Ltd. Mixture initial pressure was measured with a Druck PDC 081-0499 pressure transducer. This transducer could only withstand a maximum pressure of 1.5 MPa and was, therefore, isolated from the vessel before an explosion.

The temperature was measured by a stainless steel sheathed type K thermocouple of 1.5 mm diameter, placed, exposed to the mixture, near the vessel surface. The

mixture temperature was read using a CAL 320 temperature controller. The unit was also used to control the heater during mixture preparation.

2.2.1 Ignition System

Ignition of the mixture was achieved via a standard 6.35 mm Minimag spark plug. It was mounted in the center of the vessel using a stainless steel tube in which was fitted a PTFE insulated high voltage lead. A Lucas 12 V transistorized automotive ignition coil system was connected to the spark electrode assembly. The cathode of the ignition circuit was connected to earth via the stainless steel tube and the main body of the vessel. The average spark energy of the system was determined by Bradley *et al.* (1996)(b) to be 23 mJ. For experiments undertaken at an initial pressure of 0.1 MPa, the ignition unit was found to operate reliably with a spark gap of 1 mm. However, to achieve a reliable breakdown at higher pressures, it proved necessary to reduce the gap to 0.6 mm. The ignition system failed to provide sufficient breakdown for rich ($\phi > 1.2$) methane-air mixtures at atmospheric pressure. Therefore, in the present study rich methane-air mixture was limited to $\phi = 1.2$.

2.2.2 Mixture Preparation

Mixtures were prepared in the explosion vessel. Prior to filling, the vessel was evacuated to a pressure of less than 1 kPa and flushed twice with dry cylinder air to remove any residual products from the previous experiment. After further evacuation, the mixture components were added, methane of 99% purity first, to its respective partial pressure and then the vessel was filled to the required initial pressure with dry cylinder air, supplied by BOC. Throughout the filling process, the temperature of the mixture was maintained at within 5 K of the intended initial value. For laminar flame studies, the fans were kept running during the filling period only to ensure adequate mixing of the reactants and the fans were stopped for at least one minute before ignition to ensure a quiescent premixture. However, the fans speed were maintained at within ± 10 rpm for

turbulent flame propagation study. Pressure and temperature were measured immediately prior to ignition, which was initiated only when the temperature was within 5 K of the intended value with 2% pressure tolerance.

For explosions with an initial reactant temperature up to 358 K, the entire vessel was preheated by a 2 kW heater. However, for higher initial temperatures, it proved necessary to preheat the entire vessel with a purpose built bank of electrical heating elements totaling 8 kW. Once the vessel had attained the required temperature, the 2 kW heater element provided the required temperature control during mixture preparation. The external surfaces of the vessel were insulated to minimize heat loss.

2.3 Diagnostic Techniques

The experimental arrangement for laminar flame propagation studies using schlieren photography was described by Ali (1995), while arrangements for the PMS technique has been described by Bradley *et al.* (1996)(b). In addition, experiments using the PLIF technique were carried out by Dr. Robert Woolley of the School of Mechanical Engineering, University of Leeds, and Dr. Russel Locket of Cranfield University. Flame front contour coordinates, with a spatial resolution of 0.157 mm/pixel, were also obtained by Dr. Woolley, using suitable image processing techniques. These flame coordinates were also analysed by the present author, in addition to the PMS image coordinates, to study the curvature distribution of the turbulent flame front.

2.3.1 Schlieren Photography

Spherically expanding laminar flames were studied using high speed schlieren ciné photography at, typically, 6000 frames per second. Schlieren photography has an advantage of providing a readily definable flame surface in the images (Glassman 1996) at a certain isotherm. This isotherm depends on the initial temperature, pressure and composition

of the air-fuel mixture, as well as the curvature of the flame front (Rankin and Weinberg 1997). Therefore, a correction is required to estimate the cold front radii from the schlieren isotherm (Bradley *et al.* 1996) and is discussed in § 3.3.

The experimental arrangement for laminar flame propagation studies is shown in Fig. 2.2. In addition to schlieren photography, pressure and CH emission, generated in the combustion process, also were routinely recorded. Both of these quantities give a qualitative idea of the mass burning rate of the combustion process (Mushi 1992 and Ali 1995). In the present study, the pressure and CH data were used to observe the repeatibility of experiments at similar initial conditions.

A Spectra-Physics 10 mW He-Ne laser, model 106-1, with a beam diameter of 0.65 mm and wavelength of 632.8 nm was used as the light source. The beam was expanded by an Olympus A40 microscope objective lens and a 150 mm diameter lens with focal length 1000 mm produced the 150 mm diameter parallel beam which passed through the vessel windows. From the vessel, the parallel beam passed through another 150 mm diameter lens with a focal length of 1000 mm. This focused the beam to a 0.65 mm pinhole placed at the schlieren focus. The divergent beam then passed into a Hitachi 16HM high speed ciné camera which had a maximum speed of 10000 frames per second. The pin-hole blocked off some of the incident light and, because of the density gradient generated refraction in the flame, it caused an increase or decrease in the intensity of light passing through it. Therefore the flame reaction zone was readily visualized. The sequence of schlieren images of the expanding flame were recorded on Ilford FP4 16 mm high speed film. A sample of flame images thus obtained are shown in Figs. 3.1 to 3.3 and are discussed in § 3.3.

Because the duration of an explosion was of the order of only a few milliseconds, it was vital that the spark and all instrumentation be precisely synchronized. After mixture preparation, the experiment was initiated by activating a trigger switch attached

to a control unit to start the camera. When the camera had reached the pre-set framing speed, it sent a trigger pulse back to the control unit. Upon receiving the trigger pulse, the control unit transmitted a spark start pulse to the spark unit and also sent a signal to a personal computer through the analogue to digital converter (ADC) to start recording pressure and CH emission data. Prior to any explosion, the room lights were turned off to minimize the amount of extraneous light entering the camera and the photomultiplier (PM), which was used to record CH emission intensity.

2.3.2 Planar Mie Scattering (PMS) Technique

In the present study, PMS was used to reveal details of the two dimensional structure of three dimensional turbulent flames. The technique involved the recording of light scattered, without a change in the frequency of light, from small seed particles. The seed either evaporated, sublimed or burned as it crossed the flame front and consequently did not scatter light, while the seed in the unburned mixture scattered light, and so provided a planar section of the complex, three dimensional, flame front geometry. Scattered light was imaged perpendicular to the incident light. The cross section of the flame was identified as the frontier between the bright, unburned, and the dark, burned, regions in the illuminated zone (Durão and Heitor 1990).

The selection of seed particles was important as it effects both the image quality and the measured location of the flame front. Different particles burn or sublime at different temperatures and they have different scattering characteristics (Durão and Heitor 1990). Scott (1992) investigated various seeding materials and methods of introducing them in a V-flame burner and in the present combustion vessel. He investigated oil droplets, alumina, stabilized zirconium oxides, magnesia and titanium dioxide particles and concluded that titanium dioxide provided the best light scatting characteristics. However, titanium dioxide particles are abrasive and tended to contaminate the window. Therefore, in the present study, tobacco smoke was used. Wirth *et al.* (1993) and Pontoppidan (1995) highlighted the advantages of using tobacco smoke in their engine studies and reported that, although the smoke was composed of particles with mean

diameter less than one micron, the particle concentration was sufficient to visualize the flow field. Moreover, Wirth *et al.* (1993) reported that tobacco particles were able to survive at high compression temperature before ignition and they burned out immediately in the flame front to generate a good contrast between burned and unburned regions. In the present study, good quality of images of turbulent flame propagation were obtained using tobacco smoke. A sample of images obtained using this technique is shown in Fig. 6.1 and discussed in § 6.1.

The arrangement for flame visualization using the PMS technique in turbulent flame studies is shown in Fig. 2.3. A copper vapor laser, model CU15-A, made by Oxford Lasers, operating simultaneously at wavelengths of 510.6 nm (green) and 578.2 nm (dark yellow), was used as a lasing source. It had the advantage of a very high pulse rate (8-14kHz), with a short pulse duration (15 ns) and a relatively high pulse energy (2 mJ at 510.6 nm and 1 mJ at 578.2 nm at 5 kHz). The system consisted of a laser head, from which the laser output was obtained, the power supply and a control unit. Details of the system and its operation were described by Lee (1995).

A thin laser sheet was obtained using a combination of spherical and cylindrical lenses as shown in Fig. 2.3. A 500 mm spherical Bi-convex lens focused the laser beam, and a 1000 mm Plano-convex cylindrical lens, shortly thereafter, expanded the beam in one plane to form a sheet with an estimated thickness of 0.5 mm. The laser sheet was passed along a vertical plane just in front of the spark plug in the center of the vessel and was Mie scattered from tobacco smoke particles. The scattered light was recorded and stored using a Kodak Ektapro HS Motion Analyzer, Model 4540. It consisted of an ultra high-speed video recording system, capable of recording 4500 full frames per second. The light sensitivity of the video system was excellent and its sensitivity at the high gain setting was equivalent to ISO 3000. It had a 256x256 pixel sensor, with a 256 gray level response. A 510.6 nm interference filter was attached to the camera lens to prevent combustion generated light from obscuring the sheet images.

The electronic triggering features of the Motion Analyzer made it possible to store images prior to, after, and at both sides of the trigger pulse. In the present study, 'center recording mode' was used in which images were recorded until the trigger signal was received and then 1536 additional frames were recorded after the trigger. Prior to triggering the spark, the copper-vapor laser was synchronized to the camera framing rate at 4.5 kHz. Upon receiving the spark signal through a control switch, the motion analyzer stored digital images in Dynamic Random Access Memory (DRAM) and these were available for immediate playback or for subsequent image processing discussed in § 2.4.2.

2.4 Data Processing

Data processing techniques employed in the present study are discussed below. Analyses of data obtained from schlieren photography is presented in Chapters 4 to 6, while the analyses of data from laser sheet images are presented in Chapters 6 and 7.

2.4.1 Schlieren Photography

Films, obtained using schlieren photography were developed in the school's photographic laboratory using a Bray Film Processor. Flame images were viewed with a Vanguard Projector which used a 16 mm back projection onto a translucent screen with a reading area of 30x50 cm for analysis of still and ciné film from their blown up images (about 40 times). Films were analyzed by measuring three diameters of the flame image. Since the flame was almost circular, the difference in the three measurements was usually less than 1%. The average of the three measurements was used in subsequent analysis.

A "channel shaped" metal marker, with two arms 60 mm apart was attached to the vessel window frame to provide the scale for the recorded images. Lengths measured on the projected images from the processed film were converted to actual lengths in the explosion using the marker calibration.

The time between exposures on the ciné films was established using a timing mechanism which consisted of a light emitting diode (LED), flashing at 1 kHz, built into the high speed camera to produce a timing mark on the film at intervals of one ms. The distance between each timing mark was measured to derive the camera framing rate at that time.

From these measurements, flame radius against time data were obtained and these were later analyzed to derive the laminar burning velocities and to quantify the effects of stretch on it. These are discussed in Chapters 3 and 4. Also the study of the transition to instability of an initially laminar flame is discussed in Chapter 5.

2.4.2 PMS Technique

After each explosion, the images stored in the camera memory were played back at 1 Hz and were recorded onto video tape by a VCR connected to the processor. These video images were later captured by a program 'VIDMEM' on a Silicon Graphics computer in a 'RGB' format with a resolution of 576x768 pixels. These images were cropped down to 400x400 pixels by the program 'IMGWORKS'. The cropped images were then converted into gray scale ones with 256 gray levels and the brightness was balanced by histogram equalization (Baxes 1994) before they were saved in the 'TIFF' format. The saved images were then analyzed using 'CANTATA', a suit of subroutines, within the signal and image processing software 'KHOROS', which was installed on the UNIX based SUN workstations. CANTATA was used because of its visual programming ability in which a sequence of operations can be linked to form a worksheet which provides fast, user friendly, image processing.

The images obtained in the present experiments were 'noisy', due to the nonuniformity in pixel sensitivity, variations of the spatial distribution in laser intensity and nonuniform seeding. Hence, an initial processing sequence with CANTATA consisted of removing the noise by using a mask image and applying a Fourier transform (Baxes 1994), and then normalizing the images by a background image taken just prior to

ignition. However, this processing was not always successful in removing all the noise from the images, specially at high levels of turbulence in which the smoke particle distributions deteriorated very rapidly and resulted in images with low contrast. This was especially true near the end of flame propagation. A further difficulty resulted from the very high non uniformity of the laser sheet in which its intensity was poor on one side. Therefore, it was difficult to select a suitable threshold value to convert these grey scale images into binary format in which each pixel classifies the associated small volume in the sheet as occupied by unburned or burned gas.

Therefore, attempts were taken to extract the flame edge coordinates by tracing them with a mouse and then saving the coordinates as a text file for further analysis. However, facility to do this was not available in any commercial software. Therefore, an image viewer, 'IMAGE' was developed, by the present author', using the 'Visual Basic' programming language. It could view a bitmap of 400 by 400 pixels and could save the pixel coordinates of the flame contour when the mouse was traversed along the flame front. Flame coordinates thus obtained for flame images shown in Fig. 6.1 are shown in Fig. 6.2 and are discussed in § 6.1.

The resolution of the images was measured by imaging a ruler vertically in the focal plane. Using image processing, the number of pixels over the distance of 1 cm was then calculated to yield an image resolution of 0.32 mm per pixel.

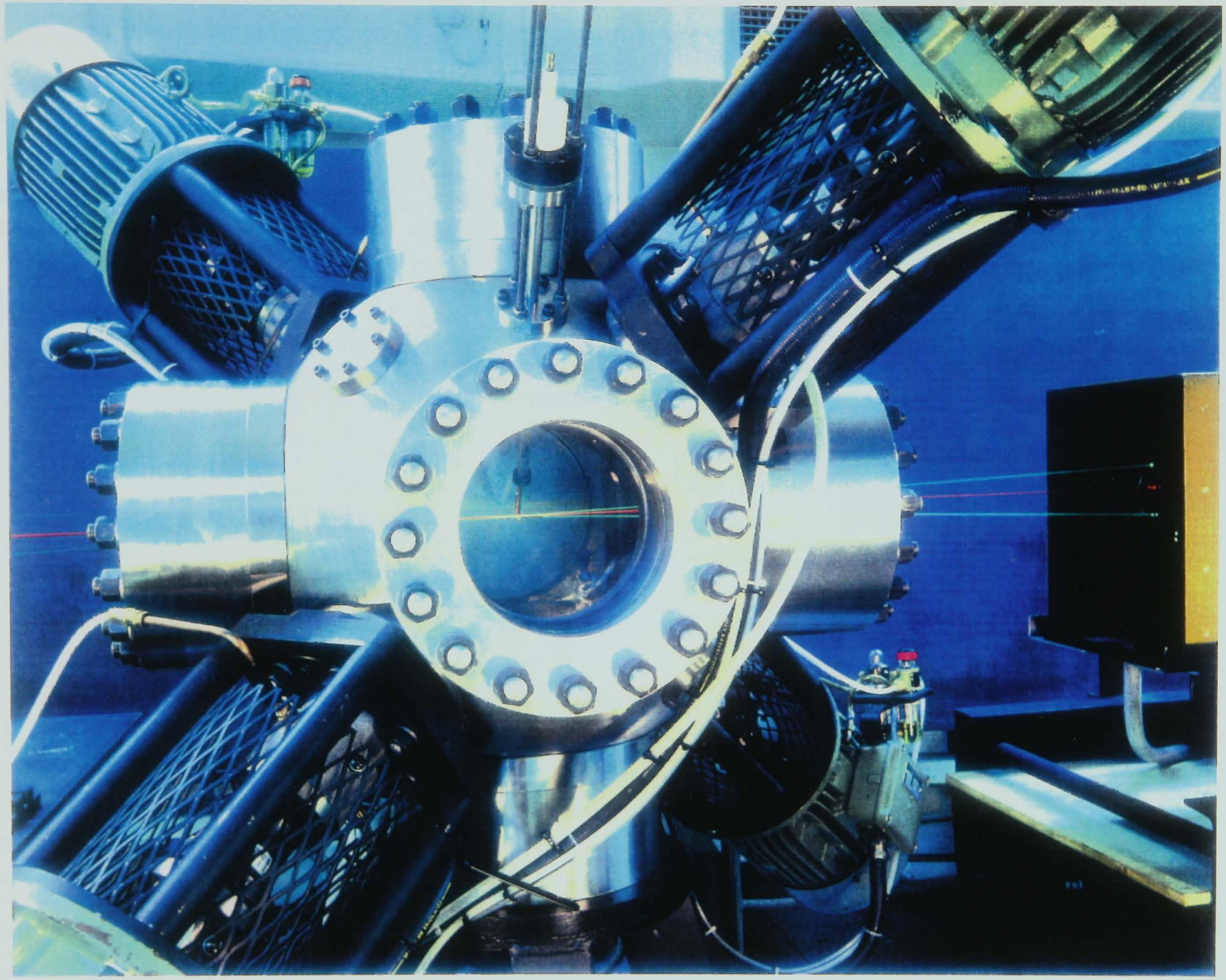

Fig. 2.1. The fan-stirred combustion vessel.

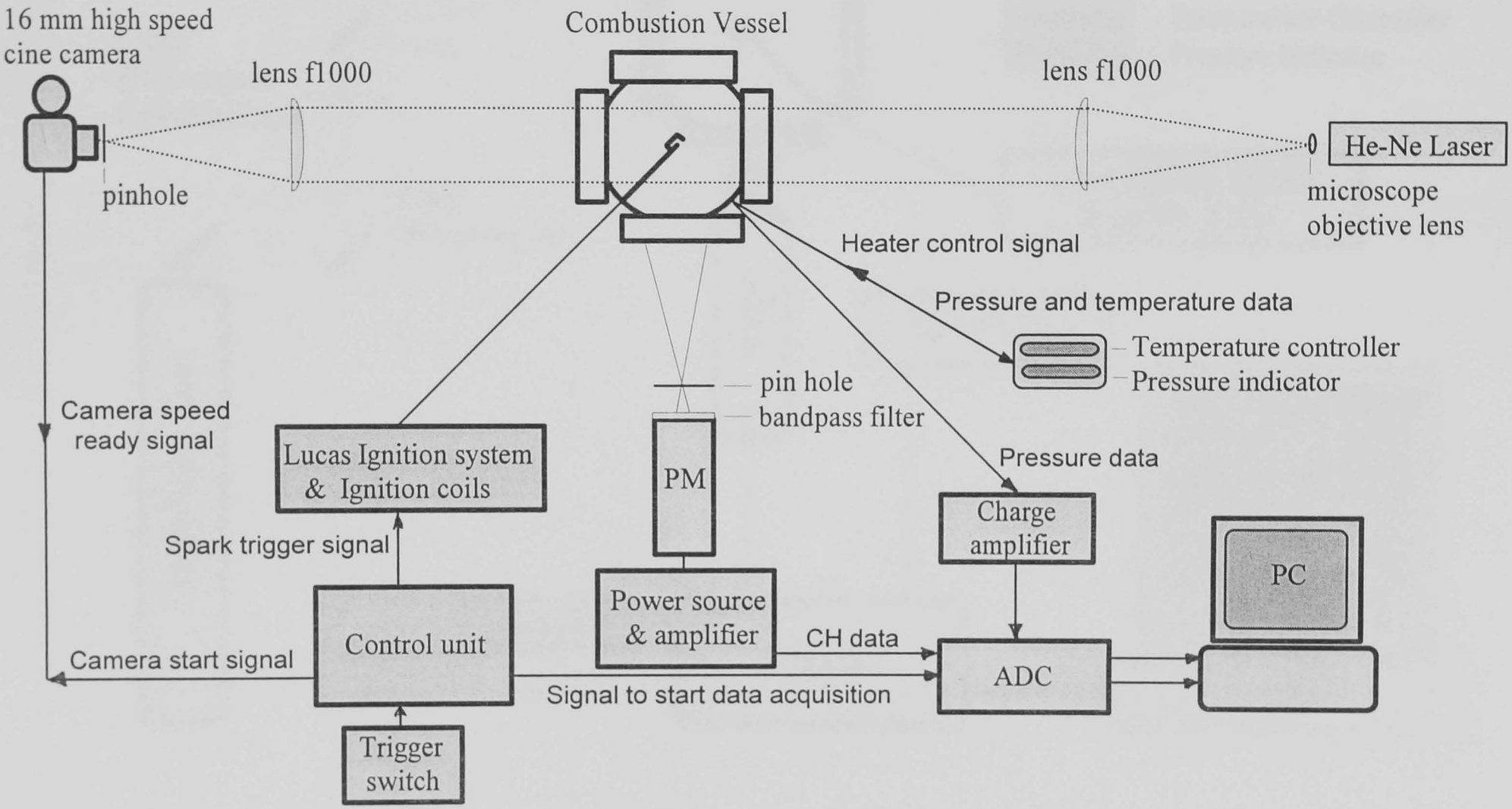

Fig. 2.2. Experimental setup for schlieren photographic studies of laminar flame propagation.

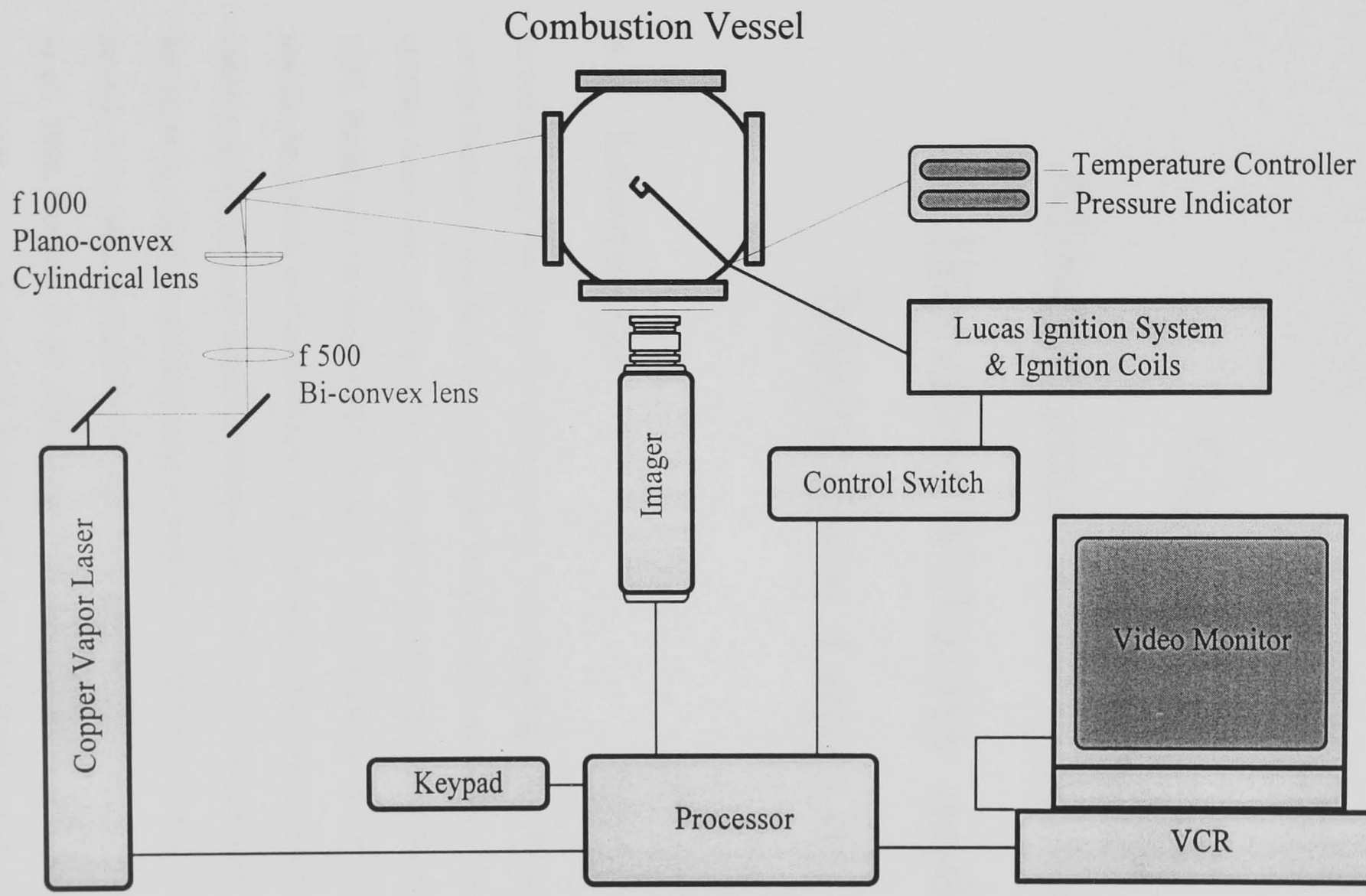

Fig. 2.3. Experimental setup for PMS measurements of turbulent flames.

Chapter 3

Measurement of Laminar Burning Velocity and Markstein Length

3.1 Introduction

In recent years there has evolved a greater understanding of the effects of flame stretch on the laminar burning velocity. Several techniques for measuring the laminar burning velocity have been used and are reviewed critically elsewhere (Andrews and Bradley 1972, Rallis and Garforth 1980). Some of these techniques do not readily yield information on stretch and instabilities, and this makes them unsuitable for precise quantitative studies. Because spherical flames have a number of advantages over other flames for burning velocity measurements, a number of experimental studies, at well defined stretch, have been undertaken in which such flames at variety of conditions (Bradley *et al.* 1996, Bradley *et al.* 1998, Bradley and Harper 1994, Dowdy *et al.* 1990, Aung *et al.* 1995, Aung *et al.* 1997, Taylor 1991, Ali 1995, Brown *et al.* 1996, Clarke *et al.* 1995). Spherical flames, following spark ignition, are well suited for measurement purposes because their flame stretch is uniform and unambiguously defined (Bradley *et al.* 1996, Dixon-Lewis 1990). In the pre-pressure period, in which no significant increase in

pressure is observed, flame speed is found directly from measurements of flame radius at different times by schlieren ciné photography. Measurements at different stretch rates are used systematically to deduce the unstretched laminar burning velocity and the associated Markstein length. Observation of the flame surface has the further advantage of revealing the onset of instabilities, first as flame cracking and then as a developed cellular structure (Bradley and Harper 1994). A small Markstein length is indicative of both a small influence of flame stretch rate on burning velocity and early onset of instabilities (Bradley and Harper 1994).

In the present study, the burning velocity and Markstein lengths of methane-air flames at $\phi = 0.8$, 1.0 and 1.2 are measured between 0.1 and 1.0 MPa and 300 to 400 K using spherically expanding flames. One dimensional planar flame structure and unstretched burning velocities also are computed using PREMIX code (Kee *et al.* 1985) over the same range of initial conditions using a full kinetic scheme, GRI-Mech (Frenklach *et al.* 1995). Methods of analyzing the experimental data and a description of computational techniques are presented in the present chapter. Both experimental and modeled results are presented in Chapter 4. Results from present study are also compared with those of other researches in Chapter 4.

3.2 Laminar Burning Velocity and Burning Rate for a Spherically Expanding Flame

For a spherical expanding flame, the rate of entrainment of reactants at an initial unburned gas density, ρ_u, and radius, r_u, is related to an associated burning velocity, u_n, by (Bradley *et al.* 1996):

$$\frac{dm_u}{dt} = -4\pi r_u^2 \rho_u u_n = -\frac{d}{dt}\left[\int_0^{r_u} 4\pi r^2 \rho dr\right] \tag{3.1}$$

where, ρ is the density at radius r, and r_u is the cold front radius defined in § 3.3. Hence,

$$u_n = \frac{1}{r_u^2 \rho_u} \frac{d}{dt} \left[\int_0^{r_u} r^2 \rho dr \right] \tag{3.2}$$

In Eq. 3.1, the gas within the sphere of radius r_u might be regarded as comprised of a mixture of burned gas at its equilibrium adiabatic temperature, with a density of ρ_b, and unburned gas with a density of ρ_u. Thus, at a radius r and density ρ, the fraction of burned and unburned gas can be expressed as $(\rho_u - \rho)/(\rho_u - \rho_b)$ and $(\rho - \rho_b)/(\rho_u - \rho_b)$, respectively, enabling the left hand side of Eq. 3.1 to be written as:

$$\frac{dm_u}{dt} = -\frac{d}{dt} \left[\int_0^{r_u} 4\pi r^2 \rho_u \left(\frac{\rho - \rho_b}{\rho_u - \rho_b} \right) dr + \int_0^{r_u} 4\pi r^2 \rho_b \left(\frac{\rho_u - \rho}{\rho_u - \rho_b} \right) dr \right] \tag{3.3}$$

The first term on the right represents the rate of entrainment by the flame front of gas that remains unburned, the second the rate of formation of burned gas (Bradley *et al.* 1996). Hence, the laminar burning velocity associated with the appearance of burned product, u_{nr} is:

$$u_{nr} = \frac{1}{r_u^2 \rho_u} \frac{d}{dt} \left[\int_0^{r_u} 4\pi r^2 \rho \left(\frac{\rho - \rho_b}{\rho_u - \rho_b} \right) dr \right] \tag{3.4}$$

Invoking Eqs. 3.1 to 3.4, u_n can be related to u_{nr} by:

$$u_n = u_{nr} + \frac{1}{r_u^2 \rho_u} \frac{d}{dt} \left[\int_0^{r_u} r^2 \rho_u \left(\frac{\rho - \rho_b}{\rho_u - \rho_b} \right) dr \right] \tag{3.5}$$

In Bradley *et al.* (1996), u_n and u_{nr} are related to the S_n by:

$$u_{nr} = \frac{\rho_b}{\rho_u - \rho_b} (S_n - u_n). \tag{3.6}$$

3.2.1 Flame Stretch and Markstein Lengths

In the pre-pressure period, a spherical flame is subjected to stretch due to both curvature, α_c, and strain, α_s. In Bradley *et al.* (1996) their values were related to the

corresponding cold front radius, r_u, by

$$\alpha_c = 2\,\frac{u_n}{r_u} \tag{3.7}$$

and,

$$\alpha_s = 2\,\frac{u_g}{r_u} \tag{3.8}$$

A Markstein length is associated with each term as shown in Eqs. 1.7 & 1.8, reproduced here as Eqs. 3.9 & 3.10:

$$u_l - u_n = L_c\alpha_c + L_s\alpha_s \tag{3.9}$$

and,

$$u_l - u_{nr} = L_{cr}\alpha_c + L_{sr}\alpha_s \tag{3.10}$$

3.3 Measurement of Laminar Burning Velocities and Markstein Lengths

Laminar burning velocities and Markstein lengths are derived from measurements of spherically expanding flame images captured using high speed schlieren ciné photography at, typically, 6000 frames per second. Shown in Fig. 3.1 are such pictures obtained from an explosion of stoichiometric methane-air at an initial pressure of 0.1 MPa and temperature of 300 K. Initial flame kernel is slightly distorted, however, they regained a spherical shape soon. Flame propagation is essentially spherical, and the flame front is smooth and is easily identifiable from these pictures. However, smooth flames don't occur at all conditions. Shown in Fig. 3.2 are schlieren photographs of a lean (ϕ = 0.8) flame propagating in a premixture at 300 K and 0.5 MPa. They reveal the grainy appearance of cell formation and the formation of dimples along the flame front, associated with thermo-diffusive and hydrodynamic instabilities (Groff 1982, Bradley and Harper 1994, Bradley *et al.* 1998, Bradley 1998). The contrast in appearance between a cellular and noncellular flame is emphasized in Fig. 3.3. The cellular flame, in Fig. 3.3, shows the distribution of cells of different sizes as described by Kuznetsov and Minaev

Minaev (1996) as a 'web' of cracks and cells. The transition to instability requires some time in which the cells continue to grow and divide during flame growth. Transition to instability is discussed in Chapter 5.

The flame speed, S_n, is found from the measured flame front radius against time by

$$S_\mathrm{n} = \frac{\mathrm{d}r_\mathrm{u}}{\mathrm{d}t} \tag{3.11}$$

where, r_u is the cold front radius defined as the isotherm that is 5 K above the temperature of the reactants. In Bradley *et al.* (1996), it was shown to be related to the flame front radius that is observed by schlieren ciné photography, r_sch, by

$$r_\mathrm{u} = r_\mathrm{sch} + 1.95\ \delta_l \left(\frac{\rho_\mathrm{u}}{\rho_\mathrm{b}}\right)^{0.5} \tag{3.12}$$

Values of ρ_u and ρ_b are found from the properties of the equilibrated adiabatic products, computed using the thermodynamic data base by Burcat and McBride (1997). Values are validated against results obtained using detailed chemistry as described in § 3.4. Pure gas viscosities are computed using the kinetic theory of gases (Bird *et al.* 1960), and the Lennard-Jones collision diameter, required to calculate the gas viscosity, is taken from Assael *et al.* (1996), while the reduced collision integral is approximated by the Neufeld-Janzen equation (Neufeld *et al.* 1972). Gas mixture viscosity is calculated using the semiempirical formula of Wilke (1950). Full details of the computations of thermodynamic and transport properties are presented in Appendix A.

Equation 3.12 assumes that the schlieren edge results from an isotherm of 460 K as suggested by Weinberg (1955). A more recent work by Rankin and Weinberg (1997) shows that for flames concave to the burned gas, as in the present work, a more appropriate isotherm is a function of flame radius and varies between 850 and 900 K. It proved difficult to derive an alternative form of Eq. 3.12 to account for this latest work. Instead, the distance between the 460 K isotherm and that at 850 K is approximated

to be similar to that of a one dimensional planar flame. This is computed using GRI-Mech which is discussed in § 3.4. Equation 3.12 is modified to include this additional thickness.

Shown in Fig. 3.4 is the variations of r_u with elapsed time from ignition for methane-air mixtures at an initial temperature of 300 K and pressure of 0.1 MPa. Flame radius at a given time depends on the equivalence ratio. Flame speed is obtained by numerical differentiation of the radius against time data. In the present study, the Savitzky-Golay algorithm (Savitzky and Golay 1964, Press *et al.* 1992), presented in Appendix B, is used for the data smoothing and numerical differentiation.

Shown in Fig. 3.5 is the variation of S_n with r_u for a stoichiometric mixture with an initial temperature of 300 K and pressure of 0.1 MPa. Experiments are shown by the crosses and the solid line is Eq. 1.5. Experiments display some scatter of a periodic nature. Similar oscillations have been reported for iso-octane-air mixtures and attributed to acoustic disturbances (Bradley *et al.* 1998). These oscillations are not studied in the present work. At approximately 5 mm radius, the flame speed attains a minimum value as the effects of the spark decay and before normal flame chemistry develops (Bradley *et al.* 1996). Shown in Fig. 3.6 is the variation of S_n with r_u for a stoichiometric methane-air mixture with an initial temperature of 300 K and pressure of 0.5 MPa. In this case the effect of the transition from spark to fully developed flame propagation is not evident as for the previous case in Fig. 3.5. This is due to the differing effect of the flame stretch which is discussed in § 4.2. Therefore, in the present study, flames with radii less than 6 mm are considered, on the basis of the computational study of Bradley *et al.* (1996) not to be fully developed and are not used in further analysis.

Shown in Fig. 3.7 is the variation of S_n with α, for a stoichiometric mixture at 0.5 MPa with an initial temperature of 300 K. At high rates of stretch (small flame radius), the flame speed is high. As the flame expands the flame speed slowly reduces

as does the flame stretch. As stretch is further reduced a point is reached where the flame becomes unstable and cellularity develops, and this is associated with an increase in flame speed. This phenomenon is observed for lean and stoichiometric methane-air mixtures at high pressures and is discussed in Chapter 5. The point at which the flame speed begins to accelerate rapidly with decreasing stretch defines a critical Peclet number, Pe_{cl}, given by the flame radius at the onset of flame acceleration, normalized by the flame thickness (Bradley *et al.* 1998, Bradley 1998). In Chapter 5, values of Pe_{cl} are related to the onset of flame cellularity.

Clavin (1985) suggested that a linear relationship exists between flame speed and the associated stretch, and this has been verified by numerical modeling (Bradley *et al.* 1996), and experimental works (Aung *et al.* 1997, Bradley *et al.* 1998). In the present study, a linear relationship is found to exist, over a wide range of radii that excludes the spark affected and cellular flame regions, and is shown in Fig. 3.7. Hence, the value of L_{b} is obtained as the slope of the plot of S_{n} against α, while S_{s} is obtained as the intercept value of S_{n} at $\alpha = 0$. The unstretched laminar burning velocity, u_l, is obtained from consideration of mass conservation of an assumed infinitely thin flame. Hence, u_l is deduced from S_{s} using:

$$u_l = S_{\mathrm{s}} \frac{\rho_{\mathrm{b}}}{\rho_{\mathrm{u}}} \tag{3.13}$$

Equation 3.13 is valid only at infinite radii for which the curvature can be neglected. For smaller radii, necessary to determine u_{n} as a function of α, Eq. 3.13 is modified to give

$$u_{\mathrm{n}} = \mathcal{S}\left[S_{\mathrm{n}} \frac{\rho_{\mathrm{b}}}{\rho_{\mathrm{u}}}\right] \tag{3.14}$$

Here $\mathcal{S}$ is a generalized function and depends upon the flame radius and density ratio. It accounts for the effects of flame thickness on the mean density of the burned gases.

Bradley *et al.* (1996) computed a generalized expression for $\mathcal{S}$ from modeled methane-air flames at 0.1 MPa and 300 K over a range of equivalence ratios. The general expression is

$$\mathcal{S} = 1 + 1.2\left[\frac{\delta_l}{r_\mathrm{u}}\left(\frac{\rho_\mathrm{u}}{\rho_\mathrm{b}}\right)^{2.2}\right] - 0.15\left[\frac{\delta_l}{r_\mathrm{u}}\left(\frac{\rho_\mathrm{u}}{\rho_\mathrm{b}}\right)^{2.2}\right]^2 \tag{3.15}$$

and this expression is used in the present work. In addition to its validity at 0.1 MPa and 300 K for methane-air mixtures, Eq. 3.15 has been confirmed by Gu (1998) to be valid for propane-air mixtures at the same conditions. Although it has not been validated at alternative temperatures and pressures, it is unlikely that its use will result in serious errors as it predicts the appropriate trends in flame thickness as a function of pressure and temperature. Moreover, it plays no role in the determination of u_l and L_b.

Values of u_l are deduced from S_s using Eq. 3.13. Values of u_n are computed using Eqs. 3.14 and 3.15. Values of u_nr are calculated using Eq. 3.6 and Markstein lengths are evaluated using Eqs. 3.9 and 3.10, employing multiple linear regression (Bradley *et al.* 1996).

3.4 Computations of Burning Velocities

In the present study, unstretched laminar burning velocities of a freely propagating, one-dimensional, adiabatic premixed flame are computed using the Sandia PREMIX code (Kee *et al.* 1985). This uses a hybrid time-integration/Newton-iteration technique to solve the steady-state comprehensive mass, species and energy conservation equations. The CHEMKIN code (Kee *et al.* 1989) evaluated the thermodynamic properties of the reacting mixture and processed the chemical reaction mechanism. The chemical reaction mechanism of GRI-Mech 1.2 (Frenklach *et al.* 1995) is used to describe the methane oxidation chemistry in terms of 177 elementary reactions of 32 species. Transport properties are processed by the Sandia transport software package, which provided for a full Dixon-Lewis, multi-component, dilute gas treatment of the gas-phase transport (Kee *et al.* 1986). Computations covered methane-air mixtures at equivalence ratios between 0.6 and 1.2, and initial temperatures and pressures between 300 and

400 K and 0.1 and 1.0 MPa. Sufficient grid points are allowed (usually 500) to ensure a converged solution.

In a parallel work, Gu (1998) has modeled the propagation of a time dependent stretched spherical flame. Because of the increased computing power required to model the time dependent influence of stretch, it is necessary, to reduce the number of species and to eschew 'full mechanisms'. Therefore the four-step reduced mechanism of Mauss and Peters (1993), based on 40 elementary reactions, is employed. The basis of such a scheme relies on sensitivity analysis and sufficiently valid steady-state and partial equilibrium assumptions. When an intermediate species is formed at a rate slower than that at which it is consumed and its concentration remains relatively small, it is assumed to be in a steady-state. The general governing conservation equations and detailed numerical procedure are presented in Bradley *et al.* (1996). A time increment of 1 μs is used. Profiles of temperature, velocity and concentrations of seven non-steady-state species are stored every 0.2 ms for subsequent post-processing. The burning velocities are calculated as described in § 3.3.

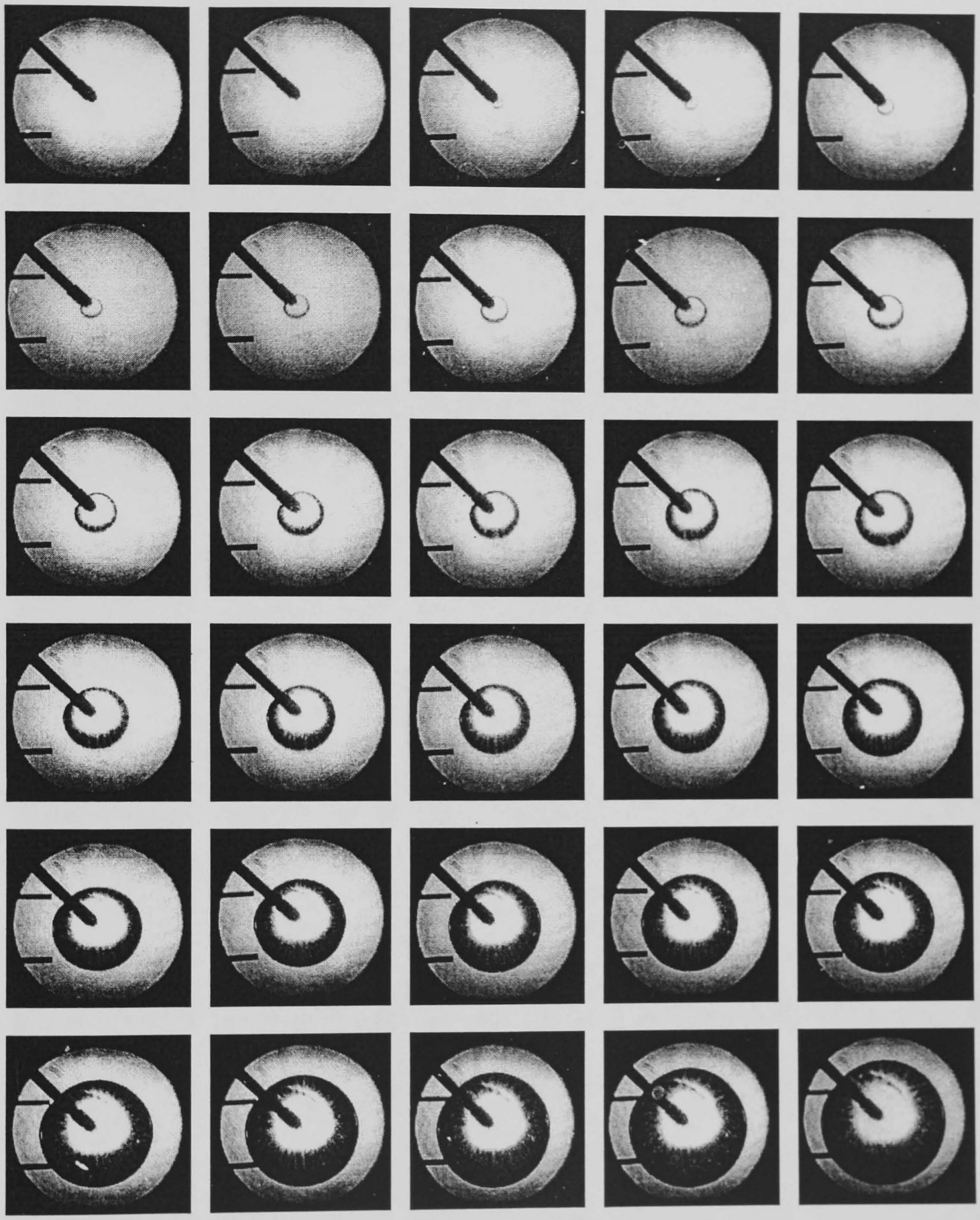

Fig. 3.1. Laminar flame propagation in a stoichiometric methane-air mixture at an initial temperature of 300 K and pressure of 0.1 MPa. First figure corresponds to the spark ignition and the last frame corresponds to 22.04 ms. The time interval between the figures are 0.76 ms. (Only every third frame is shown).

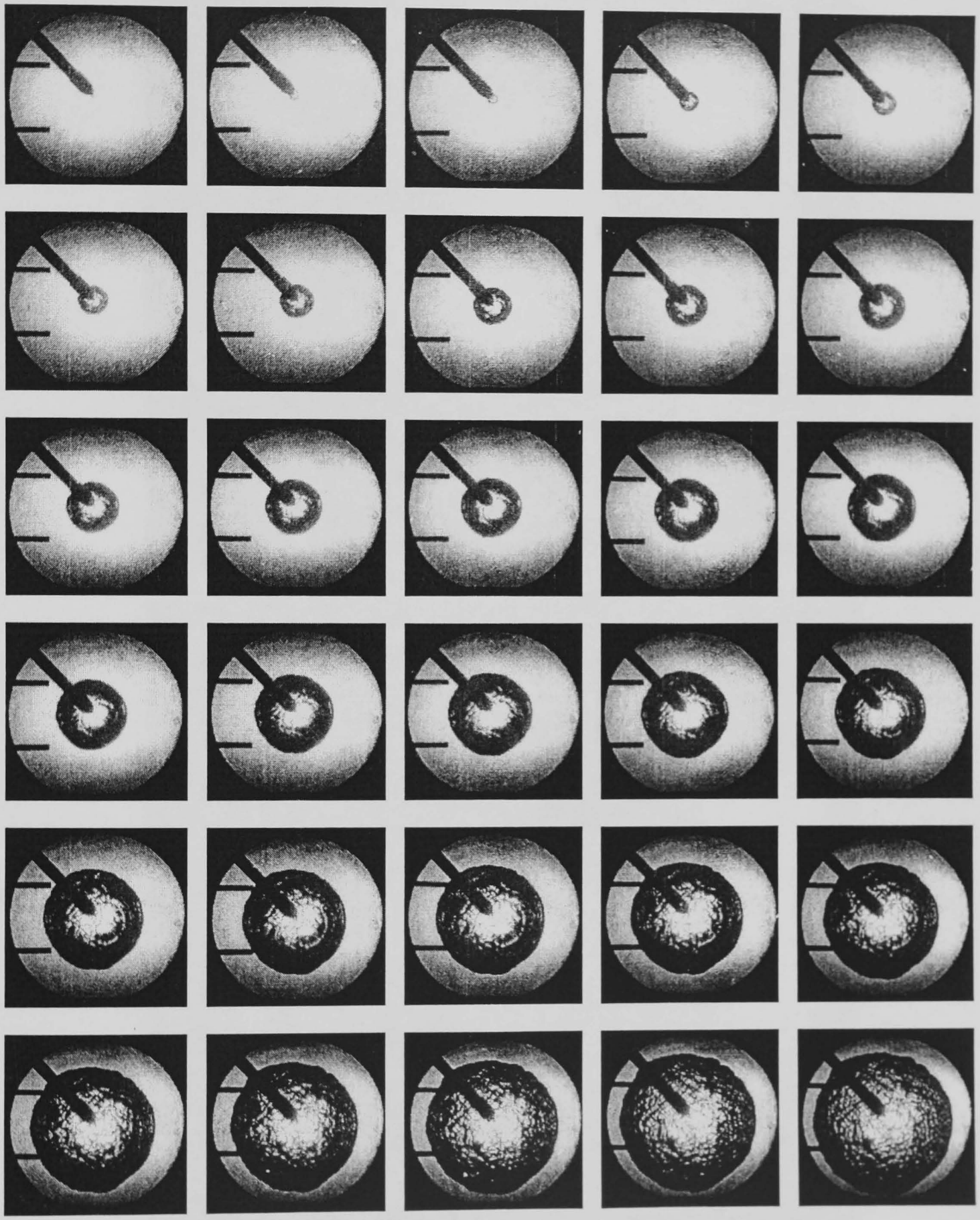

Fig. 3.2. Laminar flame propagation in a lean methane-air ($\phi = 0.8$) mixture at an initial temperature of 300 K and Pressure of 0.5 MPa. First figure corresponds to the spark ignition and time interval between the figures are 0.9 ms. (Only every fourth frame is shown).

(a)

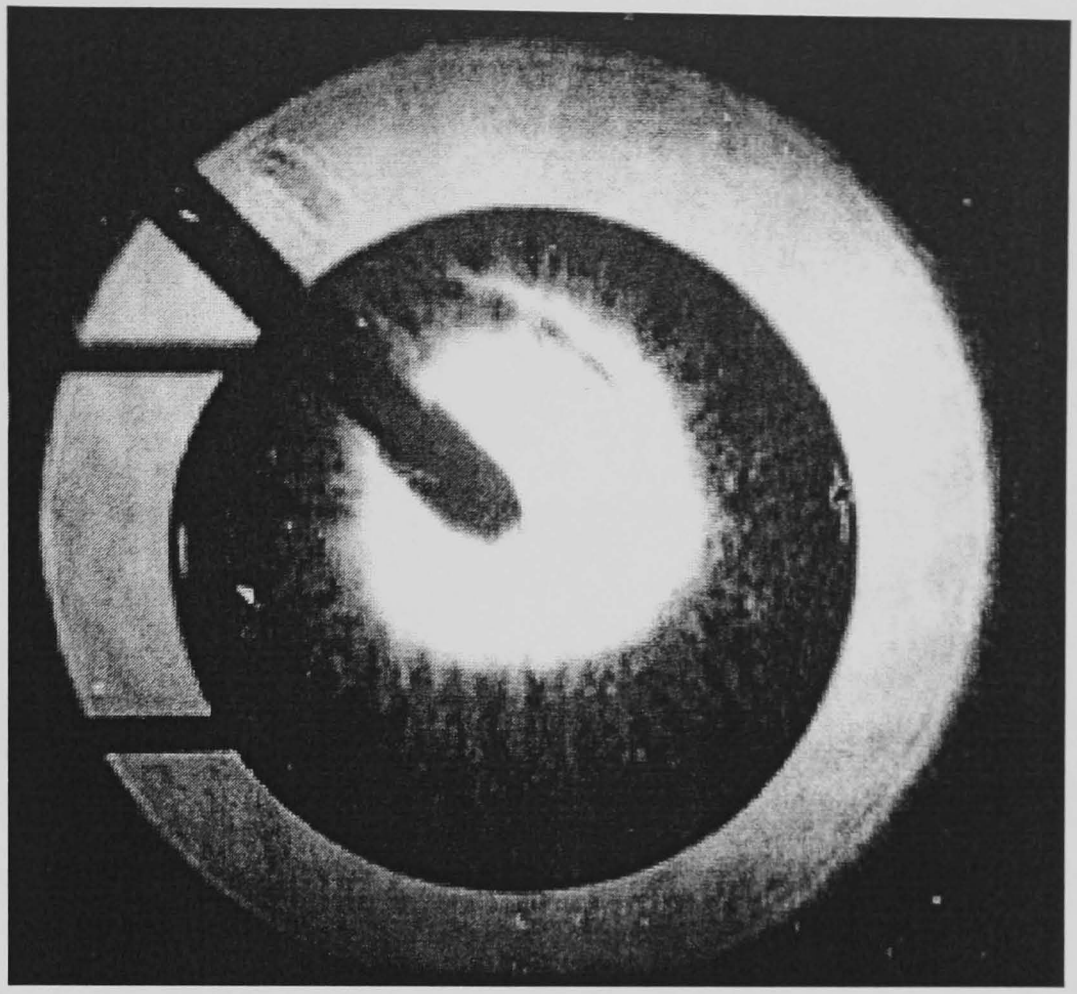

(b)

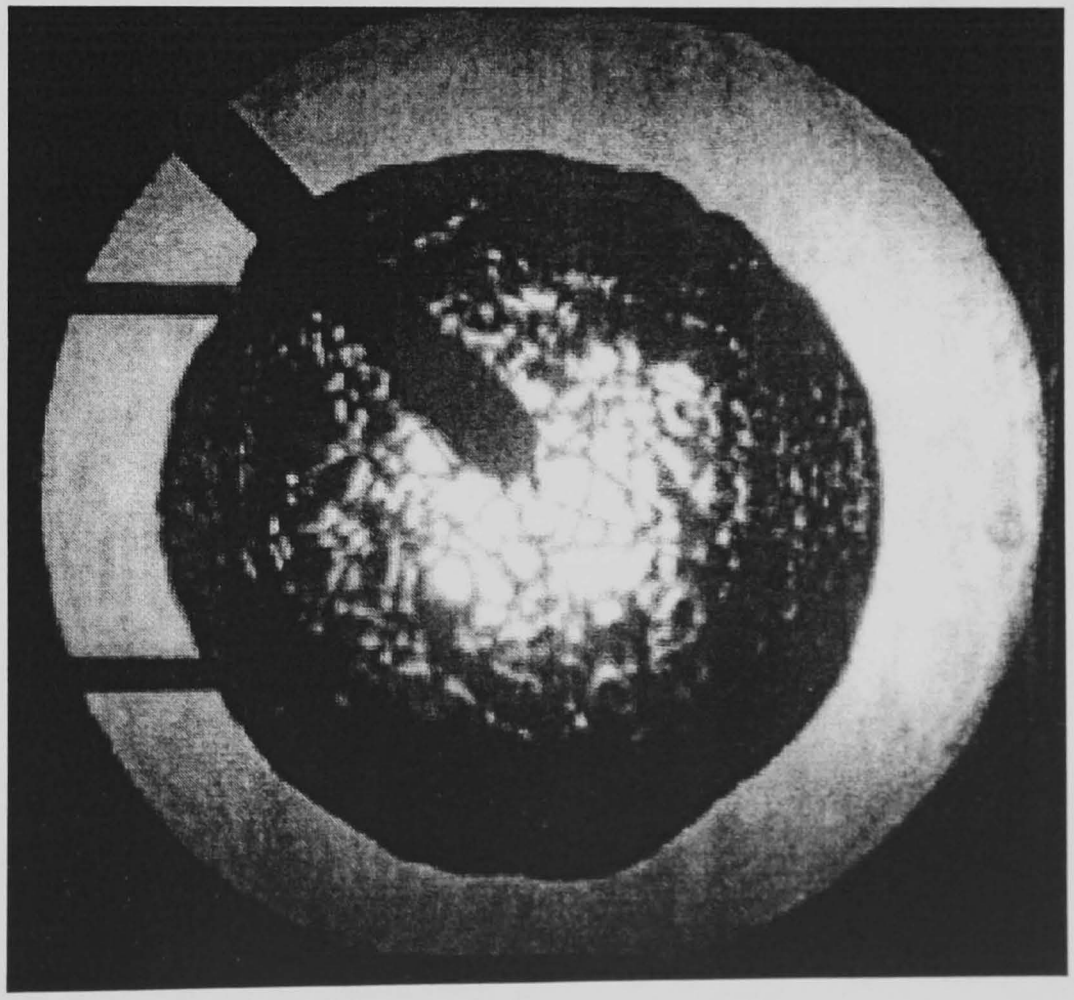

Fig. 3.3. Schlieren photograph of methane-air flame at $T_{\mathrm{u}} = 300$ K, were flame is (a) not cellular at $\phi = 1.0$ & $P_{\mathrm{u}} = 0.1$ MPa and ; (b) cellular one at $\phi = 0.8$ & $P_{\mathrm{u}} = 0.5$ MPa.

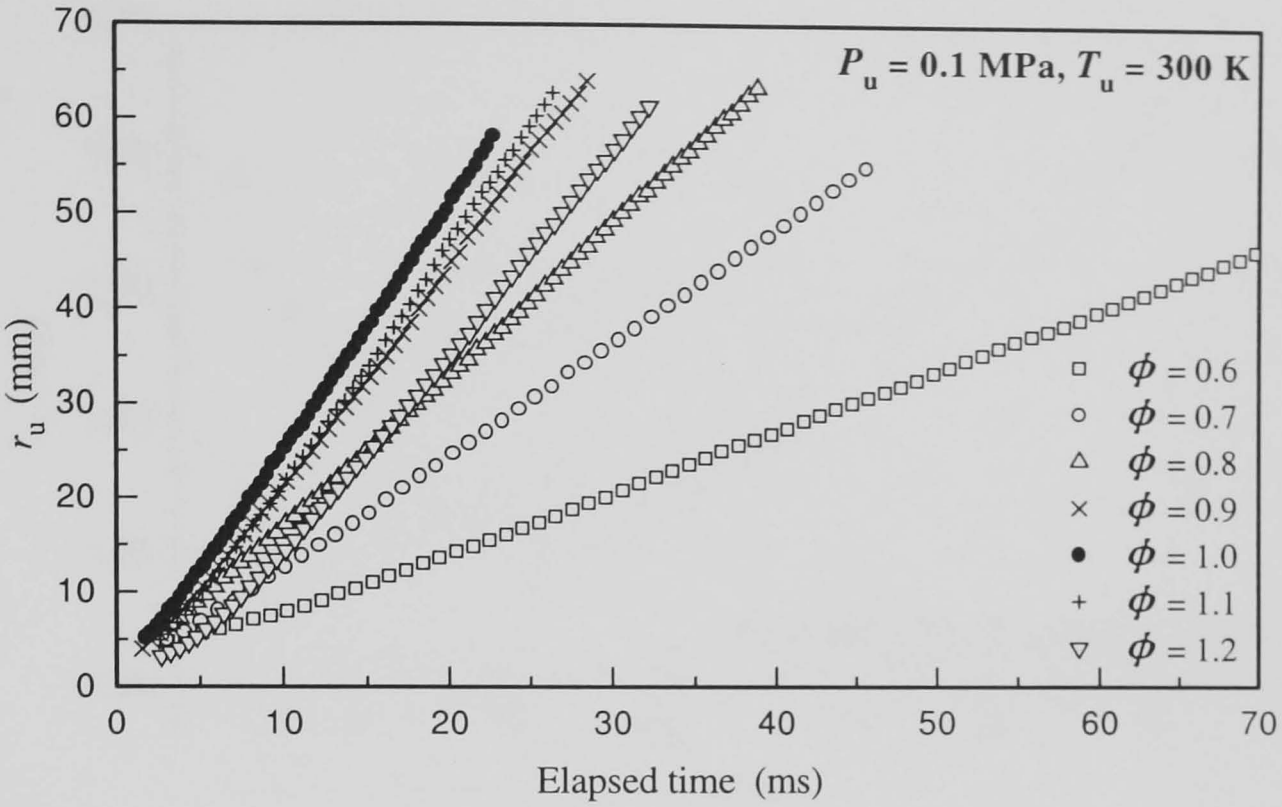

Fig. 3.4. Measured flame radii as a function of elapsed time for various methane-air mixtures at $P_u = 0.1$ MPa and $T_u = 300$ K.

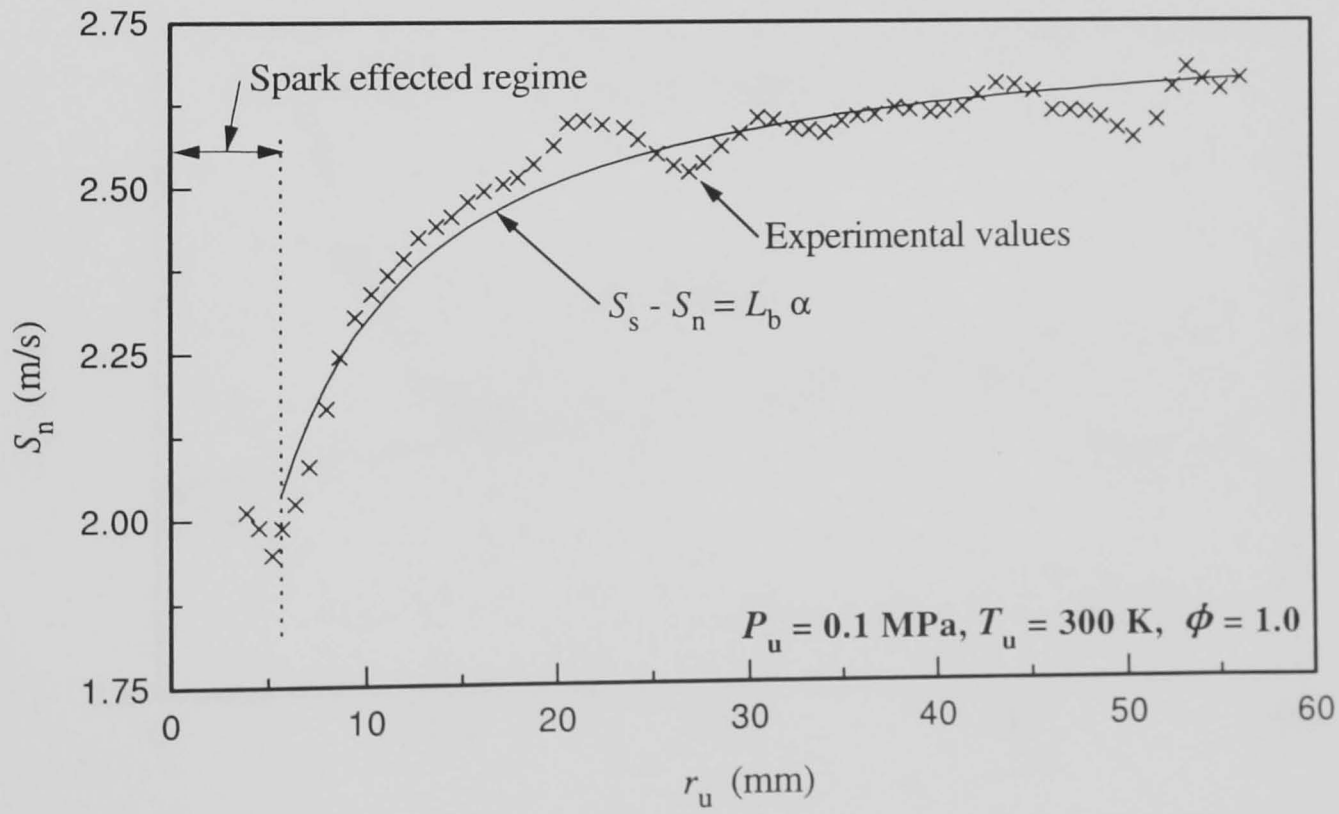

Fig. 3.5. Measured flame speeds at different flame radii for stoichiometric methane-air flame at $P_u = 0.1$ MPa and $T_u = 300$ K.

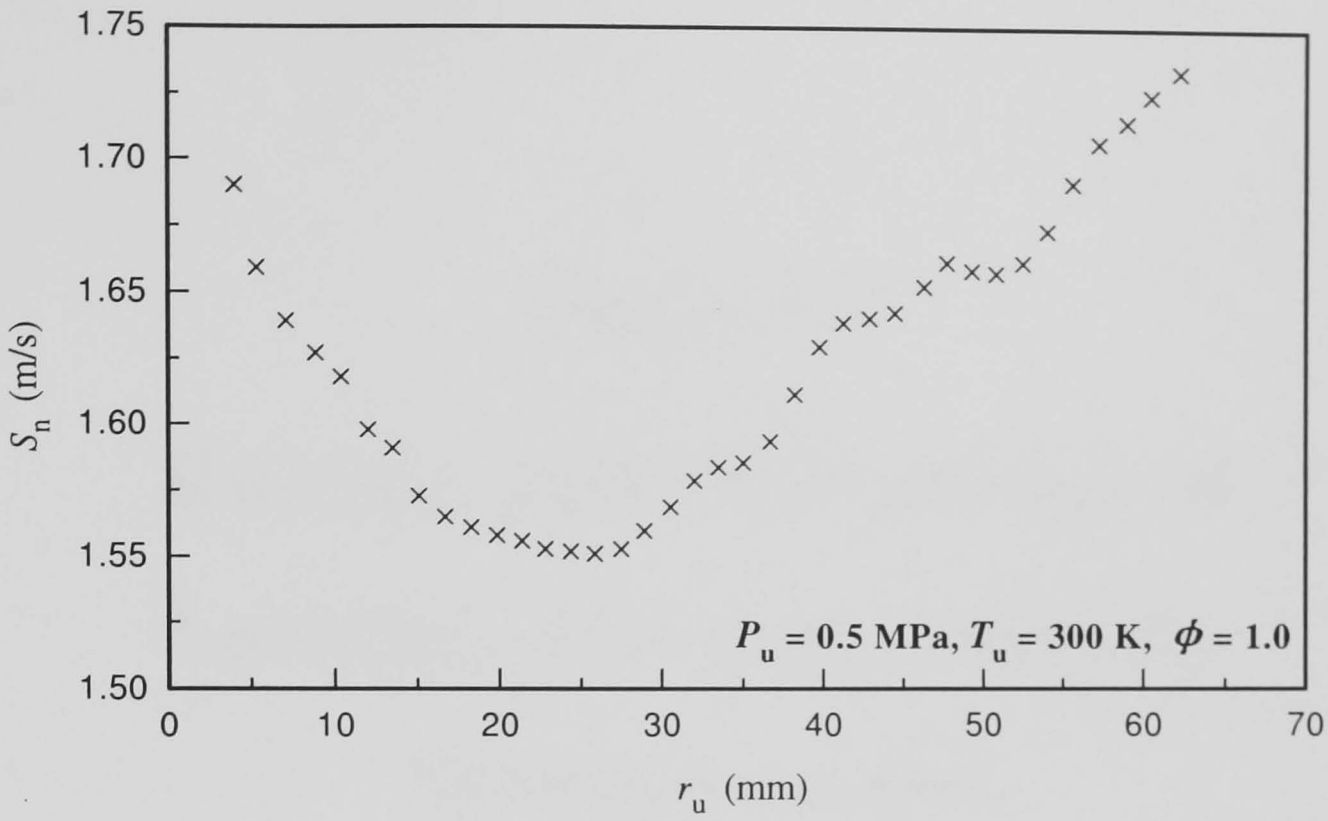

Fig. 3.6. Measured flame speeds at different flame radii for stoichiometric methane-air flame at $P_u = 0.5$ MPa and $T_u = 300$ K.

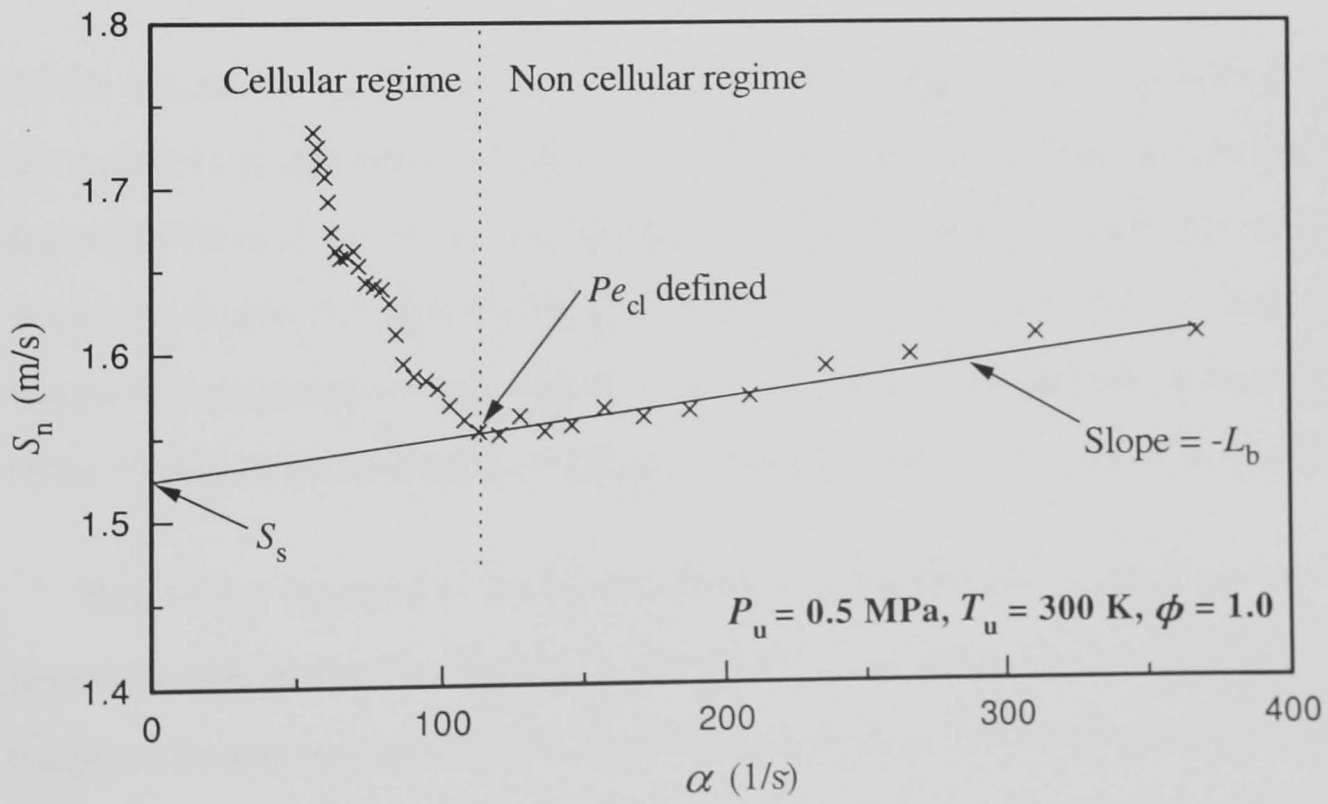

Fig. 3.7. Measured flame speeds at different flame stretch rate for stoichiometric methane-air flame at $P_u = 0.5$ MPa and $T_u = 300$ K.

Chapter 4

Results and Discussions of Laminar Burning Velocity Measurements

4.1 Introduction

In the present study, spherically expanding flames propagating at constant pressure are employed to determine the unstretched laminar burning velocity and the effect of flame stretch as quantified by the associated Markstein lengths. Methane-air mixtures at initial temperatures between 300 and 400 K, and pressures between 0.1 and 1.0 MPa are studied at equivalence ratios of 0.8, 1.0 and 1.2. This is accomplished by the analysis of the photographic observation of flames in a spherical vessel as discussed in Chapter 3.

Results are reported in the present chapter and power law correlations are suggested for the unstretched laminar burning velocity as a function of initial pressure, temperature and equivalence ratio. Zeldovich numbers are derived to express the effect of temperature on the mass burning rate and, from this, a more general correlation of unstretched laminar burning velocity, based on theoretical arguments, is presented for methane-air mixtures. Experimental results are compared with modeled predictions as discussed in Chapter 3. The results of the present work are compared with those

of other researches. Comparison also is made with iso-octane-air mixtures, reported elsewhere, to emphasize the contrast in the burning of lighter and heavier hydrocarbon fuels.

4.2 Influence of Stretch on Flame Speed and Burning Velocities

In the present study, laminar flame speed in methane-air premixture is obtained from measured radius against time data as discussed in § 3.3. Shown in Figs. 4.1 to 4.10 are the variations of flame speed, S_n, with flame radius, r_u, for different initial conditions of equivalence ratio, pressure and temperature. For each condition, results from two explosions are presented. In addition to the initial condition, flame radius has great effect on the flame speed. This additional dependency of flame speed on flame radius is a result of flame stretch, α. From S_n and r_u, corresponding values of α are estimated and are discussed in § 3.2.1 and § 3.3. From the values of S_n and α, values of S_s, u_l and various Markstein lengths and numbers are obtained as discussed in § 3.3.

Shown in Fig. 4.11(a) are the variations of S_n with α for $\phi = 0.8$, 1.0 & 1.2 at an initial pressure of 0.1 MPa and an initial temperature of 300 K. The flame speed is greatest for the stoichiometric mixture, and that is followed by that at $\phi = 1.2$ and then at $\phi = 0.8$. Here, stretch has an adverse effect on the flame speed which is indicative of a positive L_b as discussed below. Shown in Fig. 4.11(b) are the variations of S_n with α for different initial temperatures for stoichiometric mixtures at an initial pressure of 0.1 MPa. Flame speed is found to increase significantly with increase in initial temperature. Stretch has a similar adverse effect on flame speed as observed in Fig. 4.11(a). However, as shown in Fig. 4.11(c), at high pressure (0.5 and 1.0 MPa) the effect of stretch on the flame speed is more complex than for 0.1 MPa. Flame speed is found to decrease significantly with increase in pressure. Moreover, two regimes of combustion are clearly demonstrated. In the first, at stretch rates above approximately 120 s^{-1}, there is an increase of S_n with α, indicative of a negative L_b. In the second

regime, at low stretch rates (large radii) there is a rapid increase in flame speed with reduced stretch rate as a result of the onset of a cellular structure and this is discussed in Chapter 5.

Values of L_b are obtained from the slopes of the curves in Fig. 4.11 as discussed in § 3.3. For all measured conditions, L_b increases with ϕ as presented in Fig. 4.12. At pressures between 0.1 and 0.5 MPa, increasing the pressure results in a dramatic decrease in L_b, but between 0.5 and 1.0 MPa there is little variation in L_b. Moreover, at high pressures, L_b is negative for lean and stoichiometric mixtures as demonstrated by the increase of the flame speed with stretch in Fig. 4.11(c). The effect of increasing the temperature is not clear, but is small. Values of L_b for different experimental conditions are presented in Tables 4.1 to 4.3.

The four Markstein numbers Ma_s, Ma_c, Ma_{sr} and Ma_{cr} are calculated from the experimental values of S_s and L_b as discussed in § 3.3. The values of the Markstein numbers obtained from the present study are presented in Tables 4.1 to 4.3. All appear to be influenced in a similar way by equivalence ratio, temperature and pressure and therefore, for brevity, only values of Ma_{sr} are shown in Fig. 4.13. This Markstein number is important as the stretch due to strain dominates over stretch due to curvature and is discussed in § 5.2. Similar trends with pressure and temperature are observed for Ma_{sr} as for L_b.

Shown in Fig. 4.14 are the variations of u_n and u_{nr}, with stretch for different equivalence ratios, initial temperatures and initial pressures. Values of u_n and u_{nr} are obtained using Eqs. 3.9 & 3.10, and is discussed in § 3.3. The difference between u_n and u_{nr}, can be clearly seen. The rate of mixture entrainment, u_n, always increases with stretch. In contrast, u_{nr}, the burning velocity related to the production of burned gas, is usually reduced by stretch. The processes of mixture entrainment and burned gas production occur in different parts of the flame, u_n is defined at the front of the flame and u_{nr} at the back. The difference between u_n and u_{nr} expresses the influence

of flame thickness. The value of $(u_n - u_{nr})$ is largest at small radii (large stretch) where the flame thickness is of a similar order to that of the flame radius. The rich condition, $\phi = 1.2$, gives the largest differences between u_n and u_{nr}. In Fig. 4.14(b), it is evident that the initial temperature has little effect on $(u_n - u_{nr})$. However, as the initial pressure increases, the flame thickness decreases, as does the difference between u_n and u_{nr} as shown in Fig. 4.14(c). Values of u_n increase with α. However, values of u_{nr} decrease with α for 0.1 MPa explosions while their values increase with α at higher pressures.

The response of the two burning velocities to stretch varies with pressure, temperature and equivalence ratio. The matter is further complicated because their responses to flow strain and to flame front curvature are not the same. This is represented by the different Markstein numbers presented in Tables 4.1 to 4.3. Indeed, their responses to strain and curvature can be quite opposite and this underlies the importance of quoting all four Markstein numbers. An interesting case is the stationary spherical flame, in which the total stretch acting on the flame is zero because stretch due to strain and due to curvature have the same magnitude but opposite signs (Bradley *et al.* 1996). Yet, if the Markstein numbers for each effect are not equal, the net result of both effects will not be zero.

4.3 Laminar Burning Velocity and their Correlations

Shown by the symbols in Fig. 4.15 are the variations of measured unstretched laminar burning velocity with temperature and pressure at different ϕ. These are obtained from measurements at different stretch rates as discussed in § 4.2 using the method discussed in § 3.3. In all cases, increasing the temperature or reducing the pressure increase the burning velocity. The simplest correlation of burning velocities is through the empirical expression of Metghalchi and Keck (1980):

$$u_l = u_{l,0} \left(\frac{T_u}{T_o}\right)^{\alpha_T} \left(\frac{P_u}{P_o}\right)^{\beta_P} \tag{4.1}$$

Here, $u_{l,0}$ is the unstretched laminar burning velocity at a datum temperature and pressure of T_o and P_o, respectively. In the present study these are 300 K and 0.1 MPa. The parameters α_T and β_P, which depend upon ϕ, when optimized for the experimental data in Fig. 4.15 give:

$$\begin{aligned} u_l &= 0.259\left[\frac{T_u}{T_o}\right]^{2.105}\left[\frac{P_u}{P_o}\right]^{-0.504} && \text{(m/s)} \quad \text{for } \phi = 0.8 \\ &= 0.360\left[\frac{T_u}{T_o}\right]^{1.612}\left[\frac{P_u}{P_o}\right]^{-0.374} && \text{(m/s)} \quad \text{for } \phi = 1.0 \\ &= 0.314\left[\frac{T_u}{T_o}\right]^{2.000}\left[\frac{P_u}{P_o}\right]^{-0.438} && \text{(m/s)} \quad \text{for } \phi = 1.2 \end{aligned} \tag{4.2}$$

These equations are represented by the solid lines in Fig. 4.15. Here, the standard deviations of the difference between experiments and Eq. 4.2 are 0.008, 0.011 & 0.014 m/s for $\phi = 0.8$, 1.0 & 1.2 respectively.

4.4 Burning Mass Flux and Zeldovich number

Although Eqs. 4.2 are reasonable correlations of the effect of pressure and temperature on laminar burning velocity, they are essentially empirical, with no theoretical basis. Peters and Williams (1987) have derived an asymptotic structure of the flame and expressed the mass flux, $(\rho_u u_l)$, in a square root form and shown that, provided that T^o remains constant:

$$\frac{E}{R} = 2T_b^2\,\frac{\mathrm{d}(\ln(\rho_u u_l))}{\mathrm{d}T_b} \tag{4.3}$$

Hence, R is the universal gas constant and T^o is a characteristic temperature and is discussed in § 1.2. Göttgens *et al.* (1992) have computed values of T^o numerically and shown them to be primarily a function of pressure. Values of T^o are presented in Table 4.4.

Equation 4.3 can be rewritten as:

$$\frac{E}{R} = -\frac{\mathrm{d}2(\ln(\rho_\mathrm{u} u_l))}{\mathrm{d}(1/T_\mathrm{b})} \tag{4.4}$$

Integration of this gives

$$2\ln(\rho_\mathrm{u} u_l) = -\left(\frac{E}{R}\right)\frac{1}{T_\mathrm{b}} + (C)_\mathrm{p} \tag{4.5}$$

where, $(C)_\mathrm{p}$ is an empirical constant. Rearrangement gives:

$$u_l = \frac{\exp[0.5(C)_\mathrm{p}]}{\rho_\mathrm{u}} \exp\left[-\frac{E}{2RT_\mathrm{b}}\right] \tag{4.6}$$

The slope of the plot of $2\ln(\rho_\mathrm{u} u_l)$ against $1/T_\mathrm{b}$ for different pressures yield the values of E/R for the corresponding pressures. Shown in Fig. 4.16 is the variation of $2\ln(\rho_\mathrm{u} u_l)$ with $1/T_\mathrm{b}$ obtained from the experimental data in Fig. 4.15. In each case, the symbols are the experimental results and the solid lines are linear curve fits through all data at the same pressure. The gradient of these yield E/R. Göttgens *et al.* (1992) have shown that E/R is a function of ϕ; however, the functionality is weak and may be neglected over the small range of ϕ used here. Some scatter clearly is evident, probably a result of the influence of the unburned gas temperature upon the mass flux. This demonstrates that $(C)_\mathrm{p}$ is influenced by the initial pressure, and to a lesser extent, the initial temperature. Values of E/R and $(C)_\mathrm{p}$ are tabulated in Table 4.4 with a single, mean, value of E/R at each pressure.

Equation 4.6 gives an alternative correlation of laminar burning velocities to that presented by Eq. 4.2. Calculated laminar burning velocities using Eq. 4.6 together with the values in Table 4.4 are shown in Fig. 4.15 by the dotted lines. The difference between calculated velocities and the experiments have standard deviations of 0.018, 0.011 and 0.012 m/s for initial pressures of 0.1, 0.5 and 1.0 MPa, respectively. Although the deviations from the experimental data are marginally higher for Eq. 4.6 than for Eq. 4.2,

agreement is good and the former has more physical relevance than the later. The good agreement for Eq. 4.6 supports this use of the theoretical basis for the correlation of the laminar burning velocity. However, more coefficients are required than for the simple correlation in Eq. 4.2.

From values of E/R, the reduced activation energy, β, designated as the 'Zeldovich number' in 1983, can be calculated as (Clavin 1985):

$$\beta = \frac{E}{RT_b^2}(T_b - T_u) \tag{4.7}$$

It represents the sensitivity of chemical reactions to the variation of the maximum flame temperature, and the inverse of it physically denotes an effective dimensionless width of the reaction zone (Bradley 1990). More recently, another form of Zeldovich number, Ze, has been defined by Seshadri and Williams (1994) as:

$$Ze = \beta\frac{(T_b - T_u)}{(T^o - T_u)} \tag{4.8}$$

The values of Ze can be estimated using the corresponding value of T^o, and are presented in Tables 4.1 to 4.3.

Shown by the symbols in Fig. 4.17 are the variations of β with ϕ at 300 K and 0.1 MPa, 0.5 MPa and 1.0 MPa. Computed results of Göttgens *et al.* (1992) at an initial pressure of 0.1 MPa are represented by the solid curve in Fig. 4.17. Both experimental and computed values of β attains a minimum near to a stoichiometric mixture where the value of T_b is at a maximum. Although Göttgens *et al.* (1992) predicted higher values than the present ones, they both follow a similar trend. Because an increase in pressure drives the inner layer temperature to a higher value, this has the effect of increasing the global activation energy and hence β increases. Bradley *et al.* (1998) also observed this effect in their experimental study of iso-octane-air mixtures.

4.5 Comparisons between the Present Computed and Measured Values

Shown in Fig. 4.18 are calculations of $2\ln(\rho_u u_l)$ using GRI-Mech kinetics in a one dimensional flame. Here, the mass flux is plotted against the reciprocal of T_b, in order to determine the activation energies as in § 4.4. The symbols are obtained from the computations and the solid lines are a linear curve fit through the data at pressures of 0.1 and 0.25 MPa. A linear fit through the calculated values is reasonable and this allows the determination of the activation temperature in the same way as that for the present experiments in § 4.4. The modeled value of E/R at 0.1 MPa is 13000 K and this is in good agreement with experiments (Table 4.4). The value at 0.25 MPa is 14000 K and, although no experimental value is available at this pressure, interpolation of data in Table 4.4 would suggest good agreement with experimental expectations. However, at 0.5 and 1.0 MPa, a single linear curve fit does not accurately represent the calculated values.

Spherical flame propagation was computed by Gu (1998) using reduced chemistry as described in § 3.4. Shown in Fig. 4.19 are the measured and computed flame speeds plotted against stretch for three equivalence ratios with initial temperature and pressure of 300 K and 0.1 MPa. Agreement between them is good, particularly for the stoichiometric mixture. Shown in Fig. 4.20 is the flame speed plotted against stretch for different initial pressures and temperatures. For flames at 0.1 MPa with initial temperature of 400 K, the computation predicts higher values of flame speed than do the experiments. However, it exhibits the same slope and hence, yields similar values of L_b. For higher pressure flame propagation (0.5 and 1.0 MPa), the prediction of flame speeds is in good agreement with experiment at high stretch rates (small radii), but agreement is not so good at low stretch. This might be explained, to some extent, by the inability of the model to predict flame speed enhancements due to the appearance of cells. The reduced mechanism gives good qualitative agreement over the whole range of experimental conditions. Quantitative agreement is satisfactory at near atmospheric

conditions and further work is required to produce an adequate reduced scheme for other conditions, especially for higher initial temperatures.

4.6 Comparisons with other work

Experimental data for stretch free burning velocities of methane-air mixtures at above atmospheric conditions are sparse. However, the sources of such data at atmospheric conditions are increasing. Shown in Fig. 4.21 are unstretched burning velocities at 300 K and 0.1 MPa as a function of equivalence ratio. Data from the present work together with those from other sources are shown. Experimental data are presented in Fig. 4.21(a) and modeled data, together with the present experimental results, are presented in Fig. 4.21(b).

Spherically expanding flames have been used by Taylor (1991), Ali (1995), Aung *et al.* (1995) and Clarke *et al.* (1995). In the first three cases, they obtained flame radii as a function of time from schlieren images and then systematically determined the unstretched burning velocity from the measured flame speed at different stretch rates by extrapolating to zero stretch. In the last case, temporal pressure records obtained under micro gravity conditions were converted into radius against time data using the thermodynamic analysis of Lewis and von Elbe (1987), and burning velocity is reported for low stretch (80 1/s) at a flame radius of the order of 50 mm. Vagelopoulos *et al.* (1994) used a twin-flame configuration established in counterflow by impinging two identical, nozzle-generated flows of the combustible mixture onto each other. By mapping the flow field using laser Doppler velocimetry (LDV), they identified the minimum in the velocity profile as a reference upstream burning velocity and the velocity gradient ahead of the minimum point as the strain rate experienced by the flame. They used a linear extrapolation to zero stretch to yield the unstretched burning velocity. Yamaoka and Tsuji (1984) also used counterflow double flames. In their system, in which a premixed flame was stabilized in the forward stagnation region of a porous cylinder, two different regimes occurred depending on whether the mixture ejection

velocity was more or less than the burning velocity. A plot of flame position versus the mixture-ejection velocity was initially linear, but this linearity was destroyed suddenly and discontinuously at the critical ejection velocity, which was the burning velocity. They reported burning velocities for low stretch conditions by utilizing a large cylinder radius of 60 mm. Flat flame burners were used by Van Maaren *et al.* (1994) and Haniff *et al.* (1989). Van Maaren *et al.* (1994) obtained the burning velocity using a heat flux method for zero stretch conditions, while Haniff *et al.* (1989) used particle tracking and reported the burning velocities for low stretch (less than 100 1/s).

There is good agreement between values obtained by the different measurement techniques. This clearly demonstrates an improvement in consistency, when compared with earlier measurements of burning velocity (Andrews and Bradley 1972). This is due to the recognition of the influence of stretch and the resulting corrections for it, and also because of the advances in the measurement techniques.

Shown in Fig. 4.21(b) are modeled unstretched laminar burning velocities compared with the present experimental results. The modeled results of other workers include the computations by Göttgens *et al.* (1992) who used detailed numerical calculations and a detailed kinetic mechanism of 82 elementary reactions; Bui-Pham and Miller (1994) used a mechanism consisting of 239 reactions involving 53 chemical species (including up to C_6 chemistry); Bradley *et al.* (1996) used a reduced kinetic, C_1, scheme of Mauss and Peters (1993) involving 8 non-steady-state species and 40 reactions; Frenklach *et al.* (1992) used a detailed reaction mechanism consisting of 149 elementary reactions; and Warnatz *et al.* (1996) used a detailed reaction mechanism consisting of 231 elementary reactions. There is good agreement between the present experiments and the modeled data of Bradley *et al.* (1996). Bui-Pham and Miller (1994) and Göttgens *et al.* (1992) predicted values higher than the present experiments at all measured equivalence ratios. All other works are in reasonable agreement with the experiments for lean mixtures. Except for the data of Warnatz *et al.* (1996), the agreement is not so good for rich mixtures.

Shown in Fig. 4.22 is the effect of pressure on u_l from available experimental and modeled data. The present experiments are represented by the correlations given by Eq. 4.2 and are shown by the solid curves. Present modeled data, using GRI-Mech, are indicated by the dotted curves. In all cases except for rich mixtures at high pressure, the modeled data are higher than those of the measured. Experimental values reported by Law (1988) are in good agreement with the present experimental results for both lean and stoichiometric mixtures. However, for rich mixtures the agreement is moderate. Kobayashi *et al.* (1997) and Peters and Williams (1987) reported a much stronger effect of pressure. The predicted values reported by Warnatz *et al.* (1996) are in good agreement with our experimental results for all the pressures considered. However, results of Mauss and Peters (1993) and Bui-Pham and Miller (1994) predicted much higher values of burning velocities at higher pressures. Computed results for lean mixtures (Fig. 4.22(b)) by Göttgens *et al.* (1992) are in good agreement with the present experimental values at up to 0.5 MPa, but lower values are predicted at higher pressures.

4.7 Comparison with iso-octane

In the present work, iso-octane data from Bradley *et al.* (1998) are used as a representative heavier hydrocarbon to provide a contrast with methane. Shown in Figs. 4.23 and 4.24 are the effects of pressure and temperature on the measured burning velocities of lean and stoichiometric methane-air and iso-octane-air mixtures. An increase in pressure decreases the laminar burning velocity, but iso-octane-air mixtures are less effected than are methane-air mixtures. Laminar burning velocity increases with temperature and, again, iso-octane-air mixtures are less responsive to temperature variations than are the methane-air mixtures.

These two fuels respond to flame stretch differently. Shown in Fig. 4.25 are, for the two fuels, the measured variations of L_b and Ma_{sr} with ϕ. Both of these parameters

increase with equivalence ratio for methane-air mixtures, while they decrease for iso-octane-air mixtures. Here, methane-air flames with $\phi > 1.05$ are more affected by stretch than are the iso-octane-air flames at the same equivalence ratio. Conversely, iso-octane-air flames with $\phi < 1.05$ are more sensitive to flame stretch than the methane-air flames at the same equivalence ratio. Shown in Fig. 4.26 are values of L_b plotted against pressure at an initial temperature of 358 K. For both mixtures, L_b drops rapidly at pressures between 0.1 and 0.5 MPa and becomes nearly constant at higher pressures. However, values of L_b for iso-octane-air mixtures are higher than those of methane-air. Moreover, at high pressure for both of these fuel, the values of L_b are near to zero. Hence, both of these fuel are less affected by flame stretch at engine conditions where the cylinder pressures are quite high.

Table 4.1. Experimental results for methane-air mixtures at an initial pressure of 0.1 MPa.

Expt. ID.	ϕ	T_u (K)	σ	u_l (m/s)	L_b (mm)	Ma_s	Ma_c	Ma_{sr}	Ma_{cr}	β	Ze
E43	0.6	302	5.530	0.119	0.21	-4.97	-1.97	1.43	0.77	6.16	9.14
E44	0.7	301	6.129	0.205	0.74	-4.40	-0.52	2.71	1.96	5.70	9.53
E32	0.8	300	6.684	0.250	0.64	-5.05	-0.52	2.66	1.86	5.33	9.83
E41	0.8	300	6.684	0.280	0.78	-4.57	0.22	3.20	2.36	5.33	9.83
E23	0.8	358	5.571	0.372	0.61	-3.59	-0.42	2.98	2.31	5.07	9.87
E26	0.8	402	5.161	0.487	0.48	-3.07	-0.64	2.87	2.29	4.89	9.93
E46	0.9	300	7.153	0.344	1.14	-3.68	1.72	4.61	3.74	5.05	10.06
E40	1.0	301	7.461	0.368	1.00	-4.41	1.34	4.24	3.36	4.87	10.19
E30	1.0	301	7.461	0.358	0.90	-4.77	0.87	3.86	2.99	4.87	10.19
R04	1.0	360	6.324	0.473	0.65	-3.92	-0.01	3.37	2.64	4.67	10.28
R16	1.0	360	6.324	0.503	0.91	-2.82	1.12	4.48	3.74	4.67	10.28
E33	1.0	404	5.693	0.561	0.82	-2.35	0.69	4.21	3.57	4.53	10.38
E25	1.0	404	5.693	0.567	0.98	-1.73	1.38	4.85	4.20	4.53	10.38
E45	1.1	300	7.510	0.368	1.69	-2.40	3.72	6.35	5.41	4.90	10.17
E29	1.2	300	7.366	0.318	2.65	-0.20	5.39	8.32	7.07	5.05	10.05
E37	1.2	302	7.322	0.321	1.82	-2.44	3.32	6.11	5.21	5.05	10.05
E27	1.2	360	6.255	0.453	1.86	0.11	4.04	7.35	6.60	4.81	10.13
E36	1.2	361	6.239	0.427	2.23	0.91	4.76	8.12	7.39	4.81	10.13
E28	1.2	403	5.662	0.545	1.94	1.69	4.81	8.24	7.57	4.65	10.23
E42	1.2	399	5.712	0.545	2.02	1.97	5.05	8.50	7.85	4.66	10.22

Table 4.2. Experimental results for methane-air mixtures at an initial pressure of 0.5 MPa.

Expt. ID.	ϕ	T_u (K)	σ	u_l (m/s)	L_b (mm)	Ma_s	Ma_c	Ma_{sr}	Ma_{cr}	β	Ze
E31	0.8	302	6.710	0.116	-0.61	-9.87	-5.48	-2.17	-2.94	8.07	13.35
R12	0.8	306	6.592	0.122	-0.64	-10.19	-5.87	-2.51	-3.26	8.05	13.34
R11	1.0	301	7.561	0.190	-0.39	-10.66	-5.01	-1.93	-2.79	7.31	13.90
R01	1.0	301	7.561	0.201	-0.24	-9.57	-3.94	-0.85	-1.71	7.31	13.90
E09	1.2	300	7.394	0.166	0.32	-5.11	0.41	3.42	2.55	7.66	13.66
E10	1.2	297	7.463	0.166	0.49	-3.89	1.48	4.61	3.77	7.67	13.66
E03	0.8	358	5.729	0.153	-0.25	-6.97	-3.93	-0.42	-1.06	7.68	13.32
E04	0.8	360	5.701	0.161	-0.19	-6.68	-3.63	-0.12	-0.77	7.67	13.32
R02	1.0	350	6.574	0.263	-0.28	-8.84	-4.96	-1.49	-2.20	7.04	13.94
R03	1.0	359	6.423	0.274	-0.33	-9.43	-5.59	-2.08	-2.79	7.01	13.94
E01	1.2	355	6.352	0.240	0.03	-5.78	-2.09	1.41	0.71	7.32	13.68
E02	1.2	358	6.304	0.235	0.11	-5.14	-1.43	2.06	1.36	7.33	13.65
R13	0.8	401	5.188	0.219	-0.38	-7.89	-5.49	-1.95	-2.52	7.41	13.33
E38	0.8	401	5.188	0.202	-0.37	-7.52	-5.13	-1.58	-2.15	7.41	13.33
R15	1.0	404	5.768	0.320	-0.50	-10.78	-7.72	-4.14	-4.78	6.79	14.00
E39	1.0	397	5.860	0.313	-0.18	-7.31	-4.25	-0.68	-1.31	6.82	14.00
E15	1.2	404	5.666	0.286	-0.26	-7.92	-4.83	-1.27	-1.91	7.04	13.72
E16	1.2	404	5.666	0.281	0.06	-4.95	-1.87	1.69	1.05	7.04	13.72

Table 4.3. Experimental results for methane-air mixtures at an initial pressure of 1.0 MPa.

Expt. ID.	ϕ	T_u (K)	σ	u_l (m/s)	L_b (mm)	Ma_s	Ma_c	Ma_{sr}	Ma_{cr}	β	Ze
E13	0.8	310	6.529	0.088	-0.50	-10.68	-6.34	-2.98	-3.74	8.22	12.97
E14	0.8	311	6.509	0.083	-0.67	-11.80	-7.42	-4.09	-4.85	8.21	12.97
R09	1.0	297	7.702	0.144	-0.38	-12.09	-6.42	-3.32	-4.17	7.46	13.55
R10	1.0	302	7.581	0.150	-0.25	-10.76	-5.11	-2.00	-2.85	7.44	13.54
E11	1.2	300	7.413	0.101	0.31	-4.70	0.73	3.83	2.98	7.84	13.29
E12	1.2	305	7.300	0.106	0.40	-3.82	1.63	4.71	3.86	7.81	13.28
E05	0.8	358	5.734	0.120	-0.60	-11.17	-8.18	-4.63	-5.26	7.86	12.93
E06	0.8	359	5.724	0.122	-0.42	-9.56	-6.56	-3.02	-3.65	7.85	12.93
R05	1.0	356	6.501	0.205	-0.29	-10.52	-6.67	-3.15	-3.85	7.16	13.55
R06	1.0	359	6.451	0.206	-0.32	-10.90	-7.05	-3.53	-4.23	7.14	13.55
E07	1.2	359	6.309	0.156	0.29	-2.72	0.96	4.48	3.78	7.47	13.27
E08	1.2	358	5.156	0.151	0.16	-4.28	-0.60	2.91	2.22	7.47	13.27
E21	0.8	404	5.156	0.157	-0.06	-5.47	-3.08	0.47	-0.10	7.56	12.90
E22	0.8	404	5.156	0.150	-0.28	-7.95	-5.56	-2.01	-2.58	7.56	12.90
E17	1.0	401	5.830	0.238	-0.04	-6.12	-3.05	0.53	-0.10	6.93	13.59
E18	1.0	402	5.817	0.234	-0.21	-8.66	-5.58	-2.01	-2.64	6.93	13.58
E19	1.2	402	5.691	0.202	-0.04	-5.93	-2.99	0.58	-0.04	7.21	13.29
E20	1.2	402	5.691	0.220	0.01	-5.21	-2.27	1.30	0.68	7.21	13.29

Table 4.4. Values of E/R and $(C)_p$ for $\phi = 0.8$, 1.0 & 1.2.

P_u (MPa)	T_u (K)	T^o † (K)	E/R (K)	$(C)_p$
	300			3.811
0.1	358	1220	12530	3.995
	400			4.092
	300			8.674
0.5	358	1329	19030	8.797
	400			8.893
	300			9.531
1.0	358	1386	19480	9.724
	400			9.846

†Göttgens *et al.* (1992).

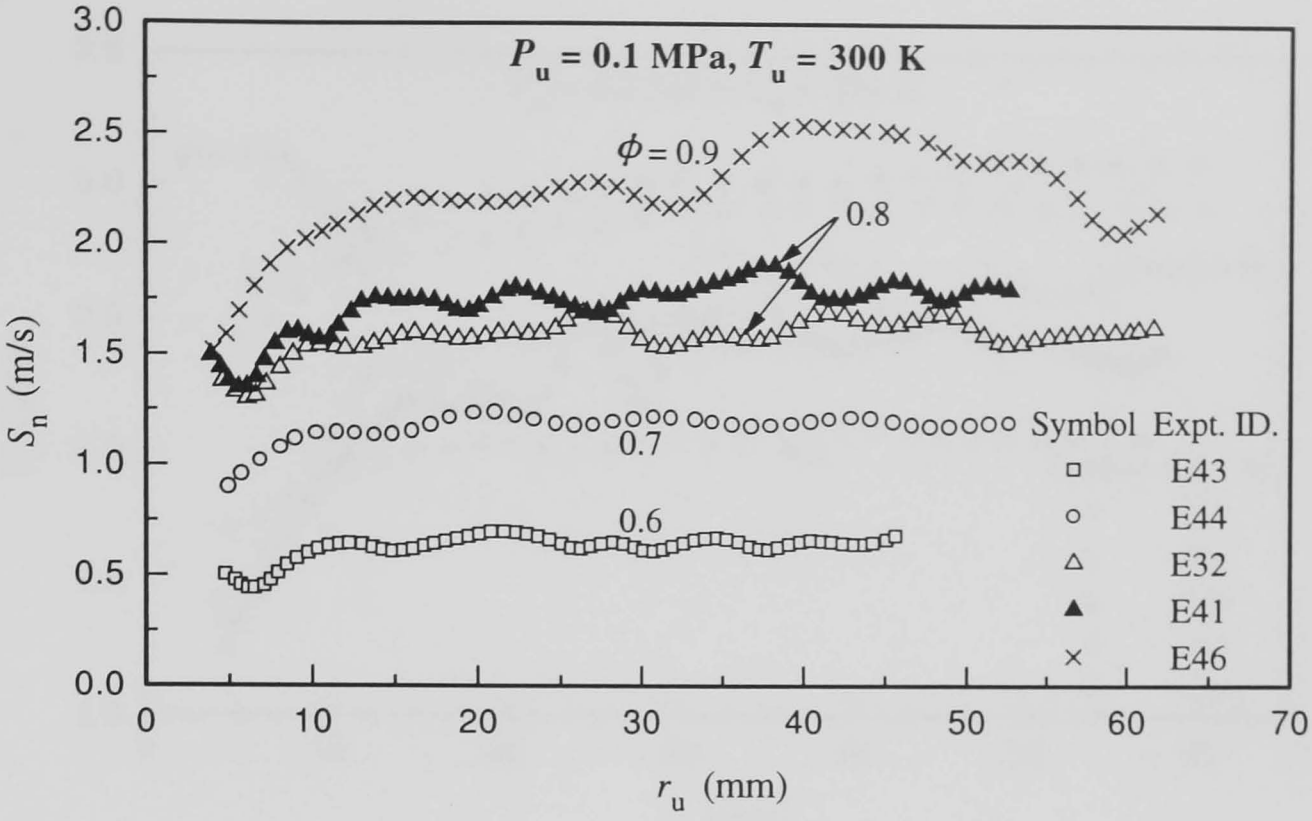

Fig. 4.1. Variations of S_n with r_u for lean methane-air mixtures at an initial temperature of 300 K and an initial pressure of 0.1 MPa. See Table 4.1 for experimental ID.

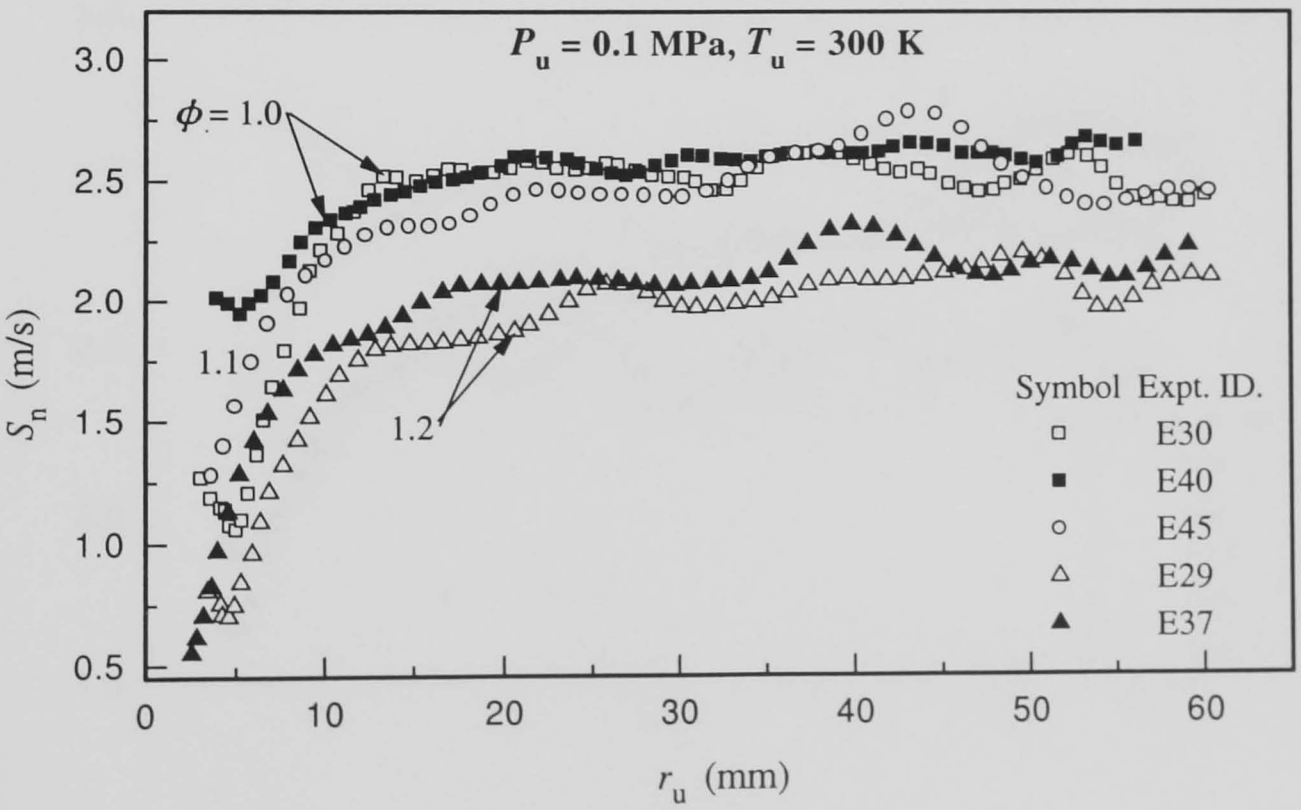

Fig. 4.2. Variations of S_n with r_u for methane-air mixtures with $\phi \geq 1$ at an initial temperature of 300 K and an initial pressure of 0.1 MPa. See Table 4.1 for experimental ID.

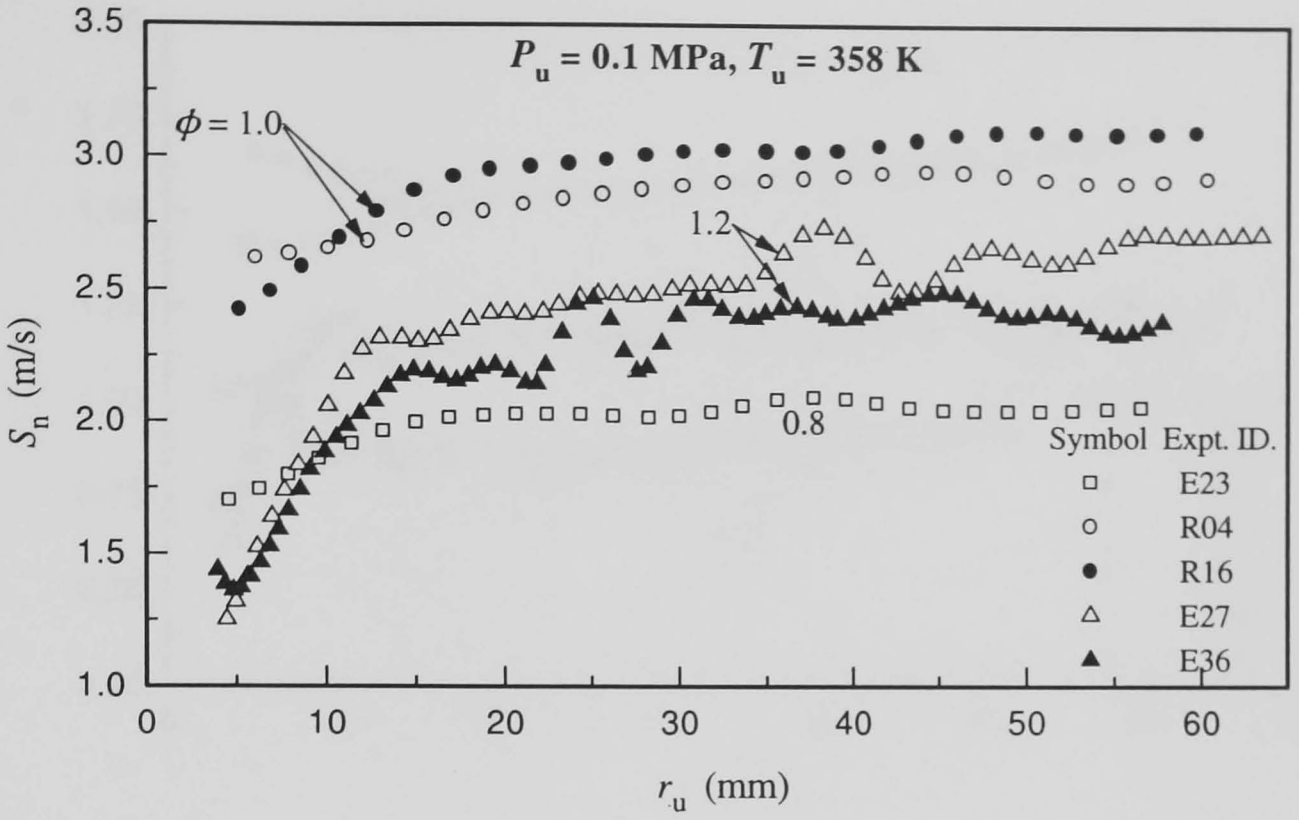

Fig. 4.3. Variations of S_n with r_u for methane-air mixtures at an initial temperature of 358 K and an initial pressure of 0.1 MPa. See Table 4.1 for experimental ID.

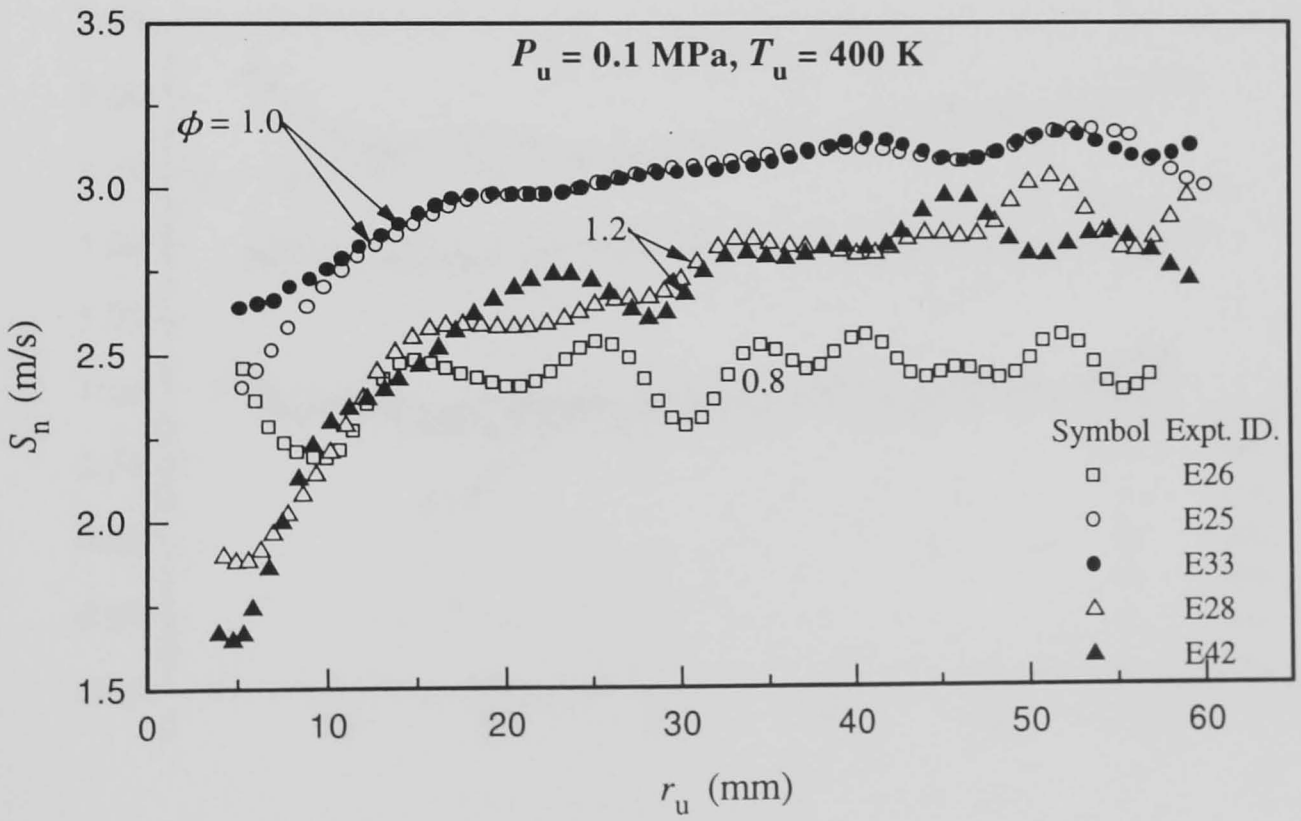

Fig. 4.4. Variations of S_n with r_u for methane-air mixtures at an initial temperature of 400 K and an initial pressure of 0.1 MPa. See Table 4.1 for experimental ID.

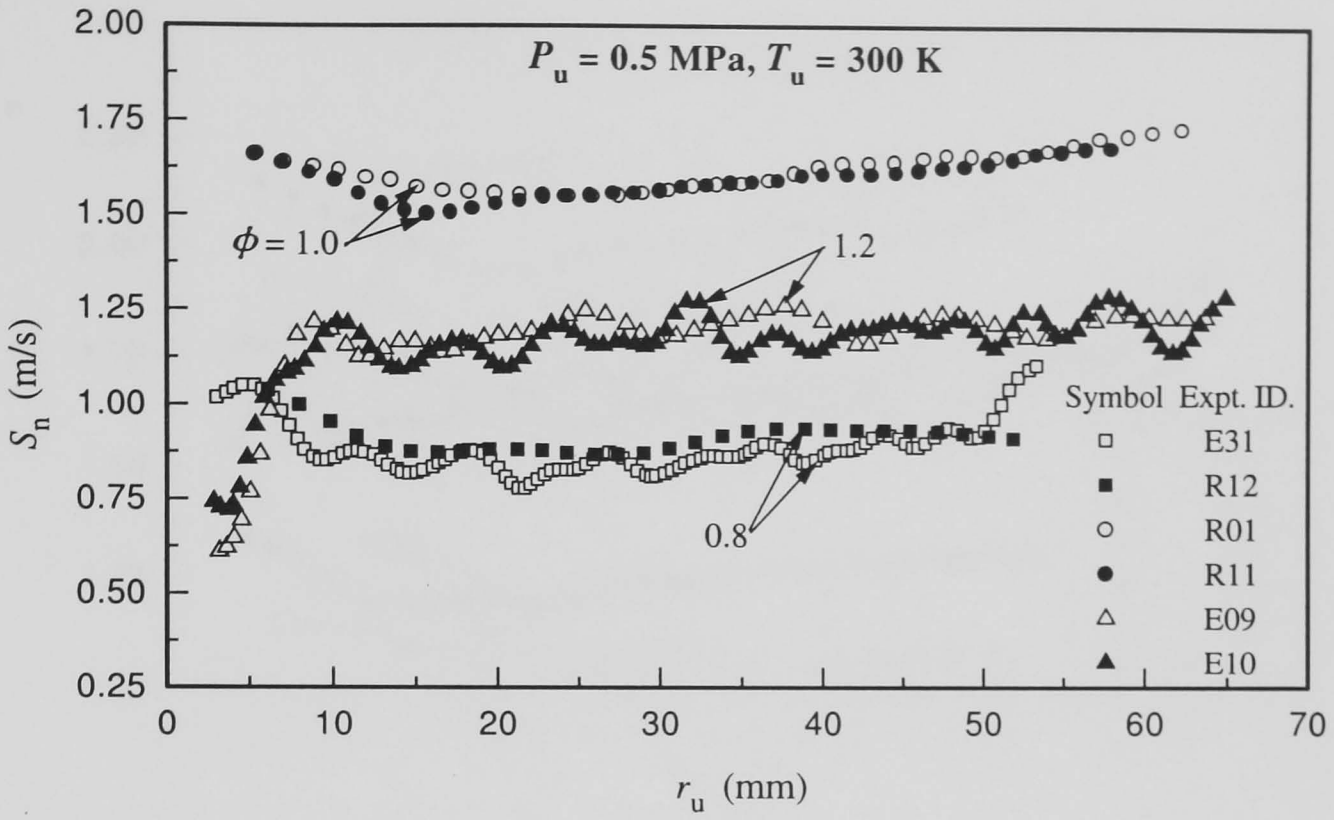

Fig. 4.5. Variations of S_n with r_u for methane-air mixtures at an initial temperature of 300 K and an initial pressure of 0.5 MPa. See Table 4.2 for experimental ID.

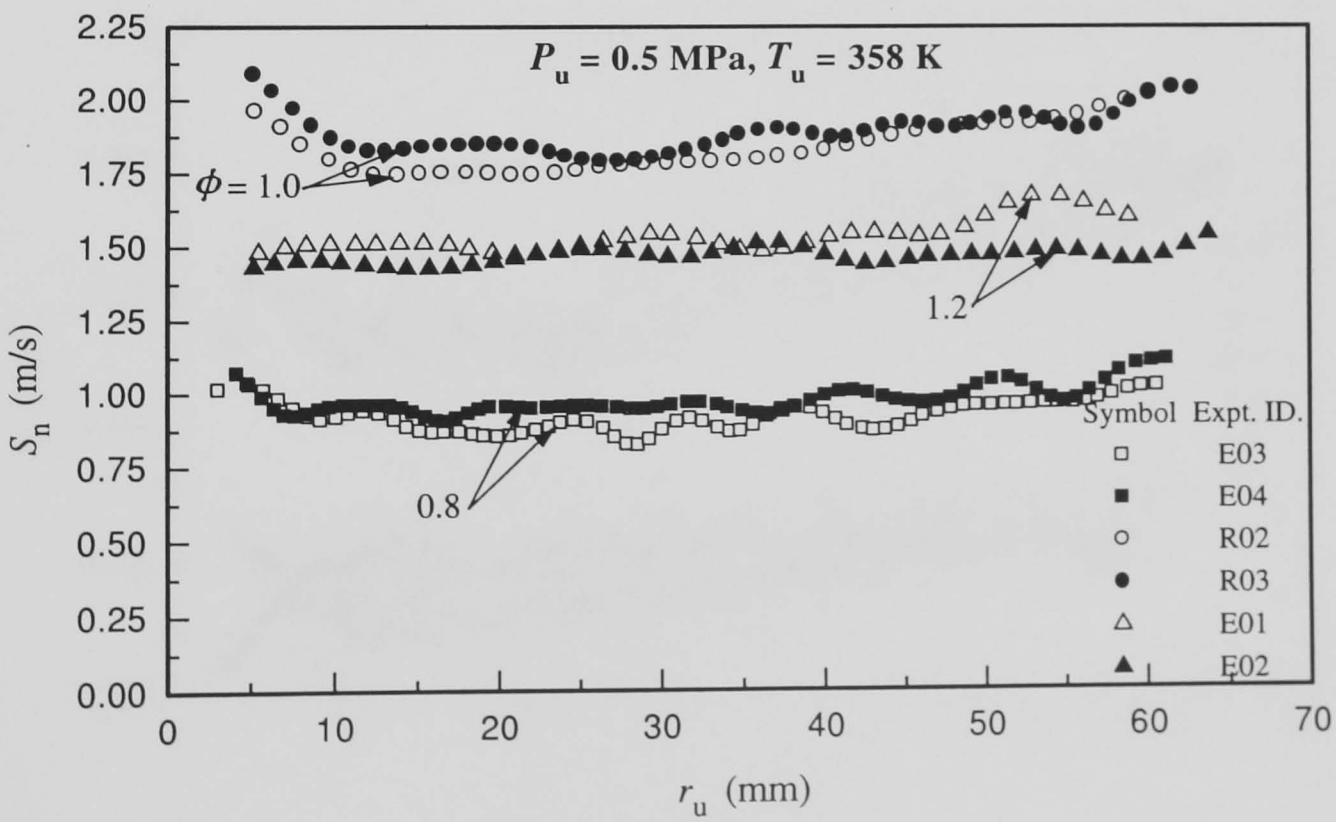

Fig. 4.6. Variations of S_n with r_u for methane-air mixtures at an initial temperature of 358 K and an initial pressure of 0.5 MPa. See Table 4.2 for experimental ID.

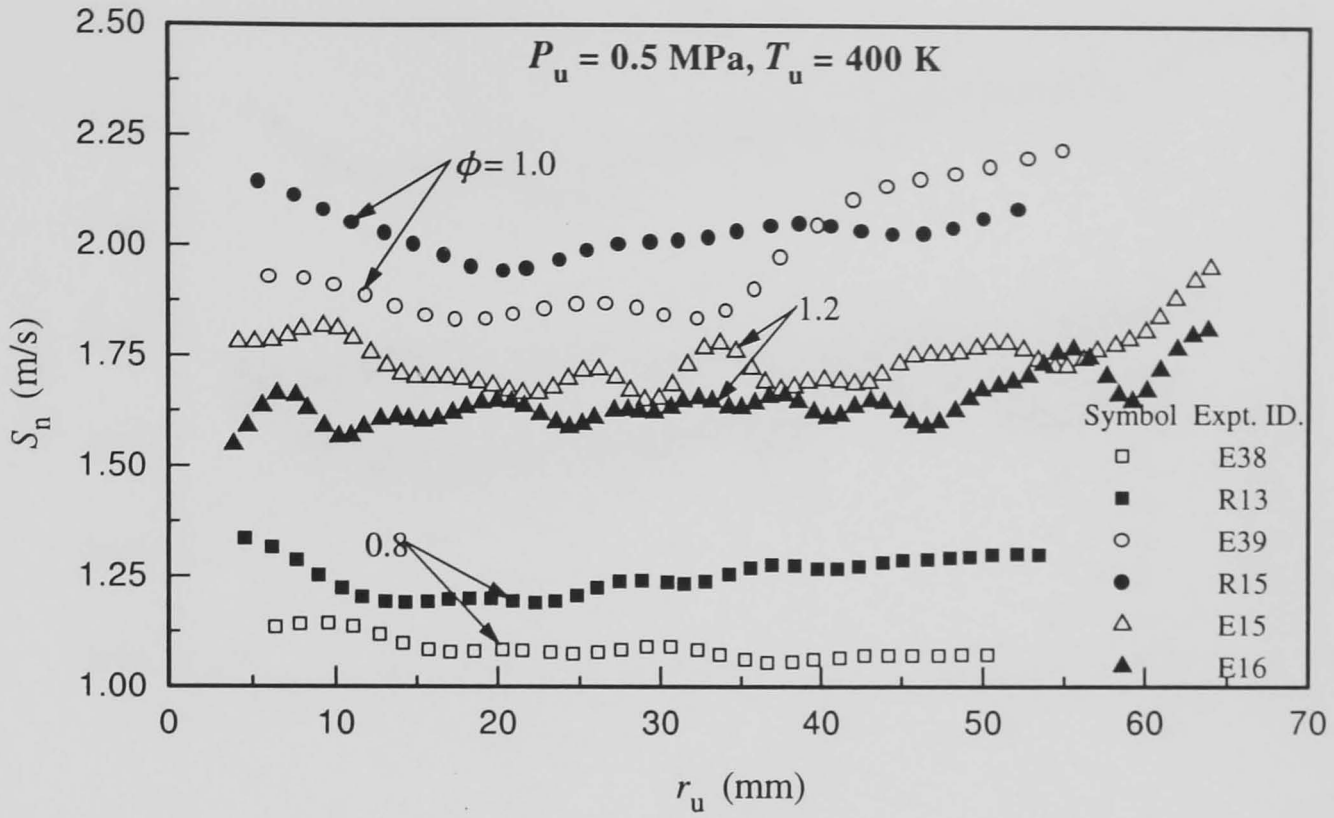

Fig. 4.7. Variations of S_n with r_u for methane-air mixtures at an initial temperature of 400 K and an initial pressure of 0.5 MPa. See Table 4.2 for experimental ID.

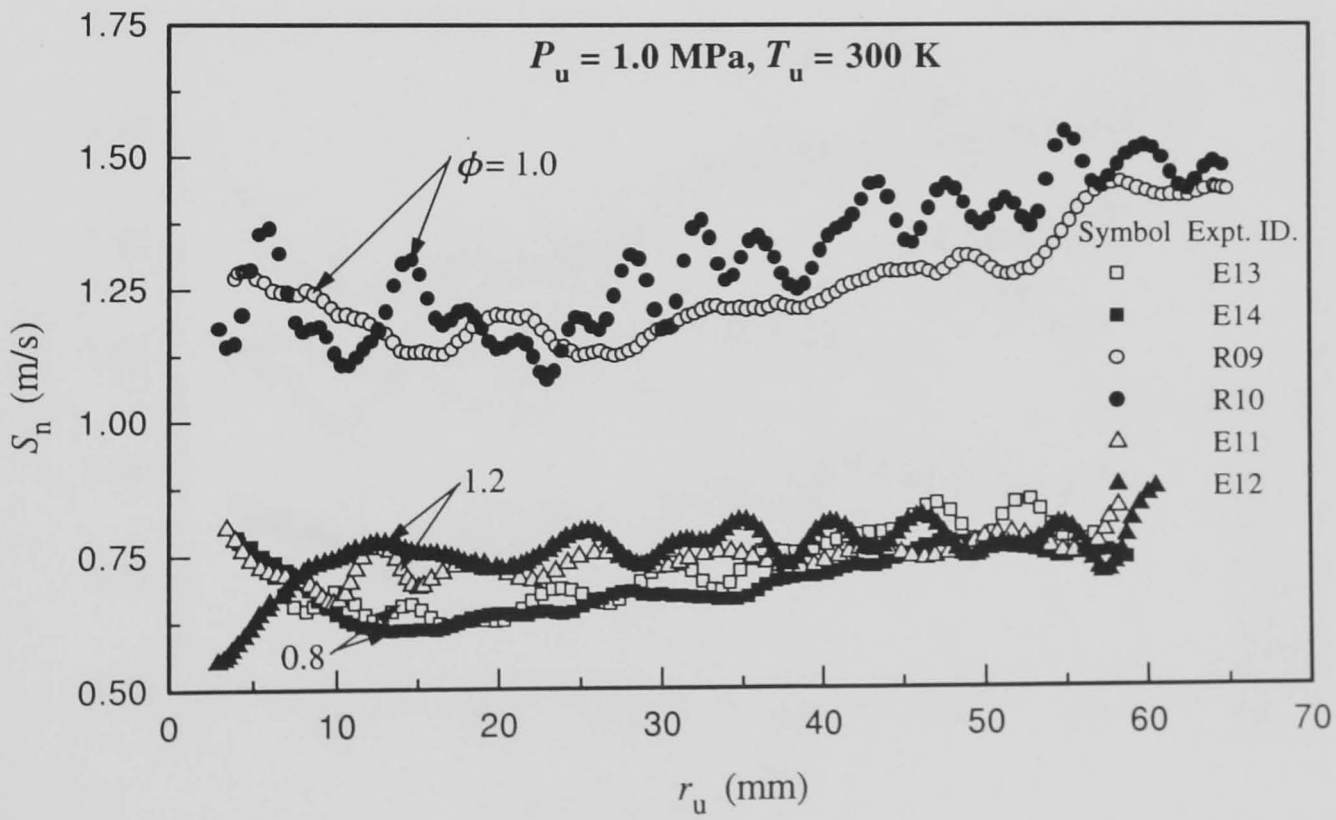

Fig. 4.8. Variations of S_n with r_u for methane-air mixtures at an initial temperature of 300 K and an initial pressure of 1.0 MPa. See Table 4.3 for experimental ID.

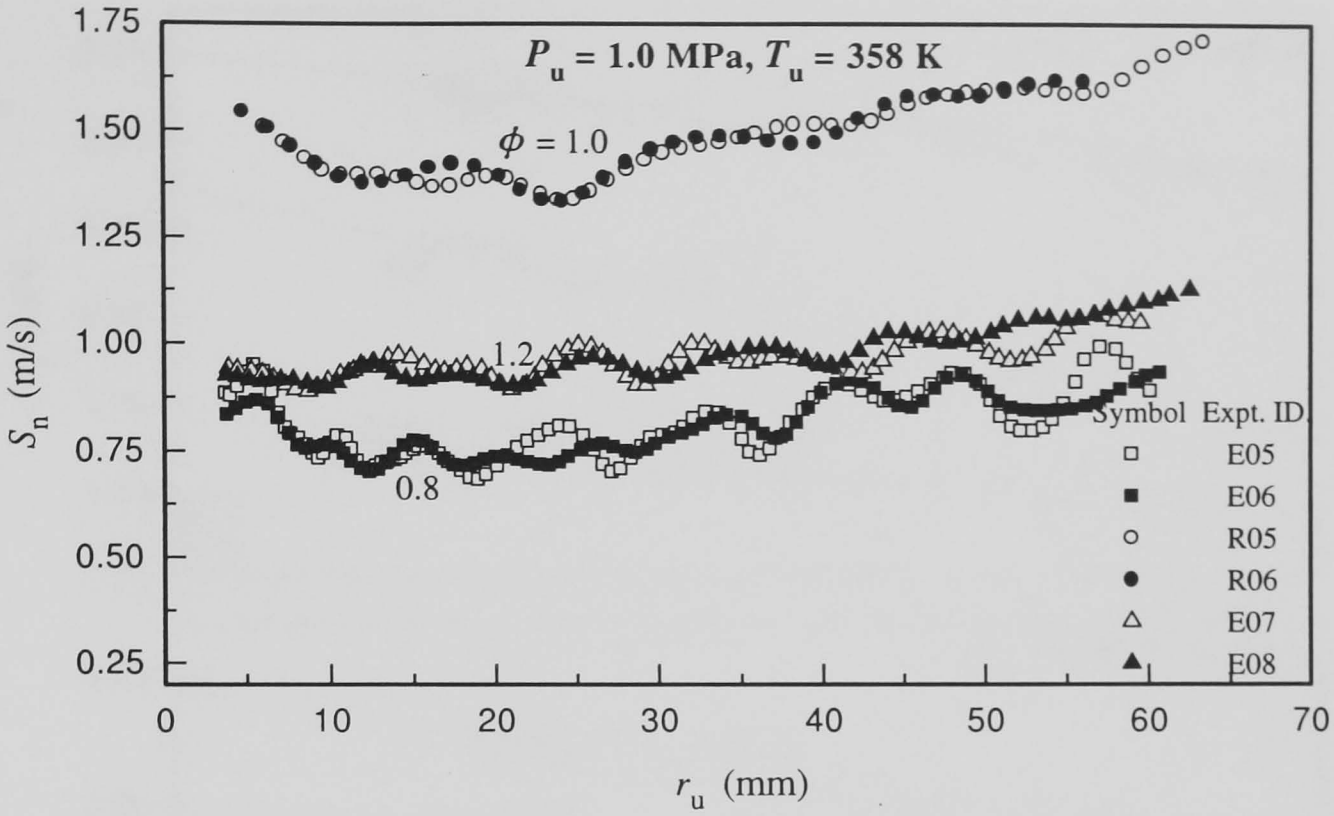

Fig. 4.9. Variations of S_n with r_u for methane-air mixtures at an initial temperature of 358 K and an initial pressure of 1.0 MPa. See Table 4.3 for experimental ID.

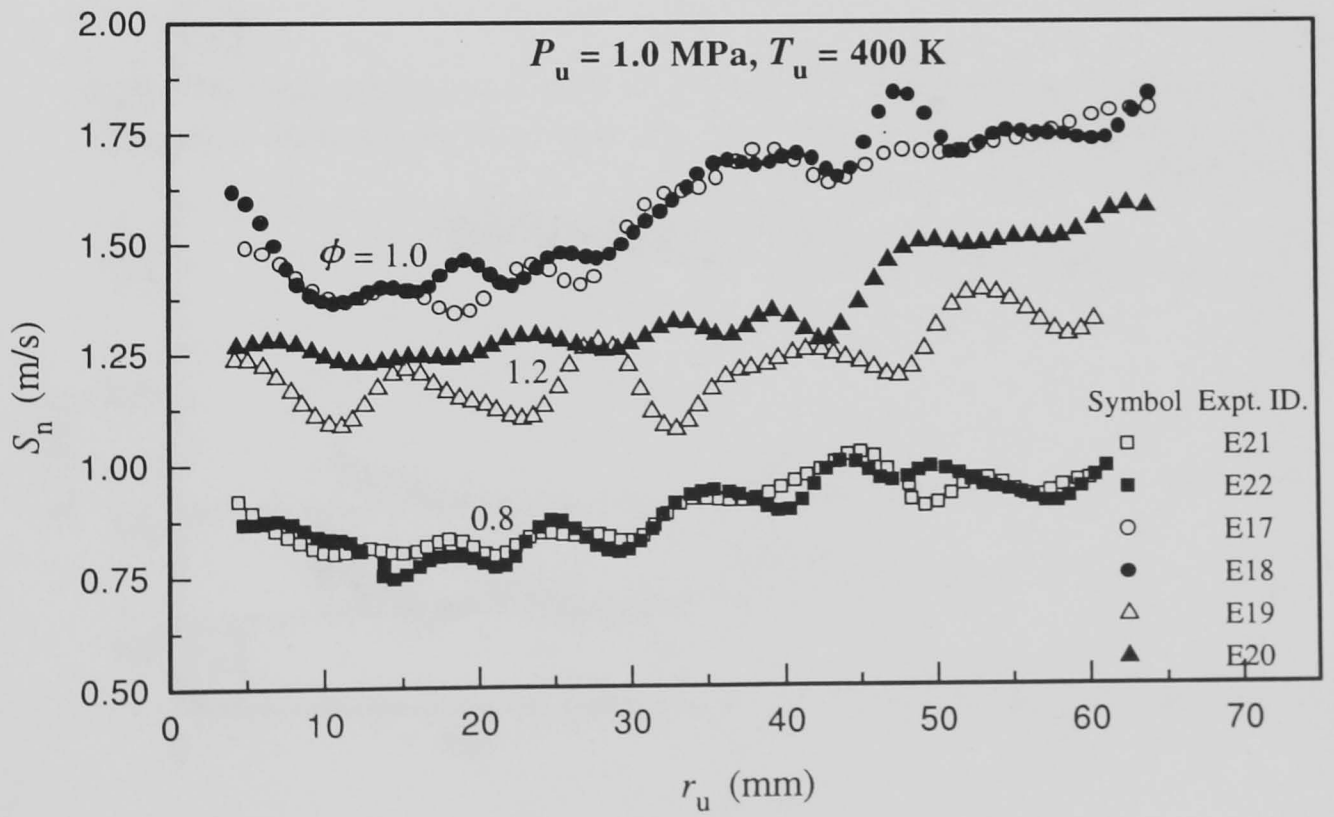

Fig. 4.10. Variations of S_n with r_u for methane-air mixtures at an initial temperature of 400 K and an initial pressure of 1.0 MPa. See Table 4.3 for experimental ID.

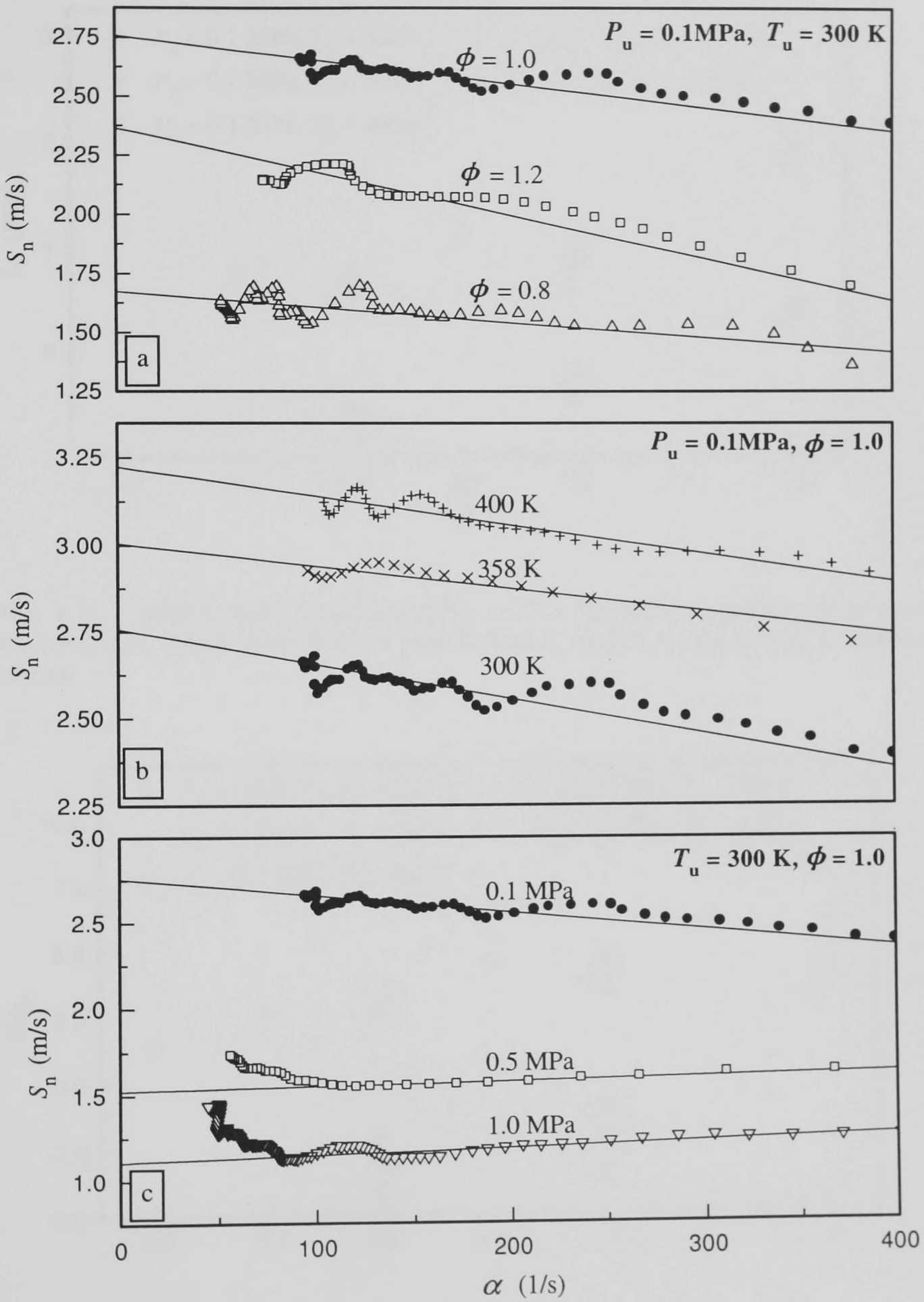

Fig. 4.11. Measured flame speeds at different stretch rates, equivalence ratios, initial pressures and temperatures.

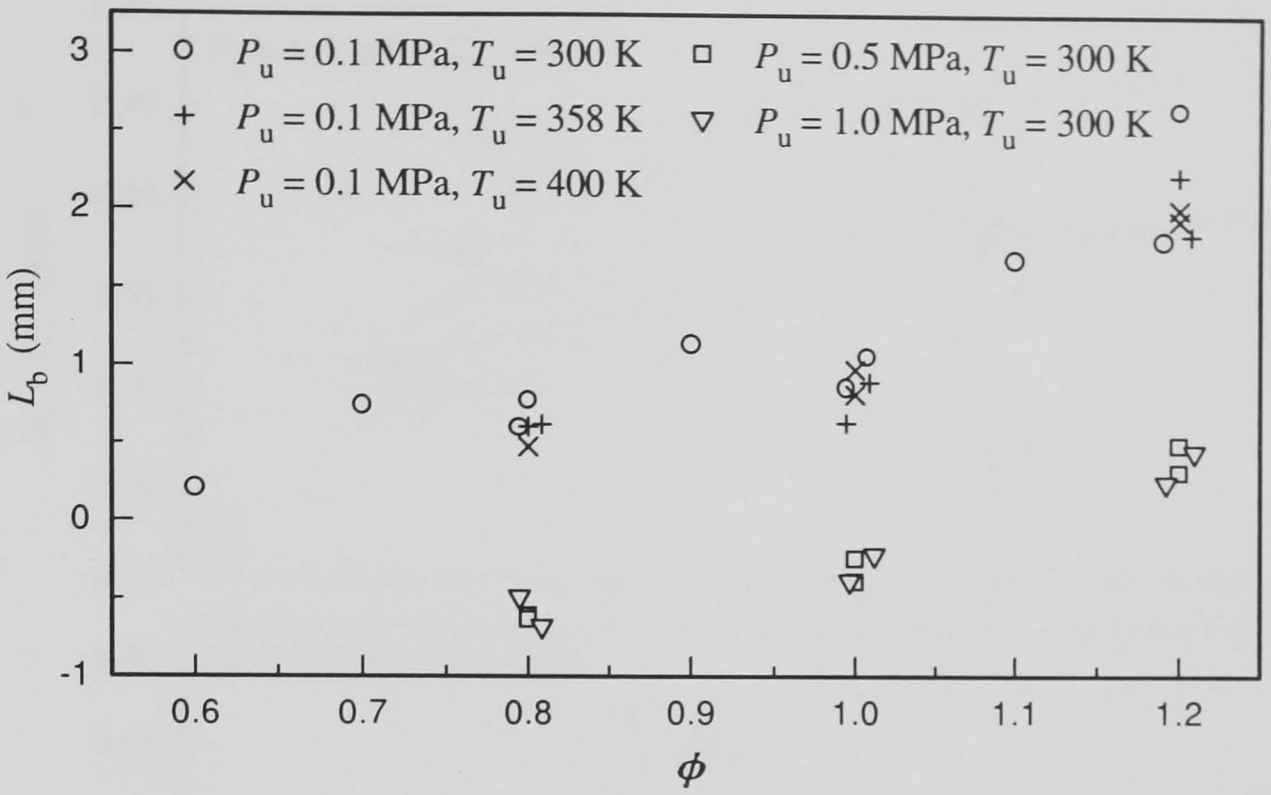

Fig. 4.12. Experimental variations of L_b with ϕ, for different initial pressures and temperatures. Some symbols have been displaced slightly on the x-axis to improve clarity.

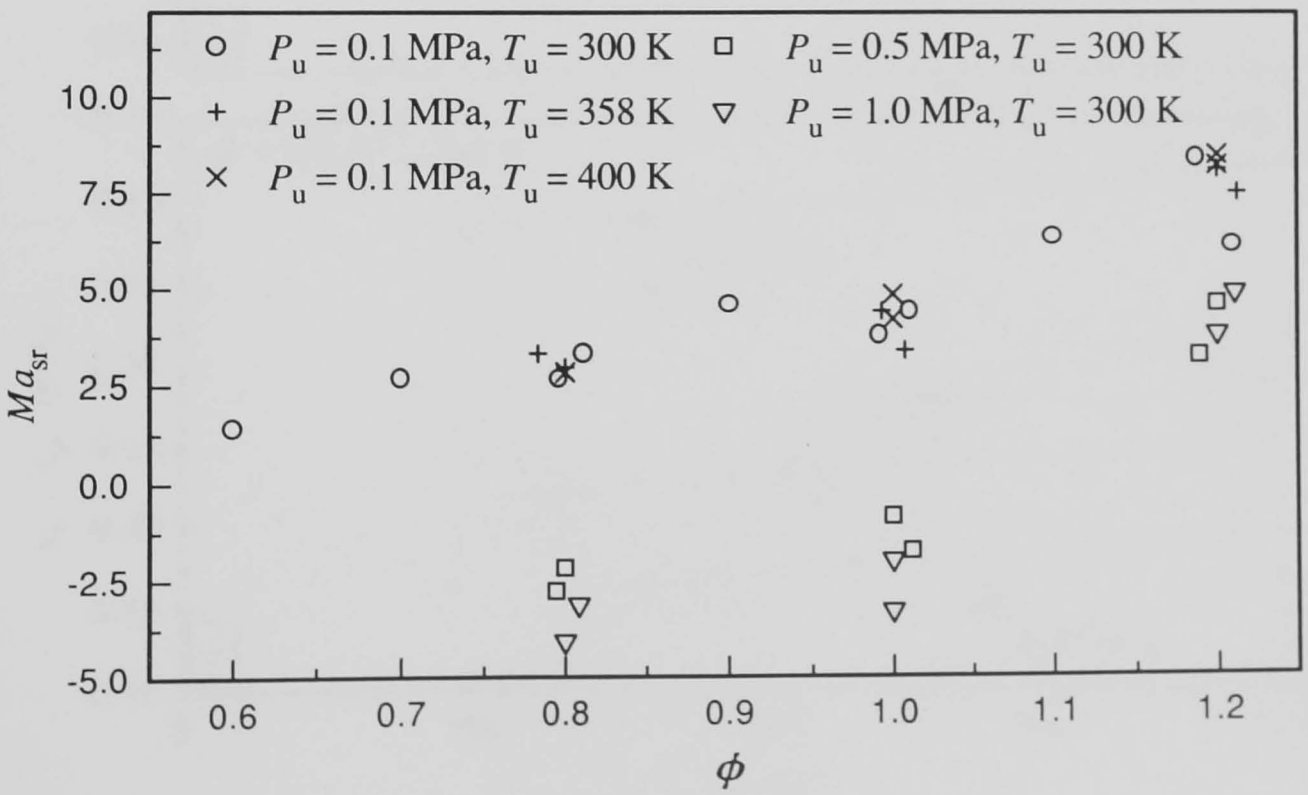

Fig. 4.13. Variation of Ma_{sr} with equivalence ratio, ϕ. Some symbols have been displaced slightly on the x-axis to improve clarity.

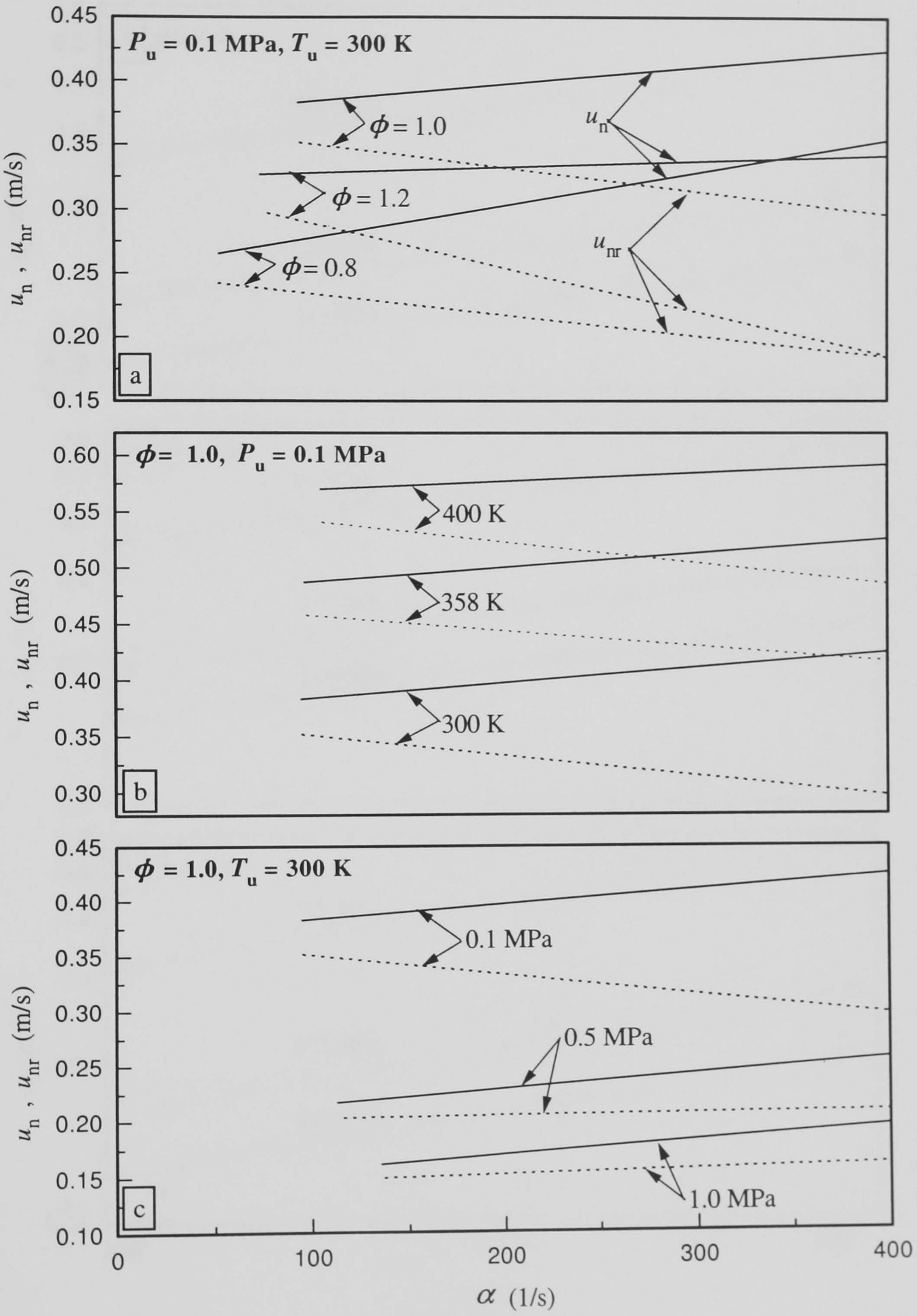

Fig. 4.14. Variation of stretched burning velocities with flame stretch for variations of equivalence ratio, initial pressure and temperature.

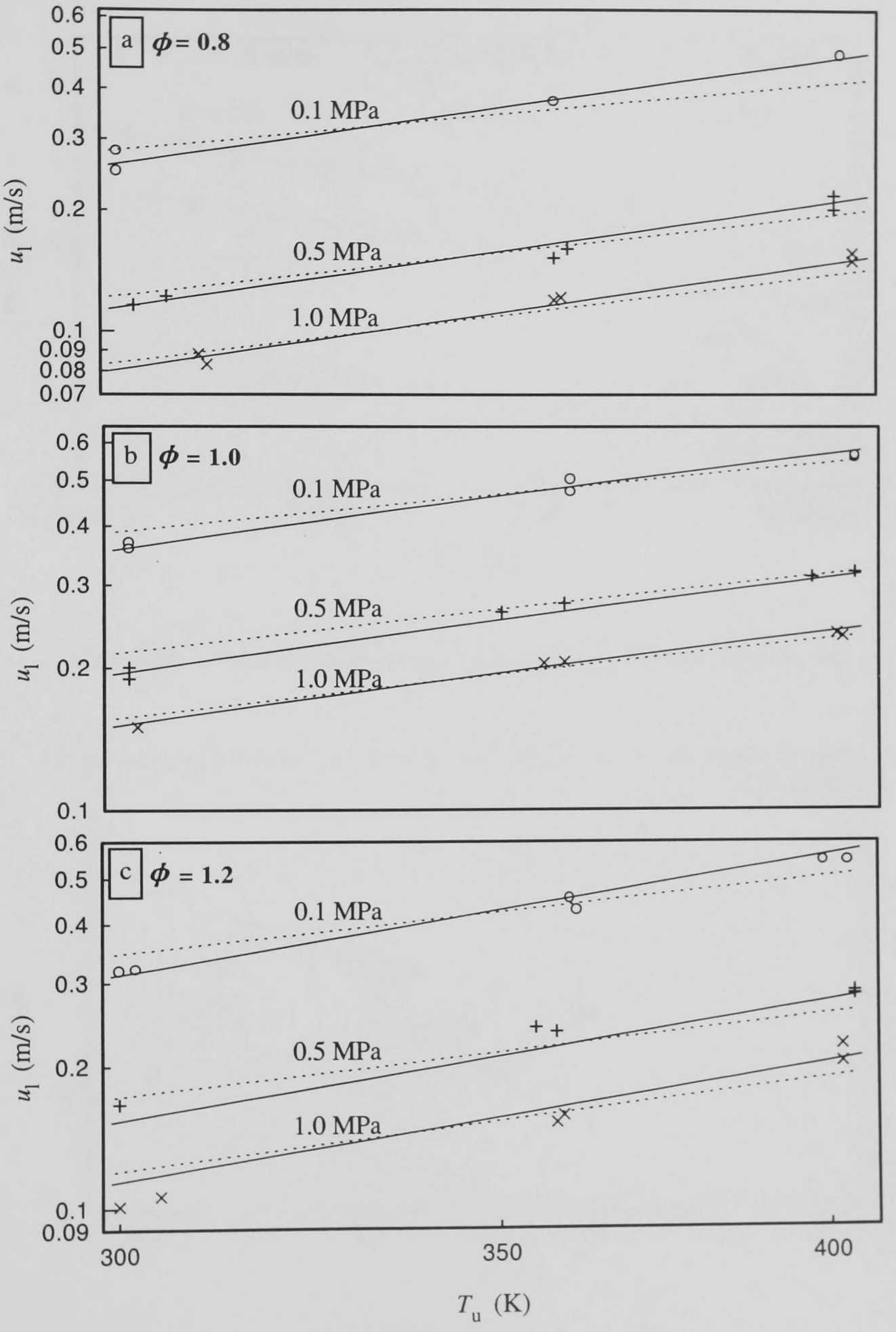

Fig. 4.15. Variation of unstretched burning velocities with initial temperature. Solid lines show the values obtained using Eq. 4.2, and dotted lines using Eq. 4.6.

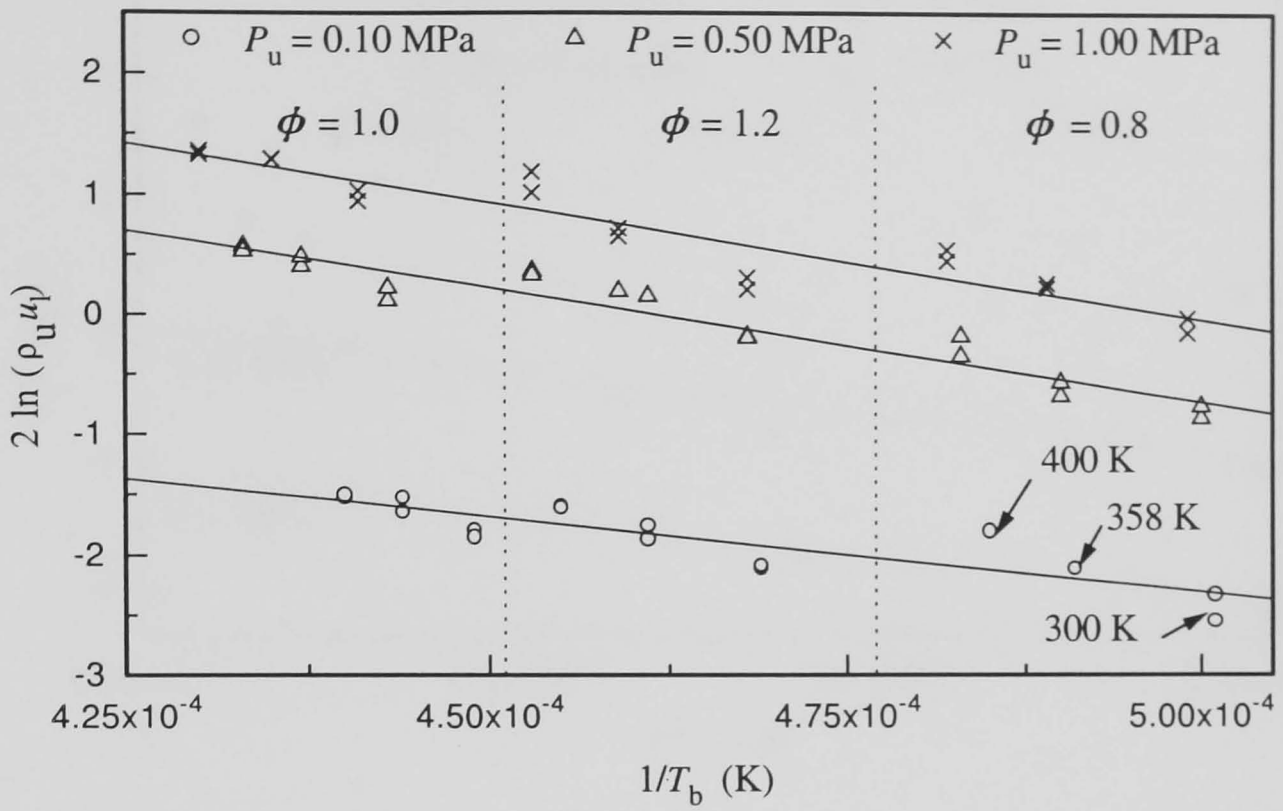

Fig. 4.16. Variation of $2\ln(\rho_u u_l)$ with $1/T_b$ for methane-air mixtures.

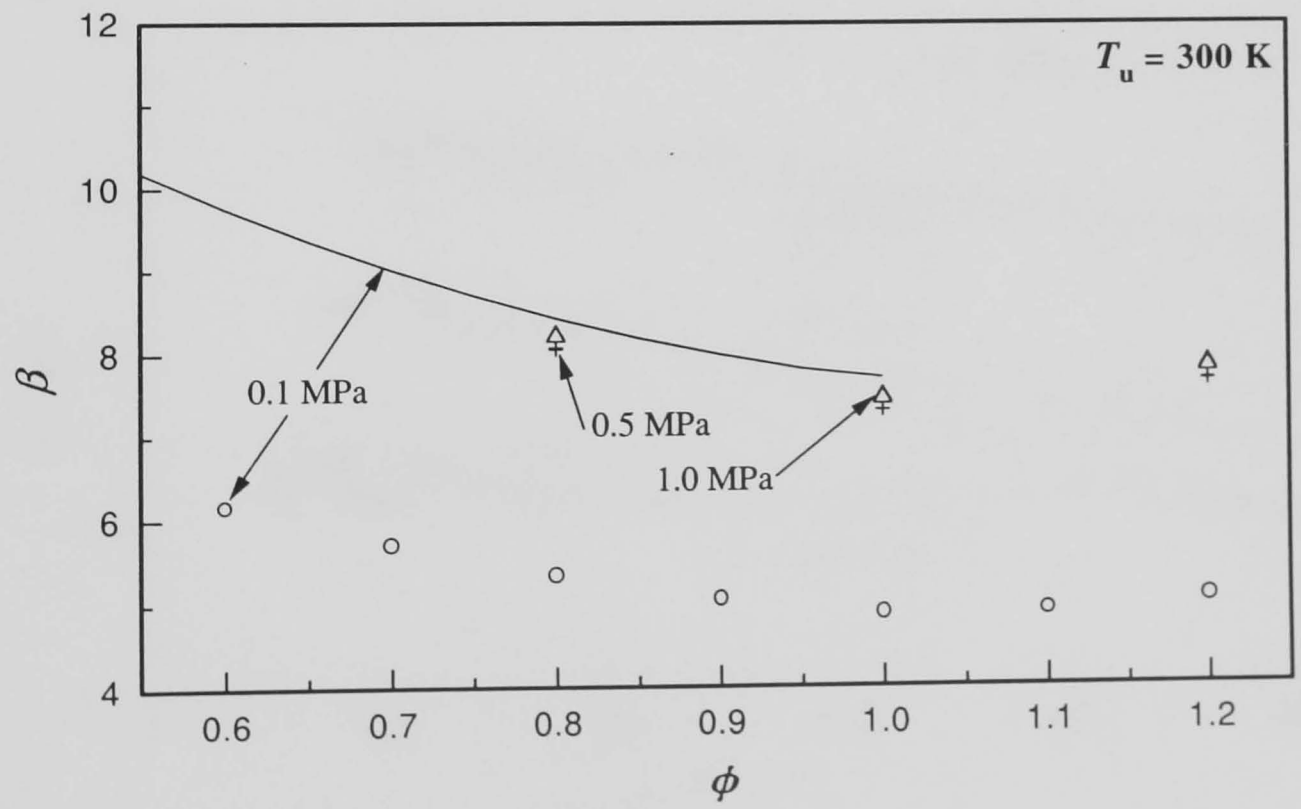

Fig. 4.17. Variation of Zeldovich number with equivalence ratio. Hence, solid lines are the results using data of Göttgen *et al.* (1992).

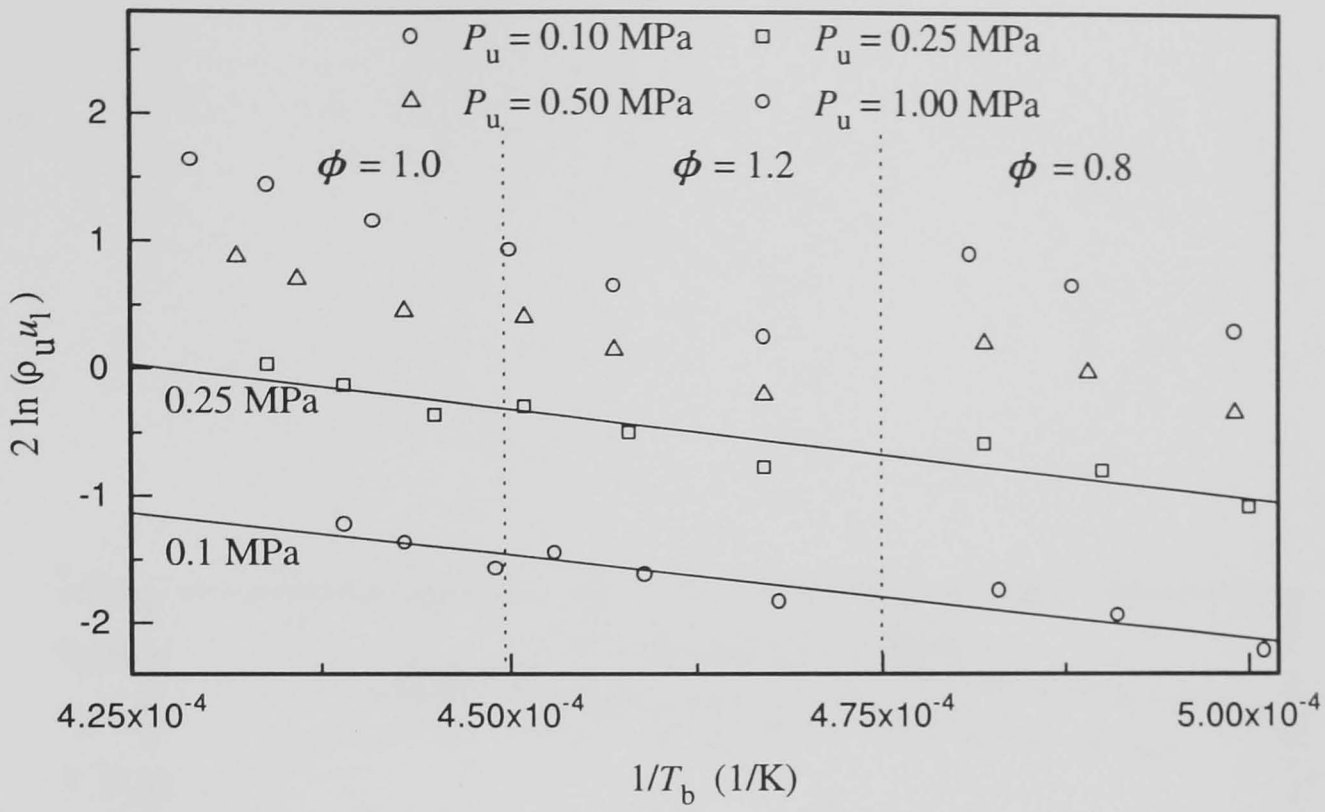

Fig. 4.18. Variation of $2\ln(\rho_u u_l)$ with $1/T_b$ for methane-air mixtures, computed using GRI-Mech.

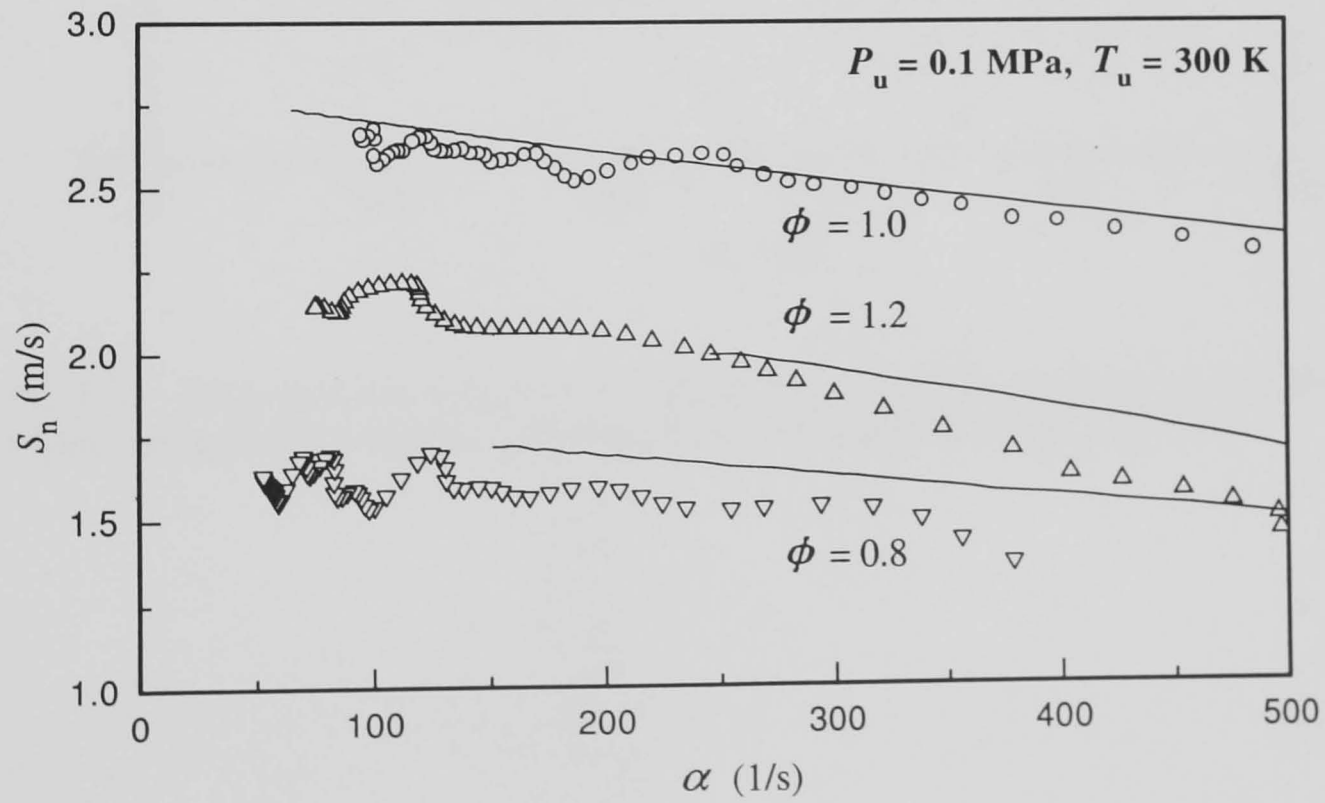

Fig. 4.19. Measured and computed using reduced mechanism, flame speeds at different stretch rates for different equivalence ratios at an initial pressure of 0.1 MPa with initial temperature 0f 300 K.

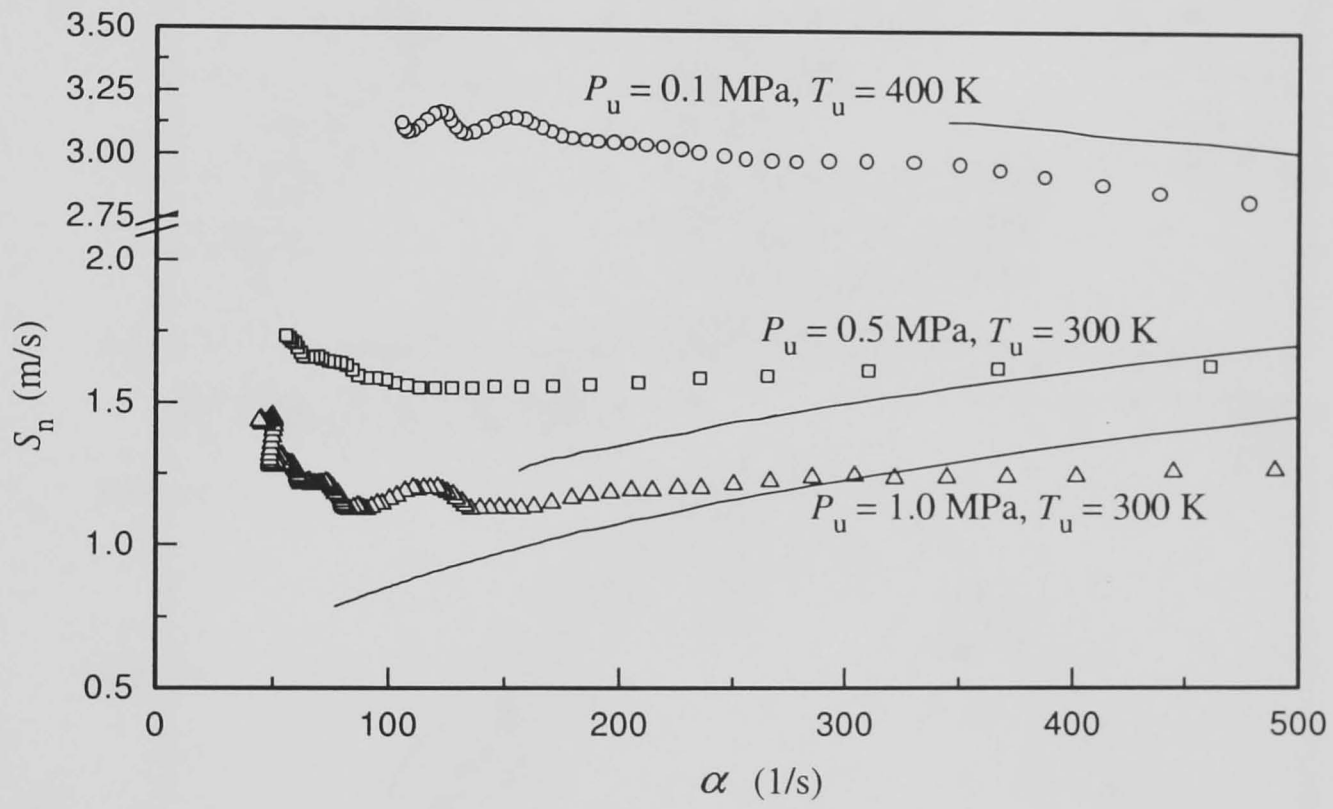

Fig. 4.20. Measured and computed, using reduced mechanism, flame speeds at different stretch rates, initial pressures and temperatures for stoichiometric mixtures.

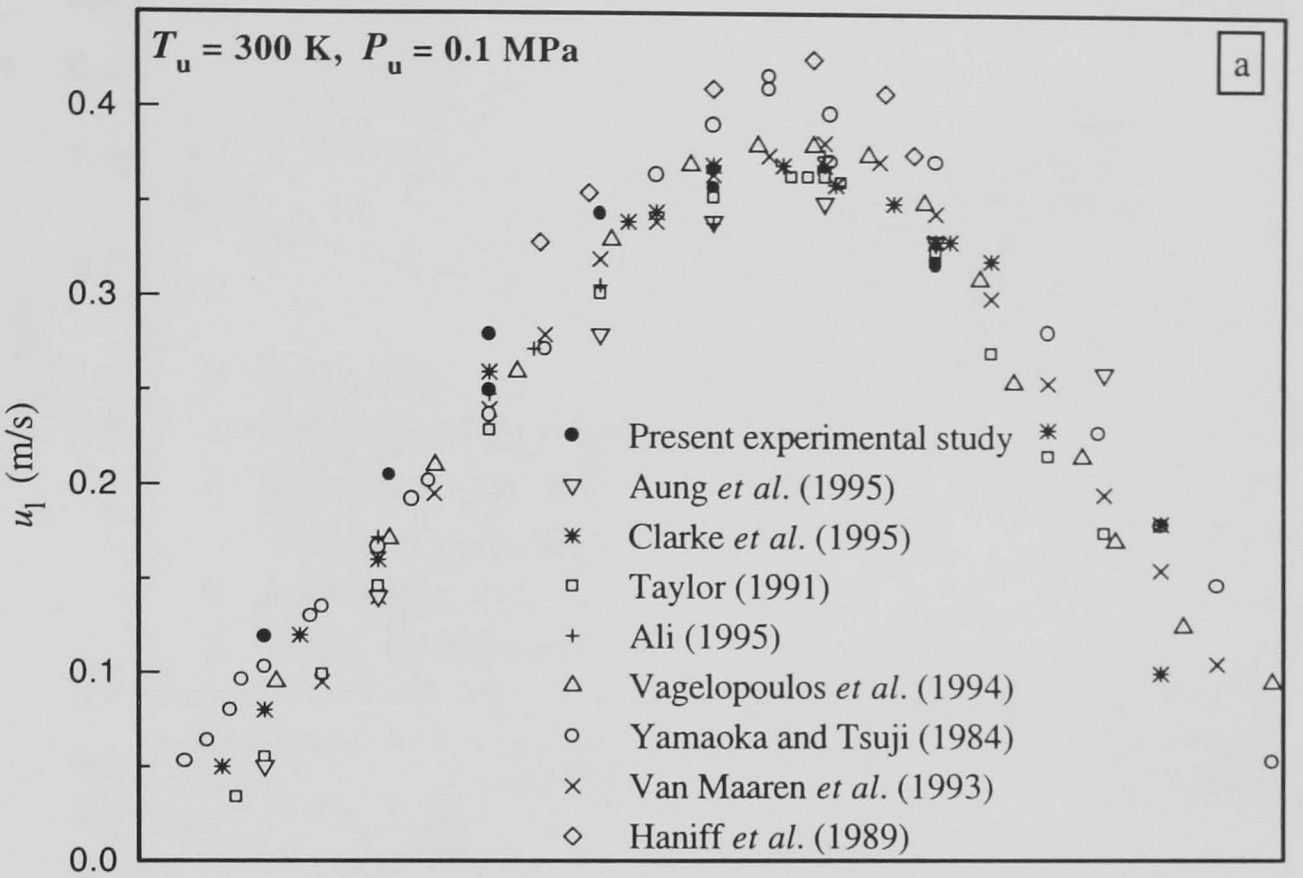

Fig. 4.21. Laminar burning velocities plotted against equivalence ratio.

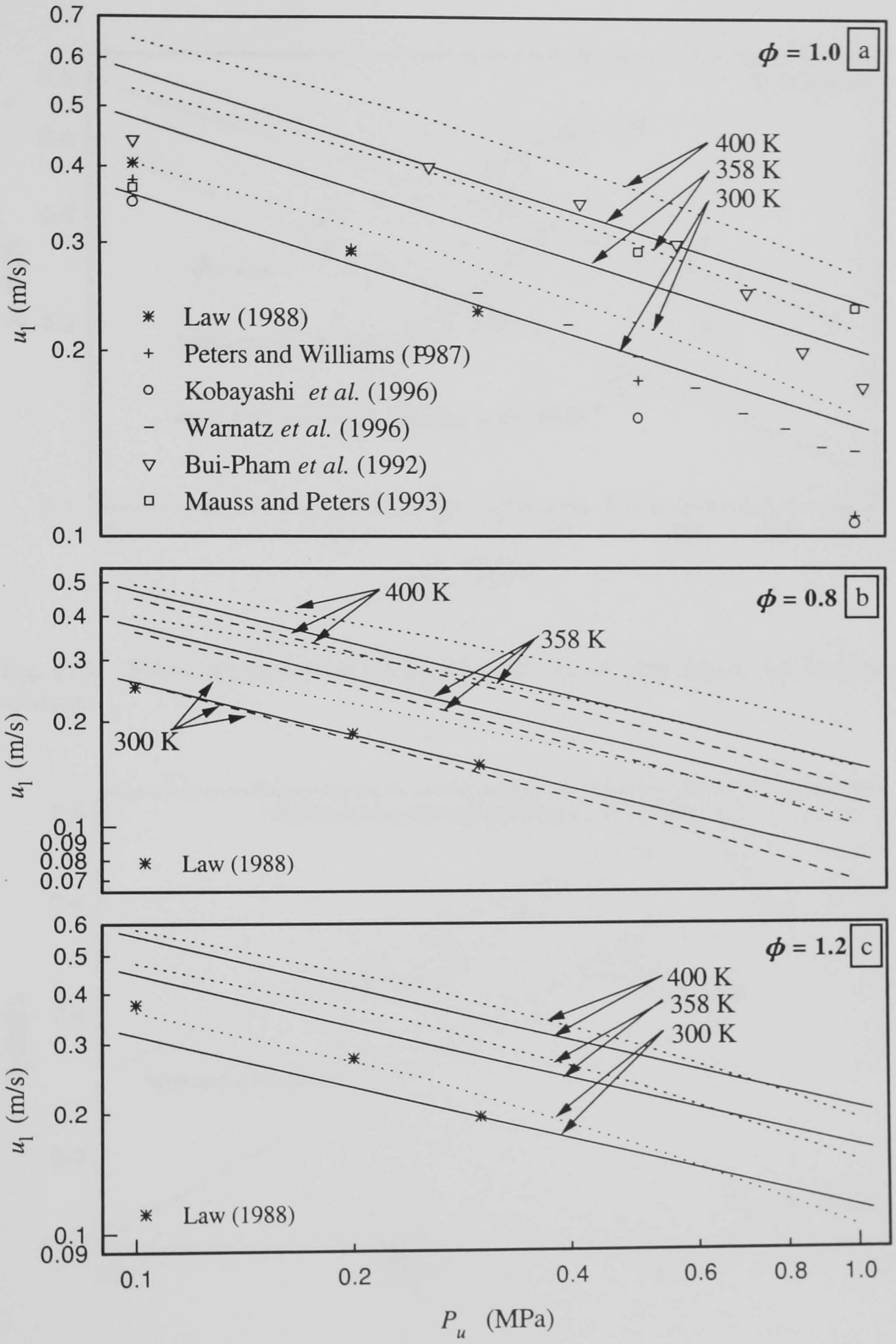

Fig. 4.22. Comparison of the present data with those of others. Solid lines are the values calculated using Eq. 4.2, dotted lines are the values obtained from computations using GRI-Mech and the dashed lines are the results form Göttgens *et al.* (1992).

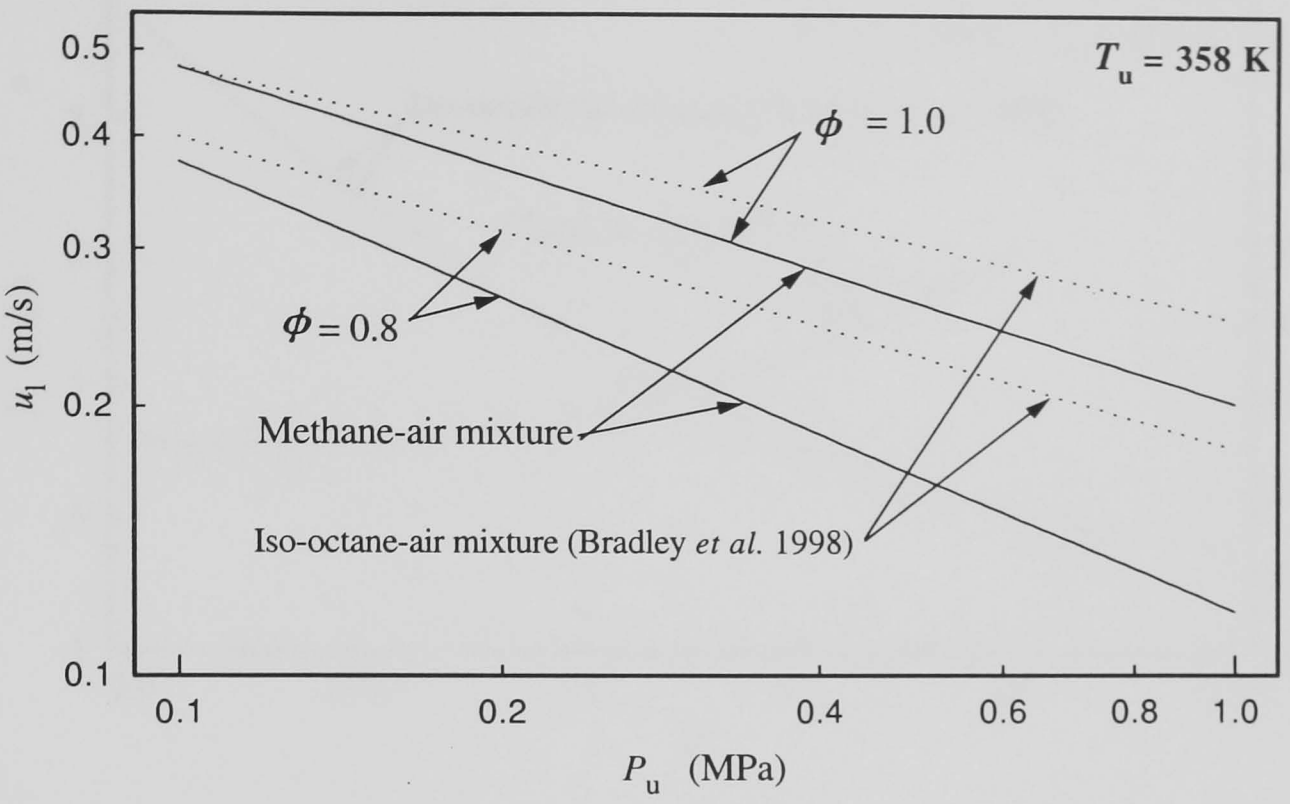

Fig. 4.23. Effect of pressure on the burning velocity of methane-air and iso-octane-air mixtures.

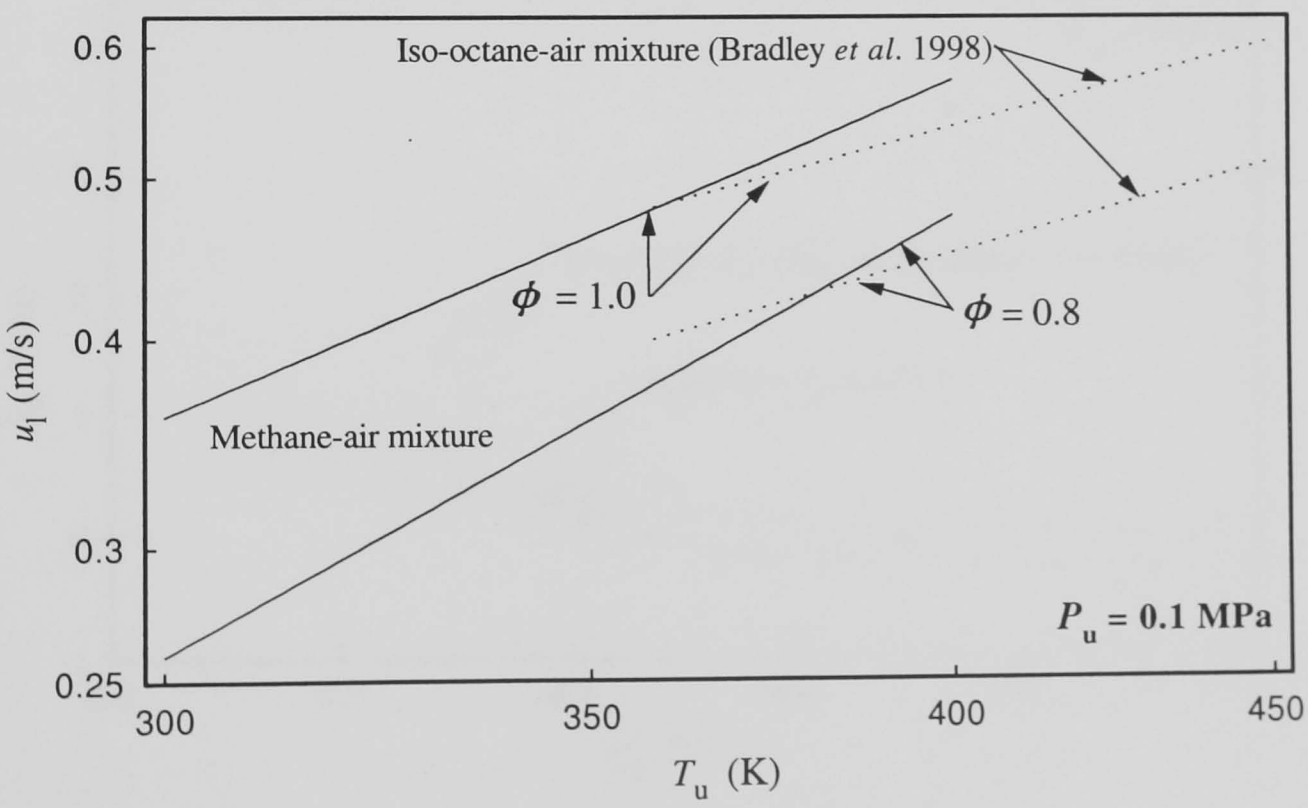

Fig. 4.24. Effect of temperature on the burning velocity for methane-air and iso-octane-air mixtures.

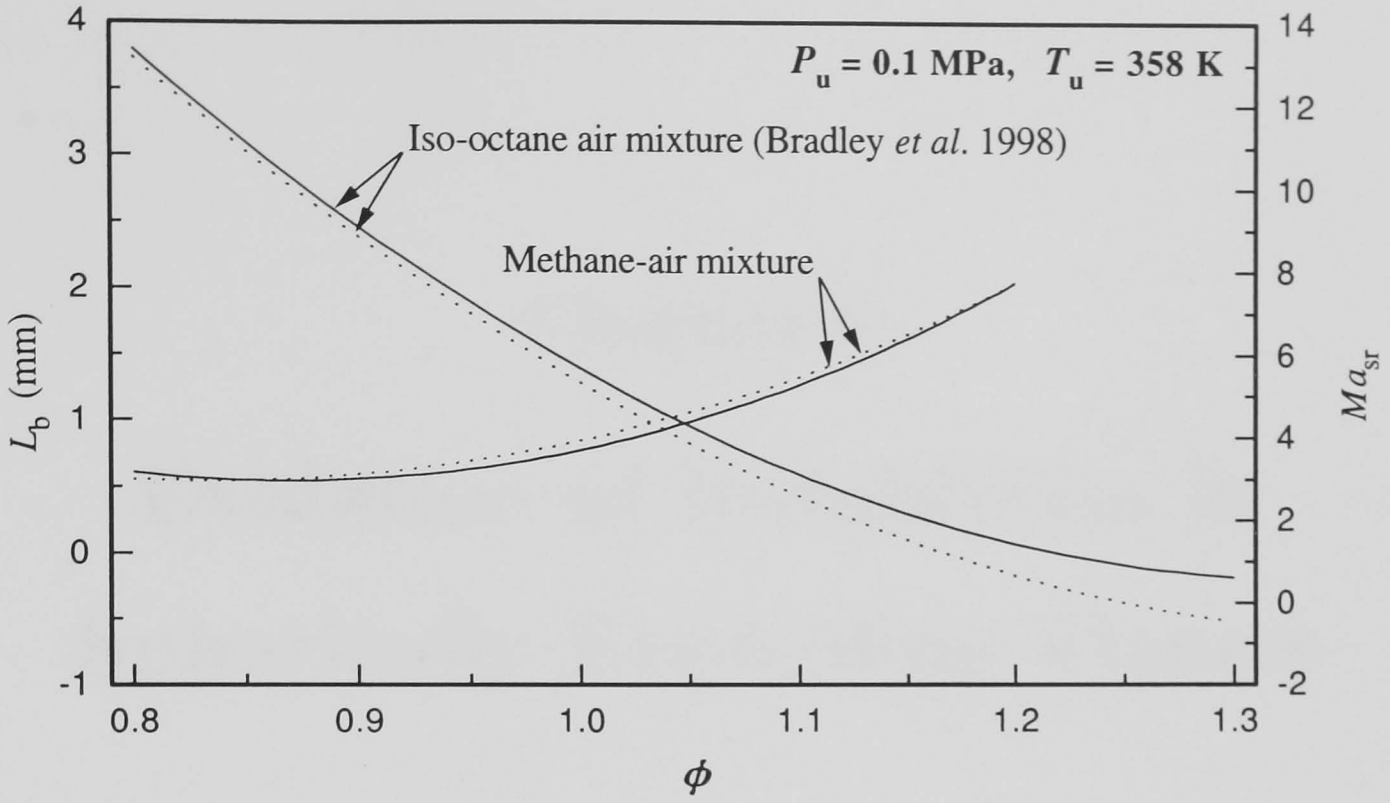

Fig. 4.25. Effect of equivalence ratio on L_b and Ma_{sr} for methane-air and iso-octane-air mixtures. Hence, solid lines represent L_b and dotted lines represent Ma_{sr}.

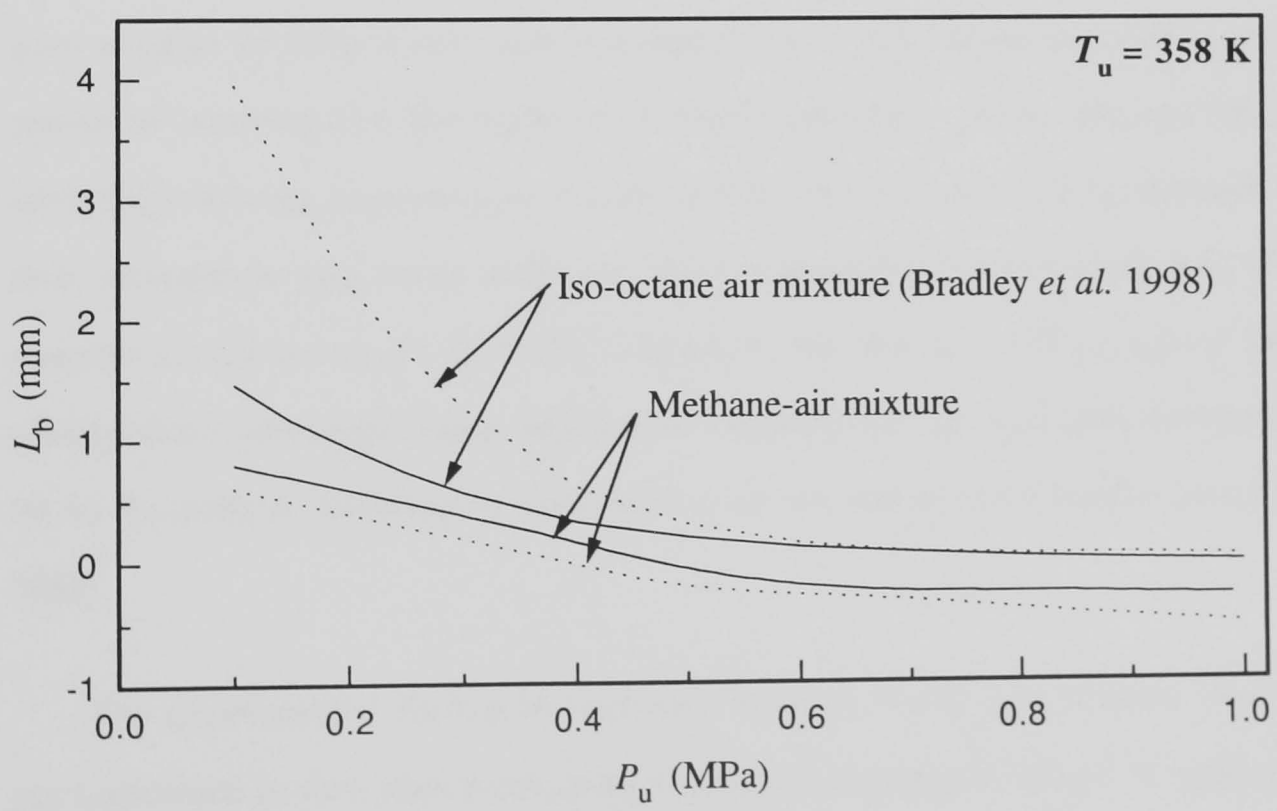

Fig. 4.26. Markstein length, L_b plotted against initial pressure for mixtures at different equivalence ratios. Dotted lines represent lean mixtures ($\phi = 0.8$) and solid lines represent stoichiometric ($\phi = 1.0$) mixtures.

Chapter 5

Evolution of Instabilities in Spherically Expanding Flames

5.1 Introduction

From both theoretical and experimental considerations, a spherical flame originated from a point ignition source and propagating in a premixture provides a convenient means of studying the development of flame instability. This arrangement has the advantage of being geometrically simple and excluding heat losses by thermal conduction, interaction with vessel walls and other undesirable factors which may affect the phenomena (Zeldovich *et al.* 1985). Moreover, the size of the flame sphere limits the perturbation wavelength range which is also growing in time, and thissetsdefinable limits to the critical wavelengths associated with the instability (Istratov and Librovich 1969).

The experimental studies of Lind and Whitson (1977) and Makeev *et al.* (1983) are important in that they cover large unconfined explosions related to explosion hazards. They clearly show how the flame speed increases with flame radius. Gostintsev *et al.* (1987) reviewed these and other results and suggested the self-turbularization and fractalization of the initially laminar flame as its radius increased. Bradley and Harper (1994) suggested the first stage of a developing instability is the propagation

of surface 'cracks' across the flame surface. The onset of these correspond with the onset of instabilities as predicted by the linear theory of Bechtold and Matalon (1987). However, experiments show that a further delay occurs before the transition to a completely developed cellular flame occurs (Groff 1982, Matalon and Erneux 1984, Bradley and Harper 1994, Bradley *et al.* 1998). Bradley (1998) extended this concept and suggested that the smallest unstable wavelength at a given Peclet number is always greater than that suggested by the theory of Bechtold and Matalon (1987). With this approach he was able to predict flame speeds in fair agreement with those correlated by Gostintsev *et al.* (1987). The expression so derived is similar to one obtained in a recent Lagrangian analysis of Ashurst (1997).

In the present study, transition to cellular flames is studied using flame photography, as discussed in previous chapters. Experimental results clearly show the acceleration of the flame, and how such flames become fully developed cellular flames after a certain value of Peclet number has been attained.

5.2 Experimental Correlation for Onset of Cellular Instability

A spherically expanding flame is subjected to stretch due to both curvature and aerodynamic strain and these have a stabilizing effect on the flame front. The effect of stretch on laminar burning velocity is discussed in § 1.4 and § 4.2. Shown in Fig. 5.1 are experimentally derived variations of the Karlovitz stretch factors due to curvature and strain, K_C and K_S, with Peclet number for a stoichiometric methane-air mixture at an initial temperature of 300 K and initial pressure of 0.1 MPa. The effect of K_S is dominant over that of K_C. Moreover, as reported in Tables 4.1 to 4.3, the values of Ma_{cr} and Ma_{sr} are found to be nearly equal for methane-air mixtures. Hence, the single value of Ma_{sr} represents the total effect quite well, as demonstrated in Fig. 5.2

and Eq. 1.10 might be approximated by:

$$\frac{u_l - u_{\rm nr}}{u_l} \approx K Ma_{\rm sr} \tag{5.1}$$

where, K is the sum $K_{\rm c}$ and $K_{\rm s}$. In the stability analysis in § 5.4, the relevant Markstein number is taken to be $Ma_{\rm sr}$.

For methane-air mixtures at high pressure, the initial flame speed, after the effects of ignition have decayed, is given by Eq. 1.10 and the flame surface is smooth. However, as it propagates, at a critical Peclet number, $Pe_{\rm cl}$, it become cellular. The estimation of $Pe_{\rm cl}$ is described in § 3.3. Flames which have higher values of $Ma_{\rm sr}$ have a higher values of $Pe_{\rm cl}$. Shown in Fig. 5.3 are critical Peclet numbers plotted against $Ma_{\rm sr}$ for methane-air mixtures obtained from the present study and for iso-octane-air mixtures from Bradley *et al.* (1998). A straight line fit describes them well and is:

$$Pe_{\rm cl} = 177\ Ma_{\rm sr} + 2177 \tag{5.2}$$

This correlation is valid for all the present experiments in which instability is observed.

5.3 Flame Propagation at Large Radii

Shown in Fig. 5.4 are the flame radii plotted against time in the large scale methane-air explosions reported by Lind and Whitson (1977). These were designed to observe the effects of flame instability in atmospheric methane-air mixtures at 298 K. Also plotted are the flame radii against time data measured in the present experiments for an initial temperature of 300 K and an initial pressure of 0.1 MPa. The experimental points are shown by the symbols. No instability is observed for explosions in the present work at this initial condition. From Eq. 5.2, the critical radius for a stoichiometric flame at an initial temperature of 300 K and an initial pressure of 0.1 MPa is calculated to

be 127 mm, much larger than is possible within the pre-pressure period in the present vessel. The corresponding value of Pe_{cl} is marked on in Fig. 5.4.

Gostintsev *et al.* (1987) have analysed the data of Lind and Whitson (1977) and reported that in the later stages the flame radius to proportional to $t^{3/2}$. The data of Lind and Whitson (1977) for methane-air mixture show different growth rate for horizontal and vertical radii. The straight lines shown in Fig. 5.4 give exponents of t equal to 1.24 for horizontal propagation and 1.32 for vertical propagation. In the present study flame propagation is much slower than is predicted by the $t^{3/2}$ rule and follows Eq. 1.10. Figure 5.4 clearly shows the evidence that the flame spread law in the present work can blend with that in the large explosions as the flame becomes progressively larger. In the present study, cell formation is only observed for methane-air mixtures at higher pressures. Clearly, at least two regimes of flame propagation can be observed. The first follows Eq. 1.10 (curvature is important in the very early stage), the second is affected by flame instabilities and is analysed in the next section, following the theoretical framework of Bradley (1998).

5.4 Theoretical Analysis of Unstable Spherical Flame Propagation

Instability criteria have been developed for the spherical symmetric flames and analyses have shown how amplitudes of the surface perturbations can increase with flame radii and time (Istratov and Librovich 1969, Zeldovich *et al.* 1985, Bechtold and Matalon 1987, Bradley and Harper 1994, Bradley 1998). Bechtold and Matalon (1987) and Bradley and Harper (1994) analyzed the perturbation of a spherical flame that incorporates the global flame stretch and related the amplitude, a, of the perturbation relative to the flame front radius, r, where the flame has propagated beyond an initial value r_o, significantly larger than the flame thickness, δ_l. Hence, a is expressed to

develop with relative to r as:

$$a = a_0 R^{\omega\left(1+\frac{\Omega}{Pe\ln R}\right)} \tag{5.3}$$

Here, a_0 is the initial dimensionless amplitude of the perturbation, R is r/r_0, ω is a growth rate parameter which depends on σ, while Ω depends upon both this and the Markstein number. Effectively, Eq. 5.1, but with no separation of curvature and aerodynamic strain contributions, is incorporated in the analysis.

The logarithmic growth rate, $\bar{A}$, of the amplitude of the perturbation with respect to the Peclet number can be derived as (Bradley 1998):

$$\bar{A}(n) = \frac{\mathrm{d}\ln(a/a_o)}{\mathrm{d}\ln Pe} = \omega\left(1 - \frac{\Omega}{Pe}\right) \tag{5.4}$$

A negative value of $\bar{A}(n)$ indicates a stable flame, a positive value an unstable flame. On the right side of the equation the first term, ω gives the contribution to the growth rate of the Darrieus-Landau (D-L) instability, while the second, $(-\omega\Omega/Pe)$, gives the contribution due to combined effect of stretch due to curvature and aerodynamic strain. Further details are given by Bradley (1998).

In a spherically expanding flame, the stabilizing effect of stretch decreases with increase in flame radius. Hence, an initially stable flame can become unstable as it grows bigger than a certain size. Shown in Fig. 5.5 are values of $\bar{A}(n)$ calculated by the author for $\sigma = 7.5$ and $Ma = 4$, when Pe increases from 200 to 600. The value of $\bar{A}(n)$ becomes just positive at $Pe \sim 411$, and $\bar{A}(n)$ is positive for $Pe > 411$. This defines the critical value of the Peclet number, Pe_C, and the critical spherical harmonic, n_C. For $Pe \geq Pe_\mathrm{C}$, the regime of instability is bounded by two values of n: the lower one is defined by n_l, the upper one by n_S and, the value of n where $\bar{A}(n)$ becomes maximum defines, n_m, as shown in Fig. 5.5.

Shown in Fig. 5.6 are the values of n normalized by n_c plotted against Pe/Pe_c for $Ma = 4$. The ratio, n_s/n_c increases linearly with Pe/Pe_c, while the ratio, n_l/n_c remains essentially constant. Theoretically, the peninsular of instability has a lower bound n_l/n_c and an upper bound n_s/n_c, while the middle curve gives values of n_m/n_c at which $\bar{A}(n)$ is a maximum. However, experimentally time lags between Pe_c and Pe_{cl} were observed for propane-air mixtures (Groff 1982), iso-octane-air mixtures (Bradley *et al.* 1998) and for methane-air mixtures in the course of the present studies. To incorporate this time lag, Bradley (1998) in the fractal analysis of flame instability introduced a new upper limit of instability as fn_s/n_c, where f is a numerical constant, less than unity and this limit is shown in Fig. 5.6 by a dotted line. The value of f is found by equating fn_s/n_c to the lower bound value $(n_l/n_c)_{cl}$ at $Pe = Pe_{cl}$. Bradley (1998) derived an expression for the flame speed, by means of a fractal analysis that used the limiting unstable wavelengths as inner and outer cut-offs. This led to a relationship between Peclet number and time given by:

$$\begin{aligned} Pe &= Pe_{cl} - \left(\frac{n_c}{n_l}\right)\frac{f}{\kappa}\left(\frac{n_s}{n_c}\right)_{cl} Pe_c + \left\{\frac{2}{3}\left(\frac{\sigma u_l^2}{\nu Pe_c^{1/3}}\right)\ \kappa^{1/3} t\right\}^{3/2} \\ &= Pe_o + \left\{\frac{2}{3}\left(\frac{\sigma u_l^2}{\nu Pe_c^{1/3}}\right)\ \kappa^{1/3} t\right\}^{3/2} \end{aligned} \tag{5.5}$$

where,

$$Pe_o = Pe_{cl} - \left(\frac{n_c}{n_l}\right)\frac{f}{\kappa}\left(\frac{n_s}{n_c}\right)_{cl} Pe_c \qquad \text{when } t = 0 \tag{5.6}$$

and,

$$\kappa = \left(\frac{n_c}{n_l}\right) f\left(\frac{\mathrm{d}(n_s/n_c)}{\mathrm{d}(Pe/Pe_c)}\right), \qquad \text{a constant.} \tag{5.7}$$

In dimensional form,

$$r = r_o + A\ t^{3/2} \tag{5.8}$$

where,

$$A = \left[\frac{0.544\sigma^{3/2}u_l^2\kappa^{1/2}}{\nu^{1/2}Pe_c^{1/2}}\right] \tag{5.9}$$

The time, t, appearing in Eq. 5.5 can also be normalized by a chemical time, given by δ_l/u_l. The normalized time, $\bar{t}$, is given by:

$$\bar{t} = \frac{t}{\delta_l/u_l} = \frac{tu_l^2}{\nu} \tag{5.10}$$

Hence, Eq. 5.5 can be written as:

$$\begin{aligned} Pe &= Pe_{\mathrm{O}} + \left[0.544\ \sigma^{3/2}\sqrt{\frac{\kappa}{Pe_{\mathrm{C}}}}\right]\ \bar{t}^{\,3/2} \\ &= Pe_{\mathrm{O}} + B\ \bar{t}^{\,3/2} \end{aligned} \tag{5.11}$$

where,

$$B = \left[0.544\ \sigma^{3/2}\sqrt{\frac{\kappa}{Pe_{\mathrm{C}}}}\right] \tag{5.12}$$

and, the constant B can be related to A, in Eqs. 5.8 and 5.9 by:

$$B = A\left[\frac{u_l^2}{\nu^{1/2}}\right] \tag{5.13}$$

Values of B calculated from Bradley's (1998) listing of A are given in Table 5.1.

The analysis of Bradley (1998) is only applicable to positive values of Ma. For negative values of Ma it is found experimentally in the present work that the flame exhibited the cracking instability from the moment of initiation, in agreement with the theory of Bechtold and Matalon (1987). Effectively, $Pe_{\mathrm{C}} = 0$ and Bradley's analysis is no longer applicable in detail, although the principles of the inner and outer cut-off in the fractal analysis still apply and it is assumed that the form of Eq. 5.11 is still applicable.

5.5 Experimental Determination of the Constant, B

Equation Eq. 5.11 is expressed as:

$$Pe = Pe_{\mathrm{O}} + B_{\mathrm{e}}\ \bar{t}^{3/2} \tag{5.14}$$

When $Pe_c = 0$, B_e is the experimentally determined at $\bar{t} = 0$ when $Pe = Pe_o$. Here, Pe_o is the experimental value of Pe when the flame becomes cellular and is taken as the value of Pe_{cl} measured in the present experiments and $\bar{t}$ is given by:

$$\bar{t} = \frac{(t - t_o)u_l^2}{\nu} \tag{5.15}$$

Hence, t is the time measured from spark ignition and t_o is the time associated with radius, r_o, which corresponds to Pe_o.

Experimental values of $(r - r_o)$ are plotted against $(t - t_o)$ in Figs. 5.7 to 5.10 for various initial conditions. From these plots it is possible to derive values of the dimensionless parameter B_e and these are plotted against $\bar{t}$ in Figs. 5.11 and 5.12, for lean and stoichiometric methane-air mixtures, respectively. It appears that the values tend to an asymptotic value for the mixture as the flame propagates.

In general, as the cellular structure first develops with some rapidity at low values of $\bar{t}$ there is a significant enhancement in values of B_e above the anticipated theoretical values of B. The value of B_e rapidly reaches a peak during the critical cell formation period and declines thereafter towards what would apparently be an asymptotic value, $B_{e\infty}$. The most probable physical explanation is that the value of f in Eq. 5.7 is initially high and then declines to a steady state value. This suggests that just after the onset of cellularity the range of effective unstable wavelengths is greater than it would have been in a steady state for those conditions. When the cells form initially they do so rapidly (making up for 'lost time'). Thereafter the rate of formation declines towards a steady state value.

The initial high value might also be associated with the zero time problem. As zero time is set at the onset of cellularity, which is related to a power law of time, the effect of zero time is very significant. The resultant term $B_e\bar{t}^{3/2}$ is not abnormally high, rather it is quite gradual and the high value of B_e is a 'mathematical artifact' of the conditions.

Shown in Fig. 5.13 are the values of $B_{e\infty}$ obtained for various initial conditions, plotted against Ma_{sr}, taken from Table 5.2. A value of $B_{e\infty}$ is obtained from a plot of B_e against $\bar{t}$ by linear extrapolation as the value of B_e corresponding to $1/\bar{t} \to 0$. Also shown in Fig. 5.13, are the values of $B_{e\infty}$ for some mixtures calculated from Bradley (1998), and reported in Table 5.1. The value of $B_{e\infty}$ decreases with increase in Ma_{sr}, although there is scatter that suggests that probably other parameters are required for a correlation, in addition to Ma_{sr}.

Table 5.1. Calculated values of A and B. Values of A, namely A_{G}, of Gostintsev *et al.* (1987) is also given.

Mixture	σ	u_l (m/s)	$\nu.10^5$ (m^2/s)	Ma	A	A_{G}	B
10% CH_4-air	7.456	0.385	1.574	4.02	8.04	5.7	0.245
4% C_3H_8-air	7.915	0.38	1.726	5.0	8.13	7.1	0.24
36.4% H_2-air	6.673	2.75	2.36	12	275	166	0.178

Table 5.2. Experimental results for flame instability in methane-air mixtures.

Expt. ID	P_{u} (MPa)	T_{u} (K)	ϕ	σ	$\nu.10^6$ (m^2/s)	u_l (m/s)	Ma_{sr}	Pe_{cl}	$B_{e\infty}$
E31	0.5	302	0.8	6.711	3.181	0.116	-2.17	1078	0.52
R12	0.5	306	0.8	6.711	3.181	0.122	-2.51	1115	0.427
E03	0.5	358	0.8	5.729	4.322	0.153	-0.42	1662	0.479
E04	0.5	360	0.8	5.729	4.322	0.161	-0.12	1081	0.41
R13	0.5	401	0.8	5.199	5.225	0.219	-1.95	937	0.334
R11	0.5	301	1.0	7.585	3.187	0.190	-1.93	1096	0.451
R01	0.5	301	1.0	7.585	3.187	0.201	-0.85	1734	0.432
R02	0.5	350	1.0	6.439	4.331	0.263	-1.49	1427	0.355
R03	0.5	359	1.0	6.439	4.331	0.274	-2.08	1927	0.371
R15	0.5	404	1.0	5.820	5.237	0.320	-4.14	1455	0.45
E39	0.5	397	1.0	5.820	5.237	0.313	-0.68	1929	0.351
E13	1.0	310	0.8	6.728	1.588	0.088	-2.98	1104	0.538
E14	1.0	311	0.8	6.728	1.588	0.083	-4.09	872	0.53
E05	1.0	358	0.8	5.734	2.161	0.120	-4.63	1599	0.451
E06	1.0	359	0.8	5.734	2.161	0.122	-3.02	1615	0.41
E21	1.0	404	0.8	5.201	2.615	0.157	0.47	1813	0.316
E22	1.0	404	0.8	5.201	2.615	0.150	-2.01	1681	0.339
R09	1.0	297	1.0	7.629	1.59	0.144	-3.32	1507	0.409
R10	1.0	302	1.0	7.629	1.59	0.150	-2.00	1797	0.414
R05	1.0	356	1.0	6.467	2.165	0.205	-3.15	2263	0.307
R06	1.0	359	1.0	6.467	2.165	0.206	-3.53	2292	0.318
E17	1.0	401	1.0	5.843	2.62	0.238	0.53	2517	0.293
E18	1.0	402	1.0	5.843	2.62	0.234	-2.01	1988	0.305

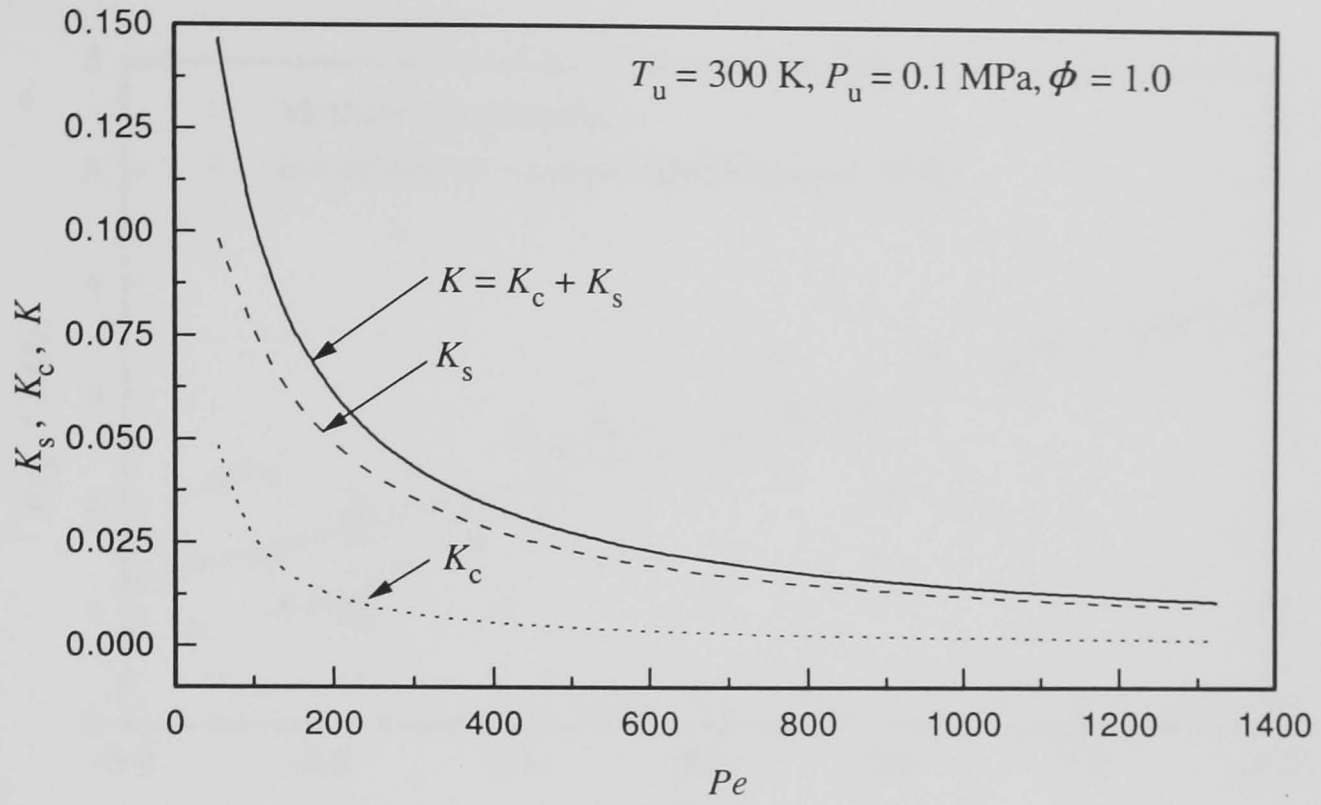

Fig. 5.1. Variations of dimensionless stretch factors, K, K_S and K_C, as a function of Peclet number, Pe, for stoichiometric methane-air mixture at an initial temperature of 300 K and initial pressure of 0.1 MPa.

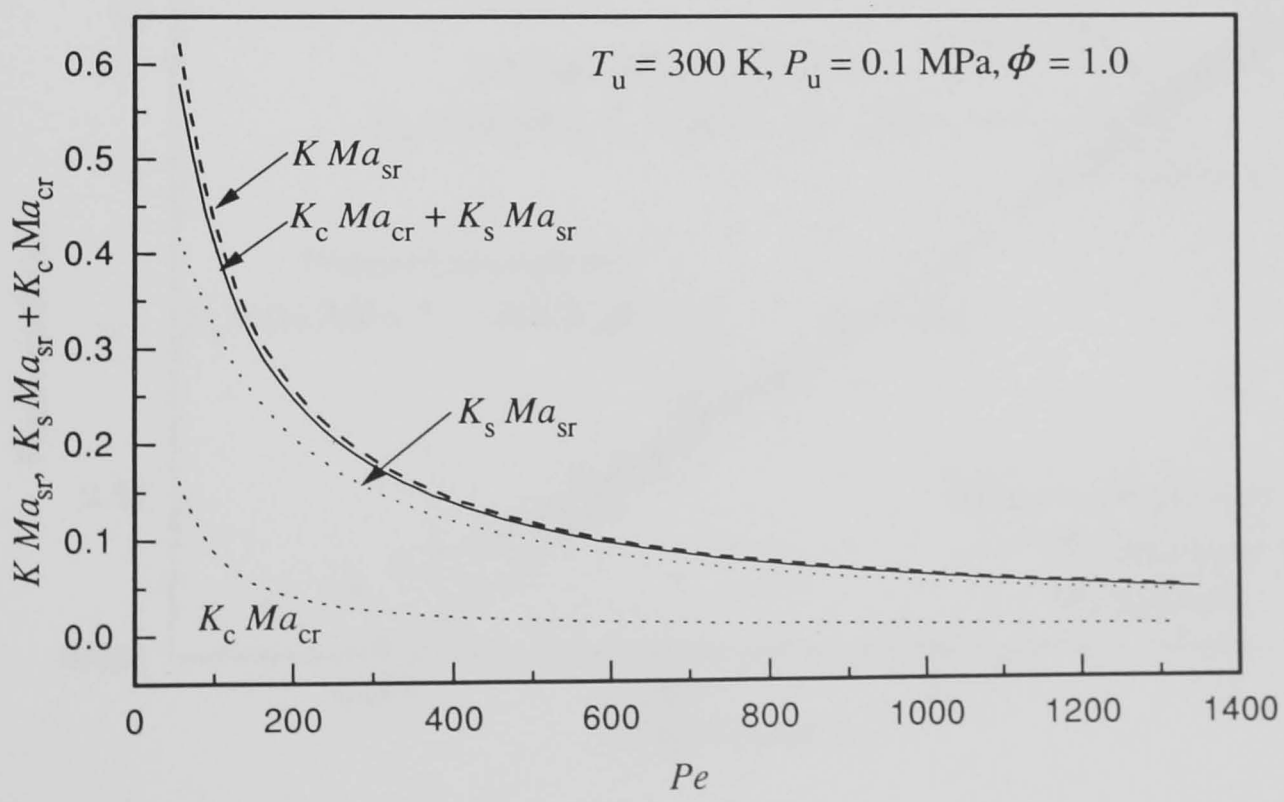

Fig. 5.2. Variations of KMa's as a function of Peclet number, Pe, for stoichiometric methane-air mixtures at an initial temperature of 300 K and initial pressure of 0.1 MPa.

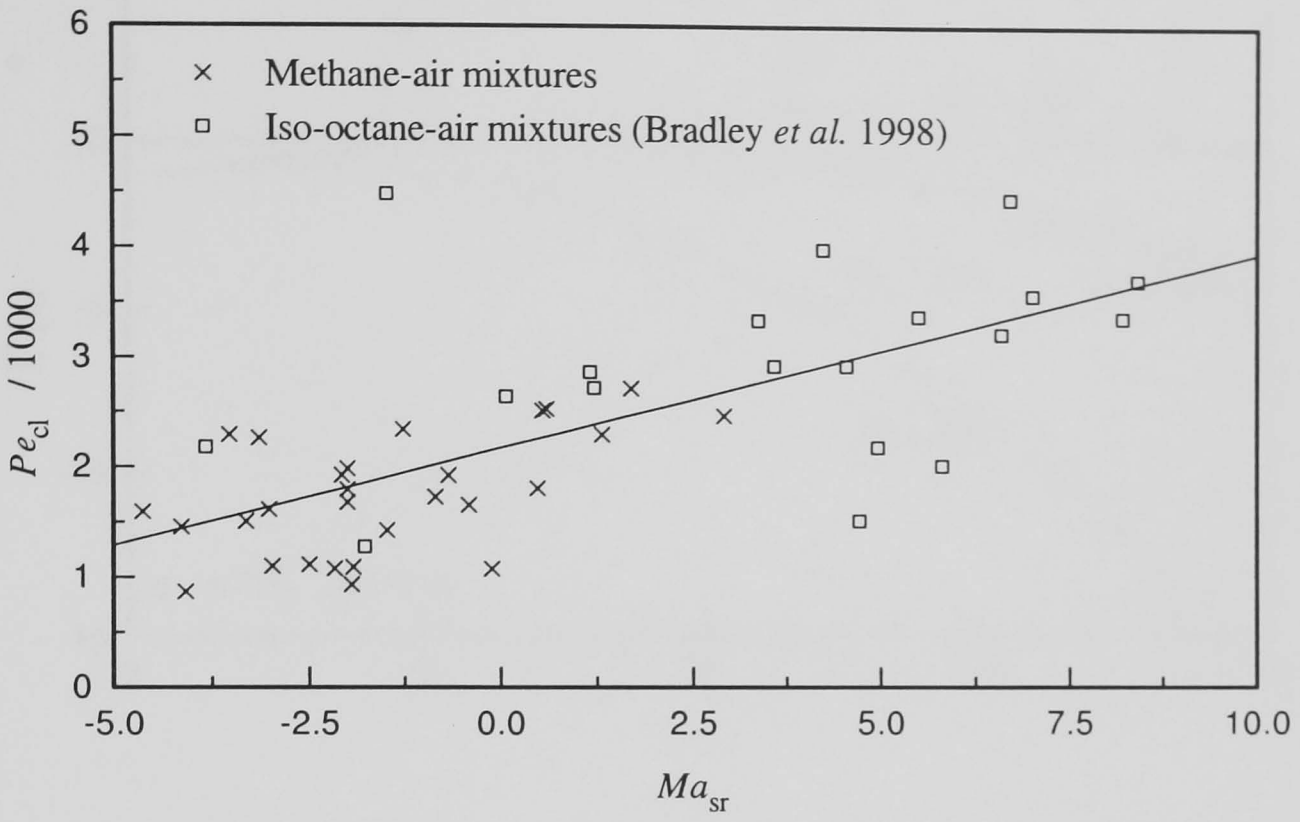

Fig. 5.3. Variation of Pe_{cl} with Ma_{sr} for onset of cellularity.

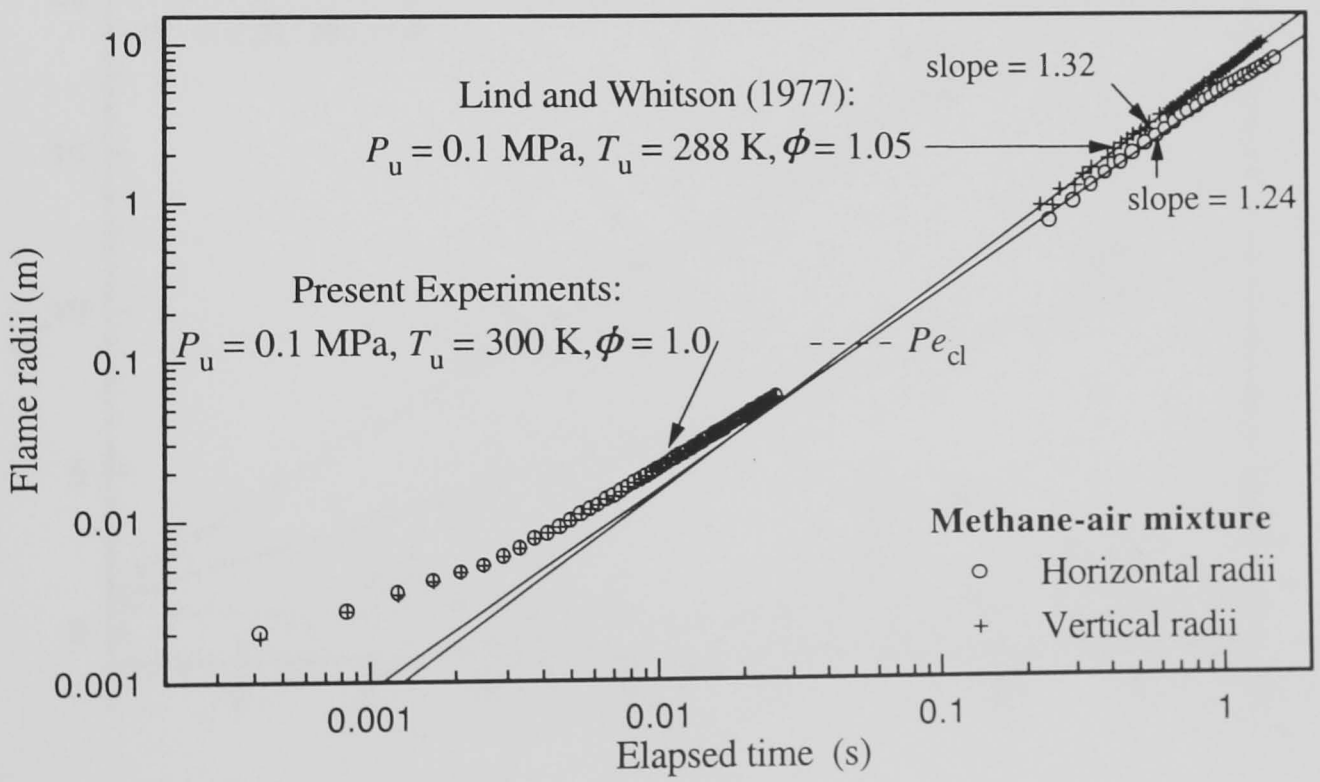

Fig. 5.4. Methane-air atmospheric flame propagation. Present work and that of Lind and Watson (1977).

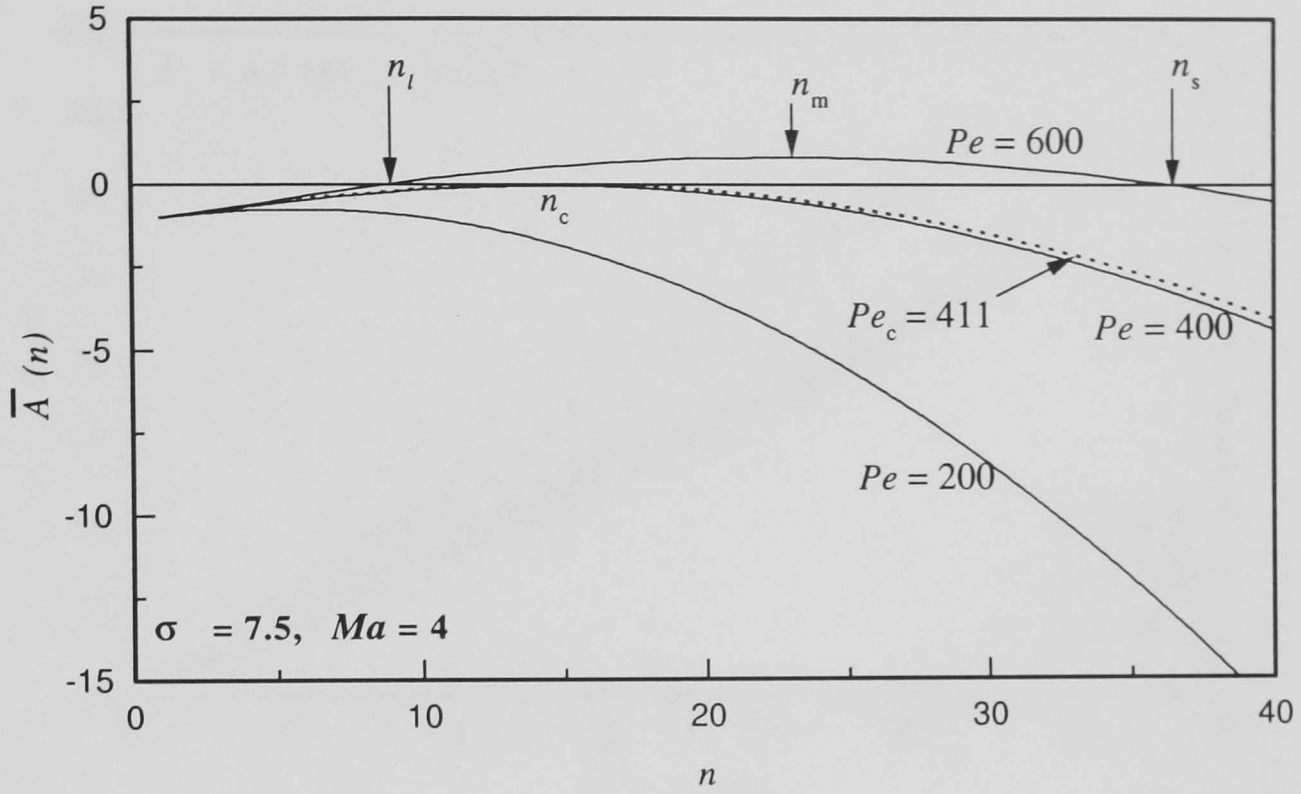

Fig. 5.5. Logarithmic growth rate, $\bar{A}(n)$, of amplitude of perturbation as a function of Pe, for $\sigma = 7.5,\ Ma = 4$.

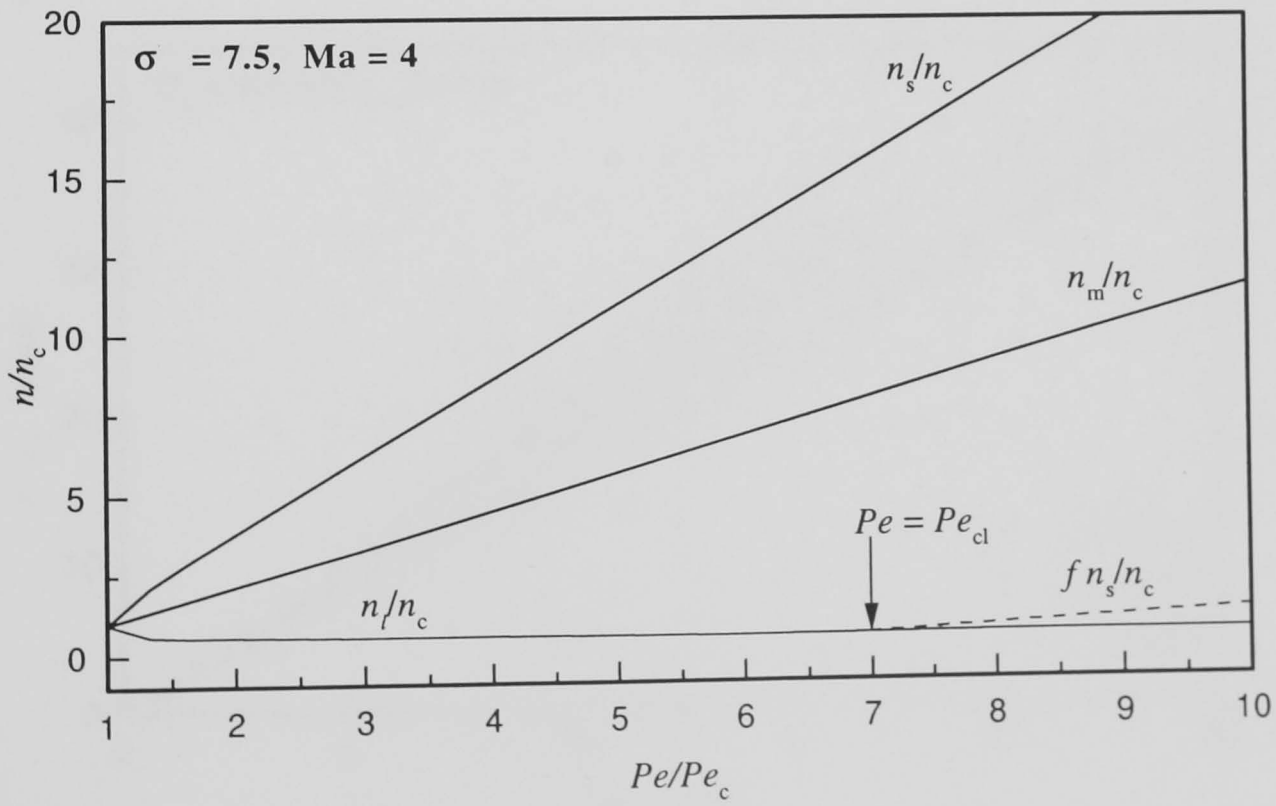

Fig. 5.6. Nomalized upper and lower bounds of instability as a function of Pe/Pe_c; (n_m/n_c) is the normalized wavenumber where $\bar{A}(n)$ is maximum, for $\sigma = 7.5,\ Ma = 4$. Dotted line is the modified upper boundary, fn_s/n_c, proposed by Bradley (1998).

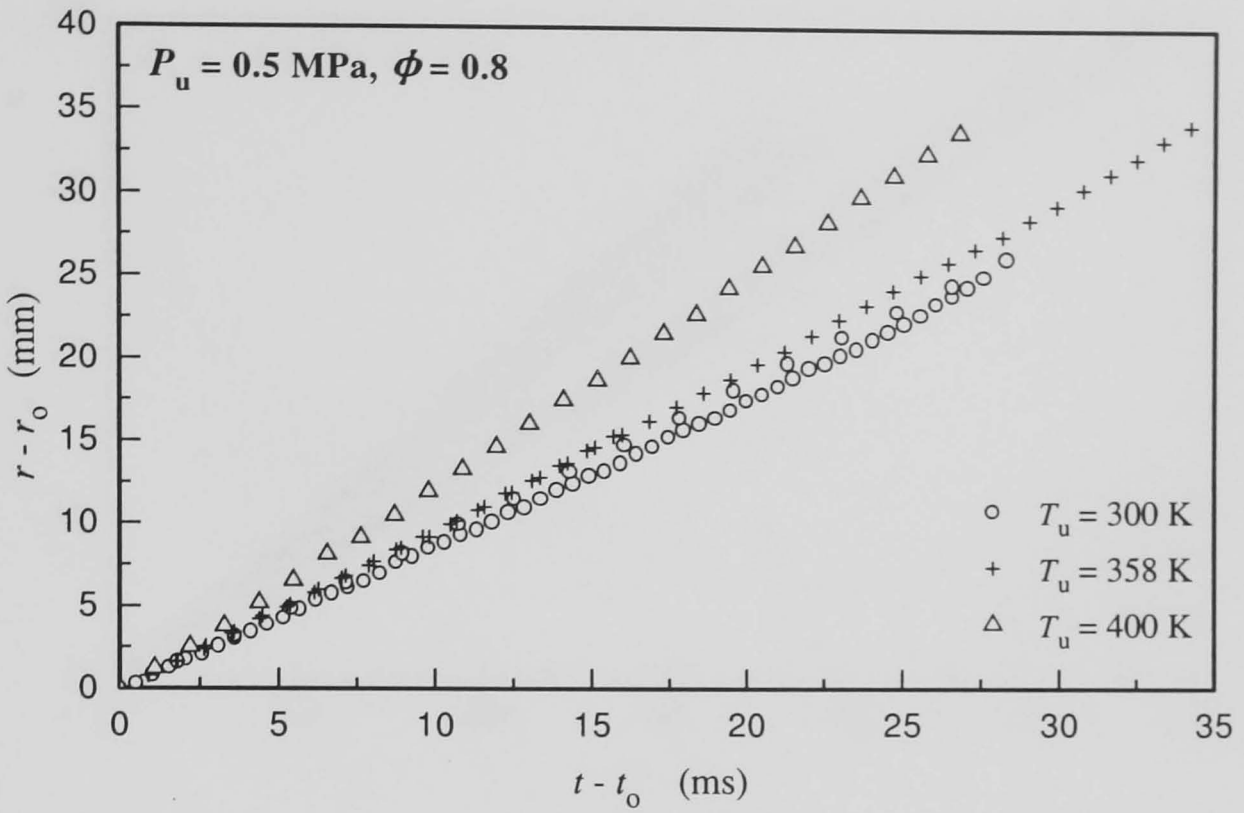

Fig. 5.7. Variation of $(r - r_o)$ with $(t - t_o)$ for lean methane-air mixtures at an initial pressure of 0.5 MPa.

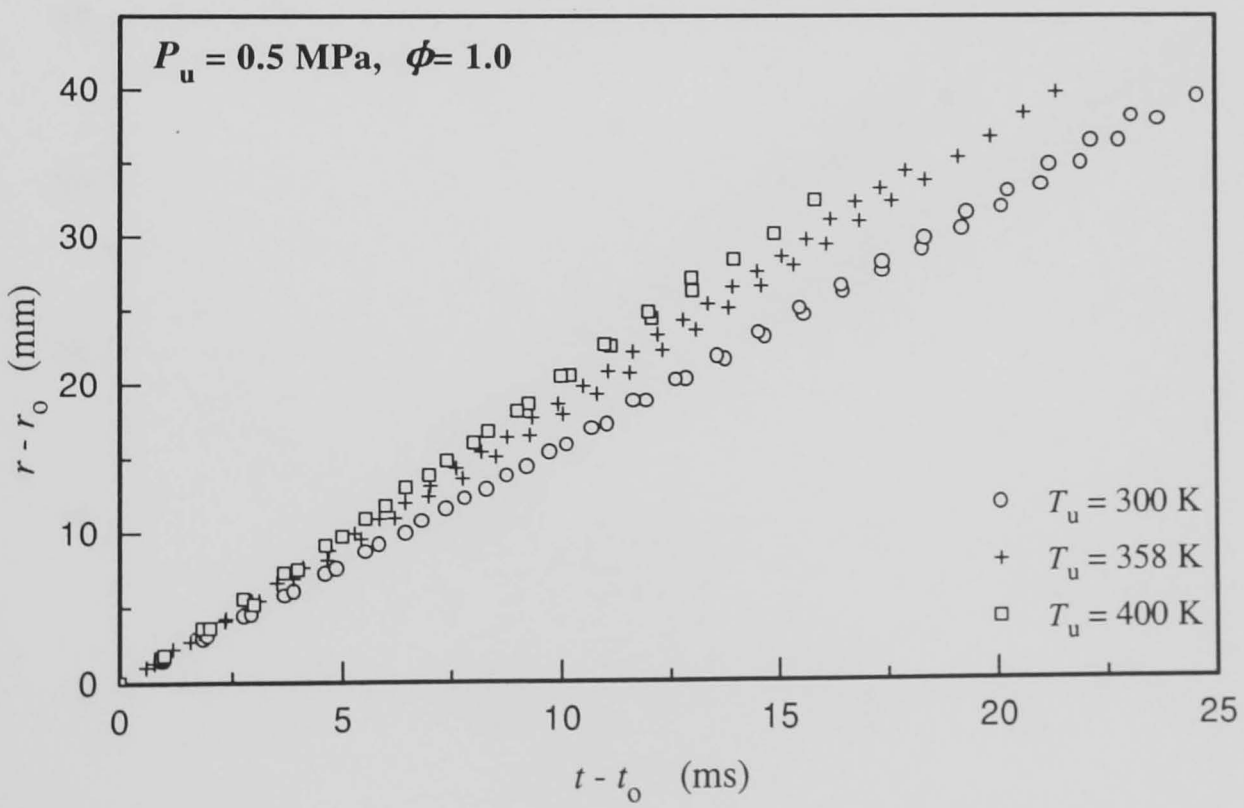

Fig. 5.8. Variation of $(r - r_o$ with $(t - t_o)$ for stoichiometric methane-air mixtures at an initial pressure of 0.5 MPa.

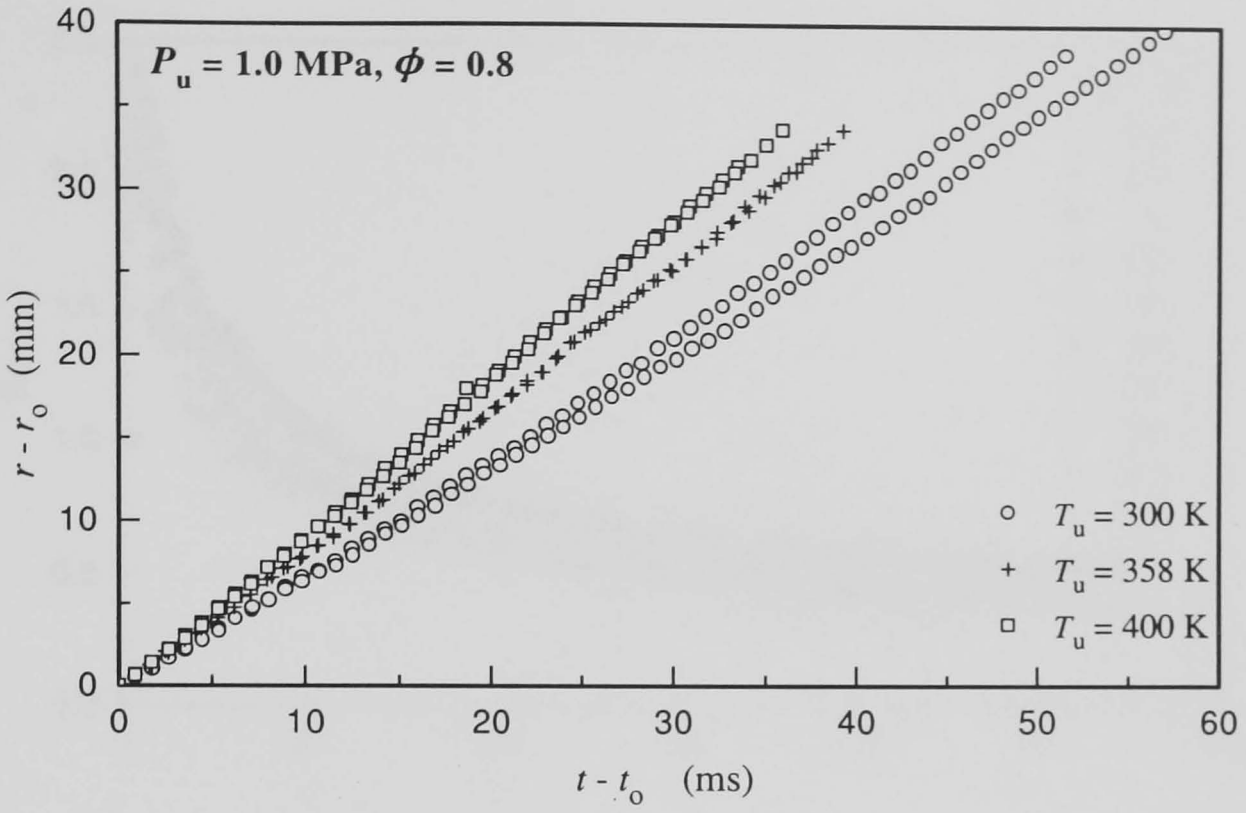

Fig. 5.9. Variation of $(r - r_o)$ with $(t - t_o)$ for lean methane-air mixtures at an initial pressure of 1.0 MPa.

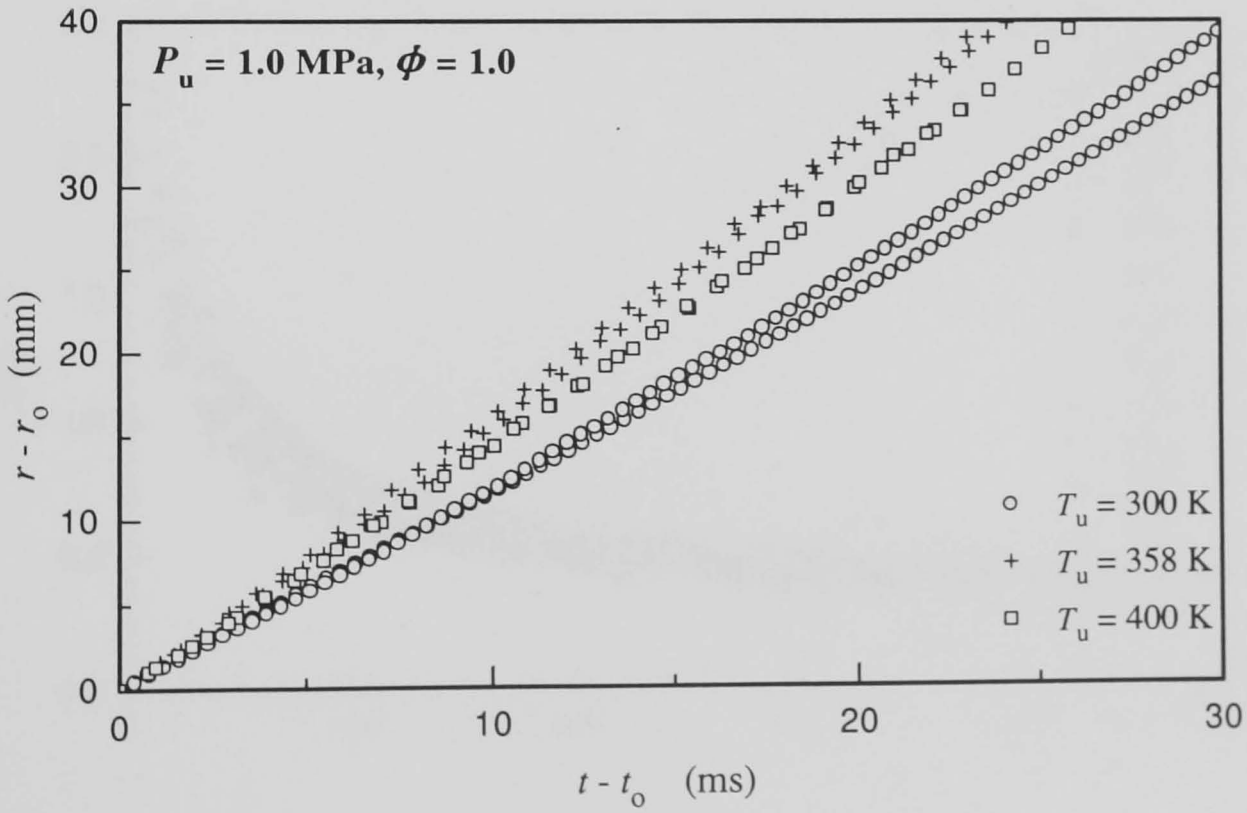

Fig. 5.10. Variation of $(r - r_o)$ with $(t - t_o)$ for stoichiometric methane-air mixtures at an initial pressure of 1.0 MPa.

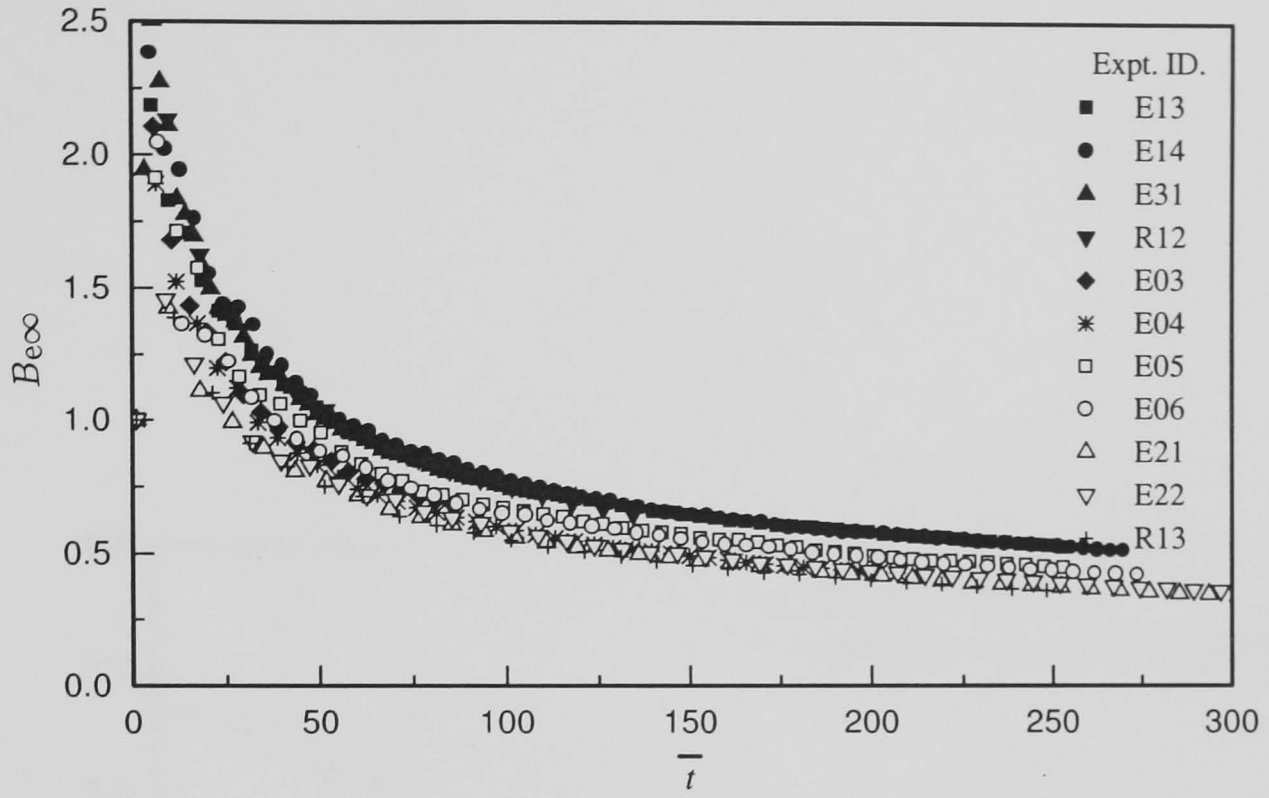

Fig. 5.11. Variation of $B_{e\infty}$ with $\bar{t}$ for lean methane-air mixtures at various initial pressures and temperatures. (See Table 5.2 for experimental ID.)

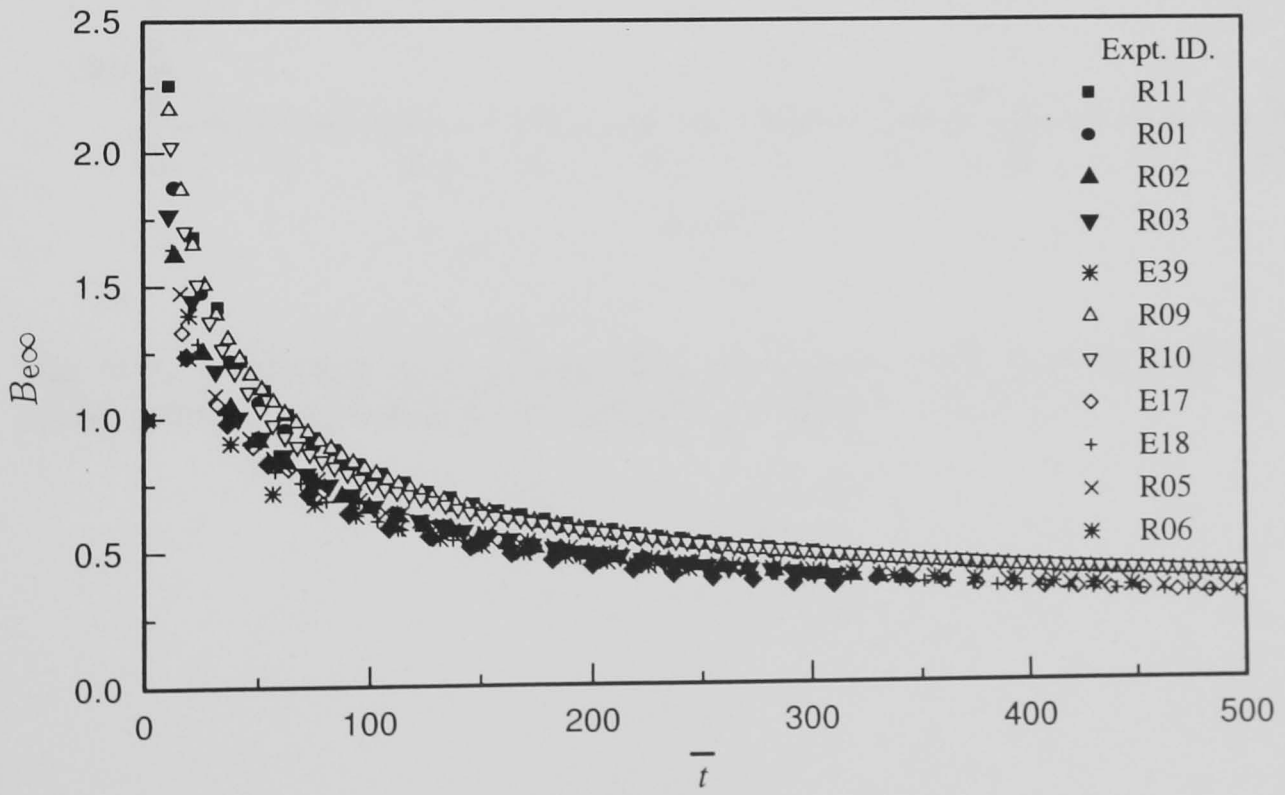

Fig. 5.12. Variation of $B_{e\infty}$ with $\bar{t}$ stoichiometric lean methane-air mixtures at various initial pressures and temperatures. (See Table 5.2 for experimental ID.)

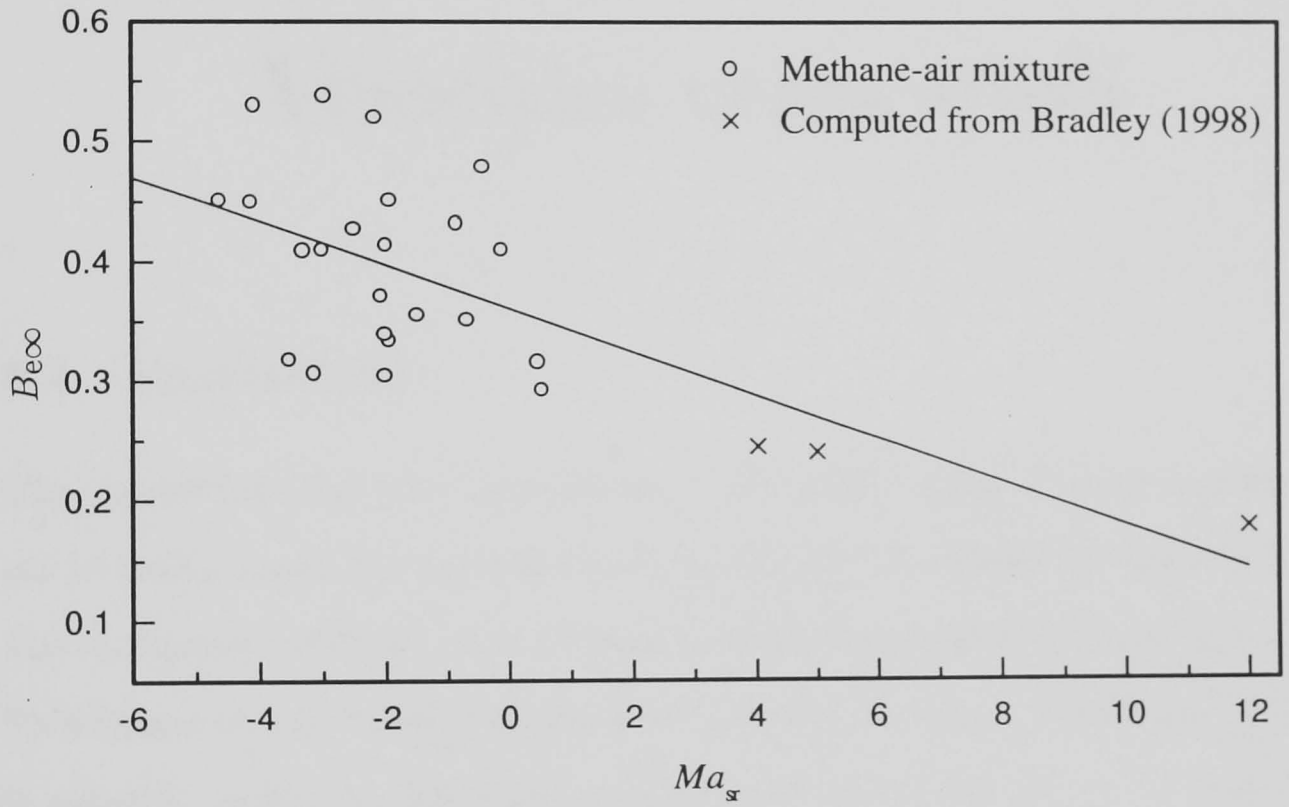

Fig. 5.13. Variation of $B_{e\infty}$ with Ma_{sr} for various initial conditions of equivalence ratios, pressure and temperature. (Data from Table 5.1 and 5.2.)

Chapter 6

Analysis of Turbulent Burning Velocities using PMS

6.1 Introduction

This chapter describes how planar Mie scattered (PMS) images of turbulent flame front can be used to obtain the distribution of burned gas and turbulent burning velocities. It also discusses the different ways in which turbulent burning velocity might be defined. PMS images obtained during explosions in a fan-stirred vessel, in which the turbulence is isotropic, enable the distribution of unburned and burned gas to be measured, at all stages of the explosion, at different mean radii. A sufficient number of explosions enables valid average values to be obtained of these quantities, as a function of radius and time, for a spherically expanding flame in the turbulent premixture.

In the present work, two dimensional laser sheet images across a complete diametral plane are acquired by Mie scattering from tobacco smoke particles. Shown in Fig. 6.1 are such images obtained from an explosion of stoichiometric methane-air mixture at an initial pressure of 0.1 MPa, initial temperature 300 K, with an isotropic r.m.s. turbulent velocity, u', of 0.595 m/s. The flame wrinkling caused by different scales of turbulence are clearly evident. Flame front coordinates are obtained by hand-tracing from images which have a spatial resolution of 0.32 mm/pixel. This is discussed in detail in § 2.4.2.

Shown in Fig. 6.2 is the sequence of flame front profiles for the explosion. These coordinates are analysed in detail to measure turbulent burning velocities, reported in this chapter and to measure the distribution of flame front curvatures reported in Chapter 7.

6.2 Definition of Turbulent Burning Velocity

For spherical turbulent flame propagation, a mass rate of burning can be expressed in the form:

$$\frac{\mathrm{d}m}{\mathrm{d}t} = -4\pi R_i^2 \rho_\mathrm{u} u_\mathrm{t} \tag{6.1}$$

where R_i is a mean general radius associated with the burning velocity, u_t, ρ_u is the unburned gas density and m is the mass of gas changing from unburned to burned. However, problems arise in defining *burned* and *unburned* and, because of the finite thickness of the flame brush, also in selecting the most appropriate value of R_i. In the present study, a thin planar sheet cutting the mean spherical flame kernel is considered. This is shown in Fig. 6.3 and the general radius, R_i, lies between a root radius, R_r and a tip radius, R_t. The inner, root, circumference of radius R_r embraces the burned gas entirely, whilst the outer, tip, circumference of radius R_t has nothing but unburned gas outside it. Two dimensional planar sheet photographs of Mie scattering of laser light are used to examine the different reference radius, R_i, and m in Eq. 6.1 and, finally, the definitions of burning velocity.

The definition of turbulent burning velocity depends upon the definition of a somewhat arbitrary flame front. The value of the radius R_i can be defined in a number of ways, some of which are given below:

1. For a mean cross section through the kernel, the area of unburned gas inside a circumference of radius R_a, is equal to that of burned gas outside that circumference. The present treatment is of planar sheets. This definition has been applied to schlieren 2D photographs of 3D turbulent flames (Abdel-Gayed *et al.* 1986, Checkel and Ting 1992).

2. The volume of unburned gas inside a circumference of radius R_{v}, is equal to that of burned gas outside that circumference. Hamamoto *et al.* (1996) in studies involving schlieren photography and simultaneously measured ion probe currents equated these two volumes of gas in the burning zone.

3. The mass of unburned gas inside a circumference of radius R_{m}, is equal to that of burned gas outside that circumference.

In the schlieren-based measurements of turbulent burning velocities, the mean radius of the two dimensional projected area of the three dimensional flame must lie somewhat between the value of R_{a} from the planar sheet and R_{t}. Because of the blurring effect of the overlapping series of two dimensional images the value is probably closer to R_{t} than R_{a}. In the present study, a number of possible ways of defining the actual flame front radius are explored by introducing a factor, ξ, to represent a radius, R_{ξ}, defined as:

$$R_{\xi} = R_{\mathrm{a}} + \xi(R_{\mathrm{t}} - R_{\mathrm{a}}) \tag{6.2}$$

Hence,

$$R_{\xi} = \begin{cases} R_{\mathrm{a}} & \text{if } \xi = 0 \\ \\ R_{\mathrm{t}} & \text{if } \xi = 1 \end{cases}$$

Three intermediate values of $\xi (= 0.25,\ 0.50\ \&\ 0.75)$ are also considered, in addition to the radii defined earlier.

It is necessary to define the masses of unburned and burned gas associated with the different zones. Let m_{ui} be the mass of unburned gas within the general perimeter of radius R_i, m_{uo} the mass of unburned gas outside perimeter radius R_i but within that of R_{t}, m_{bi} the mass of burned gas inside the perimeter of R_i, m_{bo} the mass of burned gas outside the perimeter of R_i but within R_{t}, and m_{u} is the mass remaining outside R_{t}. The definitions of these masses are also shown in Fig. 6.3.

Mass conservation implies that:

$$\frac{\mathrm{d}m_{\mathrm{ui}}}{\mathrm{d}t} + \frac{\mathrm{d}m_{\mathrm{uo}}}{\mathrm{d}t} + \frac{\mathrm{d}m_{\mathrm{bi}}}{\mathrm{d}t} + \frac{\mathrm{d}m_{\mathrm{bo}}}{\mathrm{d}t} + \frac{\mathrm{d}m_{\mathrm{u}}}{\mathrm{d}t} = 0 \tag{6.3}$$

Three possible definitions of turbulent burning velocities are now considered:

1. A burning velocity that measures the mass rate of production of burned gas:

$$\frac{\mathrm{d}\left[m_{\mathrm{bi}} + m_{\mathrm{bo}}\right]}{\mathrm{d}t} = 4\pi R_i^2 \rho_u u_{\mathrm{tr}} \tag{6.4}$$

   where u_{tr} is the turbulent burning velocity associated with the production of burned gas. Here R_i can be defined as any one of the radii previously discussed.

2. A burning velocity that measures the mass rate of consumption of unburned gas:

$$\frac{\mathrm{d}\left[m_{\mathrm{ui}} + m_{\mathrm{uo}} + m_{\mathrm{u}}\right]}{\mathrm{d}t} = -4\pi R_i^2 \rho_u u_{\mathrm{t}'} \tag{6.5}$$

   where, R_i is again the radius defining the arbitrary flame front and $u_{\mathrm{t}'}$ is the turbulent burning velocity associated with the consumption of unburned gas. Because the interpretation of the planar sheets allows of only two categories of gas, unburned and burned, it follows from Eq. 6.3 that, provided R_i is the same in Eqs. 6.4 and 6.5, $u_{\mathrm{tr}} = u_{\mathrm{t}'}$.

3. A burning velocity that measures the mass rate of consumption of unburned gas, but assumes that only gas outside the sphere of radius R_i is considered to be unburned:

$$\frac{\mathrm{d}\left[m_{\mathrm{uo}} + m_{\mathrm{u}} + m_{\mathrm{bo}}\frac{\rho_{\mathrm{u}}}{\rho_{\mathrm{b}}}\right]}{\mathrm{d}t} = -4\pi R_i^2 \rho_u u_{\mathrm{t}} \tag{6.6}$$

   This is an *apparent* mass rate of consumption of unburned gas. It is apparent because 'unburned' is here defined also to include the mass m_{bo} between R_i and R_{t}. As it is assumed to be unburned its contribution to the mass rate of consumption is for a mass of $m_{\mathrm{bo}}\rho_{\mathrm{u}}/\rho_{\mathrm{b}}$. With R_i equal to an appropriate value

between R_a and R_t, u_t corresponds to many of the measurements of the Leeds group.

6.3 Analysis of the Sheet Images

In the present study of methane-air turbulent flame propagation, the analysis of PMS images and associated coordinates is based on the following assumptions:

1. A mean radius can be defined of an essentially spherical flame. This implies identifying the centroid of the sphere.

2. The structure of the field is isotropic at any given radius.

3. The reaction zone of the laminar flamelets is negligibly thin. Thus, the 2D image consists purely of unburned and burned gaseous regions.

4. The unburned and burned gas densities (ρ_u and ρ_b) are fixed at the initial cold and adiabatic values, respectively.

5. The sheet revealed by the laser scattering is of infinitesimal thickness and measured quantities are a function of flame radius only.

The proportions of unburned and burned gas densities are measured as a function of radius at different instants during several explosions. In Fig. 6.4 '0' is the centroid of the flame kernel volume. Consider a plane perpendicular to the vertical line through the centroid and the ring, radius r from '0', thickness δr, as shown in Fig. 6.4. The radius in the horizontal plane is $r \sin\alpha$, where α is the angle with the vertical axis. The ring has a volume

$$= 2\pi r \sin\alpha \; r\delta\alpha \; \delta r \tag{6.7}$$

Let $\sigma(r)$ be the average volume fraction at radius r occupied by unburned gas. It follows that the volume of unburned gas within it must be

$$= \sigma(r) \; 2\pi r \sin\alpha \; r\delta\alpha \; \delta r \tag{6.8}$$

The total volume of unburned gas within the spherical shell of radius r, thickness δr is

$$\int_0^{\pi} \sigma(r)\ 2\pi r^2 \sin\alpha\ \delta r\ \mathrm{d}\alpha = \sigma(r)\ 4\pi r^2\ \delta r \tag{6.9}$$

Hence, the mass of unburned gas within any general radius R_i, m_{ui}, is

$$m_{\mathrm{ui}}(R_i) = 4\pi\rho_{\mathrm{u}} \int_0^{R_i} \sigma(r)\ r^2 \mathrm{d}r \tag{6.10}$$

Similarly, the mass of burned gas within any general radius R_i, m_{bi}, is

$$m_{\mathrm{bi}}(R_i) = 4\pi\rho_{\mathrm{b}} \int_0^{R_i} (1-\sigma(r))\ r^2 \mathrm{d}r \tag{6.11}$$

The integrations of Eqs. 6.10 and 6.11 enable all the mass terms that appear in Eq. 6.3 to be evaluated.

6.4 Implementation

Figure 6.4 and Eqs. 6.10 and 6.11 show how the masses of burned and unburned can be found for any plane through the flame kernel. To obtain the fullest information at all radii the plane should pass through the centroid of the kernel and extend to R_{t}. This is achieved by analyzing two dimensional laser sheet images obtained across a complete diametral vertical plain just ahead of the spark plug, as described in Chapter 2. Implementation of the approach outlined in the previous sections is undertaken in four stages with three FORTRAN programs:

1. `sigma.for`
2. `radii.for`
3. `burnvel.for`

These programs require a data file '`filename.inf`' in addition to the series of files containing the flame coordinates. Hence '`filename`' is the common name of the sequence of images and this file contains the following data:

- the number of files in the sequence,
- the initial time delay between the spark and the first image in the sequence,
- the inter-image time spacing,
- the scaling factor for both 'x' and 'y' coordinates,
- the unburned and burned gas densities of the mixture, and
- a sequence list of file names containing the flame edge coordinates.

6.4.1 Estimation of σ as a function of r

Flame edge coordinates are first analysed by `sigma.for` to generate $\sigma(r)$ as a function of r. To accomplish this, `sigma.for` at first reads the flame coordinates for a flame image, scales it using the scale factor, calculates the centroid of the image's burned gas region and translates the coordinates with respect to the centroid. These coordinates are then transformed into polar coordinates and values of R_r and R_t determined as:

$$R_\mathrm{r} = \min\{r_i,\ i = 1, 2, \cdots, N\} \tag{6.12}$$

$$R_\mathrm{t} = \max\{r_i,\ i = 1, 2, \cdots, N\} \tag{6.13}$$

where, N is the number of coordinates for the flame image. Then for each radius, r, starting from R_r with an increment of 1 mm, a function $c(\theta)|_r$ is generated which is zero for an unburned and unity for a burned zone. Hence, the value of $\sigma(r)$ is obtained as:

$$\sigma(r) = 1 - \frac{1}{2\pi r}\int_0^{2\pi} c(\theta)|_r \ \mathrm{d}\theta \tag{6.14}$$

Once σ is determined for $R_\mathrm{r} \leq r \leq R_\mathrm{t}$, $\sigma(r)$ is fitted for r as

$$\sigma(r) = a_0 + a_1 r + a_2 r^2 + a_3 r^3 \tag{6.15}$$

The coefficients 'a' are written to a file `filename.out`, along with R_r and R_t for each sequence of the flame images.

The estimation of $\sigma(r)$ as a function of r is demonstrated in Fig. 6.5, where a hypothetical square flame of 50 mm length is considered. After estimating the values of R_r and R_t, the program generates a profile of $c(\theta)|_r$ for a number of radii, R, where $R_\mathrm{r} \leq r \leq R_\mathrm{t}$. It is accomplished by moving along the circumference of a circle of a given radius, r, and assigning a value of unity in a burned zone, and, otherwise a value of zero, as shown in Fig. 6.5. The value of $\sigma(r)$ is obtained from Eq. 6.14. Values of $\sigma(r)$ thus obtained are fitted to a third order polynomial and are shown in Fig. 6.5.

6.4.2 Estimation of Different Flame Radii

For each flame image, `radii.for` derived values of R_a, R_m and R_v using $\sigma(r)$. Their values are estimated as follows:

- R_a is estimated from the flame coordinates as:

$$R_\mathrm{a} = \sqrt{\frac{A}{\pi}} \tag{6.16}$$

  Hence, A, is the area of the burned gas in the flame images and is estimated by numerical integration using the 'Trapezoidal Rule' (Press *et al.* 1992).

- R_m is estimated by equating m_ui in Eq. 6.10 and m_bo in Eq. 6.11, and its value is computed using the 'Bisection Method' (Press *et al.* 1992).

- R_v is estimated by equating $m_\mathrm{ui}(R_i)/\rho_\mathrm{u}$ from Eq. 6.10 and $4\pi \int_{R_i}^{R_\mathrm{t}} (1-\sigma(r))r^2 \mathrm{d}r$ from Eq. 6.11, and computing its value using the 'Bisection Method' (Press *et al.* 1992).

- R_ξ is estimated for $\xi = 0.25$, 0.50 & 0.75 in Eq. 6.2.

Estimated flame radii are written to a file `filename.rad`.

Shown in Fig. 6.6 are the changes, for a single explosion, in $\sigma(r)$, with radius, r, at two different elapsed times for explosion of a stoichiometric methane-air premixture at an initial temperature of 300 K at 0.1 MPa pressure. Clearly, as the flame kernel grows following ignition, the flame brush thickness, defined as $(R_t - R_r)$, increases as the flame experiences more of the turbulence spectrum. It is also noted that at the greater time the flame brush thickness exceeds the integral length scale L (= 20 mm).

Figure 6.6 shows values for different reference radii at elapsed times of 7.51 and 15.51 ms, calculated using `radii.for`. Clearly, R_r and R_t correspond to $\sigma(r) = 0$ and 1.0, respectively. R_a is found to correspond to $\sigma(r) \approx 0.5$, while R_m corresponds to $\sigma(r) < 0.5$. R_v corresponds to $\sigma(r) > 0.5$, as a result of the density difference between burned and unburned gases, and because for two consecutive spherical shells, with the same thickness, the shell with the larger radius occupies more volume. Shown in Fig. 6.7 are the variations of six reference radii with time, estimated from the sequence of flame images. The increase in flame brush thickness is clearly observed. All six reference radii increase with elapsed time, although the values of R_r have the largest scatter. These values of reference radii are later used to estimate turbulent burning velocities and flame speeds.

6.4.3 Estimation of u_{tr}

It has already been demonstrated in § 6.2 that with the binary recording of burned or unburned gas $u_{tr} = u_{t'}$. This is confirmed numerically in Fig. 6.8 where it can be seen that $\frac{d[m_{bi}+m_{bo}]}{dt} = -\frac{d[m_{ui}+m_{uo}+m_u]}{dt}$. Hence, only the values of u_{tr} are estimated for different radii. The values of the masses are estimated by the program `burnvel.for`.

Shown in Fig. 6.9 by the symbols are the values of u_{tr} and $u_{t'}$ plotted against elapsed time from ignition for different reference radii, with the value of u_l shown by the broken line. Because $\frac{d[m_{bi}+m_{bo}]}{dt}$ does not depend on the definition of radii, from Eq. 6.4 it can be seen that $R_i^2 u_{tr}$ is constant. Therefore, the highest value of u_{tr} is associated with the smallest radius, R_r and the smallest value of u_{tr} is associated with

R_t. Interestingly, for R_t and $R_{\xi=0.5}$, the turbulent burning velocity is lower than the laminar burning velocity, while conversely, R_r yields a much higher value. This graphically shows the importance of the way in which the reference radius is defined.

6.4.4 Estimation of u_t

For each flame image, `burnvel.for` also computes the values of m_u, m_{bo} and m_{uo} for different values of R_ξ. Shown in Figs. 6.10 to 6.12 are the values of these masses as a function of time for different values of ξ, while Fig. 6.13 shows $(m_{uo} + m_u + m_{bo}\frac{\rho_u}{\rho_b})$. In Fig. 6.10, m_u is independent of ξ, and the values of m_{uo} and m_{bo} are zero for $\xi = 1, (R_\xi = R_t)$. Their value increase as ξ decreases. However, m_u remains as a dominating factor in determining the value of u_t. Hence, u_t is obtained by using Eq. 6.6 and numerical differentiation employs the Savitzky-Golay algorithm (Press *et al.* 1992). Shown in Fig. 6.14 are variations of u_t with time for different values of ξ. The values of u_t are a maximum for $\xi = 1$, while they are a minimum for $\xi = 0$. For $\xi = 0$, the value of u_t does not increase with time.

6.5 Relationship of u_t to u_{tr}

Adding Eqs. 6.4 and 6.6 and using Eq. 6.3, it can be shown u_t and u_{tr} are related by:

$$4\pi R_i^2 \rho_u (u_t - u_{tr}) = \frac{dm_{ui}}{dt} - \frac{dm_{bo}\rho_u/\rho_b}{dt} \tag{6.17}$$

Three conditions are considered:

1. When $R_i = R_r$ then $m_{ui} = 0$, and the second term on the right of Eq. 6.17 is a maximum. Clearly $u_{tr} > u_t$.

2. When $R_i = R_t$ then $m_{bo} = 0$, and $u_t > u_{tr}$.

3. The condition for $u_t = u_{tr}$ is:

$$\frac{dm_{ui}}{dt} = \frac{d(m_{bo}\rho_u/\rho_b)}{dt} \tag{6.18}$$

For a given R_i, let $V_{\rm ui}$ = volume occupied by $m_{\rm ui}$ and $V_{\rm bo}$ = volume occupied by $m_{\rm bo}$. Then

$$\frac{\mathrm{d}(V_{\rm ui}\rho_{\rm u})}{\mathrm{d}t} = \frac{\mathrm{d}(V_{\rm bo}\rho_{\rm b}\rho_{\rm u}/\rho_{\rm b})}{\mathrm{d}t} \tag{6.19}$$

and

$$\frac{\mathrm{d}V_{\rm ui}}{\mathrm{d}t} = \frac{\mathrm{d}V_{\rm bo}}{\mathrm{d}t} \tag{6.20}$$

Clearly if $V_{\rm ui} = V_{\rm bo}$ at all times (for a consistent definition of R_i) this condition is met and $u_{\rm t} = u_{\rm tr}$. This condition is the defines $R_i = R_{\rm v}$ in § 6.2.

The relationship $u_{\rm t}(R_{\rm v}) = u_{\rm tr}(R_{\rm v})$ has been verified from the experimental data and an example of this is shown in Fig. 6.15. Values of $u_{\rm t}(R_{\rm v})$ are plotted against $u_{\rm tr}(R_{\rm v})$ with data from four different explosions of stoichiometric methane-air mixtures with $u' = 0.595$ m/s. Within the limits of experimental error, the agreement is very good.

6.6 Expressions for the Flame Speed

The total volume of burned gas at a given time, if concentrated in a sphere of radius $R_{\rm s}$, is

$$\frac{4}{3}\pi R_{\rm s}^3 = \frac{4}{3}\pi R_{\rm r}^3 + V_{\rm bi} + V_{\rm bo} \tag{6.21}$$

It may also be expressed in terms of the volume $\frac{4}{3}\pi R_{\rm v}^3$ as follows:

$$\frac{4}{3}\pi R_{\rm s}^3 = \frac{4}{3}\pi R_{\rm v}^3 + V_{\rm bo} - V_{\rm ui} \tag{6.22}$$

For the condition $u_{\rm t} = u_{\rm tr}$, $V_{\rm ui} = V_{\rm bo}$ and it follows from Eq. 6.22 that $R_{\rm s} = R_{\rm v}$. In general, the mass rate of production of burned gas is given by

$$\frac{\mathrm{d}(\frac{4}{3}\pi R_{\rm s}^3\rho_{\rm b})}{\mathrm{d}t} = 4\pi R_{\rm s}^2\frac{\mathrm{d}R_{\rm s}}{\mathrm{d}t}\rho_{\rm b} = 4\pi R_i^2\rho_{\rm u}u_{\rm tr} \tag{6.23}$$

With $u_t = u_{tr}$, $R_i = R_s = R_v$ and from Eq. 6.23, the corresponding turbulent flame speed, can be written as:

$$\frac{dR_v}{dt} = \frac{\rho_u}{\rho_b} u_t \tag{6.24}$$

Otherwise,

$$\frac{dR_s}{dt} = \frac{\rho_u}{\rho_b} \left(\frac{R_i}{R_s}\right)^2 u_{tr} \tag{6.25}$$

Equation 6.24 also has been verified using experimental data and an example is shown in Fig. 6.16, where values of dR_v/dt are plotted against $u_t(R_v)\rho_u/\rho_b$, using data obtained from four different explosions of stoichiometric methane-air mixtures at $u' = 0.595$ m/s. The experimental results satisfies the relationship quite closely; the observed scatter probably arises from the numerical methods employed in estimating these values.

6.7 The Role of Turbulence Spectrum

As the flame propagates after spark ignition, the flame front is at first wrinkled by the smallest scales of turbulence - larger length scales merely convecting the kernel bodily. During this period, the r.m.s. turbulent velocity effective in wrinkling the flame is $u'_k, (< u')$. However, as the kernel continues to grow it becomes progressively wrinkled by the larger length scales until eventually the size of the kernel is sufficient for it to experience the entire turbulence spectrum. The effect of turbulence (embodied in u'_k) on flame wrinkling and the turbulent burning velocity is then fully developed and equal to u' (Abdel-Gayed *et al.* 1987, Bradley 1990). Abdel-Gayed *et al.* (1987) derived a nondimensional power spectrum from laser-doppler measurements of isotropic turbulence in a fan-stirred fan. They assumed the frequency band affecting flame propagation to extend from the highest frequency to a threshold frequency given by the reciprocal of the time elapsed from ignition.

Scott (1992) improved the nondimensional power spectrum by replacing the dimensionless frequency with a dimensionless wave number, $\bar{k}_\eta$, defined as:

$$\bar{k}_\eta = k\ \eta \tag{6.26}$$

,where k is the wave number and η is the Kolmogorov length scale. The wave number provides the link to the time scale. At the elapsed time, t_k, measured from ignition, the corresponding value of k, is given by:

$$k = \frac{2\pi}{s\ t_k} \tag{6.27}$$

Here s is the mean cold gas speed and in the fan-stirred vessel, where there is no mean velocity, it is related by Abdel-Gayed *et al.* (1987) to u' by:

$$s = u'\left[\frac{8}{\pi}\right]^{0.5} \tag{6.28}$$

η is related to the turbulent Reynolds number, R_λ, defined by $u'\lambda/\nu$, and the Taylor microscale, λ, by:

$$\eta = \frac{\lambda}{15^{0.25} R_\lambda^{0.5}} \tag{6.29}$$

R_λ and λ are related to integral length scale, L, by:

$$\frac{\lambda}{L} = \frac{A}{R_\lambda} \tag{6.30}$$

where A is a numeric constant. Scott (1992) suggested that a value of A of 16, with bounds of $\pm$ 1.5, gives the best fit to the spectral measurements, over a wide range of the data reported by McComb (1990). Values of ν and L, required to estimate R_λ, for the initial conditions studied in the present work, are presented in Table 6.1.

These values of $\bar{S}(\bar{k}_\eta)$, measured over a wide range of physical situations, reveal that the spectra at the higher wavenumbers collapse to a universal form of $k^{-5/3}$ (McComb 1990) and, as the Reynolds number decreases, the spectra show shorter

ranges of universal behaviour. Scott (1992) studied measured spectra for a wide range of Reynolds numbers and produced a universal best fit correlation to those for $\bar{S}(\bar{k}_\eta)$ as a function of $\bar{k}_\eta$ and R_λ:

$$\bar{S}(\bar{k}_\eta) = \frac{0.01668R_\lambda^{2.5} + 3.74R_\lambda^{0.9} - 70R_\lambda^{-0.1}}{1 + \left(0.127R_\lambda^{1.5}\bar{k}_\eta\right)^{5/3} + \left(1.15R_\lambda^{0.622}\bar{k}_\eta\right)^{4} + \left(1.27R_\lambda^{0.357}\bar{k}_\eta\right)^{7}} \tag{6.31}$$

The agreement between Eq. 6.31 and the data of other researches is excellent, as can be seen from Fig. 6.17, where the symbols are the measured values reported in McComb (1990) and the lines corresponds to the values obtained from the correlation.

Using the approach followed by Abdel-Gayed *et al.* (1987), at an elapsed time of t_k, the r.m.s. turbulent velocity effective in influencing flame propagation, u'_k, is given by:

$$u'_k = u'\left\{\frac{15^{0.5}}{R_\lambda}\int_{\bar{k}_\eta}^{\infty}\bar{S}(\bar{k}_\eta)\mathrm{d}\bar{k}_\eta\right\}^{1/2} \tag{6.32}$$

Values of u'_k/u' are obtained at different values of $\bar{k}_\eta$ by numerical integration of Eq. 6.32 using Eq. 6.31. Shown in Fig. 6.18 are such variations of u'_k/u' plotted against $\bar{k}_\eta^{-1}$ for a range of values of R_λ. Hence, the values of u'_k/u' for different t_k are estimated using Eqs. 6.26, 6.27 and 6.32 and are plotted in Fig. 6.19, for the experimental conditions of the present study.

6.8 Results and Discussions

The present study involves spherically expanding premixed flames of stoichiometric methane-air mixtures at initial pressures of 0.1 MPa and 0.5 MPa, at three different r.m.s. turbulence velocities, u', of 0.595, 1.19 and 2.38 m/s, all at 300 K. For each condition the data are the averages from four different explosions. The initial conditions and the relevant data are presented in Table 6.1.

Turbulent burning velocities and the associated reference radii and masses are computed from the measured values of σ as a function of r for each set of flame images.

as discussed in § 6.4.1. Typical values of σ at different reference flame radii have been shown in Fig. 6.6 for one explosion. Averaged values of σ as a function of r for different elapsed times in four different explosions are now shown in Figs. 6.20 and 6.21 for 0.1 MPa at $u' = 0.595$ m/s and 0.5 MPa at $u' = 2.38$ m/s, respectively. Different reference radii are obtained from the averaged values of $\sigma(r)$, as discussed in § 6.4.2, and these are shown in Figs. 6.22 to 6.27 plotted against elapsed time, for the different conditions of Table 6.1. In all cases the flame brush thickness increases with time and radius.

Shown in Fig. 6.28 are the values of $u_{\rm tr}/u_l$ for the different reference radii, plotted against u'_k/u_l, for stoichiometric methane-air mixtures at 0.1 MPa with $u' = 0.595$ m/s. The values of $u_{\rm tr}/u_l$ for all reference radii increase with u'_k/u_l. The highest values of $u_{\rm tr}/u_l$ are associated with the smallest radius, $R_{\rm r}$. Conversely, smaller values of $u_{\rm tr}/u_l$ are associated with $R_{\xi=0.5}$ and $R_{\rm t}$. At the lowest values of u'_k/u_l, these values of $u_{\rm tr}/u_l$ are even less than unity. Hence, only the reference radii of $R_{\rm a}$, $R_{\rm m}$ and $R_{\rm v}$ are further considered and only the values of $u_{\rm tr}$ corresponding to $R_{\rm v}$ are reported. Values of $u_{\rm tr}$ for other reference radii can be obtained from flame radii presented in Figs. 6.22 to 6.27, as $u_{\rm tr}R_i^2$ is a constant (§ 6.4.3).

Shown in Fig. 6.29 and 6.30 are the values of $u_{\rm tr}(R_{\rm v})/u_l$ plotted against u'/u_l for stoichiometric methane-air mixtures at 0.1 MPa and 0.5 MPa respectively at three different level of turbulence intensity at an initial temperature of 300 K. In all cases, turbulence enhances the mass burning rate.

It is fruitful, on the basis of the present work, to examine which definitions of radius and burning velocity appear to be in the best agreement with the correlations of turbulent burning velocity presented by Bradley *et al.* (1992). For values of $(KLe)_{\rm B}$ between 0.01 and 0.63, they suggested turbulent burning velocities are correlated by

$$\frac{u_{\rm t}}{u_l} = 0.88\ (KLe)_{\rm B}^{-0.3}\left(\frac{u'_k}{u_l}\right) \tag{6.33}$$

Here,

$$(KLe)_{\mathrm{B}} = 0.157Le\left(\frac{u'}{u_l}\right)^2 R_{\mathrm{L}}^{-0.5} \tag{6.34}$$

with a value of A, in Eq. 6.30, equal to 40.4, as reported by Abdel-Gayed *et al.* (1984). Equation 6.33 is plotted in Figs. 6.29 to 6.35. Over much of the present range of conditions, the empirical expression is close to the present correlation of u_{t} based on R_{V}. It follows that the correlation is a good representation of both the mass rate of burning and the progress of the advancing flame front.

Table 6.1. Initial conditions and corresponding turbulence parameters for PMS studies of premixed turbulent stoichiometric methane-air flames at an initial temperature of 300 K. Integral length scale for all the conditions is 20 mm. Kinematic viscosity, ν, is $1.597.10^{-5}$ m^2/s and $3.187.10^{-6}$ m^2/s for initial pressures of 0.1 and 0.5 MPa, respectively.

P_u (MPa)	ρ_u (Kg/m^3)	ρ_b (Kg/m^3)	u_l (m/s)	u' (m/s)	η (mm)	λ (mm)	R_λ	R_L	$(KLe)_B$
0.10	1.1083	0.1481	0.36	0.595	0.142	2.930	109	746	0.0157
0.10	1.1083	0.1481	0.36	1.19	0.085	2.072	154	1491	0.0444
0.10	1.1083	0.1481	0.36	2.38	0.050	1.465	218	2982	0.1256
0.50	5.5504	0.7318	0.19	0.595	0.043	1.309	244	3734	0.0252
0.50	5.5504	0.7318	0.19	1.19	0.025	0.926	346	7468	0.0713
0.50	5.5504	0.7318	0.19	2.38	0.015	0.655	489	14936	0.2016

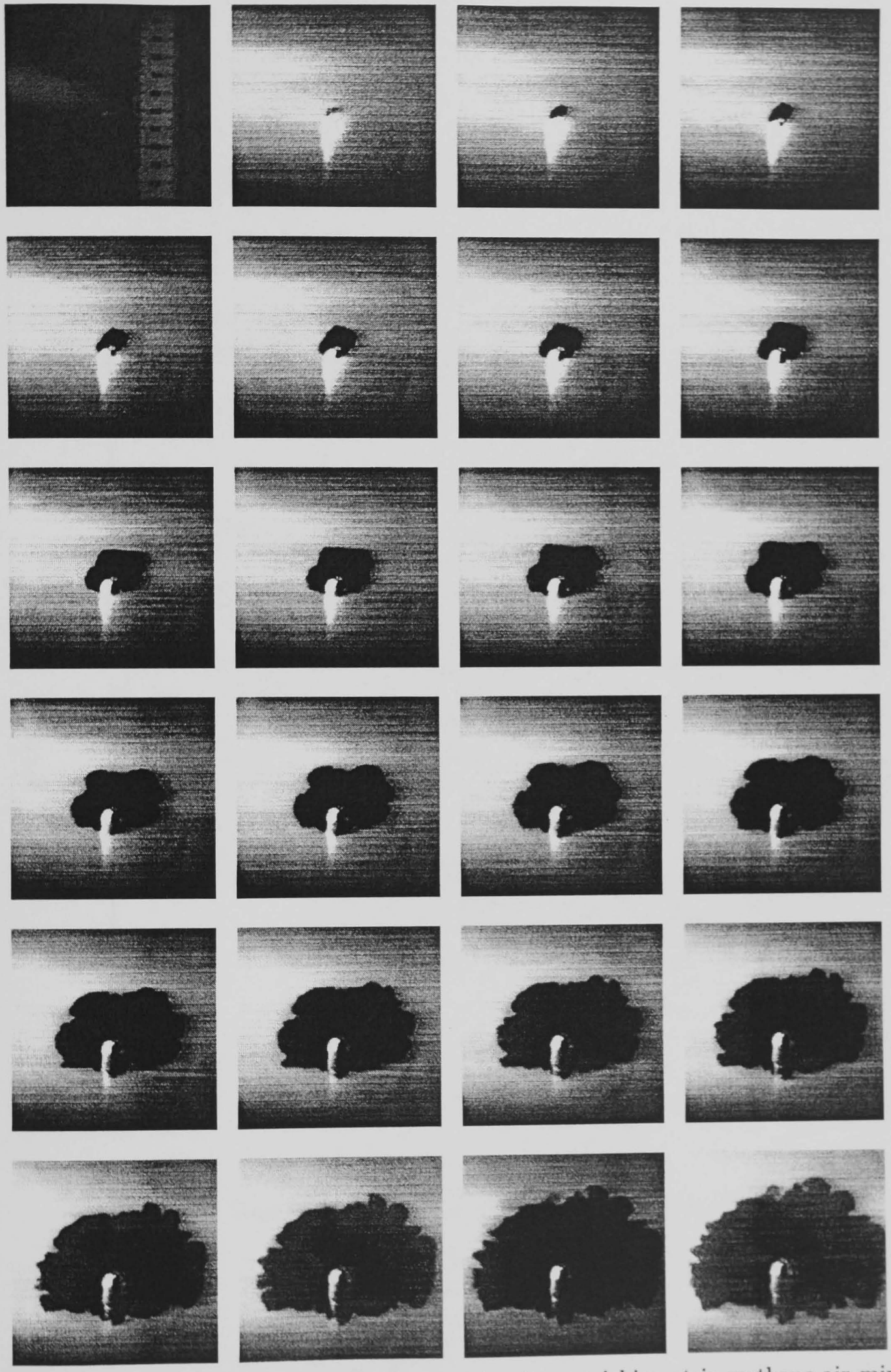

Fig. 6.1. Flame images for the propagation in a stoichiometric methane-air mixture at an initial temperature of 300 K and pressure of 0.1 MPa with an isotropic r.m.s turbulence velocity of 0.595 m/s.

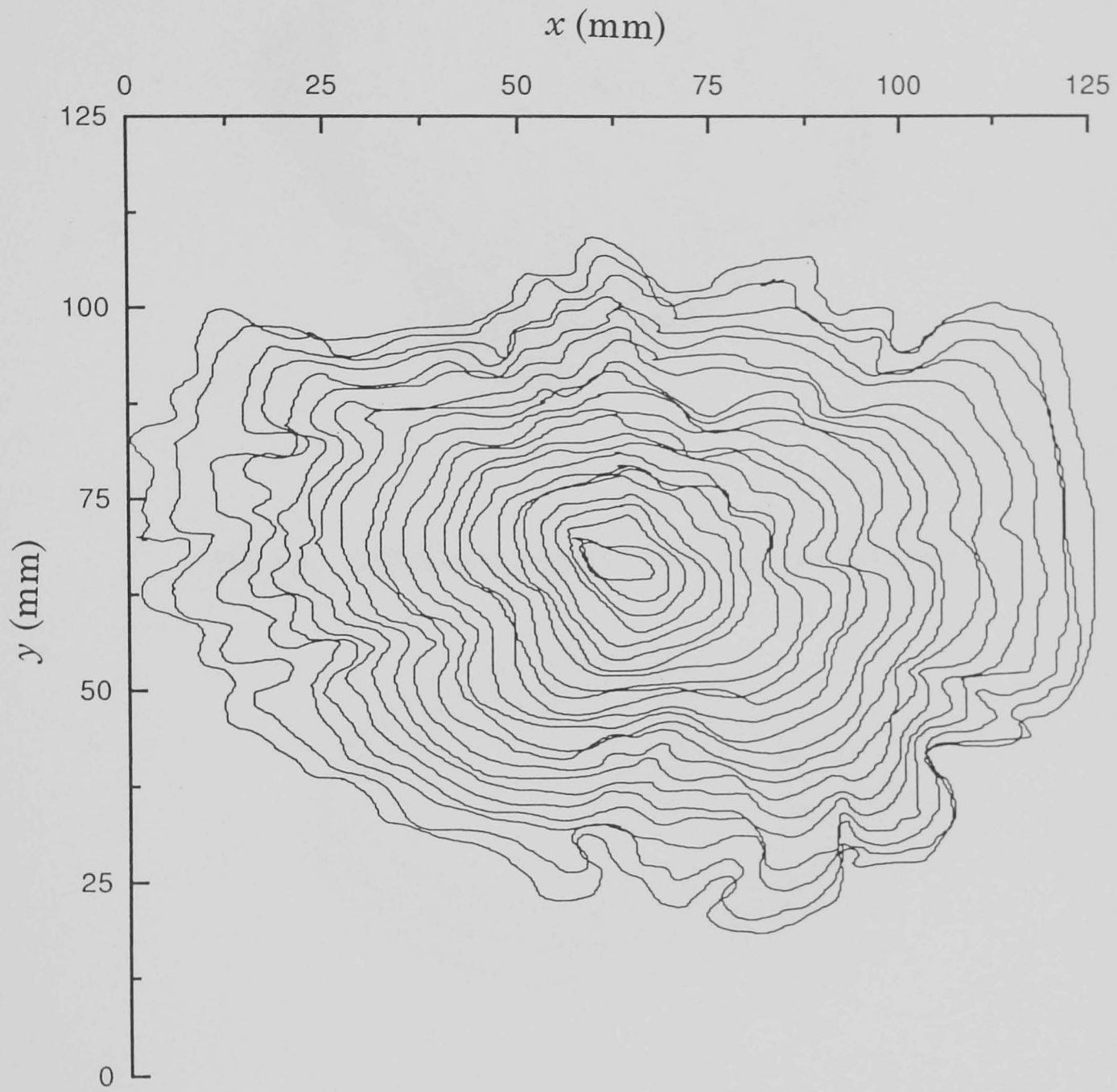

Fig. 6.2. Flame coordinates for the flame images shown in Fig. 6.1.

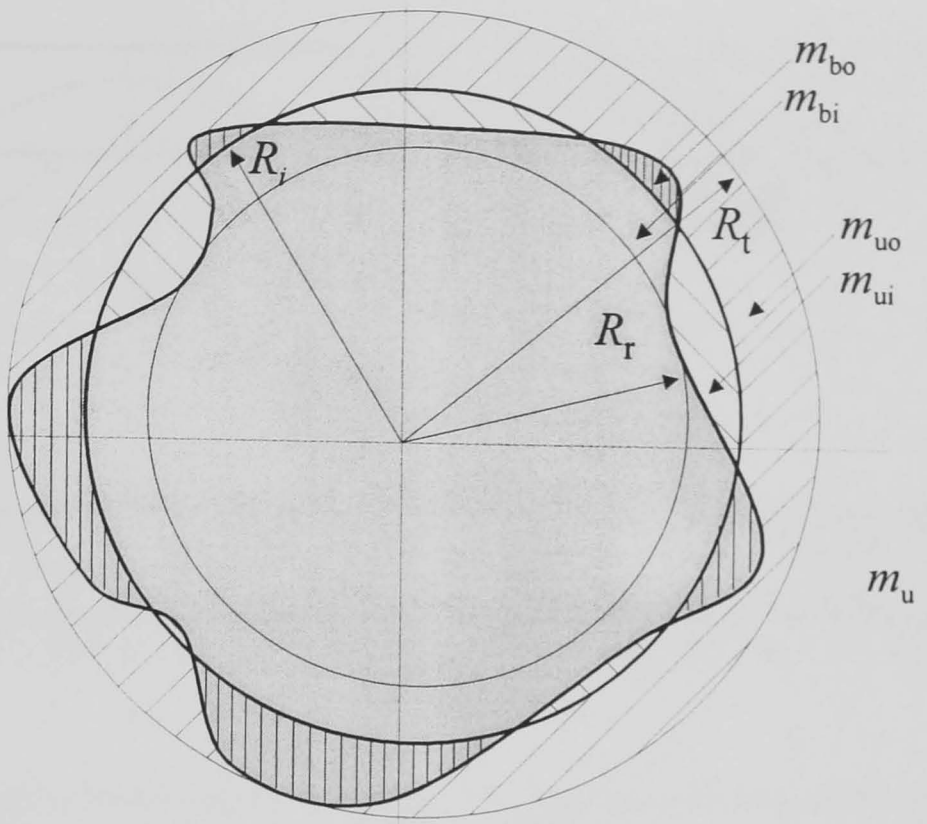

Fig. 6.3. Definition of different masses for a flame images.

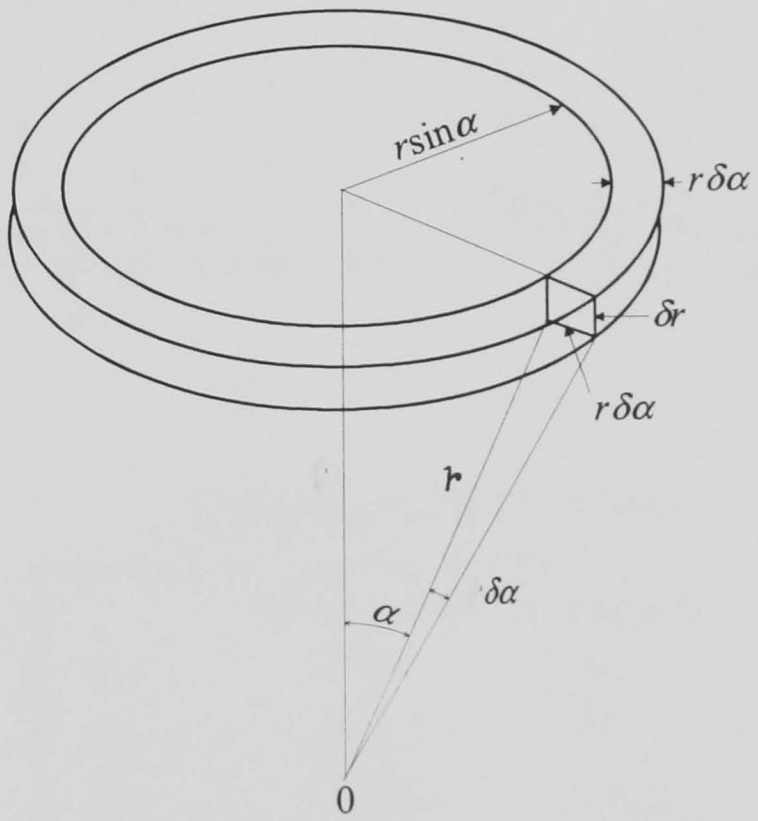

Fig. 6.4. Definition of a volumetric slice on the surface of a sphere of radius r and at an angle, α.

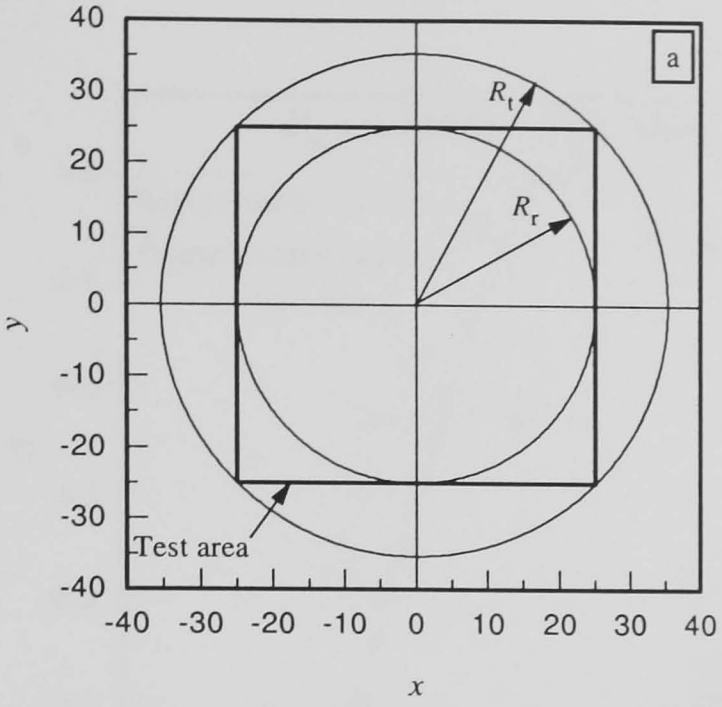

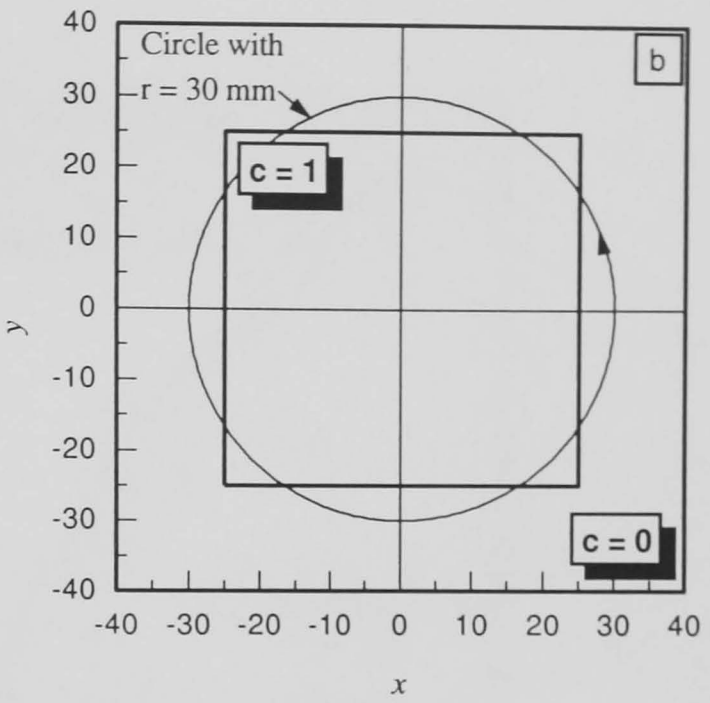

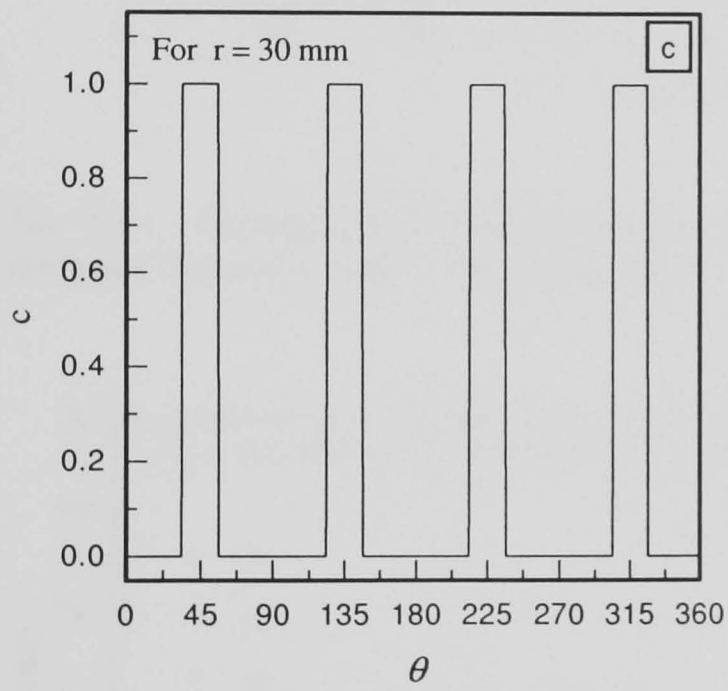

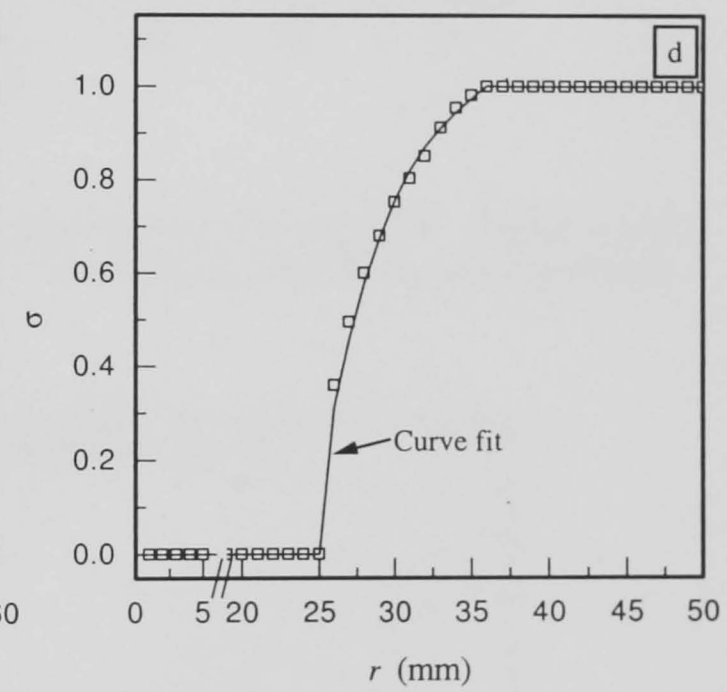

Calibration of the results

	Prog. results	Theoretical value
R_r	25.00	25.00
R_a	28.21	28.21
R_t	35.36	35.36
at r = 30	σ = 0.75	σ = 0.75

Fig. 6.5. Procedure to estimate and calibrate the value of σ as a function of flame radii.

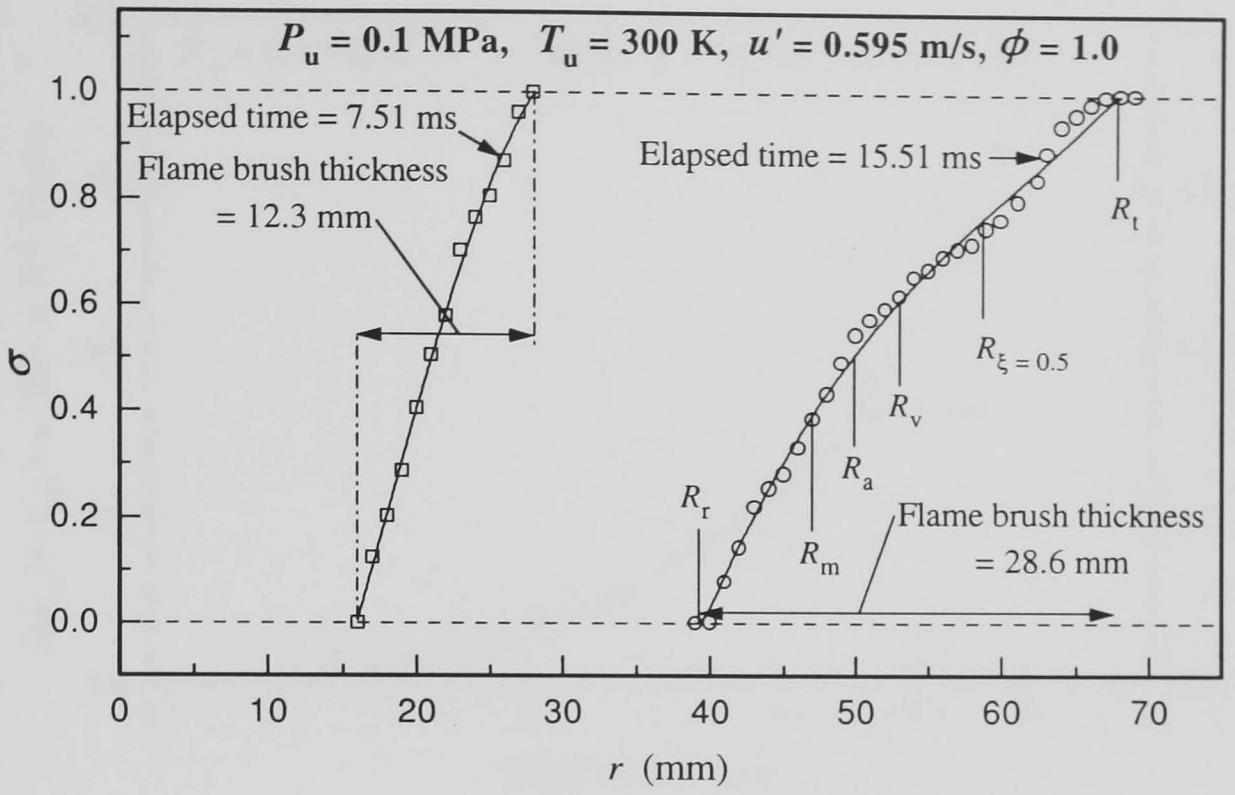

Fig. 6.6. Changes in σ with increasing elapsed time from ignition. Flame brush thickness defined by $(R_t - R_r)$ and estimated values of R_a, R_m & R_v are also shown.

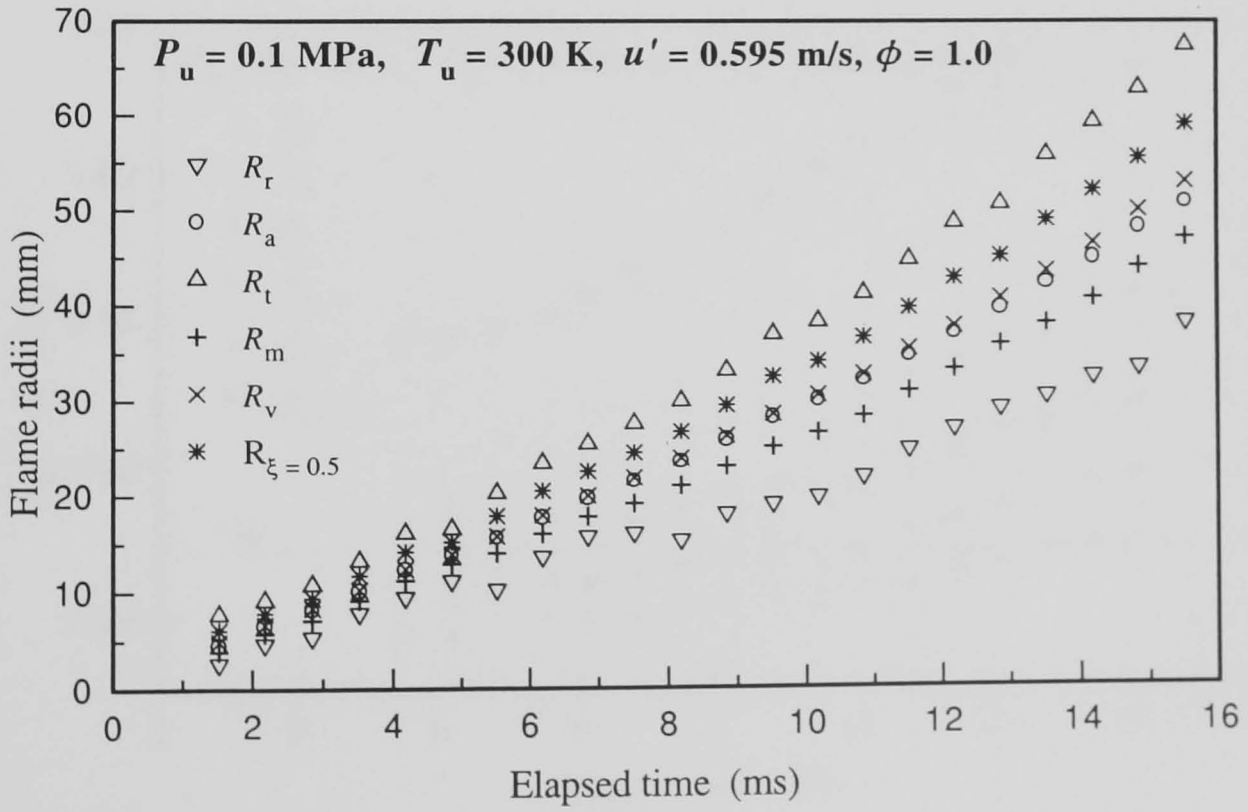

Fig. 6.7. Variation of six reference flame radii with elapsed time.

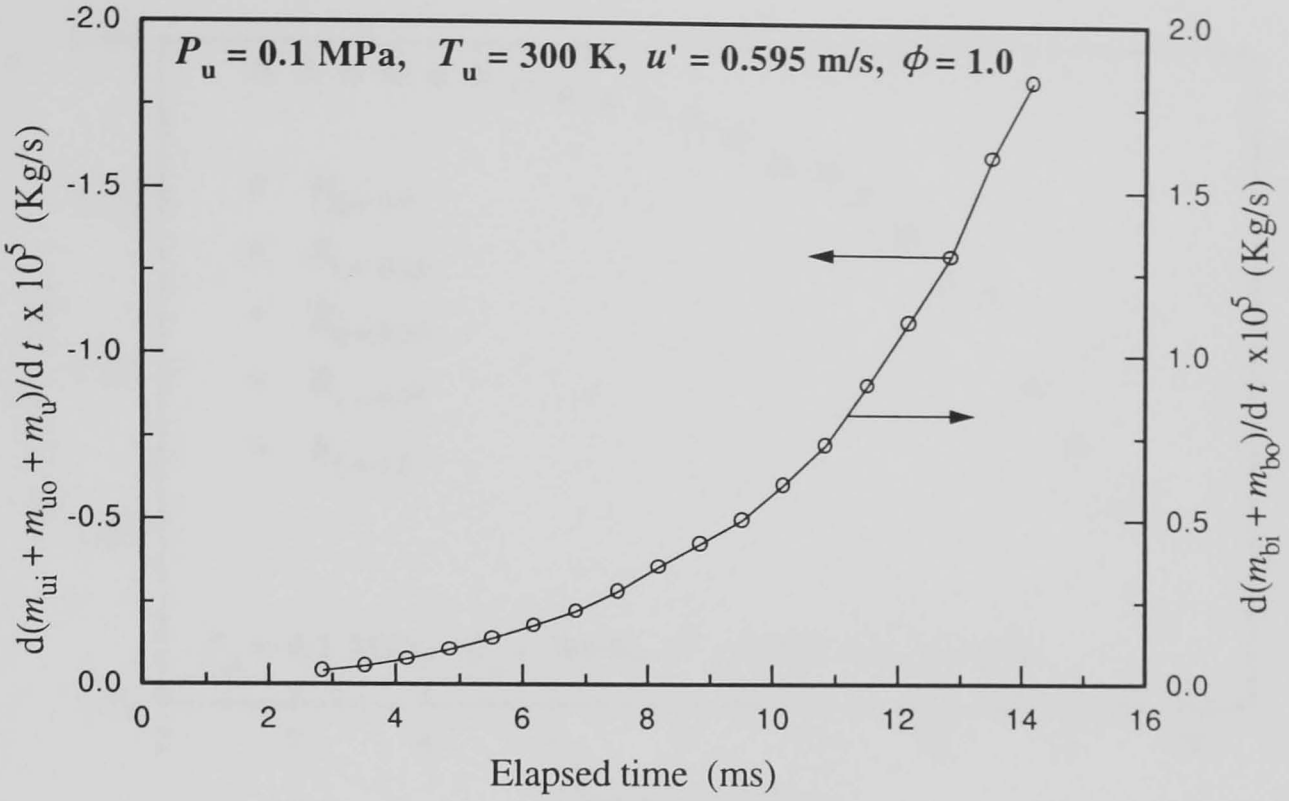

Fig. 6.8. Rate of the appearance of burned gas and the disappearance of the unburned gas with elapsed time.

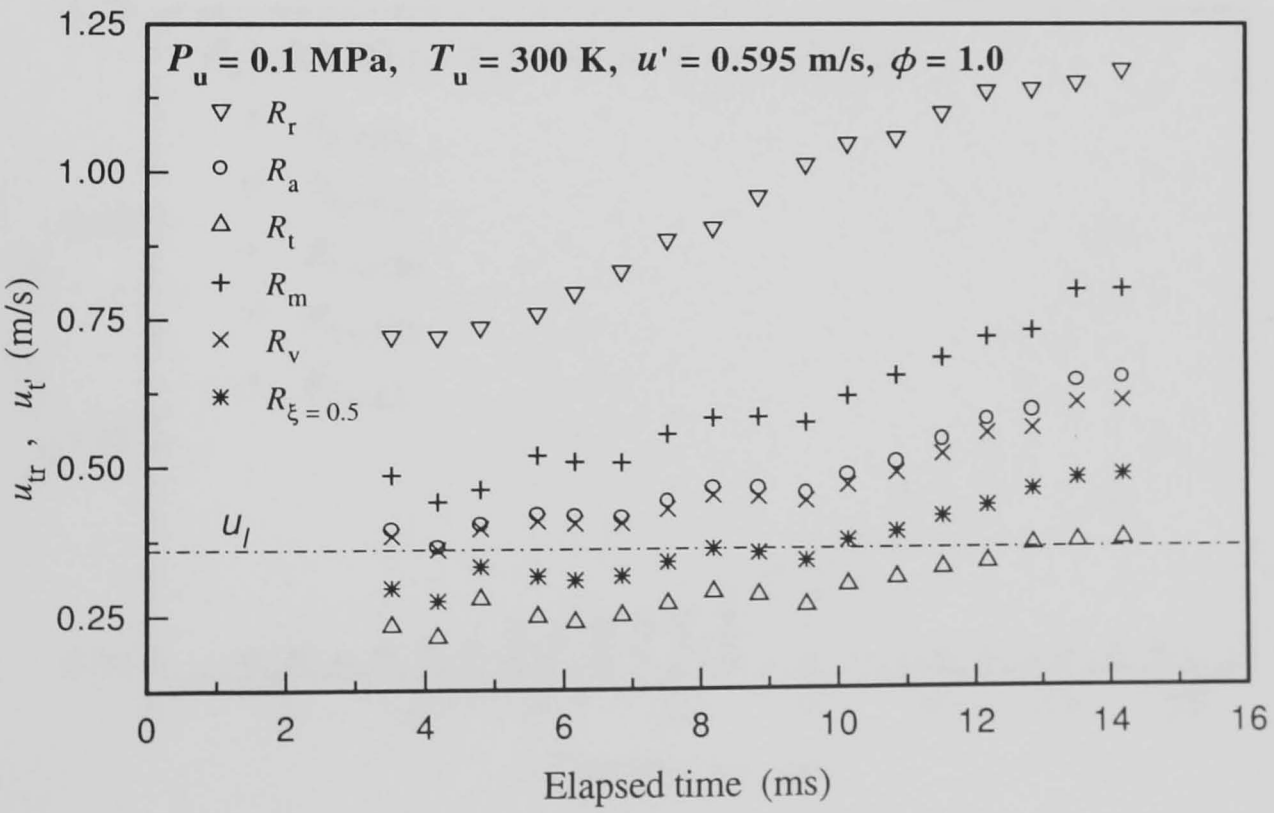

Fig. 6.9. Variation of $u_{tr} = u_{t'}$ with elapsed time from ignition.

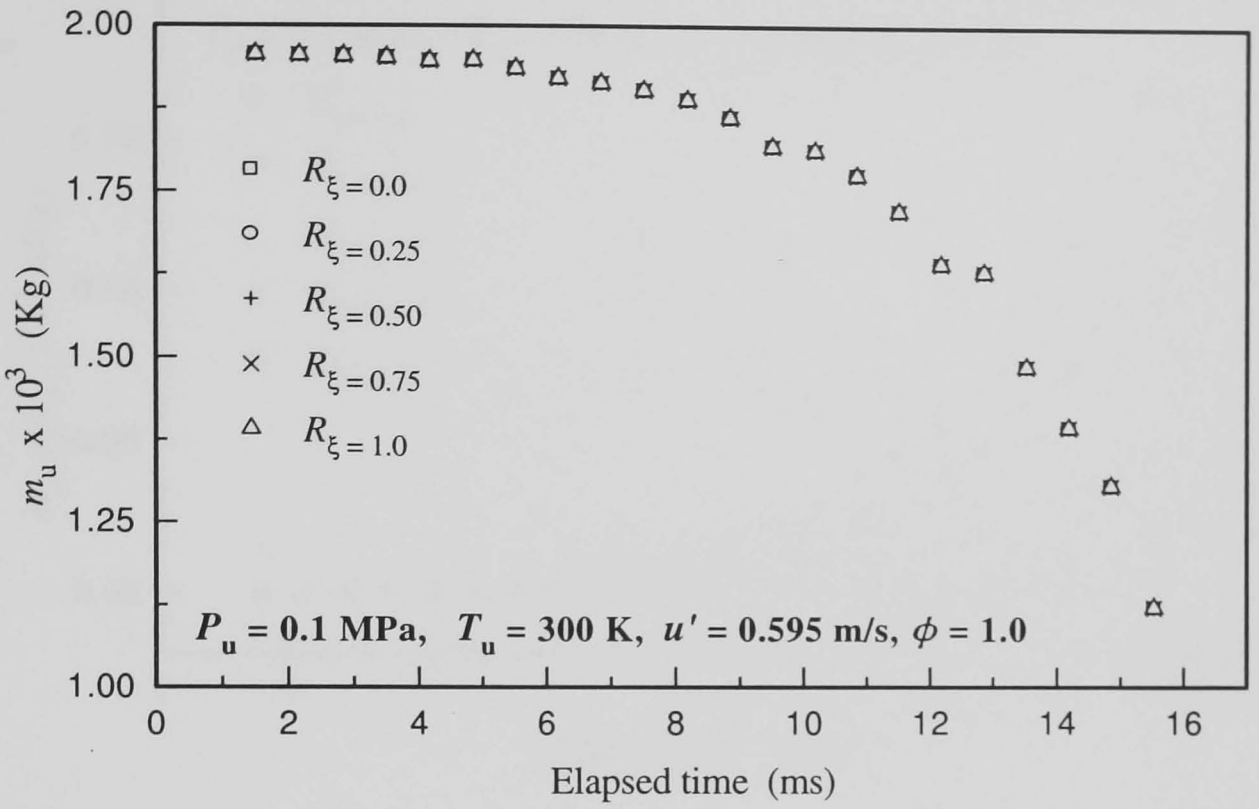

Fig. 6.10. Variation of m_{u} with elapsed time from ignition for different values of ξ.

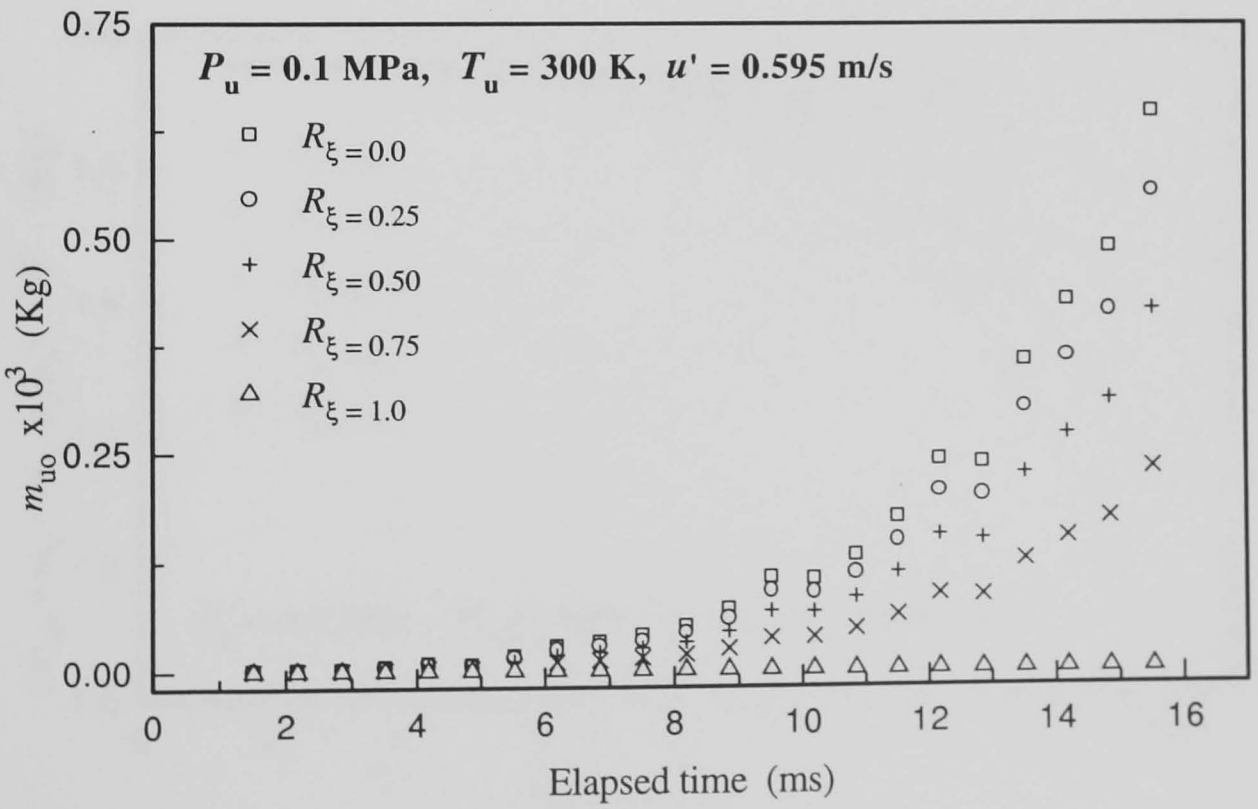

Fig. 6.11. Variation of m_{uo} with elapsed time from ignition for different values of ξ.

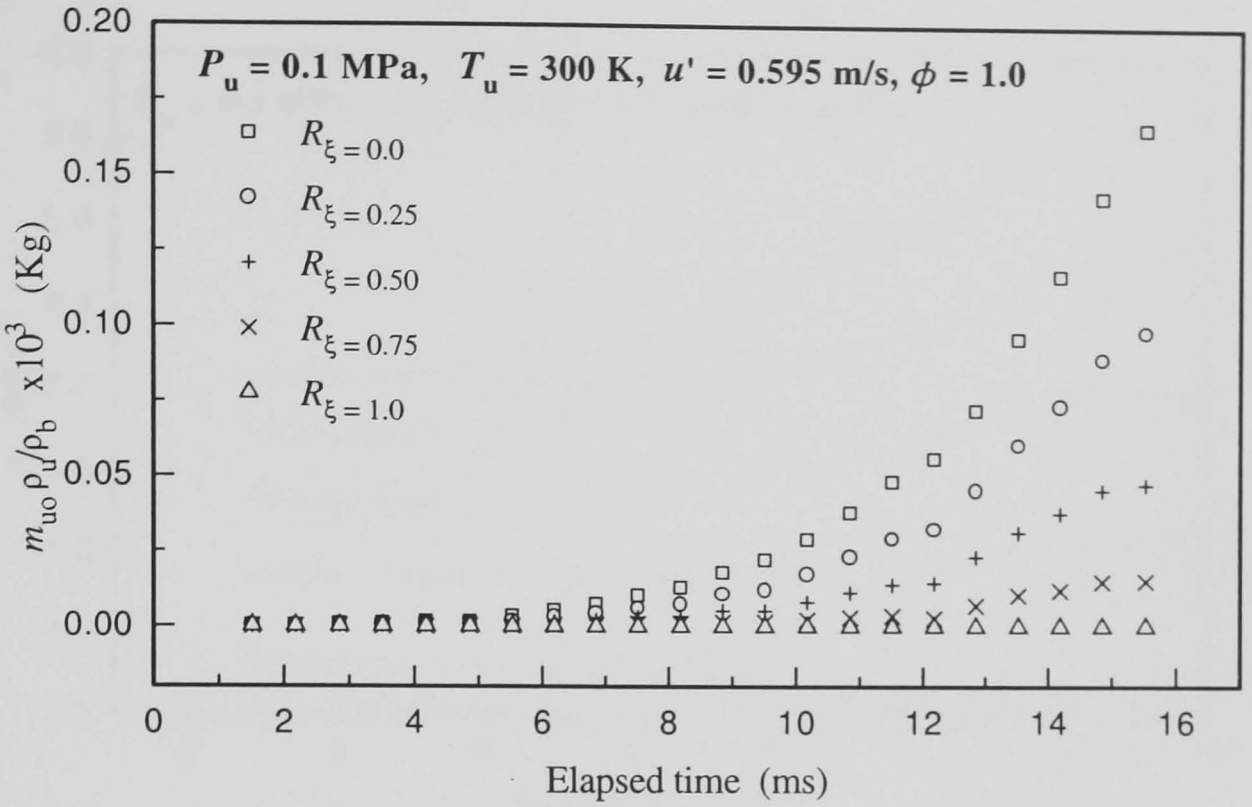

Fig. 6.12. Variation of $m_{\mathrm{bo}}\frac{\rho_{\mathrm{u}}}{\rho_{\mathrm{b}}}$ with elapsed time from ignition for different values of ξ.

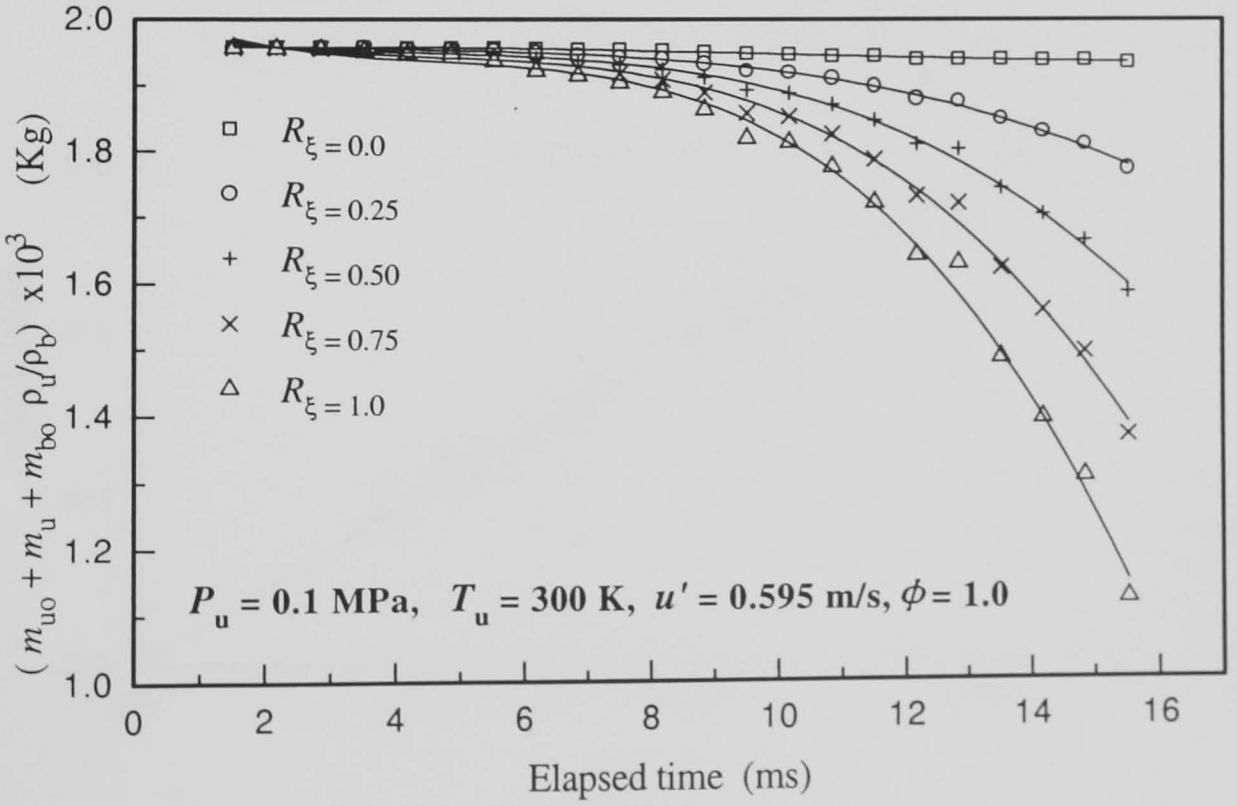

Fig. 6.13. Rate of change of $(m_{\mathrm{u}} + m_{\mathrm{uo}} + m_{\mathrm{bo}}\frac{\rho_{\mathrm{u}}}{\rho_{\mathrm{b}}})$ for different values of ξ.

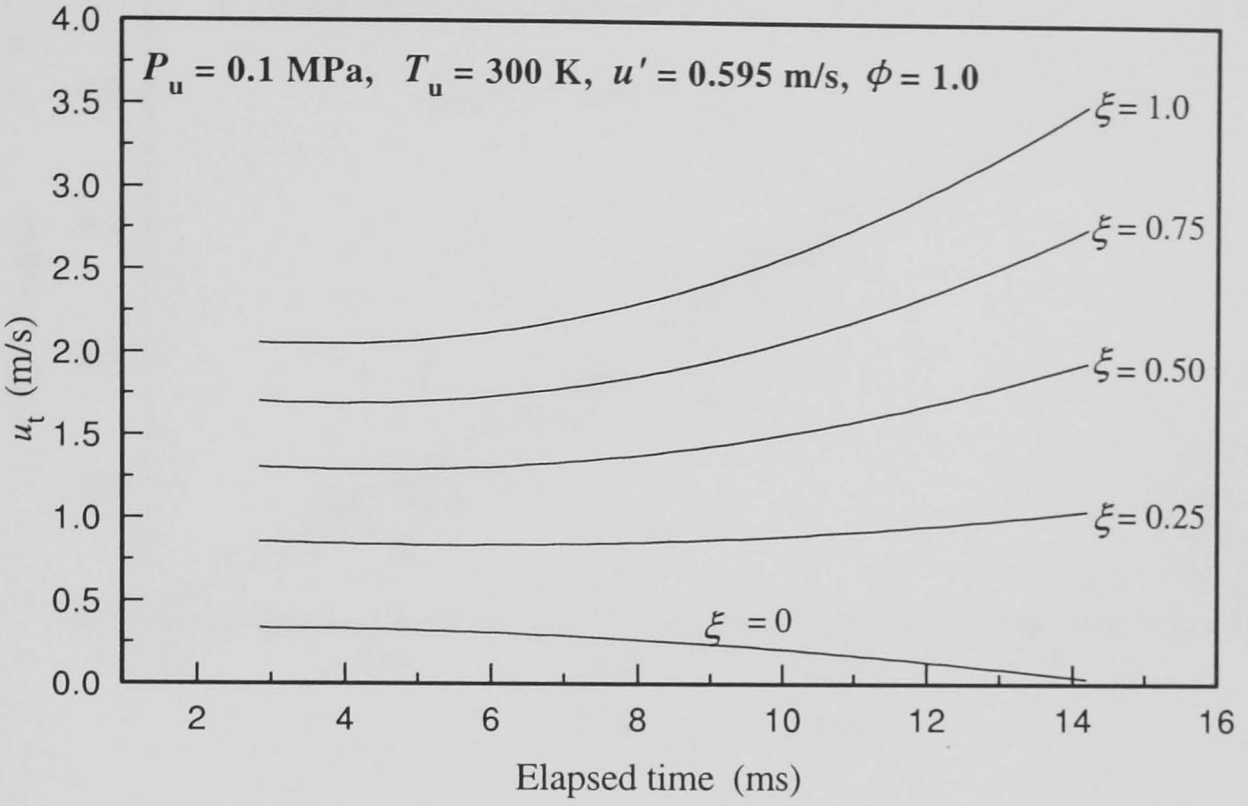

Fig. 6.14. Variation of u_t with elapsed time for different values of ξ.

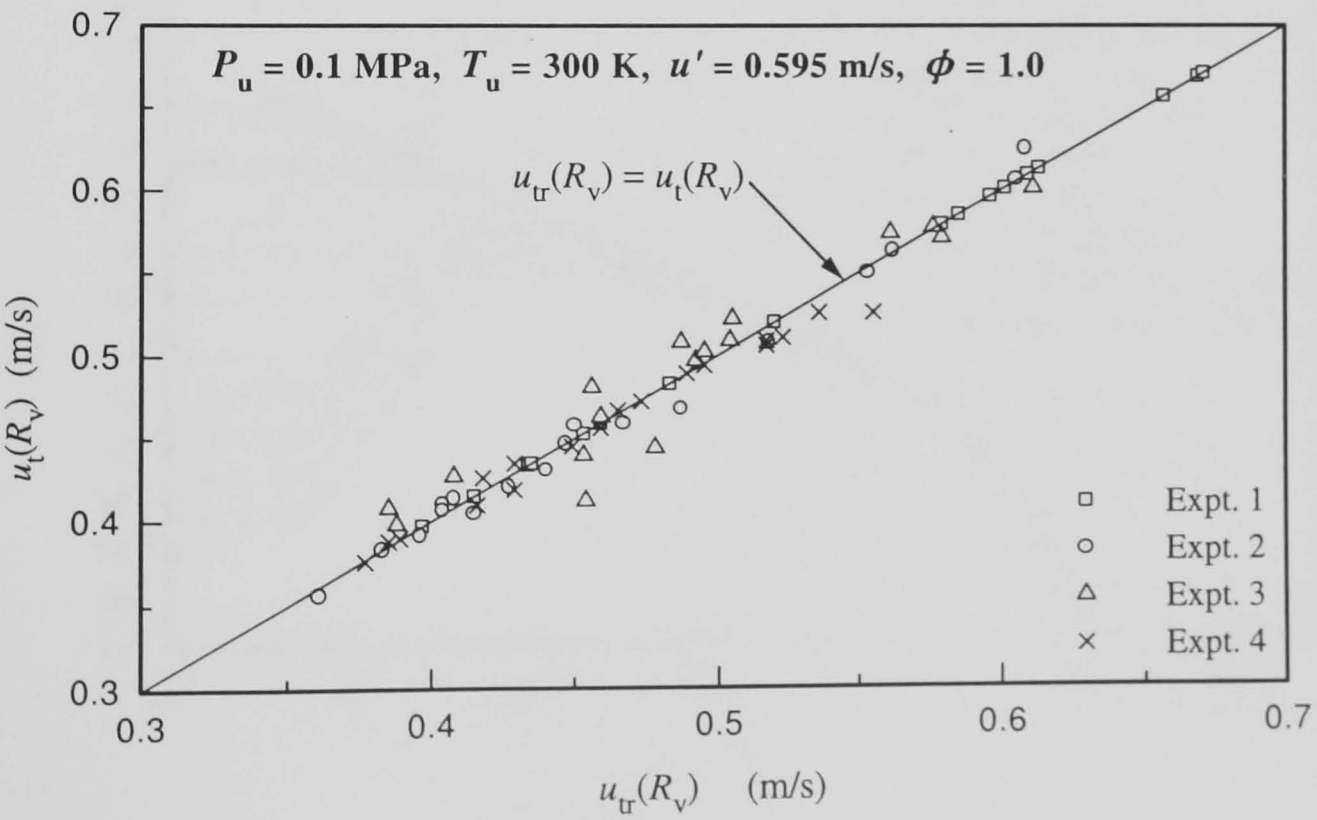

Fig. 6.15. Experimental relationship between $u_t(R_v)$ and $u_t(R_v)$.

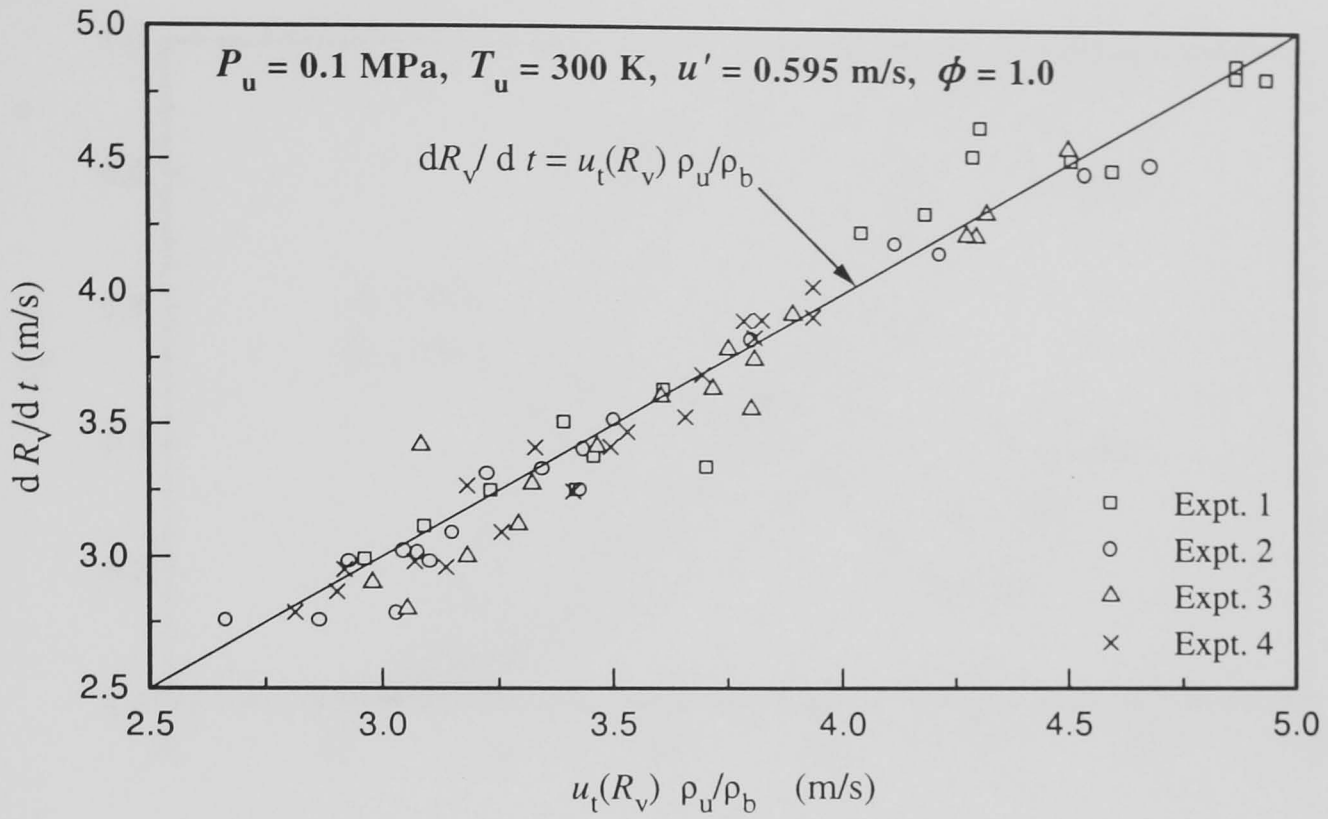

Fig. 6.16. Experimental relationship between R_v/dt and $u_t(R_v)$.

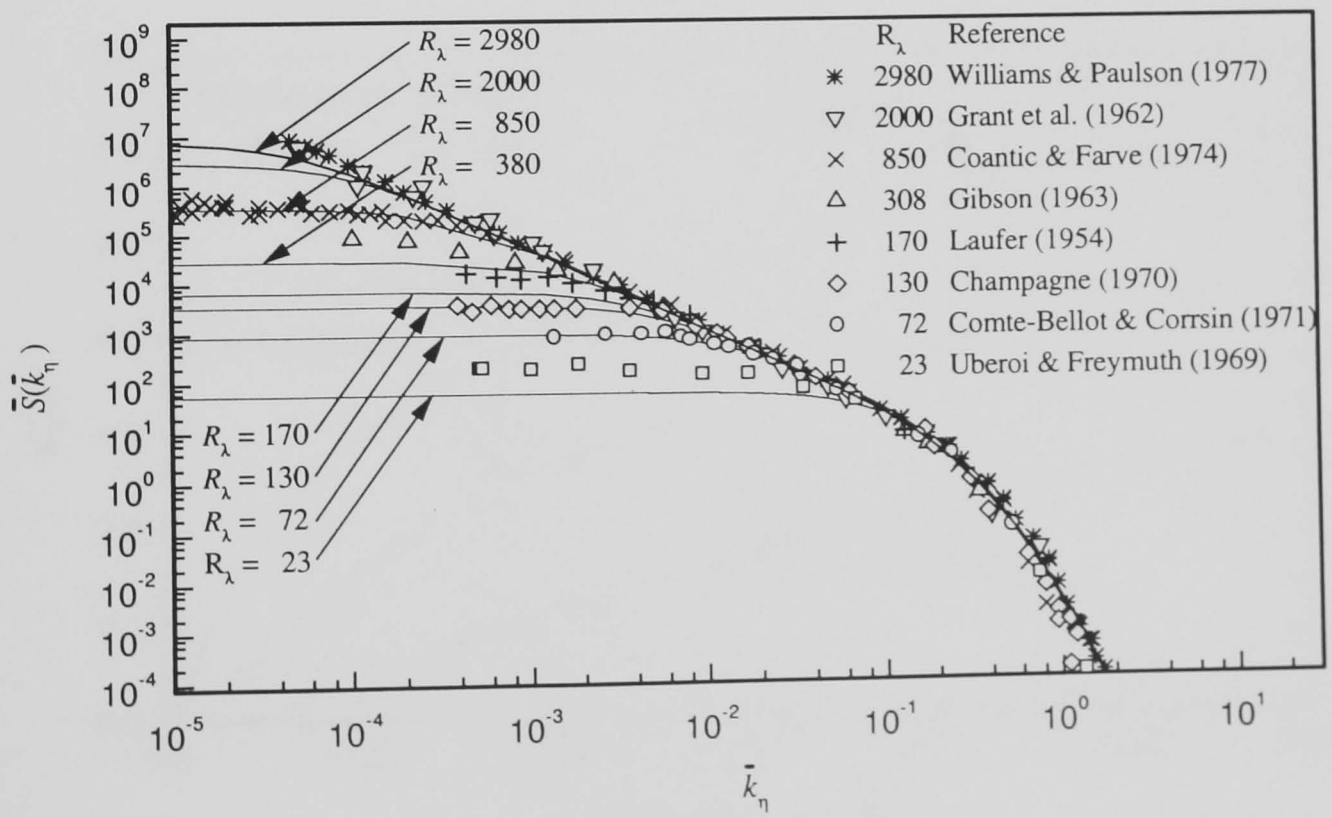

Fig. 6.17. Generalized psd function showing the spectrum of turbulent energy. The solid lines are the calculated values using Eqs. 6.31 and 6.32, and the symbols are the experimental results reported in McComb (1990).

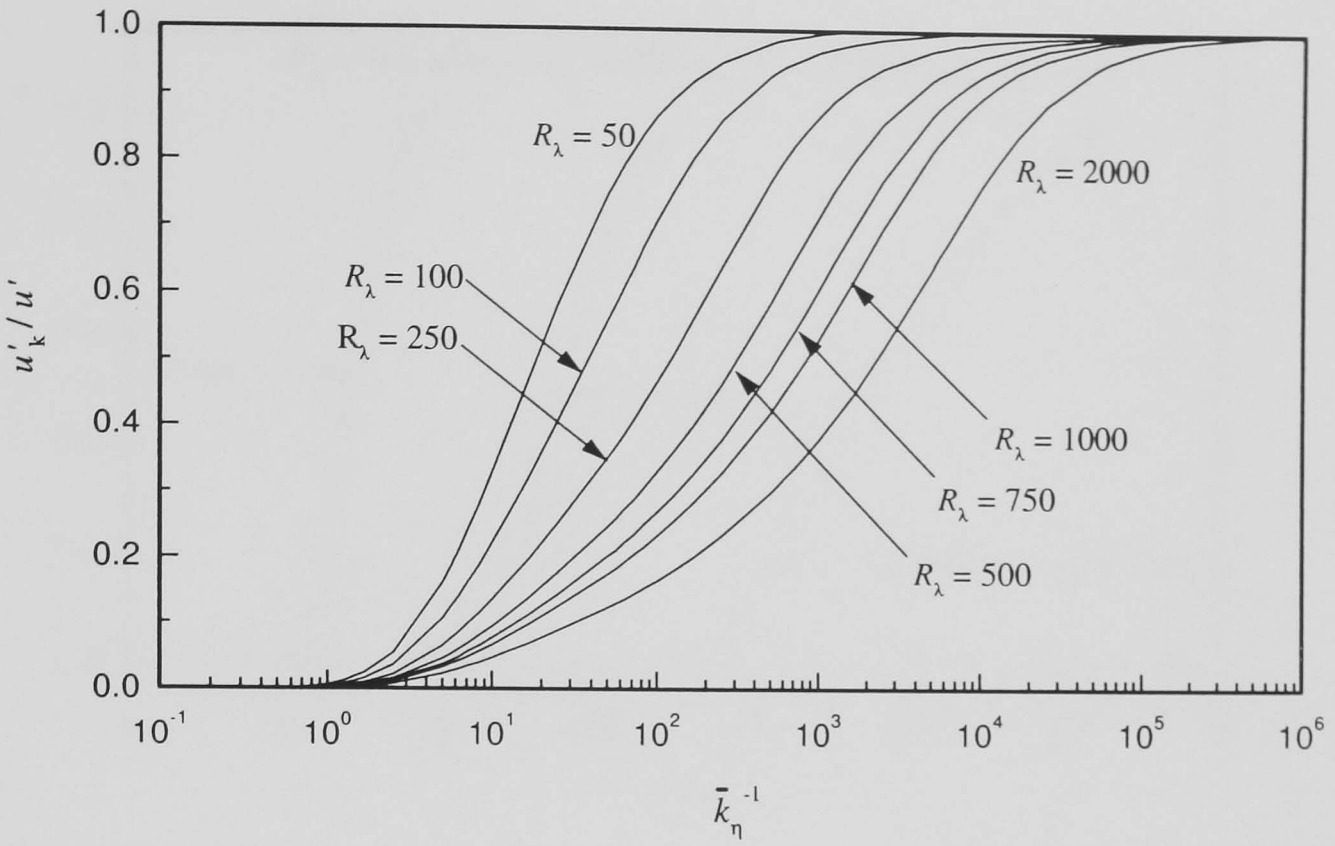

Fig. 6.18. Development of effective r.m.s. turbulent velocity.

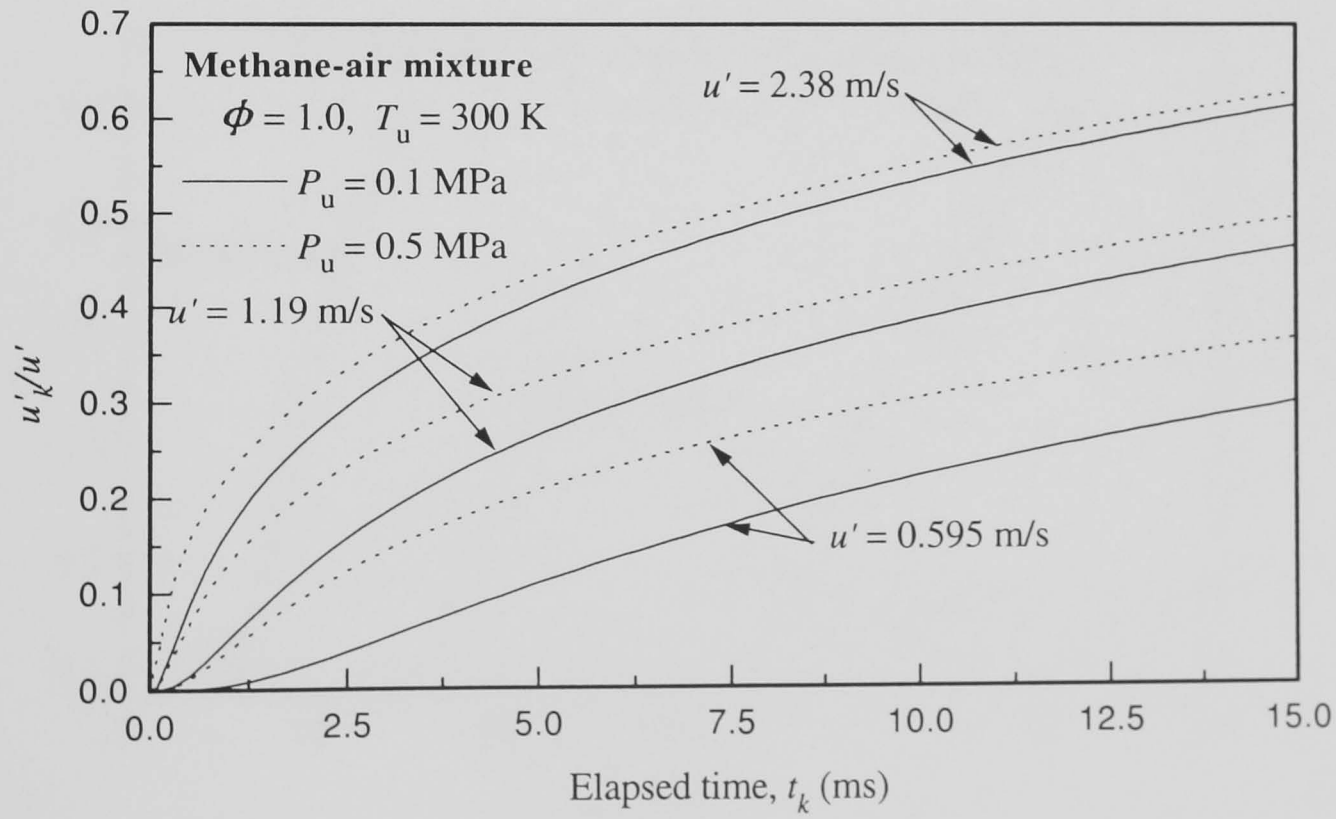

Fig. 6.19. Temporal development of the effective r.m.s. turbulent velocity for the initial conditions presented in Table 6.1

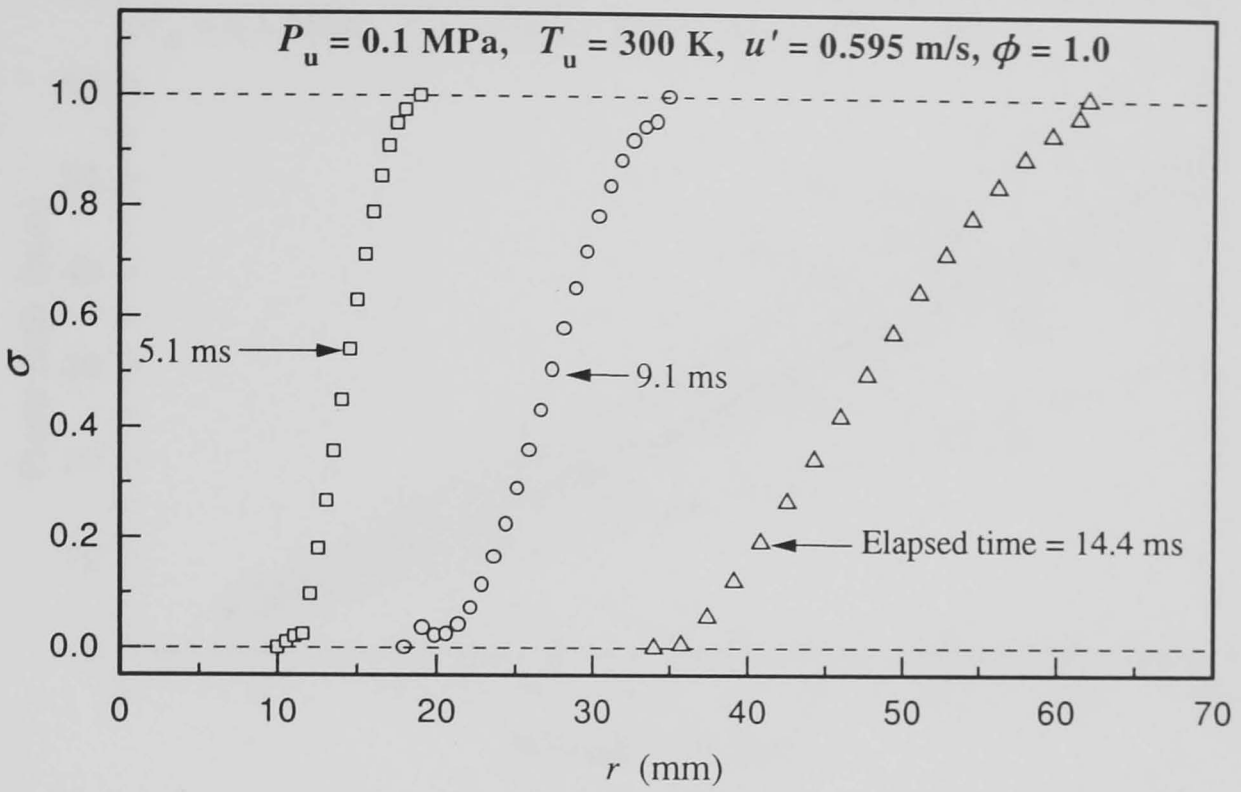

Fig. 6.20. Changes in σ, averaged for four different explosions, with elapsed time from ignition for stoichiometric methane-air mixtures at 0.1 MPa with $u' = 0.595$ m/s.

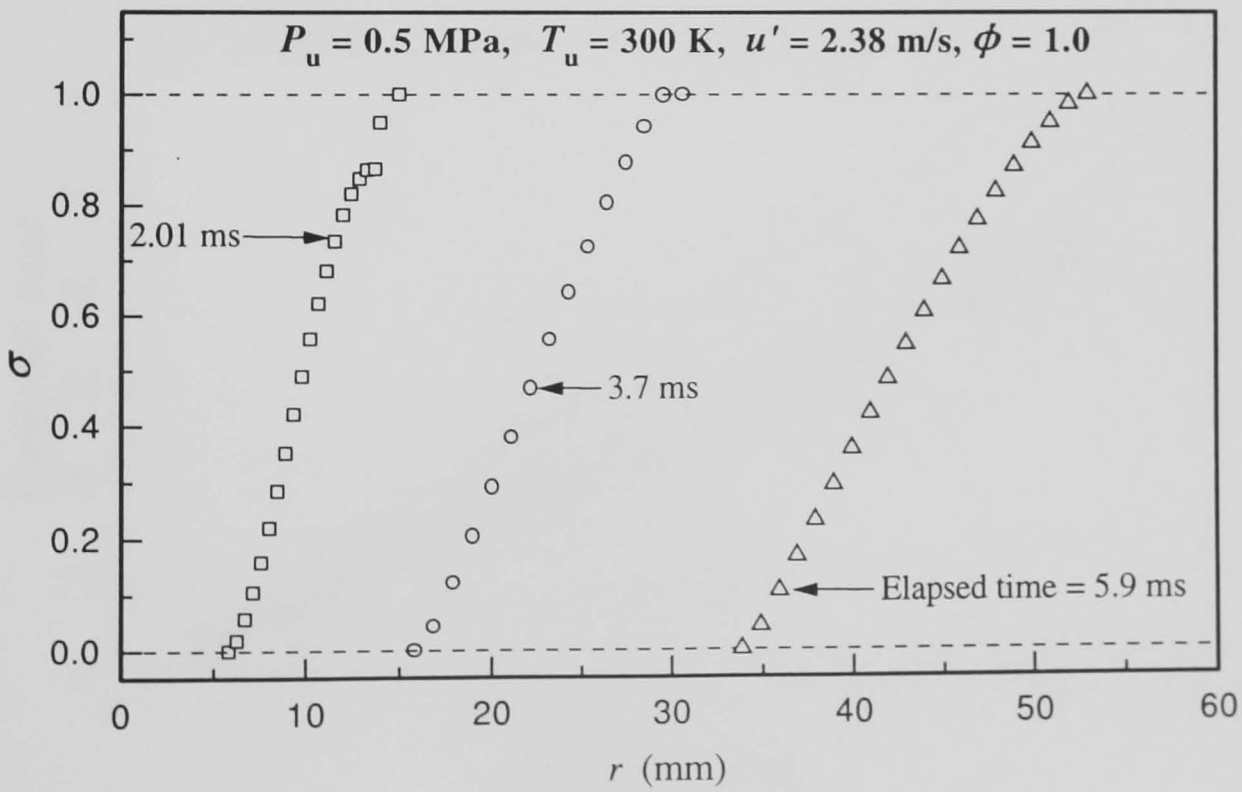

Fig. 6.21. Changes in σ, averaged for four different explosions, with elapsed time from ignition for stoichiometric methane-air mixtures at 0.5 MPa with $u' = 2.38$ m/s.

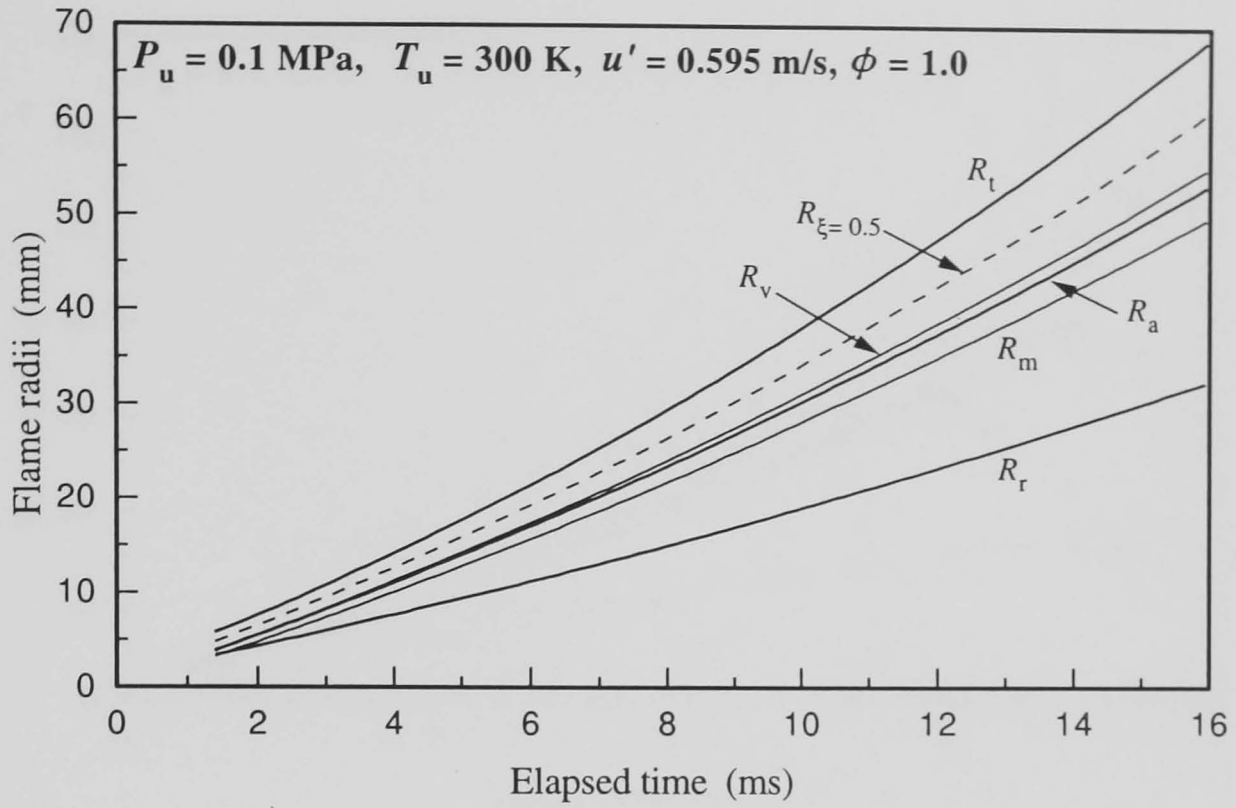

Fig. 6.22. Variation of various reference flame radii with elapsed time from ignition for stoichiometric methane-air mixture at 0.1 MPa with $u' = 0.595$ m/s.

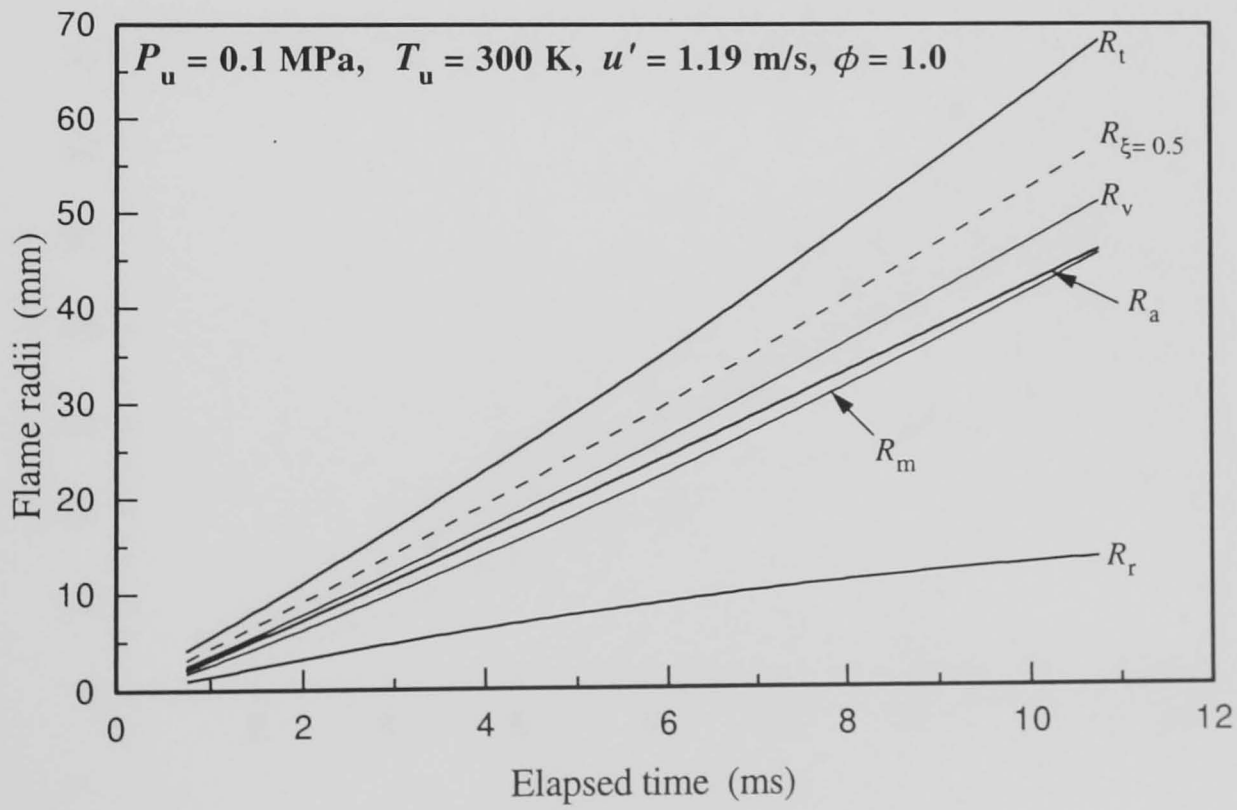

Fig. 6.23. Variation of various reference flame radii with elapsed time from ignition for stoichiometric methane-air mixture at 0.1 MPa with $u' = 1.19$ m/s.

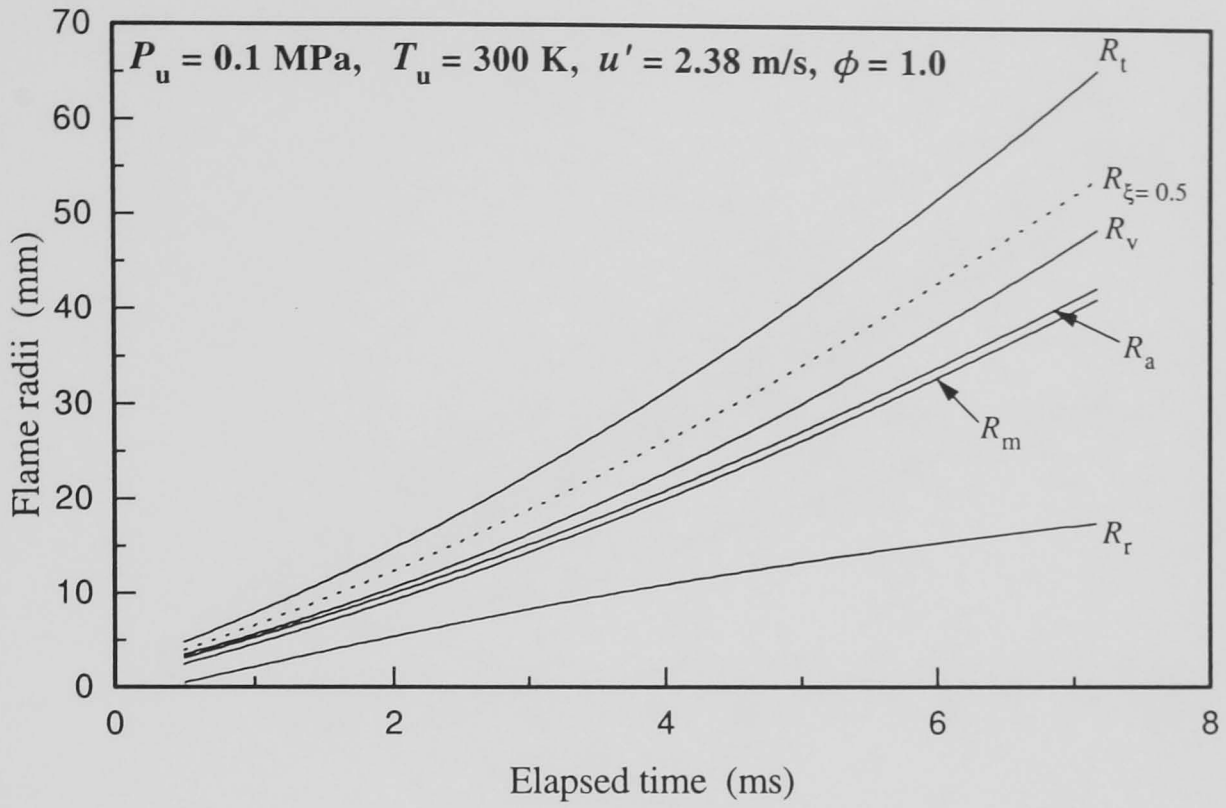

Fig. 6.24. Variation of various reference flame radii with elapsed time from ignition for stoichiometric methane-air mixture at 0.1 MPa with $u' = 2.38$ m/s.

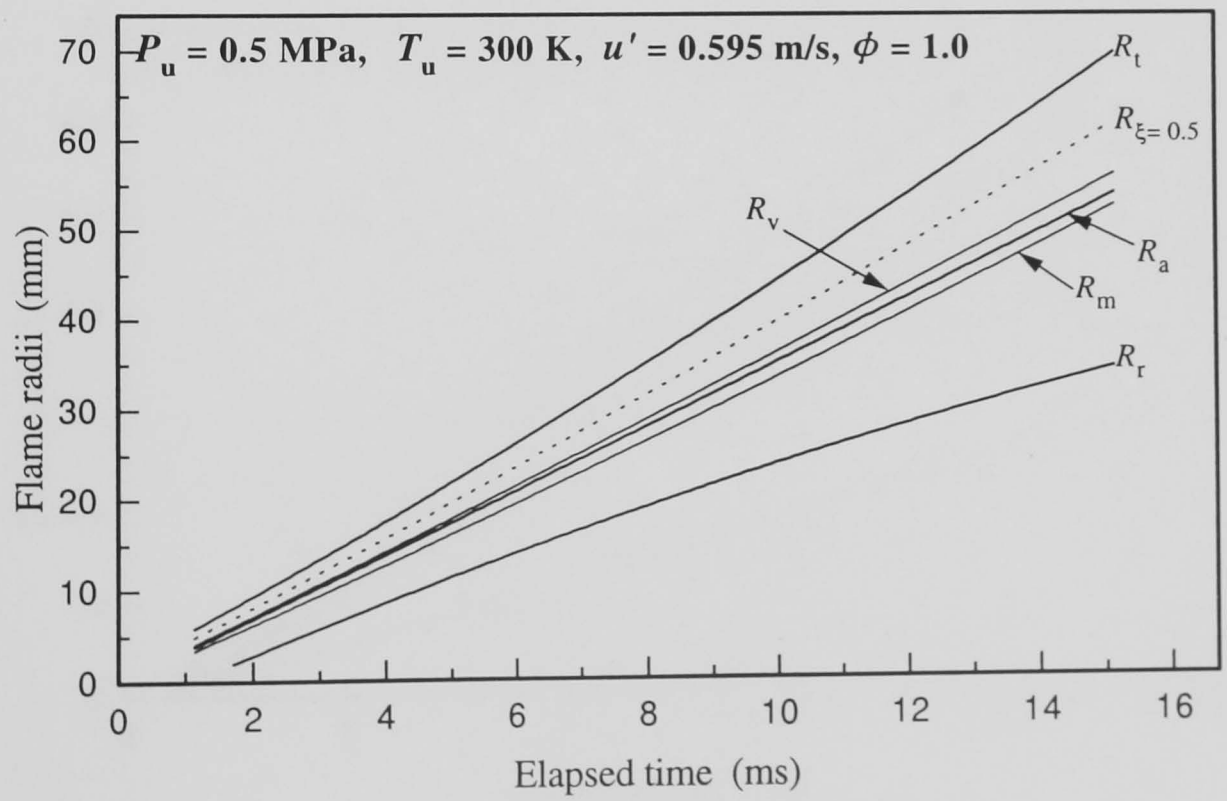

Fig. 6.25. Variation of various reference flame radii with elapsed time from ignition for stoichiometric methane-air mixture at 0.5 MPa with $u' = 0.595$ m/s.

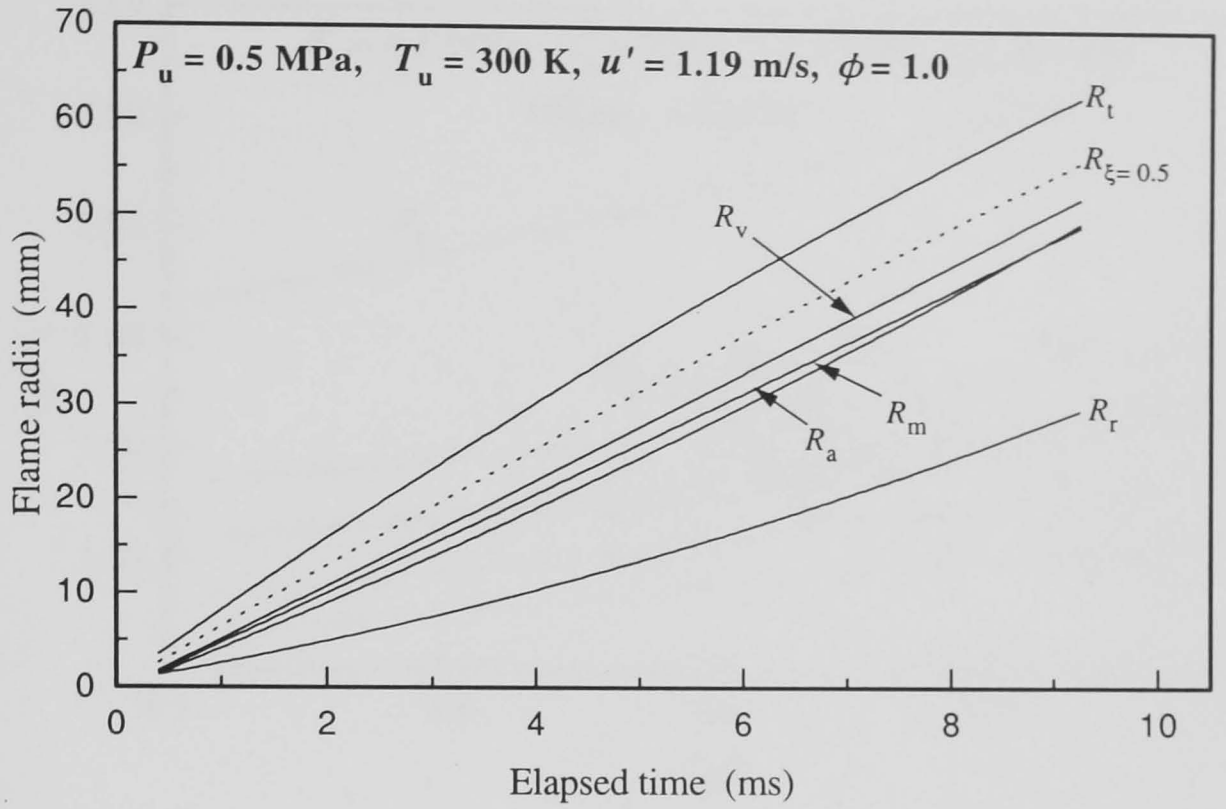

Fig. 6.26. Variation of various reference flame radii with elapsed time from ignition for stoichiometric methane-air mixture at 0.5 MPa with $u' = 1.19$ m/s.

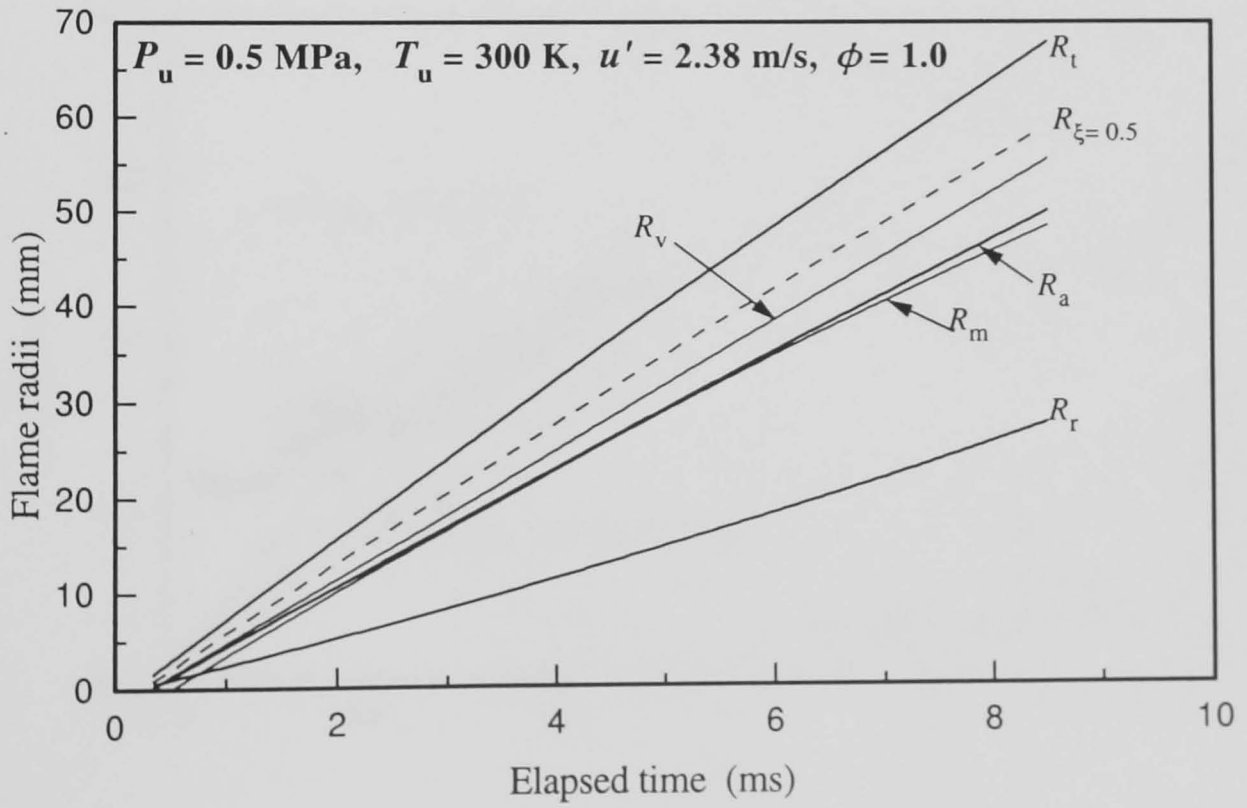

Fig. 6.27. Variation of various reference flame radii with elapsed time from ignition for stoichiometric methane-air mixture at 0.5 MPa with $u' = 2.38$ m/s.

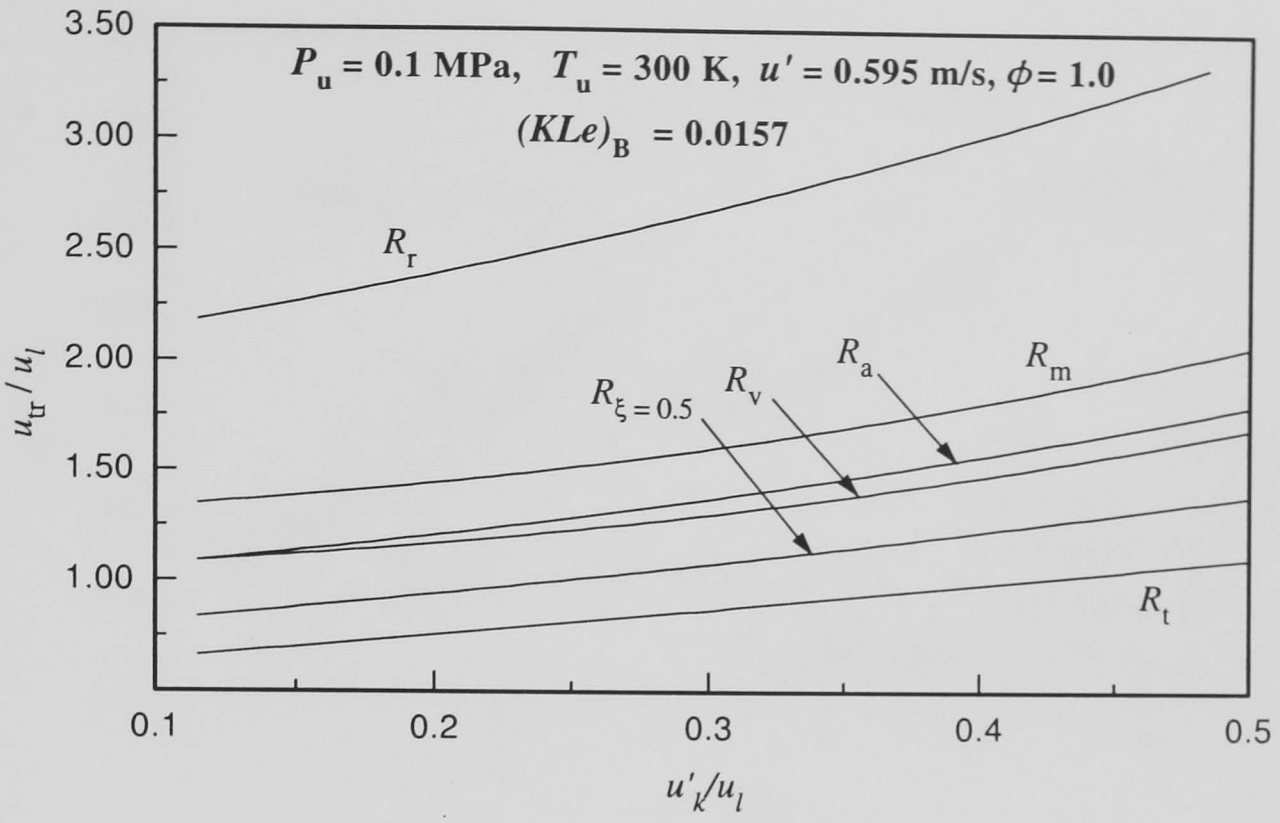

Fig. 6.28. Variation of $u_{\rm tr}/u_l$ with u'_k/u_l for different reference flame radii for stoichiometric methane-air mixture at 0.1 MPa with $u' = 0.595$ m/s.

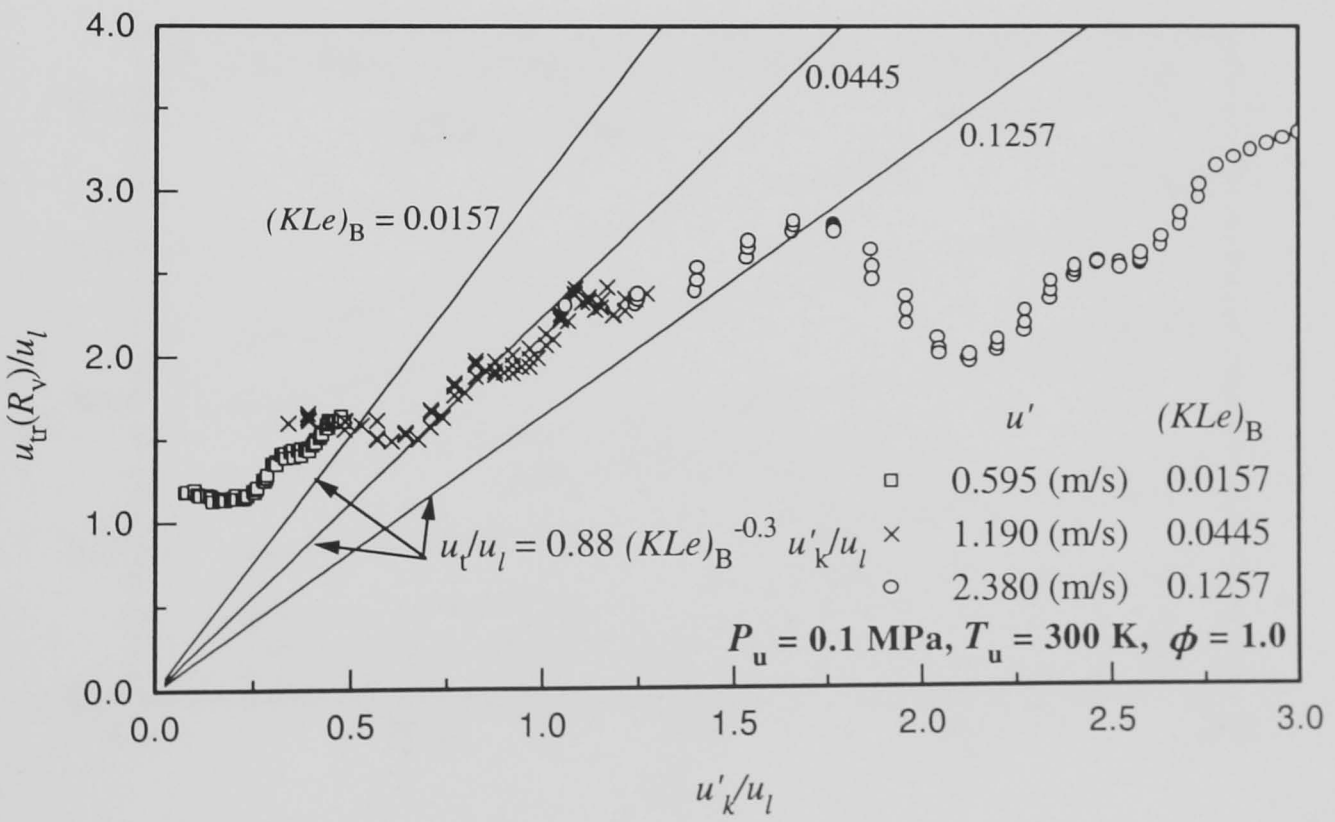

Fig. 6.29. Variation of $u_{\rm tr}(R_{\rm v})/u_l$ with u'_k/u_l for stoichiometric methane-air mixture at three r.m.s. turbulence velocities of $u' = 0.595$, 1.19 and 2.38 m/s at 0.1 MPa.

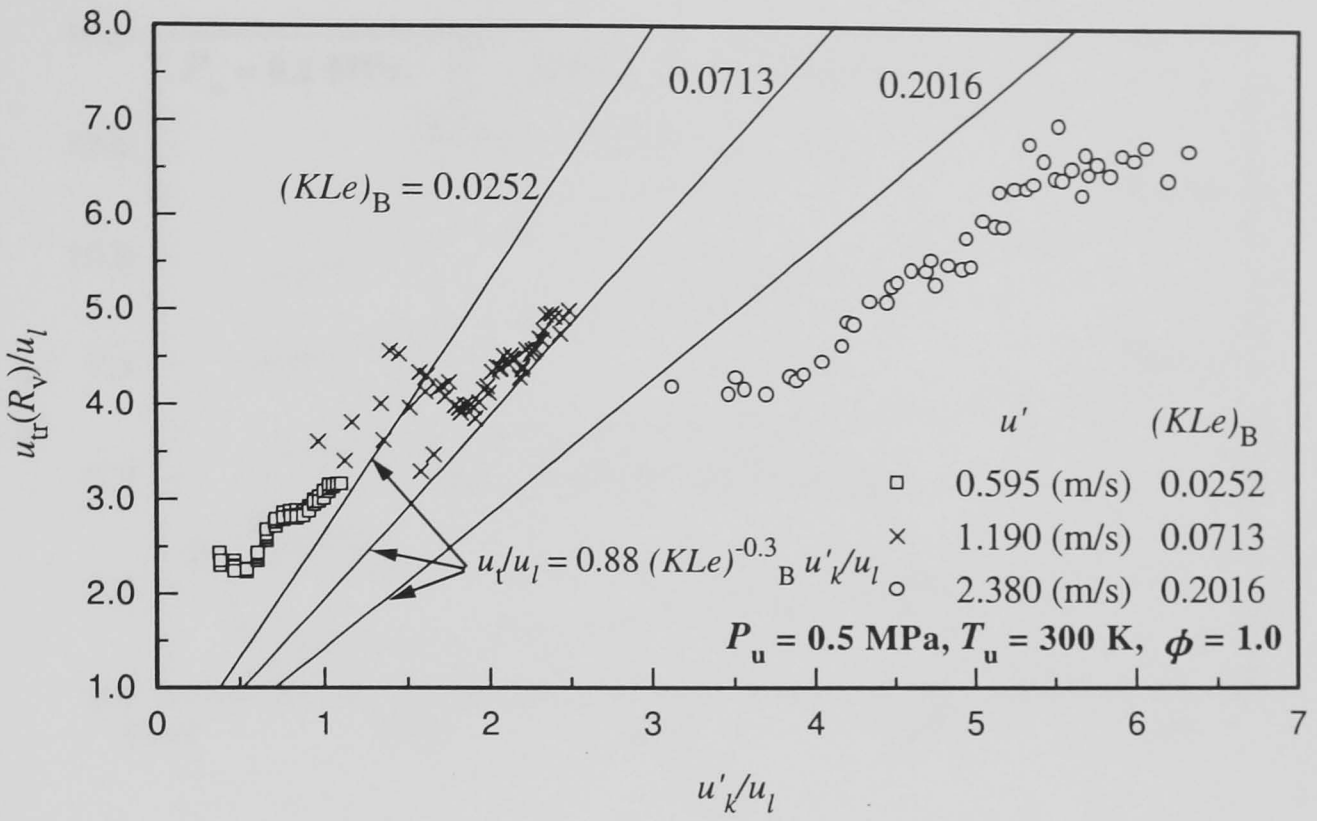

Fig. 6.30. Variation of $u_{\rm tr}(R_{\rm v})/u_l$ with u'_k/u_l for stoichiometric methane-air mixture at three r.m.s. turbulent velocities of $u' = 0.595$, 1.19 and 2.38 m/s at 0.5 MPa.

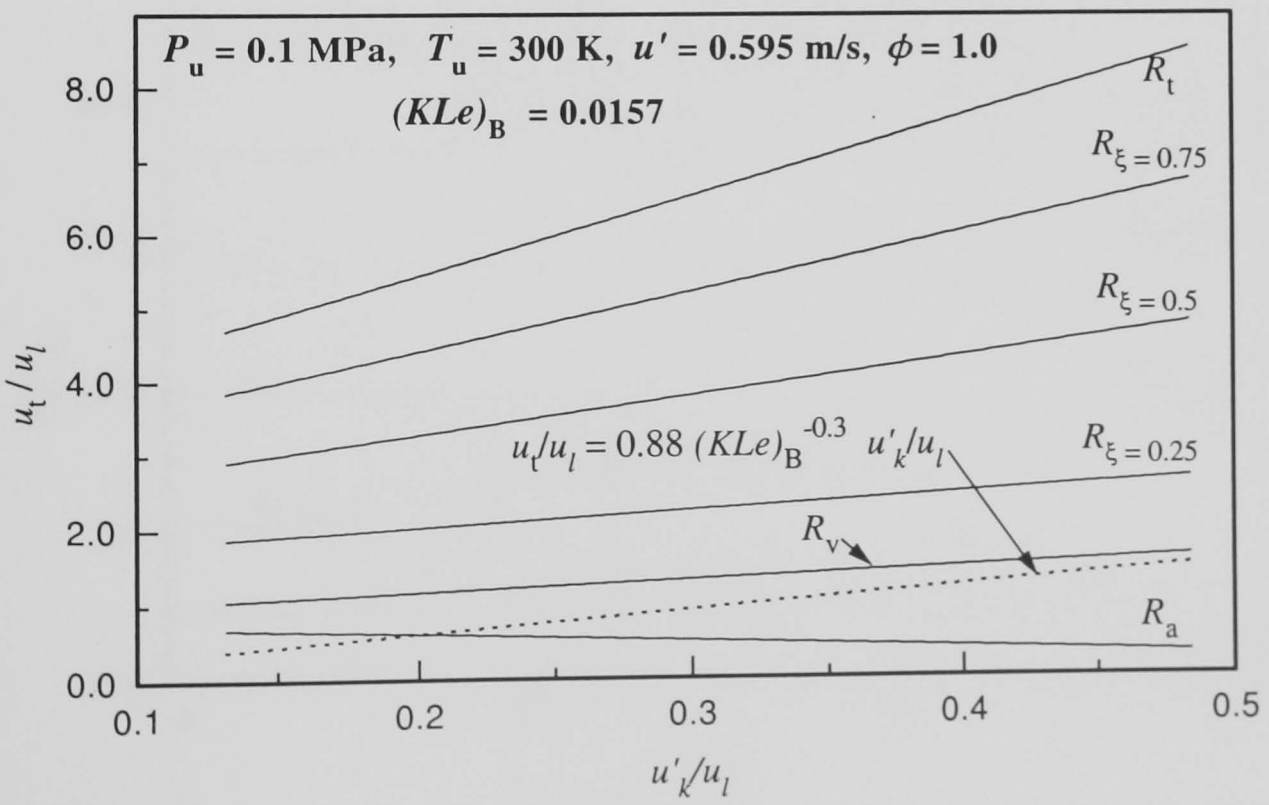

Fig. 6.31. Variation of $u_{\rm t}/u_l$ with u'_k/u_l for different reference flame radii for stoichiometric methane-air mixture at 0.1 MPa with $u' = 0.595$ m/s.

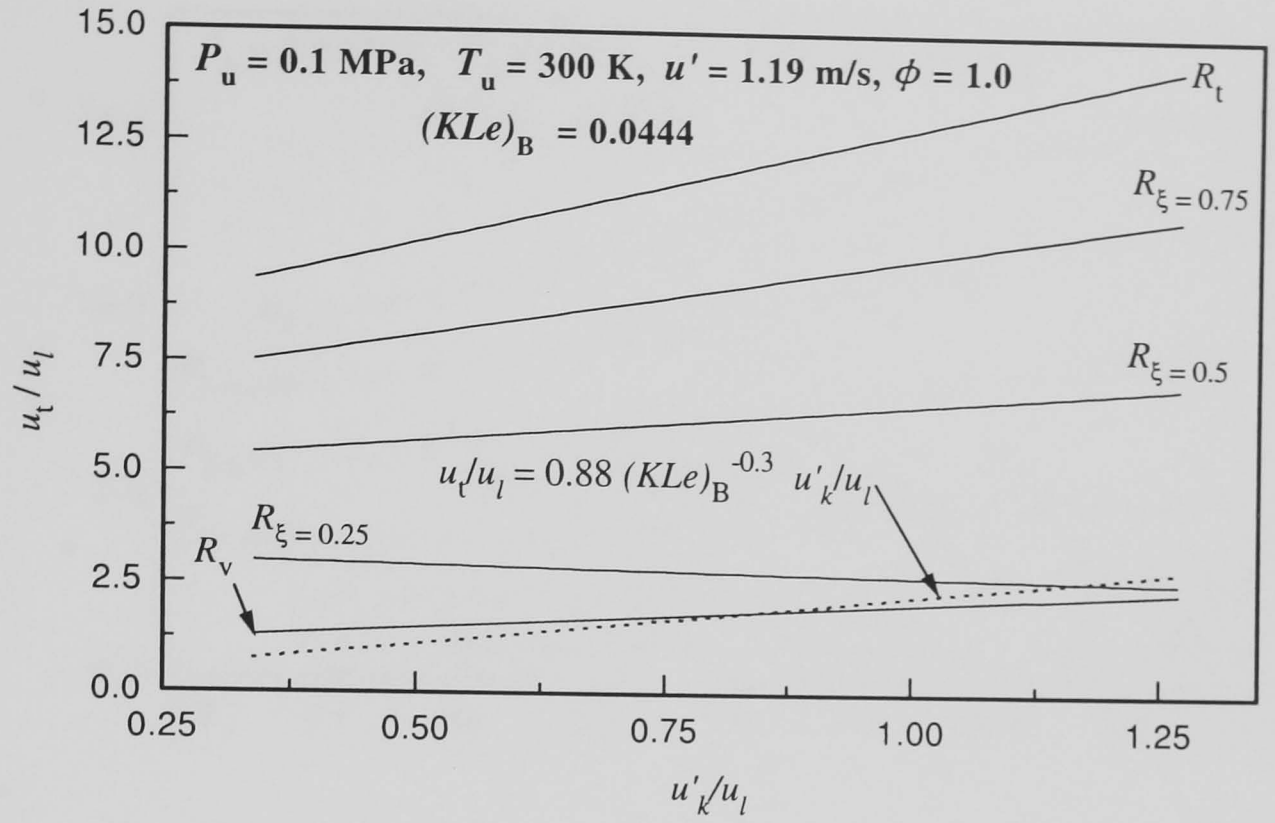

Fig. 6.32. Variation of u_t/u_l with u'_k/u_l for different reference flame radii for stoichiometric methane-air mixture at 0.1 MPa with $u' = 1.19$ m/s.

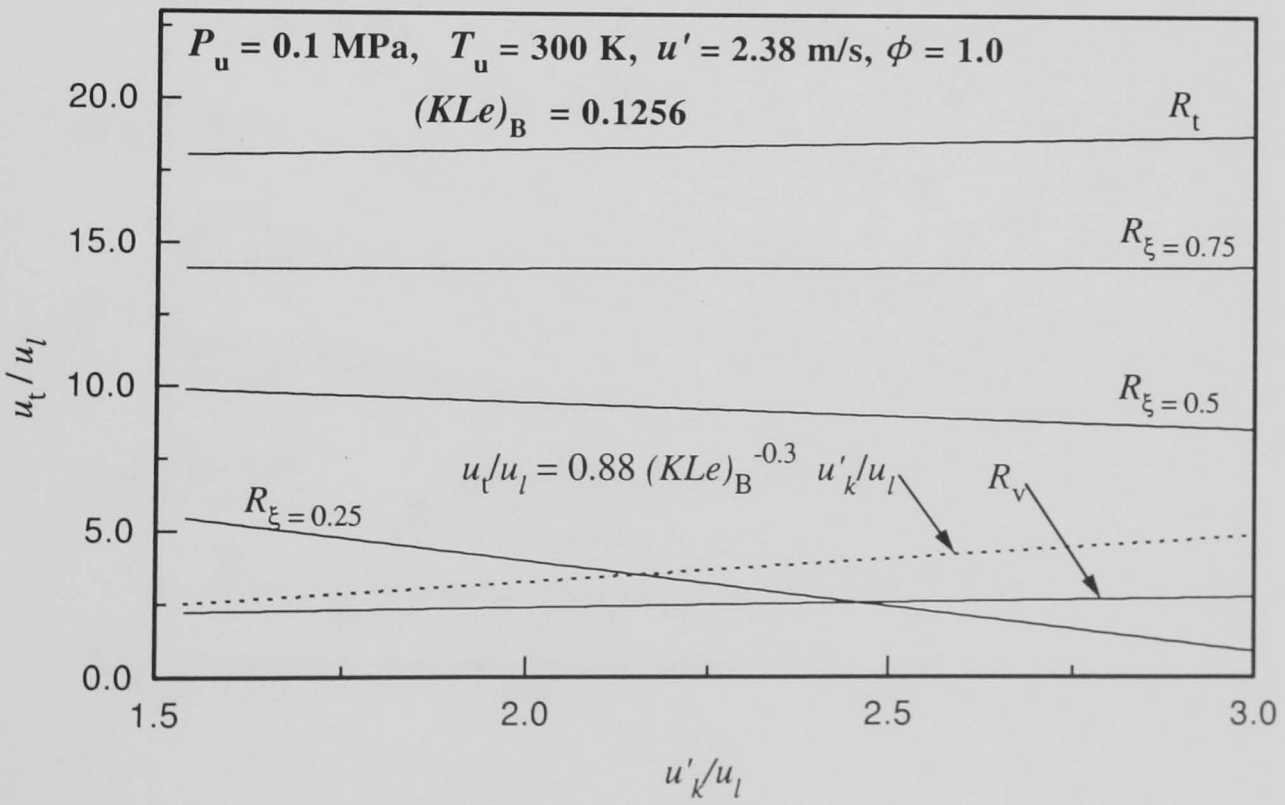

Fig. 6.33. Variation of u_t/u_l with u'_k/u_l for different reference flame radii for stoichiometric methane-air mixture at 0.1 MPa with $u' = 2.38$ m/s.

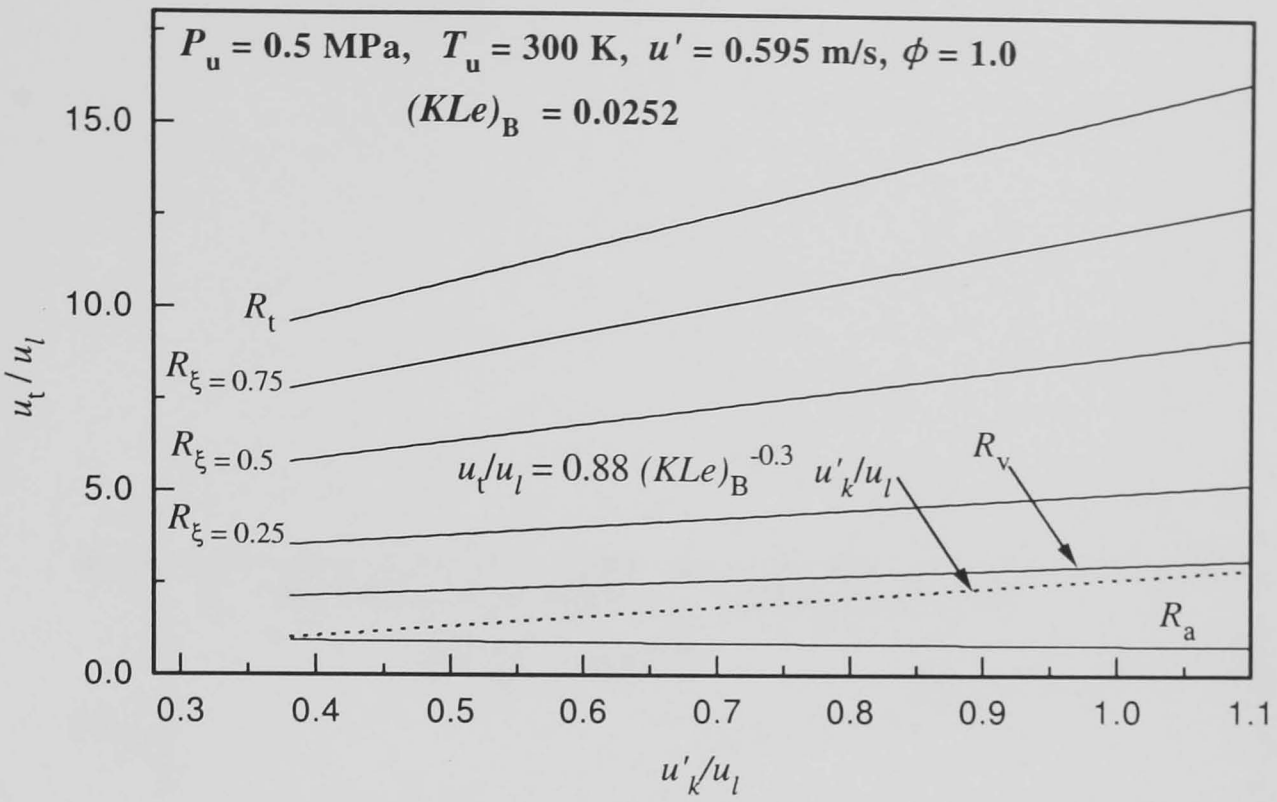

Fig. 6.34. Variation of u_t/u_l with u'_k/u_l for different reference flame radii for stoichiometric methane-air mixture at 0.5 MPa with $u' = 0.595$ m/s.

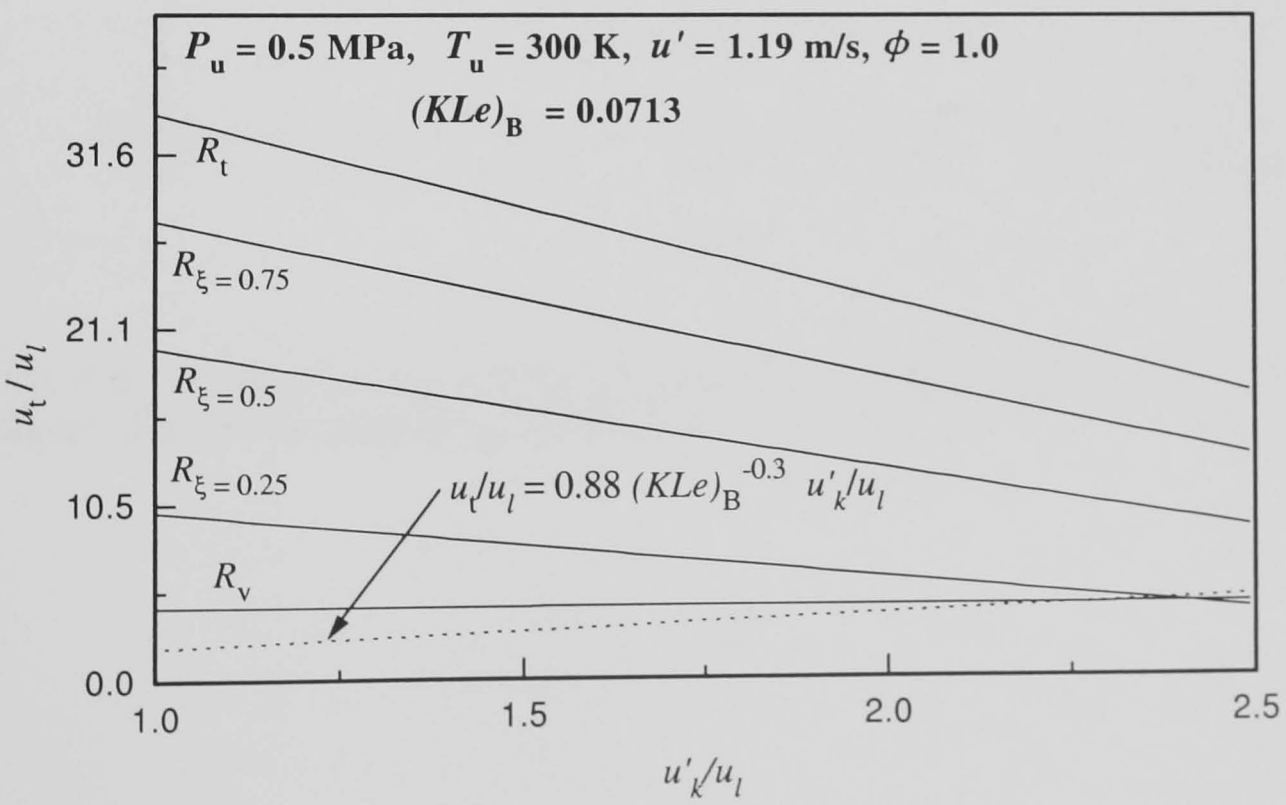

Fig. 6.35. Variation of u_t/u_l with u'_k/u_l for different reference flame radii for stoichiometric methane-air mixture at 0.5 MPa with $u' = 1.19$ m/s.

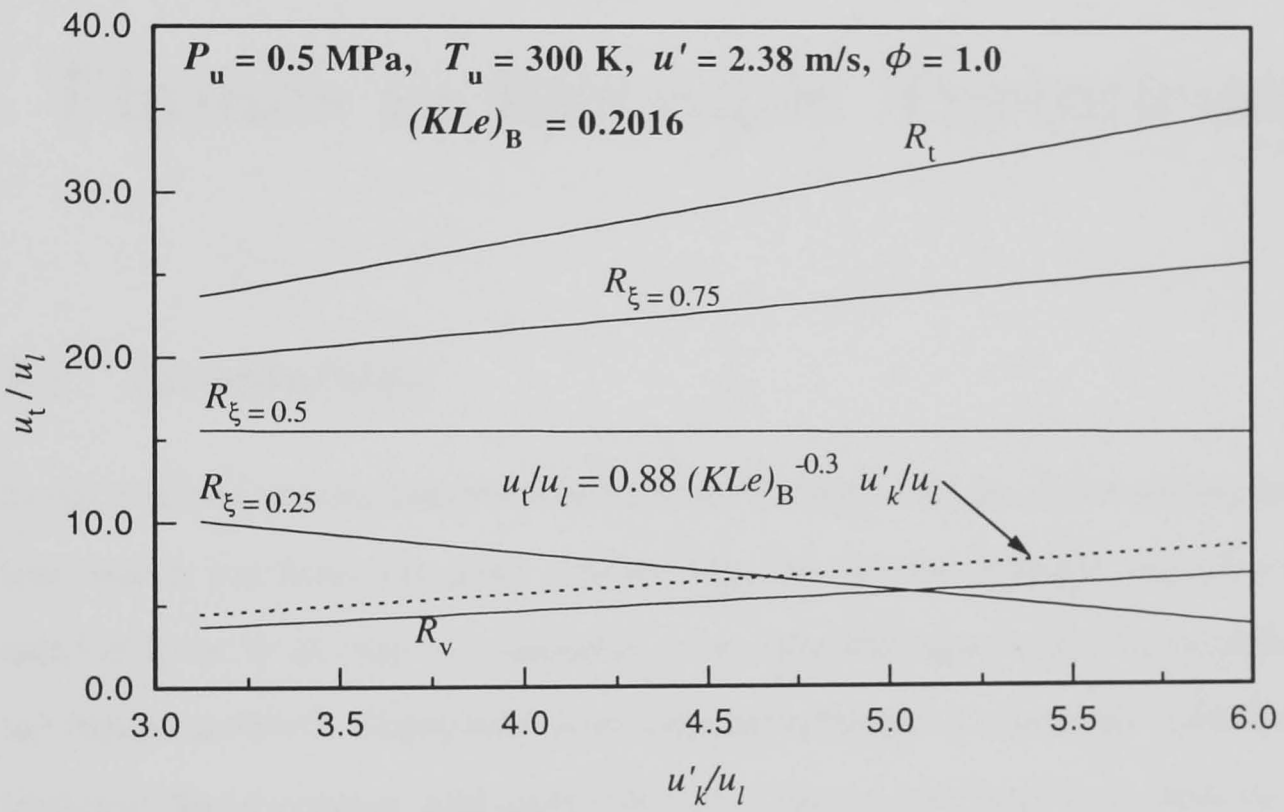

Fig. 6.36. Variation of u_t/u_l with u'_k/u_l for different reference flame radii for stoichiometric methane-air mixture at 0.5 MPa with $u' = 2.38$ m/s.

Chapter 7

The Curvature of Premixed Flames in Isotropic Turbulence

7.1 Introduction

In the wrinkled laminar flamelet regime, flame thickness and the characteristic chemical time within the flame are much smaller than the turbulence length and time scales, and the flame front may be considered as an interface separating cold reactants and the burned products. Using laser sheet imaging techniques it is possible to visualize the turbulent flame surfaces, and derive the curvatures of the flame front from the flame images. This reveals information about the response of the flame to the turbulent flow field and also gives insights into the influence of flame shape on flamelet burning.

Many computational studies (both two and three dimensional, with and without heat release) have derived the distributions of flame front curvature and studied its influence (Haworth and Poinsot 1992, Bray and Cant 1991, Shepherd and Ashurst 1992, Echekki and Chen 1996 and Rutland and Trouvé 1993). The ways in which the burn rate of a methane-air flame is affected by the curvature have been studied by Echekki and Chen (1996) by DNS with reduced chemistry. Curvature strongly influences the distribution of fast diffusing radicals such as H, the concentration of which increases

in regions of negative curvature, as a consequence of flame focusing. This results in a further increase in local displacement speed of the flame.

The chapter reports the studies of flame front curvature using laser sheet images and PMS and PLIF techniques. PLIF images are analysed to obtain flame curvatures of turbulent iso-octane-air flames, while PMS images are used to study methane-air flames. The sequence of PMS images also are analysed to show the effect of the developing flame front curvature.

7.2 Calculation of Flame front curvature

Analytically, flame front curvature, H, can be calculated from the flame coordinates, (x, y), from (Lee *et al.* 1992):

$$H = \frac{\frac{\mathrm{d}^2 y}{\mathrm{d}x^2}}{\left[1 + \left(\frac{\mathrm{d}y}{\mathrm{d}x}\right)^2\right]^{3/2}} \tag{7.1}$$

However, the use of an independent variable, s, has been reported by Lee *et al.* (1993) to improve this procedure, since the flame curvature can be analyzed regardless of the slope and complexities of the flame contour. Here, s, is the distance along the flame front from a fixed origin located on it. The curvature, H, is obtained from (Lee *et al.* 1993, Haworth and Poinsot 1992):

$$H = \left[\left(\frac{\mathrm{d}^2 x}{\mathrm{d}s^2}\right)^2 + \left(\frac{\mathrm{d}^2 y}{\mathrm{d}s^2}\right)^2\right]^{1/2} \tag{7.2}$$

The flame curvature is positive if the flame element is convex towards the reactant.

The flame coordinates obtained from digital images require some smoothing of the flame edge. In the present study, the Savitzky-Golay algorithm (Savitzky and Golay 1964, Press *et al.* 1992) is used for data smoothing and differentiation. This algorithm is briefly reported in Appendix B. Data smoothing and numerical differentiation are

performed by a program `savit.for`, written for the present study and embodying a subroutine `savgol.for` from Press *et al.* (1992). Shown in Fig. 7.1 are the raw flame coordinates and the smoothed values using this algorithm. The smoothing clearly reduces digital effects. Shown in Fig. 7.2 are the values of H for the input data of a digitized sine wave, in which the theoretically estimated values of H are shown by the solid line and the computed values, using the Savitzky-Golay algorithm, by symbols. Clearly, the algorithm estimates H quite accurately, although some values of H are slightly less than those estimated theoretically. Equispaced flame coordinates as required for `savit.for` were obtained by cubic spline interpolation of the raw flame coordinates using subroutine `spline.for` and `splint.for` from Press *et al.* (1992).

7.3 Estimation of Probability Density Function (pdf)

The probability density function of a random variable, u, is defined such that the probability of finding u between x and $x + \mathrm{d}x$ is $pdf(x)\mathrm{d}x$. The pdf is normalized to the condition (Frisch 1995):

$$\int pdf(x)\mathrm{d}x = 1. \tag{7.3}$$

Hence, its value is estimated from a probability distribution function, $F(x)$, as:

$$pdf(x) = \frac{\mathrm{d}F(x)}{\mathrm{d}x} \tag{7.4}$$

The probability distribution function, $F(x)$, is also a function of the the random variable, u, defined as (Kuo 1986):

$$F(x) \equiv \mathrm{Prob}\{u < x\} \tag{7.5}$$

$F(x)$ is always a real-valued, non-negative and non-decreasing function. It can be estimated from a given number of observations by calculating the number frequency in a number of bins and estimating the cumulative fraction up to x. Hence, the pdf is estimated by numerical differentiation of $F(x)$. The estimation of pdf of H for a

stoichiometric methane-air flame at an initial pressure of 0.1 MPa, with $u' = 0.595$ m/s, is shown in Fig. 7.3, where it is compared with a gaussian distribution.

7.4 Development of Curvature in Spherically Expanding Flame

The experimental conditions studied are summarized in Tables 7.1 and 7.2. The flames observed are not fully developed (§ 6.7). As a flame grows in size it is subjected to the influence of larger length scales of turbulence. Curvatures have been measured throughout this temporal development. Shown in Fig. 7.4 is the development of flame contours of a stoichiometric methane-air flame from ignition, with $u' = 0.595$ m/s. The persistence of a 'history' can be seen clearly, whereby features generated in the early development of the flame are still evident on the flame surface after as long as 15 ms. Shown in Fig. 7.5 are the pdfs of curvature, normalized by flame thickness, δ_l, $H\delta_l$, for the same flame with time. The pdfs spreads with the passage of time, with an increase in the variance, and remain symmetric about near-zero curvature.

From such flame curvature pdfs, it is possible to compute the positive, negative, and overall mean flame curvatures, $\langle H^+\delta_l \rangle$, $\langle H^-\delta_l \rangle$ and $\langle H\delta_l \rangle$. Shown in Fig. 7.6 are values of $\langle H^+\delta_l \rangle$, $\langle H^-\delta_l \rangle$ and $\langle H\delta_l \rangle$ plotted against time for four different explosions with $u' = 0.595$ m/s. The positive and negative values of curvature clearly increase with time, while the mean remains close to zero. Shown in Fig. 7.7 are the values of variance of nondimensional curvature, obtained from these four different explosions. It is evident from Figs. 7.6 and 7.7 that the curvature increases with time. However, this increase, associated with u'_k, is much less significant than that due to the increase in the overall turbulent r.m.s. velocity, u'. Hence, the global quantity of u' is used to identify the primary effect of turbulence on flame front curvature, rather than the developing value of u'_k.

7.5 Experimental Results

Results are presented for both the PMS and PLIF techniques. Because a pixel with PMS represents an actual distance of 0.32 mm and a pixel with PLIF represents one of 0.157 mm, the latter is more accurate. These resolutions are not comparable to the laminar flame thickness to guarantee the complete accuracy of the pdfs. Nevertheless, certain overall conclusions can be drawn.

Shown in Fig. 7.8 are the pdfs of curvature, from four different explosions, all found using the PMS technique for stoichiometric methane-air mixtures at an initial pressure of 0.1 MPa and initial temperature of 300 K, with $u' = 0.595$ m/s. The pdfs of curvature are nearly symmetrical with a gaussian distribution and a mean of small negative value. The four different explosions have consistent pdfs.

Figure 7.9 gives the pdfs of curvature for stoichiometric methane-air mixtures for three values of u', at an initial pressure of 0.1 MPa and initial temperature of 300 K. The pdfs are symmetric with respect to a very small negative mean value. The width (variance) increased with increase in u', commensurate with increased flame wrinkling. The mean value approaches zero with increase in u'.

Figure. 7.10 displays four representative flame edges for stoichiometric iso-octane-air mixtures at increasing values of u', this time using the PLIF technique. The flames become increasingly wrinkled as the flame speed is increased. At high levels of turbulence long deep cuts of unburned gas can be observed, possibly the result of vortex tubes burning in the flame front, in which case high curvature would be present in a plane normal to the sheet (Shepherd and Ashurst 1992). The pdfs of curvature for each value of u' are commensurate with Fig. 7.10 and are shown in Fig. 7.11. Again, as u' increases the pdfs are broadened and the probability of a zero or near zero curvature decreases, as for the methane-air mixtures. The effect of u' in dispersing the flame front curvature pdfs is again clearly revealed.

A similar effect of u' on curvature pdfs is observed at 0.5 MPa, as shown in Fig. 7.12, where pdfs for stoichiometric methane-air mixtures using PMS at three values of u' are plotted. Again, the pdfs are symmetric with respect to a very small negative mean value, while the width (variance) increased with increase in u'. However, the increase in the variance in not as marked as for the explosions at 0.1 MPa.

The influences of pressure and equivalence ratio on the curvature pdfs are compared in Fig. 7.13 for methane-air mixtures using PMS. The pdfs of normalized curvature are displayed for stoichiometric methane-air mixtures at both 0.1 MPa and 0.5 MPa initial pressure, and also for a lean ($\phi = 0.8$) methane-air mixture at 0.1 MPa initial pressure. In all the cases the initial temperature is 300 K. Here, nondimensional pdfs are symmetric with respect to a very small negative value. However, the flame at 0.5 MPa has the lowest variance. Values of Markstein number, Ma_{sr}, are also shown for each condition.

Figure 7.14 shows the flame edges of stoichiometric, rich and lean iso-octane-air flames obtained using PLIF at 0.1 and 0.5 MPa with $u' = 1.19$ m/s. The pdfs of curvature are shown in Fig. 7.15. That for stoichiometric iso-octane-air flame at 0.5 MPa has the lowest variance, similar to the methane-air flame at 0.5 MPa, in Fig. 7.13. For 0.1 MPa flames, curvature pdf of the stoichiometric flame has the lowest variance. Shown in Fig. 7.16 are curvature pdfs obtained from PLIF for three different iso-octane-air equivalence ratios at 0.1 MPa and with $u' = 0.595$ m/s. Values of Ma_{sr} are also given on these two figures.

7.6 Discussion

There are many factors that influence the pdf of curvature. In so far as this pdf is a measure of the flame wrinkling, and hence of turbulent burning velocity, it might by anticipated that, in dimensionless terms, as with u_t/u_l, it is affected by the flame wrinkling factor u'_k/u_l and also the product of KMa_{sr}. Here, K is the Karlovitz stretch factor and is discussed in Chapter 6. It is difficult to isolate these variables and study

each one separately. The influence of u'_k/u_l seem to be clearly revealed in Figs. 7.9, 7.11 and 7.12, which show an increasing variance of $H\delta_l$ as u'_k/u_l is increased. The increase in the flame wrinkling with increasing turbulence is to be anticipated. As other researches have also found the pdf is slightly skewed towards negative values (Shepherd and Ashurst 1992, Haworth and Poinsot 1992 and Rutland and Trouvé 1993).

The influence of $Ma_{\rm sr}$ is less clear. This parameter varies with equivalence ratio and pressure, as does also the pdf of $H\delta_l$. A complicating factor is that δ_l has been given throughout by ν/u_l. This expression is simplistic, with the result that errors in it create errors in $H\delta_l$. This is perhaps most serious for the pressure changes. In addition, because of the limited spatial resolution at high pressure, where δ_l is smaller the higher values of curvature may not be resolved accurately. This may contribute to the more peaked pdfs that occur at high pressure in Figs. 7.13, 7.15 and 7.16.

To reduce this effect it is useful to examine the influence of $Ma_{\rm sr}$ at constant pressure. A consistent trend in Figs. 7.13, 7.15 and 7.16, is that for the same pressure, the lowest values of $Ma_{\rm sr}$ is always associated with the greatest variance of the pdf.

This increase in variance of $H\delta_l$ as $Ma_{\rm sr}$ decreases might be anticipated, because $H\delta_l$ is inversely proportional to the localized Peclet number. When the curvature is small the flame is less stable and this is particularly so at low values of $Ma_{\rm sr}$. That is to say, such curvatures cannot be stabilized and the variance of $H\delta_l$ will increase. This effect will be more marked, the smaller the value of $Ma_{\rm sr}$ and this is observed. It is to be noted that the value of $H\delta_l$ corresponding to $(Pe_{\rm cl})^{-1}$ or the smallest normalized cell curvatures is quite small.

Table 7.1. Summary of results for methane-air data obtained using PMS imaging at an initial temperature of 300K.

Expt. ID.	P_u (MPa)	ϕ	u_l (m/s)	δ_l (mm)	Ma_{sr}	u' (m/s)	λ (mm)	K	$\overline{H\delta_l}$	var$(H\delta_l)$
M01	0.1	1.0	0.36	0.0443	4.1	0.595	2.93	0.025	-0.0003	0.0104
M02	0.1	1.0	0.36	0.0443	4.1	0.595	2.93	0.025	0.0000	0.0096
M03	0.1	1.0	0.36	0.0443	4.1	0.595	2.93	0.025	-0.0003	0.0092
M04	0.1	1.0	0.36	0.0443	4.1	0.595	2.93	0.025	0.0001	0.0099
M06	0.1	1.0	0.36	0.0443	4.1	1.19	2.07	0.071	-0.0002	0.0127
M09	0.1	1.0	0.36	0.0443	4.1	1.19	2.07	0.071	0.0001	0.0110
M10	0.1	1.0	0.36	0.0443	4.1	1.19	2.07	0.071	0.0001	0.0115
M12	0.1	1.0	0.36	0.0443	4.1	1.19	2.07	0.071	-0.0001	0.0120
M13	0.1	1.0	0.36	0.0443	4.1	2.38	1.46	0.200	-0.0003	0.0170
M15	0.1	1.0	0.36	0.0443	4.1	2.38	1.46	0.200	0.0000	0.0174
M16	0.1	1.0	0.36	0.0443	4.1	2.38	1.46	0.200	-0.0003	0.0158
M18	0.1	1.0	0.36	0.0443	4.1	2.38	1.46	0.200	-0.0005	0.0153
M52	0.5	1.0	0.19	0.0168	-1.4	0.595	1.31	0.040	0.0001	0.0065
M53	0.5	1.0	0.19	0.0168	-1.4	0.595	1.31	0.040	0.0000	0.0067
M55	0.5	1.0	0.19	0.0168	-1.4	0.595	1.31	0.040	-0.0001	0.0064
M56	0.5	1.0	0.19	0.0168	-1.4	0.595	1.31	0.040	0.0001	0.0059
M59	0.5	1.0	0.19	0.0168	-1.4	1.19	0.93	0.113	0.0002	0.0055
M67	0.5	1.0	0.19	0.0168	-1.4	1.19	0.93	0.113	0.0000	0.0067
M68	0.5	1.0	0.19	0.0168	-1.4	1.19	0.93	0.113	0.0001	0.0065
M69	0.5	1.0	0.19	0.0168	-1.4	1.19	0.93	0.113	0.0000	0.0064
M72	0.5	1.0	0.19	0.0168	-1.4	2.38	0.65	0.321	-0.0002	0.0069
M73	0.5	1.0	0.19	0.0168	-1.4	2.38	0.65	0.321	0.0000	0.0070
M74	0.5	1.0	0.19	0.0168	-1.4	2.38	0.65	0.321	-0.0001	0.0076
M77	0.5	1.0	0.19	0.0168	2.9	2.38	0.65	0.321	0.0001	0.0072
M22	0.1	0.8	0.259	0.0615	2.9	0.595	2.93	0.048	0.0000	0.0152
M23	0.1	0.8	0.259	0.0615	2.9	0.595	2.93	0.048	-0.0005	0.0169
M24	0.1	0.8	0.259	0.0615	2.9	0.595	2.93	0.048	0.0004	0.0158
M25	0.1	0.8	0.259	0.0615	2.9	0.595	2.93	0.048	0.0000	0.0155

Table 7.2. Summary of results for iso-octante-air data obtained using PLIF imaging at an initial temperature of 358K.

Expt. ID.	P_u (MPa)	ϕ	u_l (m/s)	δ_l (mm)	Ma_{sr}	u' (m/s)	λ (mm)	K	$\overline{H\delta_l}$	var$(H\delta_l)$
L582	0.1	1	0.45	0.0438	6	0.595	3.25	0.018	-0.0007	0.0099
L583	0.1	1	0.45	0.0438	6	0.595	3.25	0.018	-0.0002	0.0111
L584	0.1	1	0.45	0.0438	6	0.595	3.25	0.018	0.0000	0.0146
L587	0.1	1	0.45	0.0438	6	1.19	2.30	0.050	0.0029	0.0201
L588	0.1	1	0.45	0.0438	6	1.19	2.30	0.050	-0.0002	0.0187
L589	0.1	1	0.45	0.0438	6	1.19	2.30	0.050	0.0001	0.0201
L590	0.1	1	0.45	0.0438	6	3.57	1.33	0.261	-0.0001	0.0263
L591	0.1	1	0.45	0.0438	6	3.57	1.33	0.261	-0.0007	0.0250
L592	0.1	1	0.45	0.0438	6	3.57	1.33	0.261	-0.0020	0.0276
L593	0.1	1	0.45	0.0438	6	3.57	1.33	0.261	-0.0002	0.0254
L595	0.1	1	0.45	0.0438	6	5.95	1.03	0.562	-0.0026	0.0339
L596	0.1	1	0.45	0.0438	6	5.95	1.03	0.562	-0.0009	0.0306
L597	0.1	1	0.45	0.0438	6	5.95	1.03	0.562	0.0011	0.0308
L702	0.5	1	0.32	0.0123	3	1.19	1.03	0.044	-0.0001	0.0096
L703	0.5	1	0.32	0.0123	3	1.19	1.03	0.044	0.0003	0.0093
L704	0.5	1	0.32	0.0123	3	1.19	1.03	0.044	0.0001	0.0092
L707	0.5	1	0.32	0.0123	3	3.57	0.59	0.231	-0.0002	0.0106
L708	0.5	1	0.32	0.0123	3	3.57	0.59	0.231	-0.0002	0.0100
L709	0.5	1	0.32	0.0123	3	3.57	0.59	0.231	0.0001	0.0098
L553	0.1	0.75	0.38	0.0530	13	0.595	3.29	0.025	0.0018	0.0181
L554	0.1	0.75	0.38	0.0530	13	0.595	3.29	0.025	0.0007	0.0172
L555	0.1	0.75	0.38	0.0530	13	0.595	3.29	0.025	-0.0011	0.0175
L558	0.1	0.75	0.38	0.0530	13	1.19	2.33	0.071	0.0000	0.0229
L560	0.1	0.75	0.38	0.0530	13	1.19	2.33	0.071	0.0009	0.0223
L562	0.1	0.75	0.38	0.0530	13	3.57	1.34	0.371	-0.0035	0.0295
L710	0.5	0.75	0.23	0.0175	4	1.19	1.04	0.087	-0.0028	0.0118
L711	0.5	0.75	0.23	0.0175	4	1.19	1.04	0.087	0.0000	0.0096
L712	0.5	0.75	0.23	0.0175	4	1.19	1.04	0.087	0.0004	0.0122
L418	0.1	1.4	0.32	0.0595	-1	0.595	3.20	0.035	-0.0002	0.0223
L419	0.1	1.4	0.32	0.0595	-1	0.595	3.20	0.035	-0.0015	0.0247
L422	0.1	1.4	0.32	0.0595	-1	1.19	2.26	0.098	0.0003	0.0309

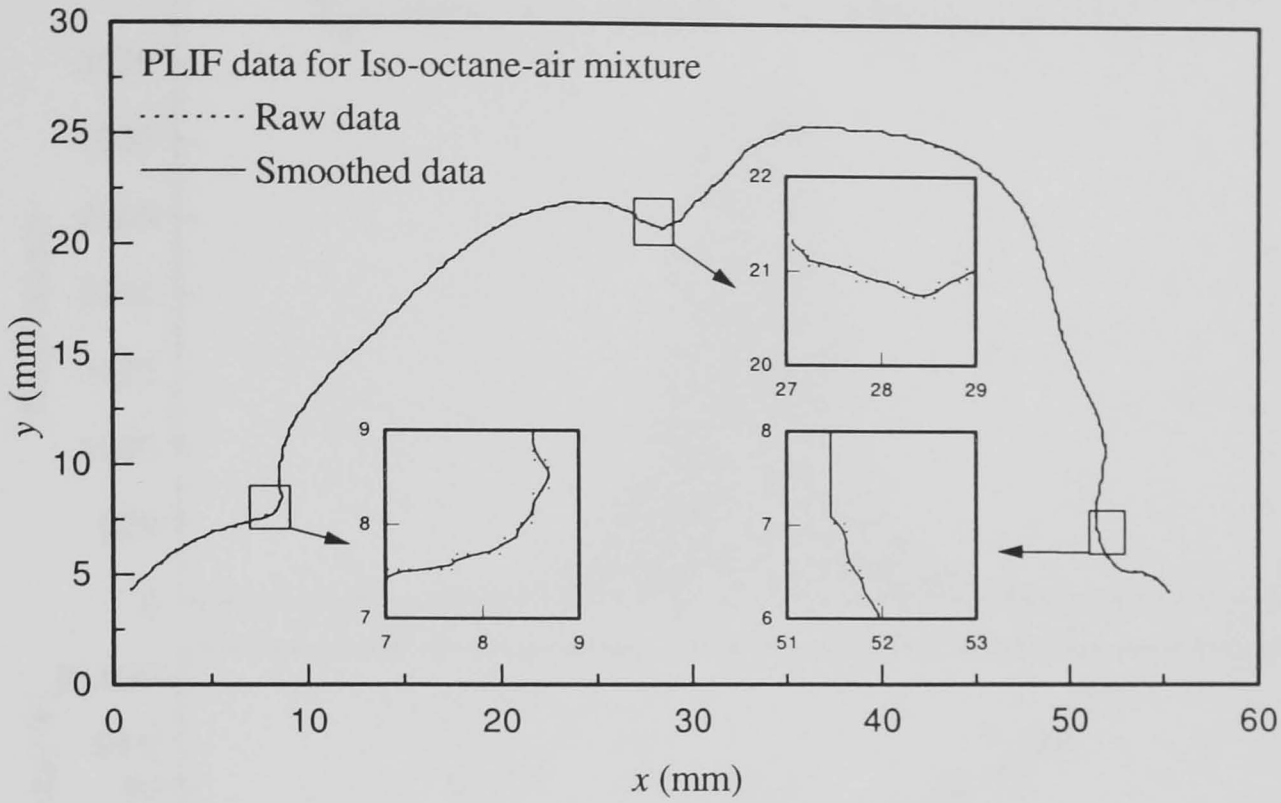

Fig. 7.1. An illustration of the smoothing performed by Savitzky-Golay algorithm on a digitized flame edge.

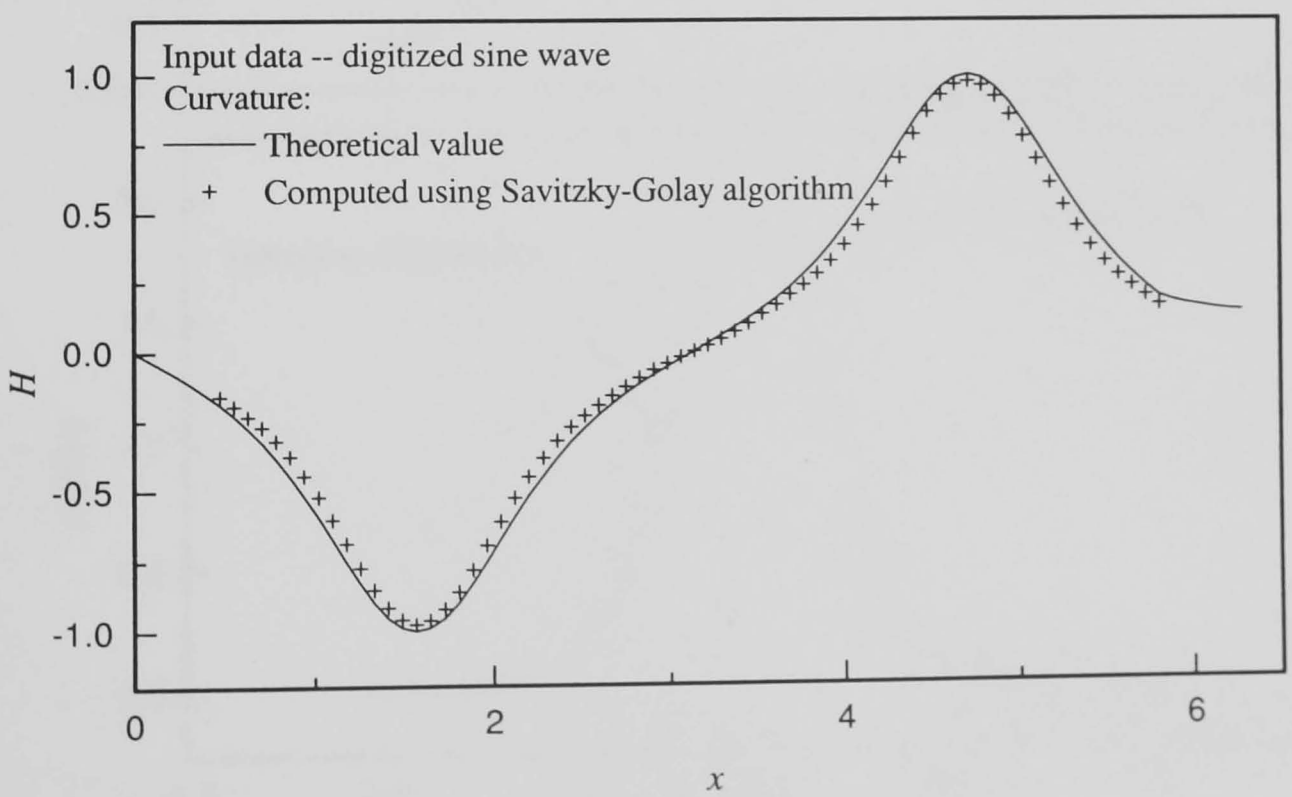

Fig. 7.2. An illustration of the estimation of H using Savitzky-Golay algorithm for a digitized sine wave.

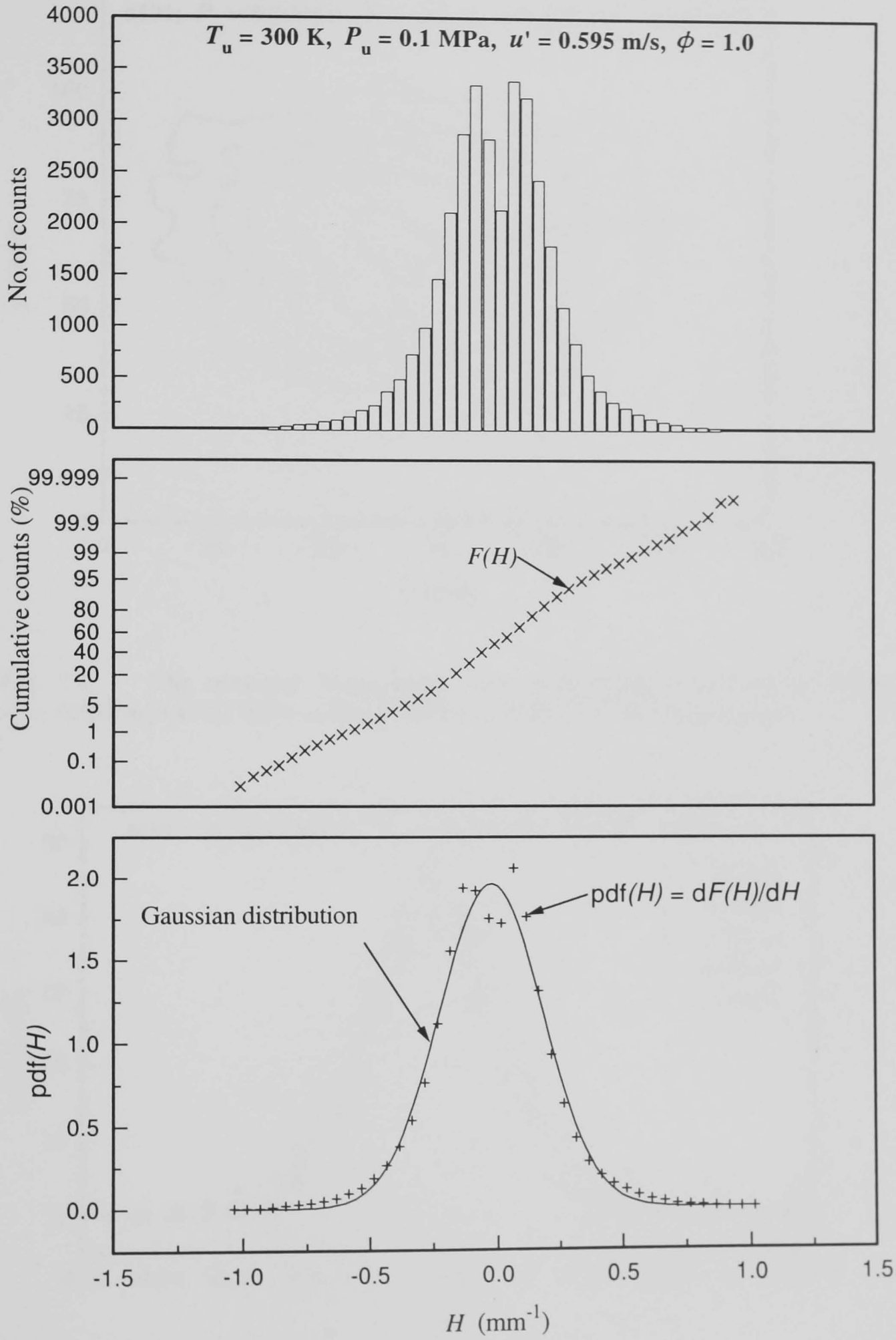

Fig. 7.3. An illustration of the estimation of pdf of curvature.

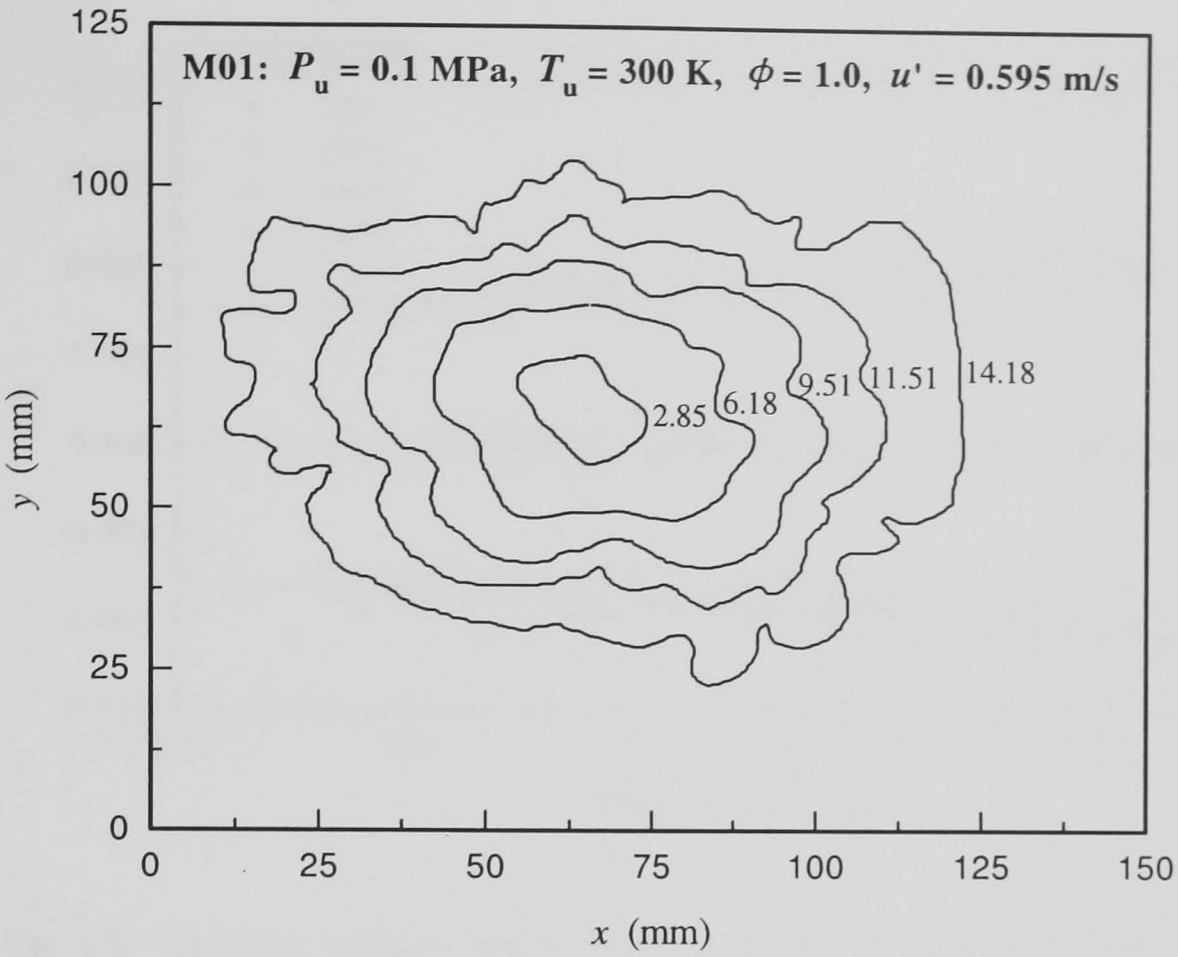

Fig. 7.4. The temporal development of a stoichiometric methane-air flame at $u' = 0.595$ m/s at 0.1 MPa initial pressure and 300 K initial temperature.

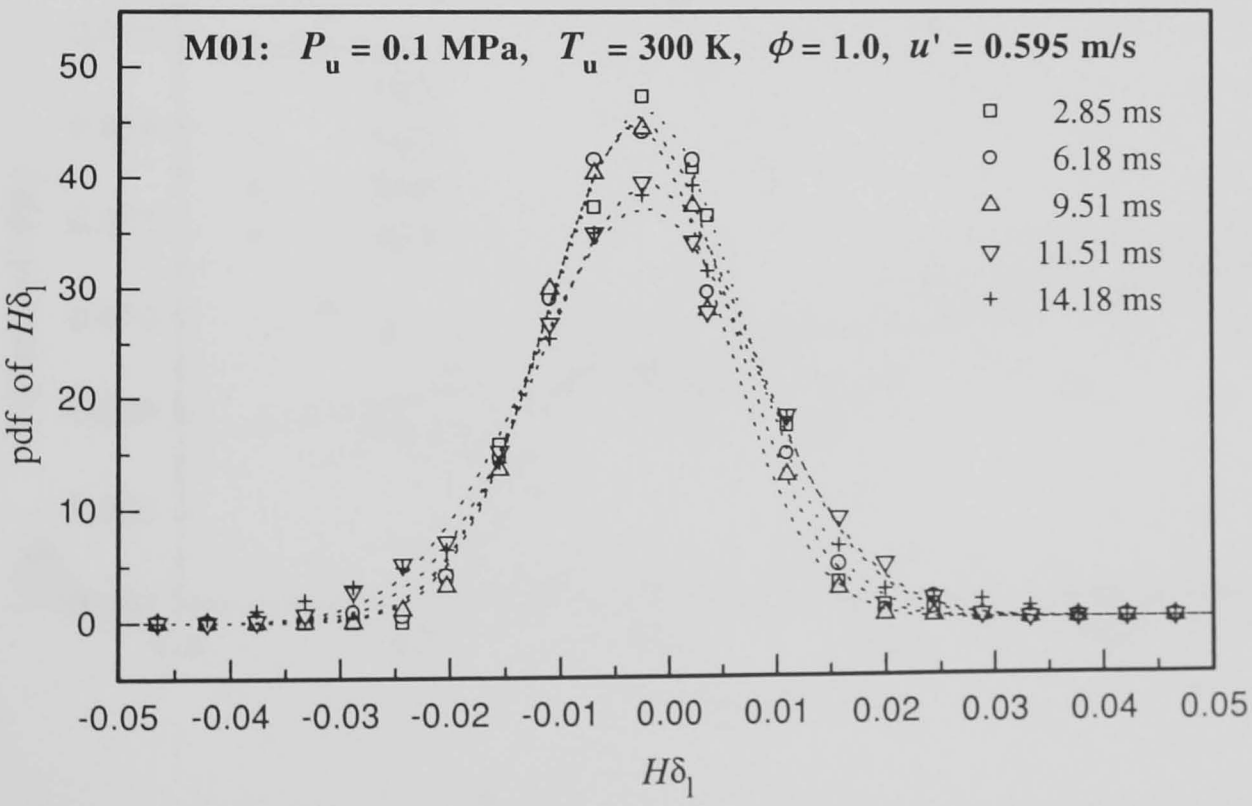

Fig. 7.5. Curvature pdfs for a developing stoichiometric methane-air flame at $u' = 0.595$ m/s at 0.1 MPa initial pressure and 300 K initial temperature.

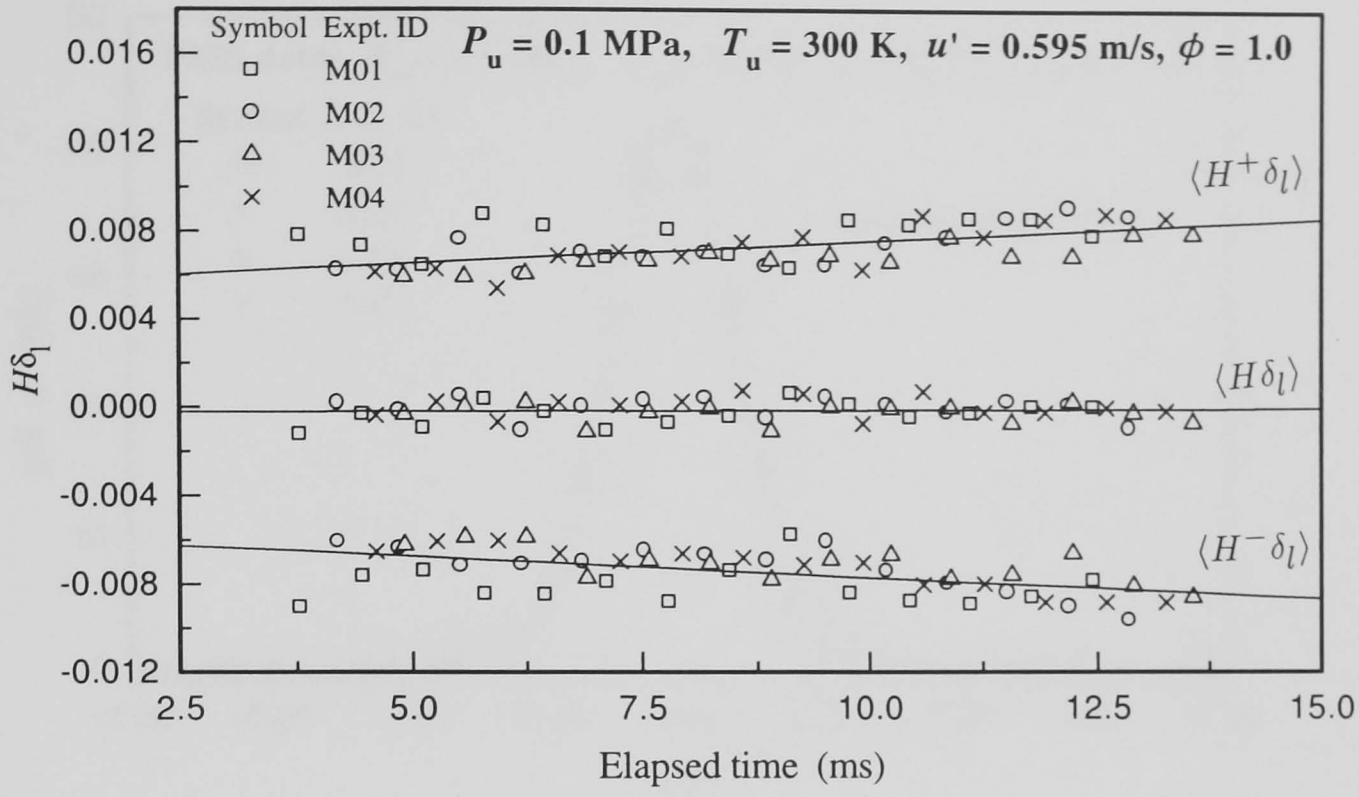

Fig. 7.6. Positive, negative and mean flame curvatures of a developing stoichiometric methane-air flame at $u' = 0.595$ m/s at 0.1 MPa initial pressure and 300 K initial temperature.

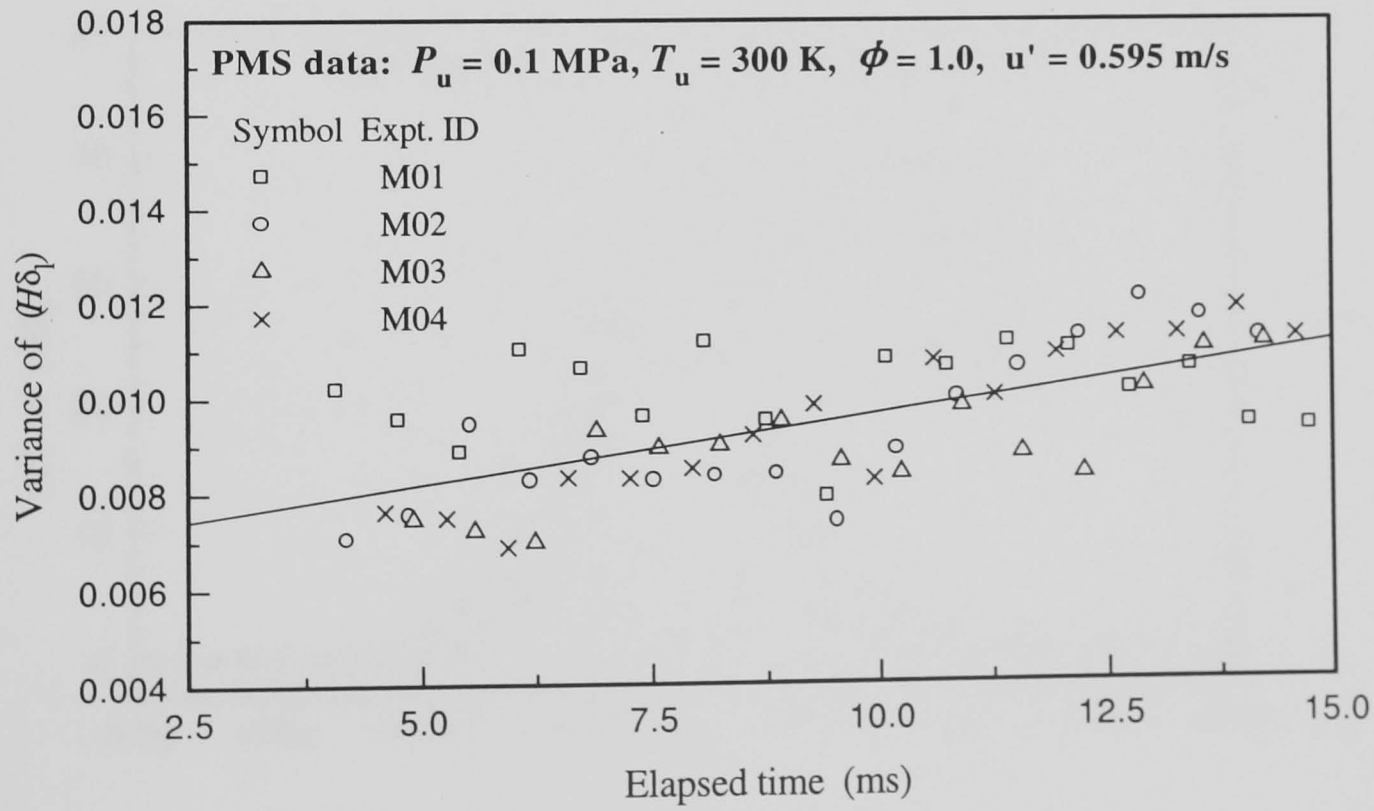

Fig. 7.7. Variance of the curvature pdfs obtained from four different explosions for stoichiometric methane-air flame at $u' = 0.595$ m/s at 0.1 MPa initial pressure and 300 K initial temperature.

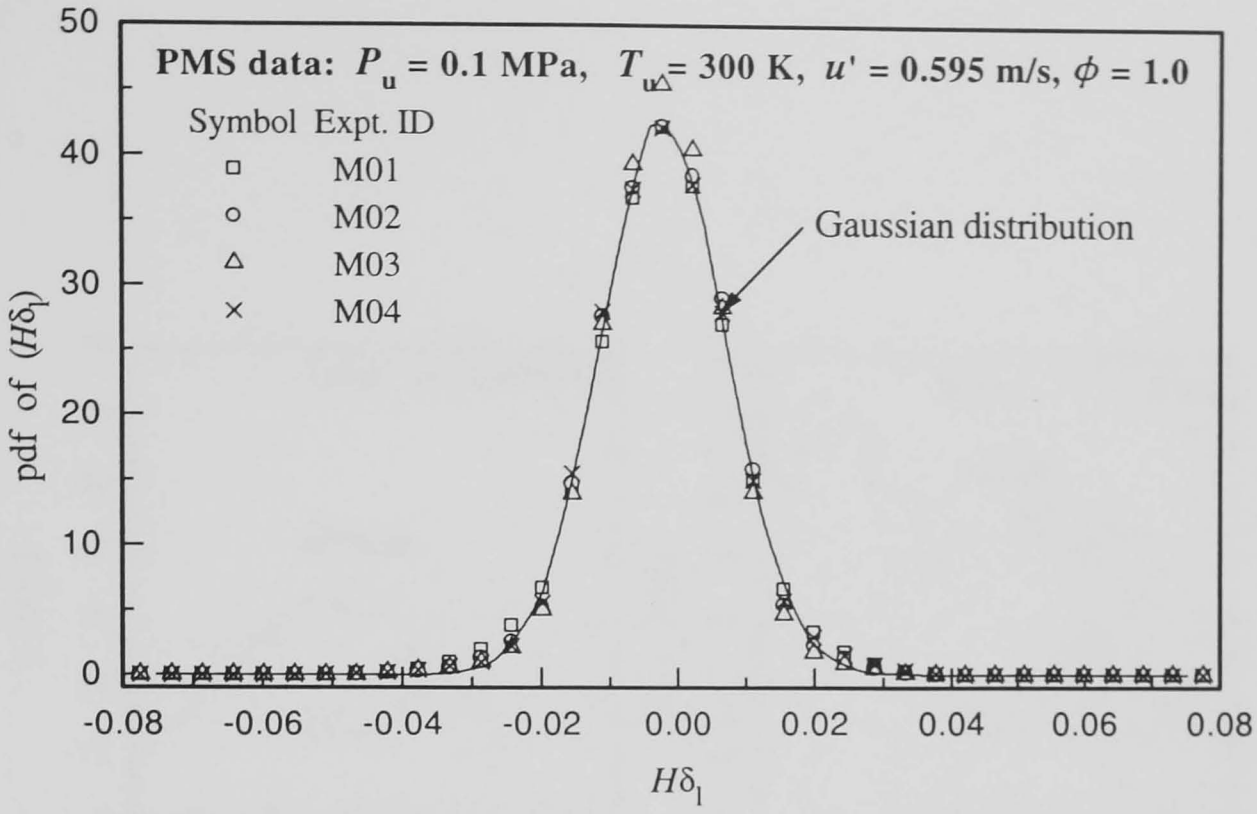

Fig. 7.8. Curvature pdfs obtained from four different explosions for stoichiometric methane-air for $u' = 0.595$ m/s at 0.1 MPa initial pressure and 300 K initial temperature.

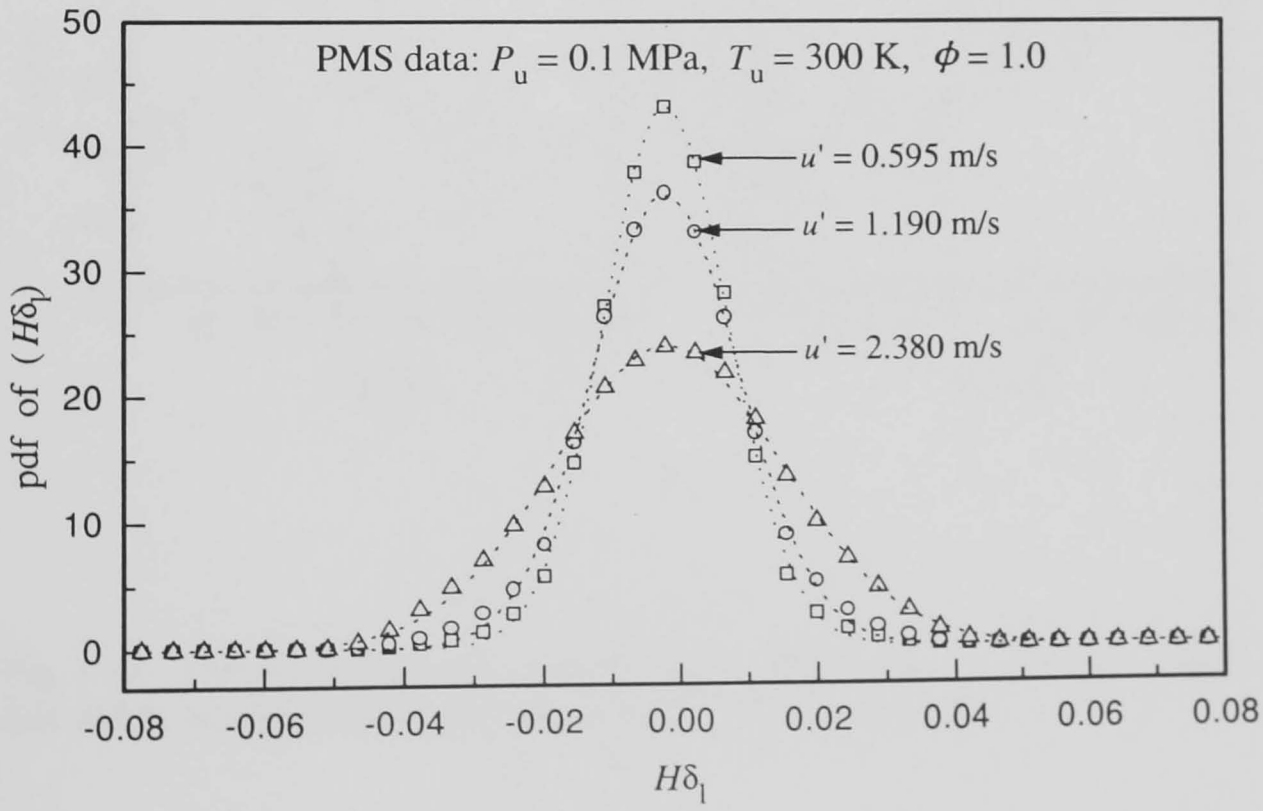

Fig. 7.9. Curvature pdfs for stoichiometric methane-air flame at 0.1 MPa initial pressure and 300 K initial temperature for a range of u'. Symbols denote experimental data, lines are Gaussian fits.

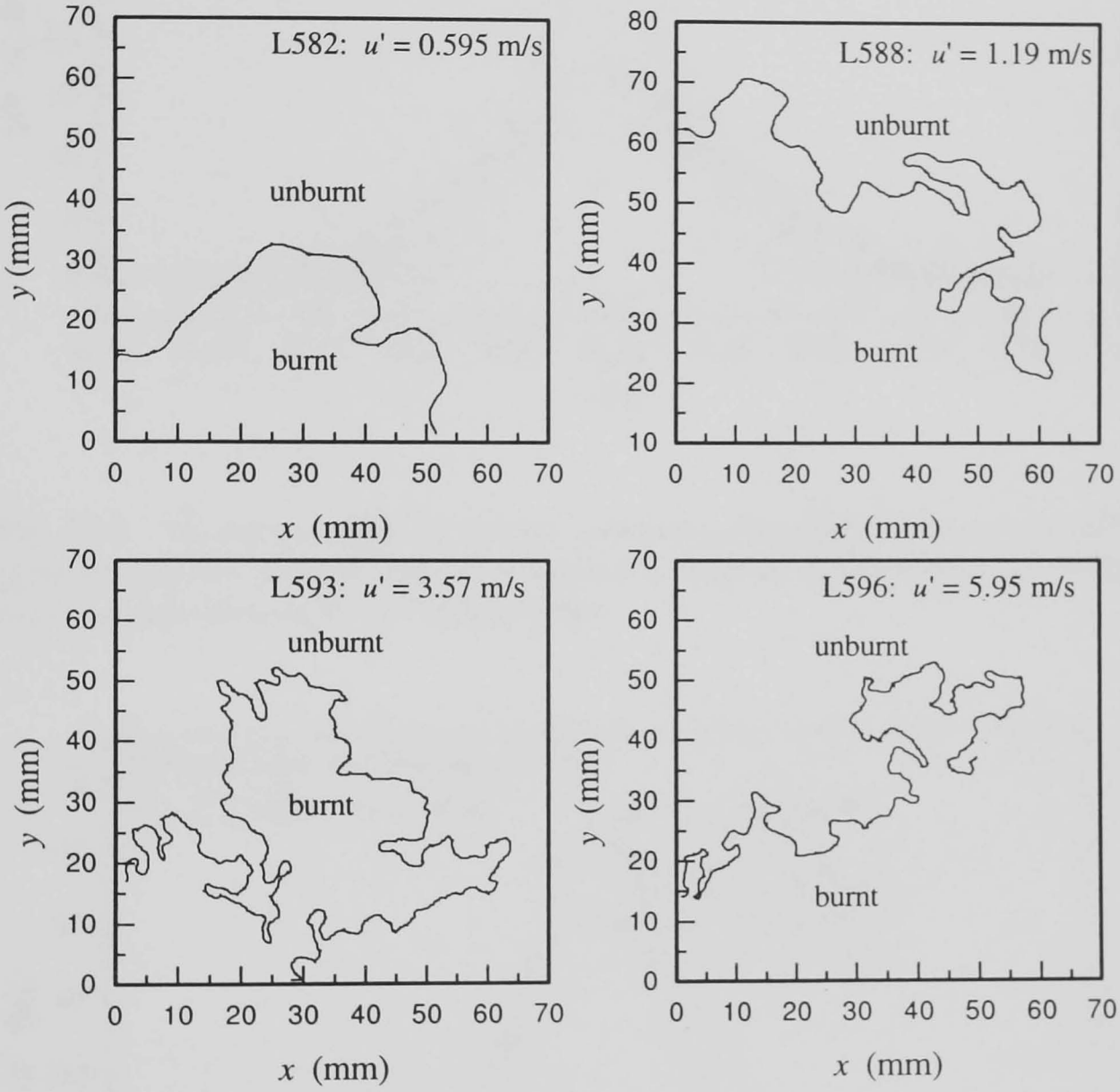

Fig. 7.10. Flame edges of stoichiometric iso-octane-air flame at 0.1 MPa initial pressure and 358 K initial temperature over a range of u' using PLIF.

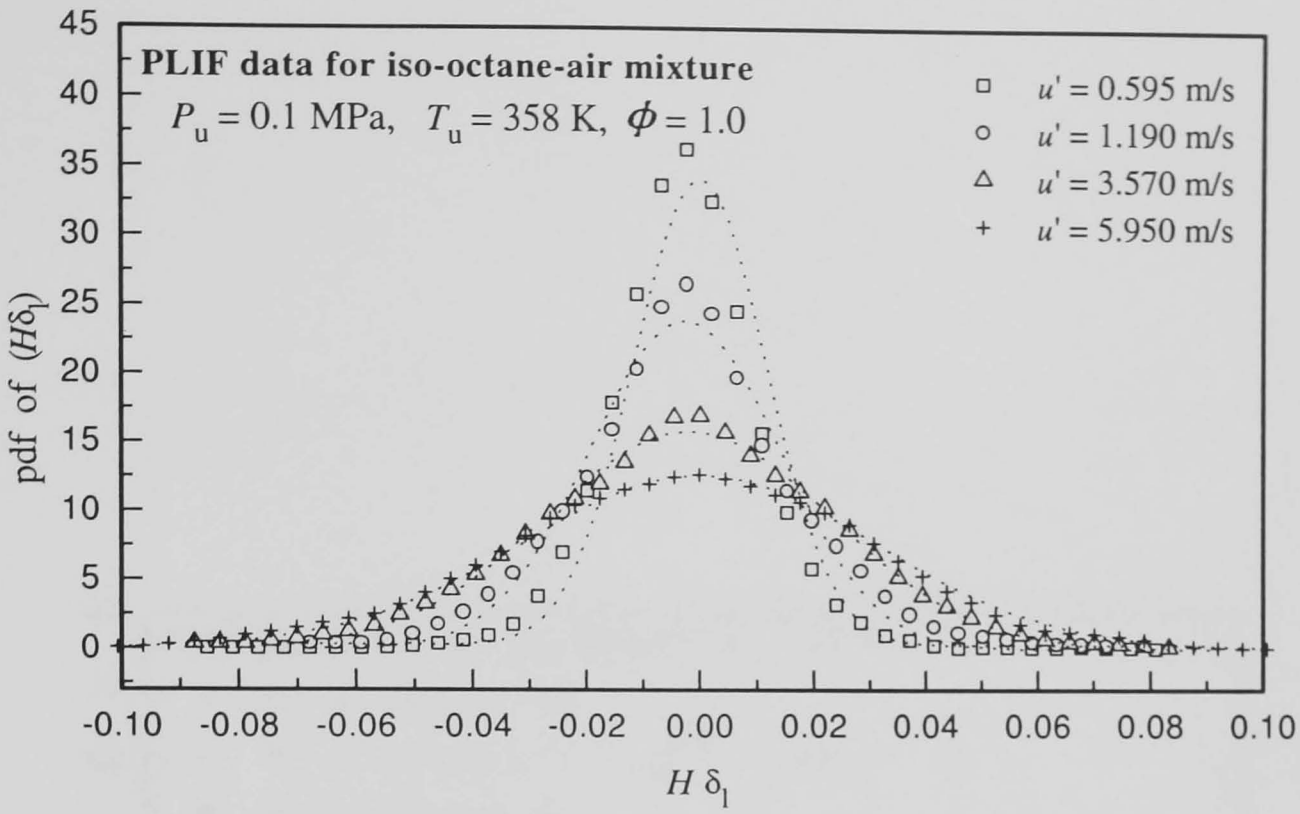

Fig. 7.11. Curvature pdfs for stoichiometric iso-octane-air flame at 0.1 MPa initial pressure and 358 K initial temperature over a range of u' using PLIF. Symbols denote experimental data, lines are Gaussian fits.

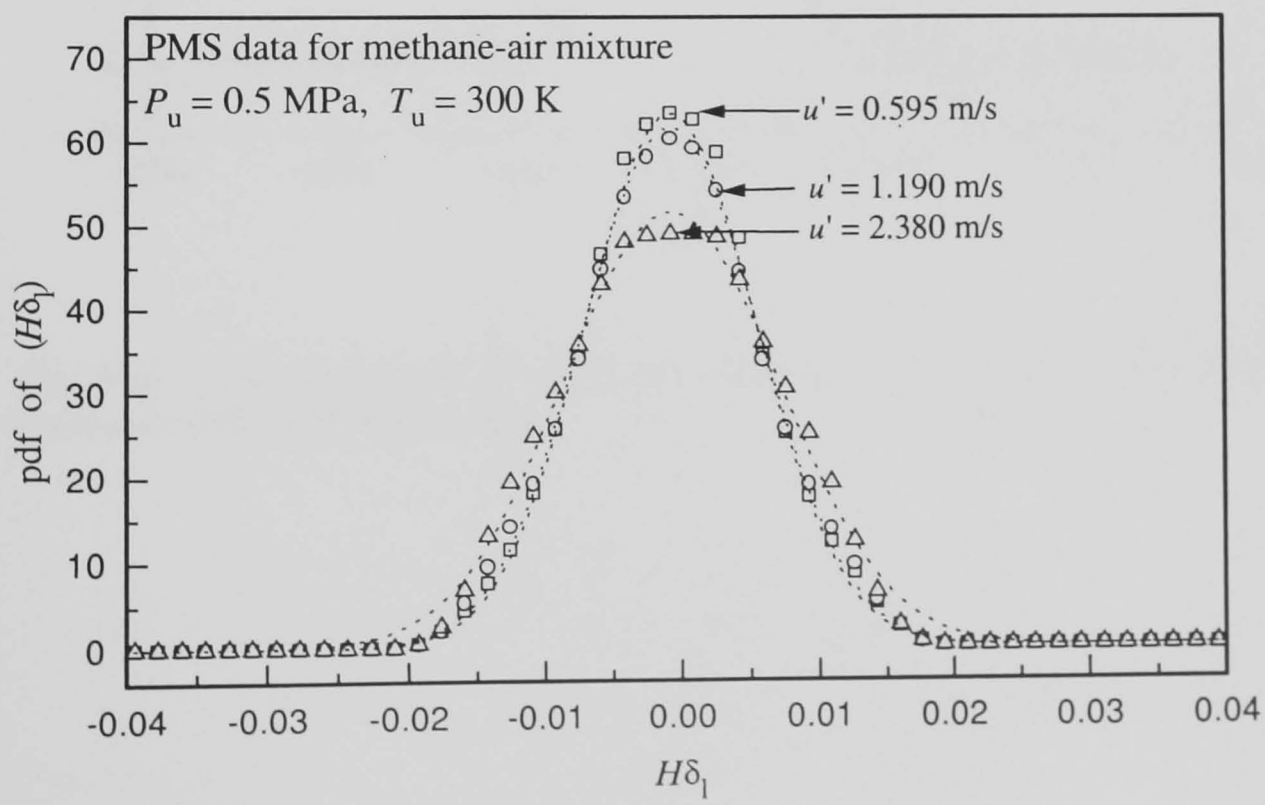

Fig. 7.12. Curvature pdfs for stoichiometric methane-air flame at at 0.5 MPa initial pressure and 300 K initial temperature for a range of u' using PMS. Symbols denote experimental data, lines are Gaussian fits.

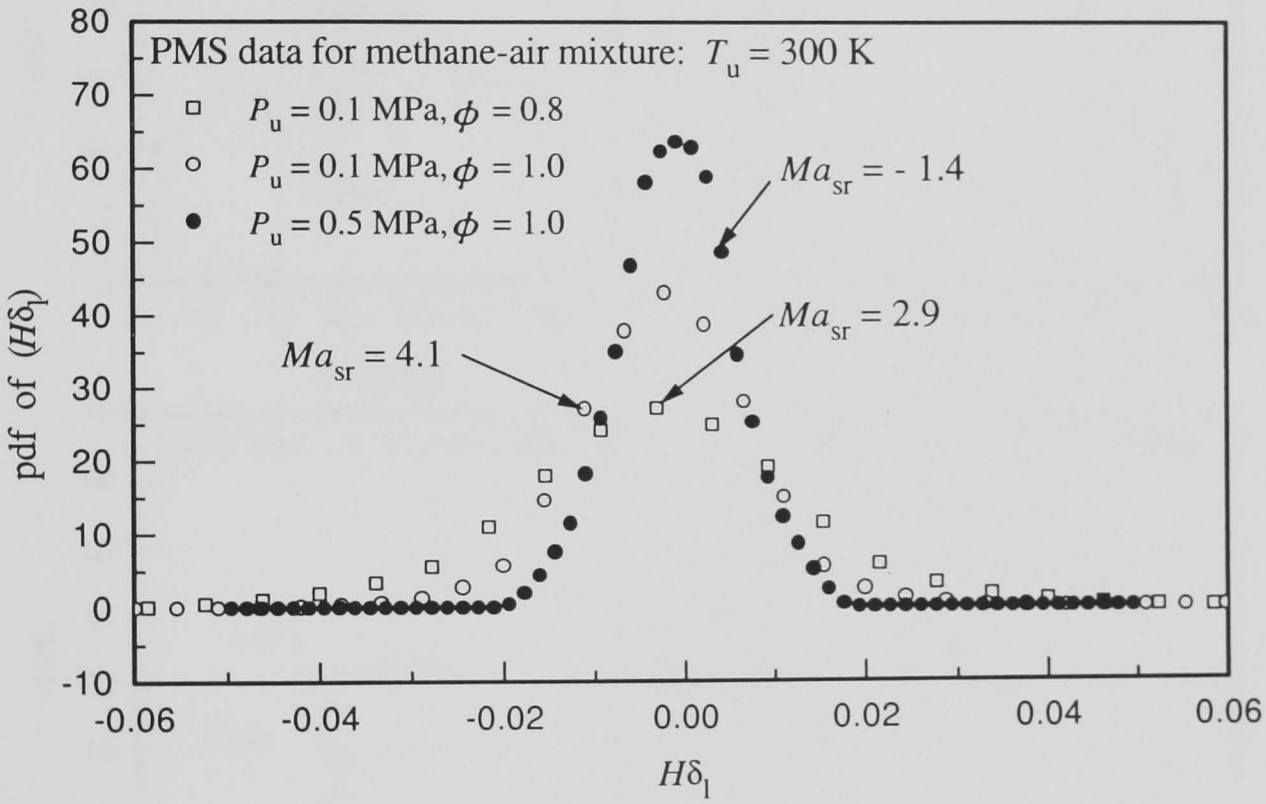

Fig. 7.13. Curvature pdfs for methane-air flame for $u' = 0.595$ m/s over a range of pressures and equivalence ratios.

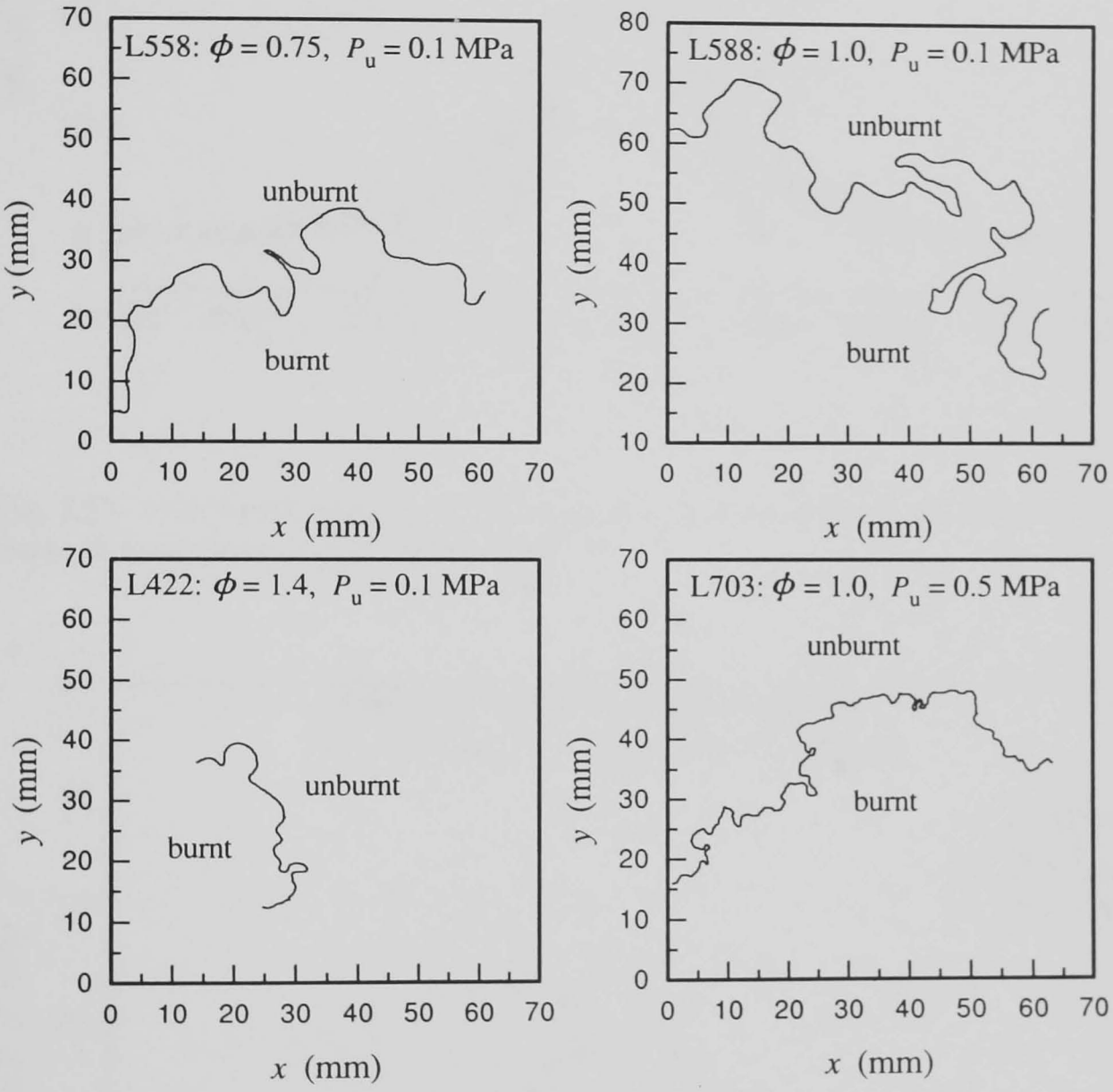

Fig. 7.14. Flame edges of stoichiometric iso-octane-air flame at u' 1.19 m/s for a range of pressure and equivalence ratio using PLIF.

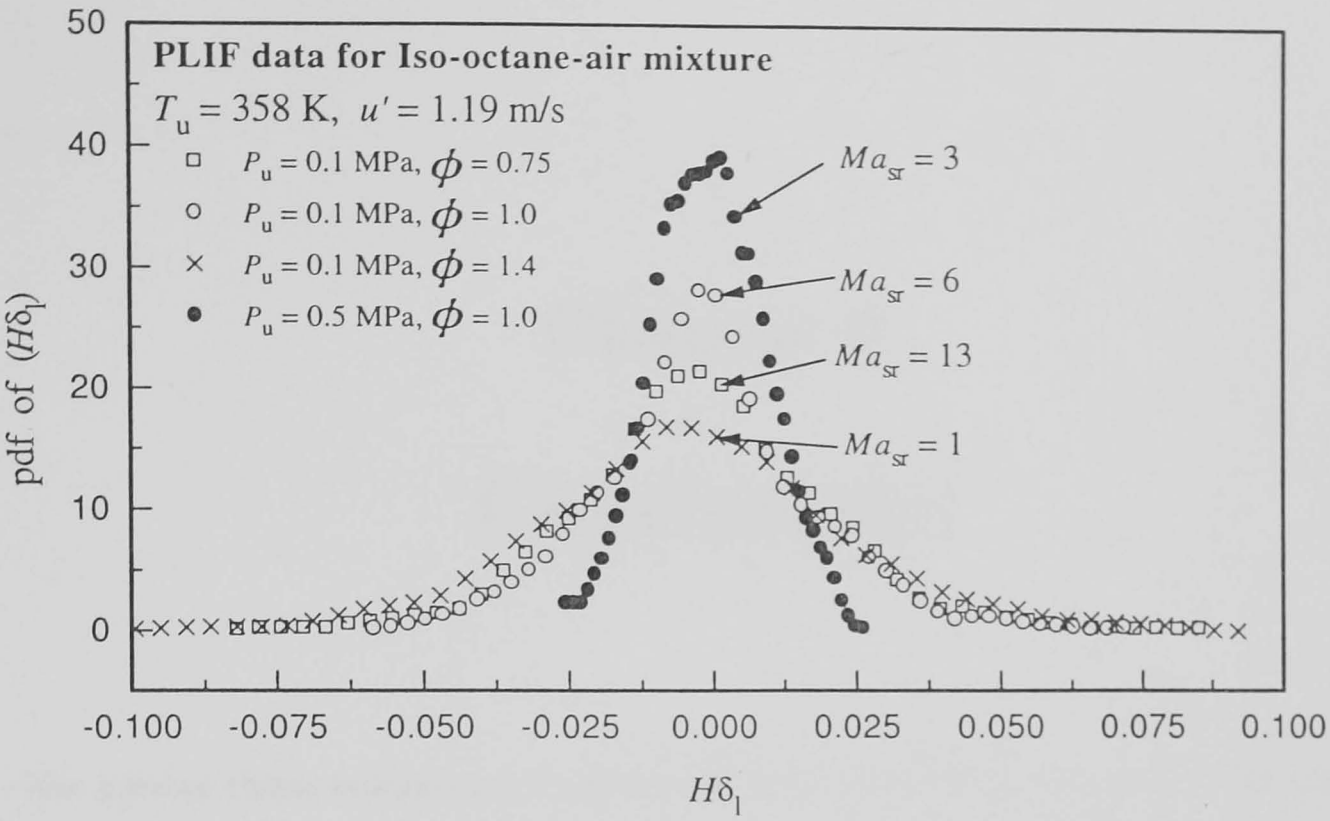

Fig. 7.15. Curvature pdfs for stoichiometric iso-octane-air flame at u' 1.19 m/s over a range of pressure and equivalence ratio.

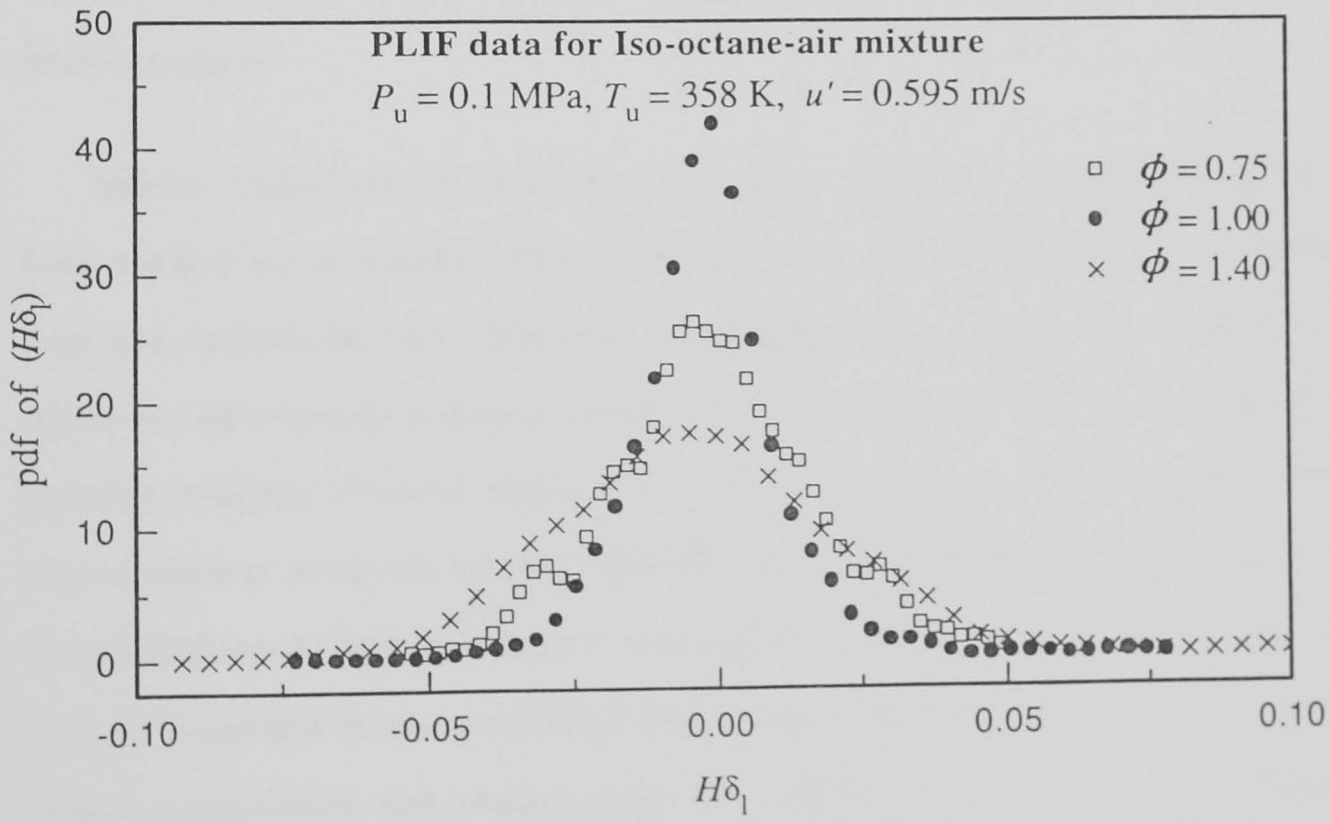

Fig. 7.16. Curvature pdfs for stoichiometric iso-octane-air flame at u' 0.595 m/s over a range of equivalence ratio.

Chapter 8

Conclusions

The present thesis comprises a fundamental study of spherical premixed flame propagation originating at a point under both laminar and turbulent propagation. Schlieren ciné photography has been employed to study laminar flame propagation, while planar mie scattering (PMS) has elucidated important aspects of turbulent flame propagation. Turbulent flame curvature has also been studied using planar laser induced fluorescence (PLIF) images.

Effects of flame stretch on laminar burning velocities of methane-air mixtures have been studied experimentally and numerically over wide ranges of pressure, temperature and equivalence ratio. Spherically expanding flame speeds, were measured, from which the corresponding laminar burning velocities were derived. Unstretched laminar burning velocities of freely propagating, one dimensional, adiabatic, premixed flames were computed using the Sandia PREMIX code using GRI-Mech reaction mechanism. Two definitions of burning velocity were explored and their response to stretch due to curvature and flow strain quantified by appropriate Markstein numbers. Data from the present experiments and computations are compared with those reported elsewhere. Comparisons are made with iso-octane-air mixtures and the contrast between fuels lighter and heavier than air is emphasized.

Flame instability in laminar flame propagations becomes more pronounced at high pressures, especially for lean and stoichiometric methane-air mixtures. Critical Peclet numbers for the onset of cellularity were measured and related to the Markstein number, Ma_{sr}. Flame photography clearly shows the flame to accelerate as the instability develops, giving rise to a cellular flame structure.

PMS images have been analysed to obtain the distributions of burned and unburned gas in turbulent flames. Turbulent burning velocities have been derived from these for stoichiometric methane-air at different turbulent r.m.s. velocities, at initial pressures of 0.1 MPa and 0.5 MPa. A variety of ways of defining the turbulent burning velocity have been fruitfully explored. Relationships between these different burning velocities are deduced and their relationship with the turbulent flame speed derived. The deduced relationships have also been verified experimentally.

The major conclusions of the study are:

- Measured unstretched burning velocities of methane-air increase with decreasing pressure and increasing temperature. These values are in good agreement with the reported data obtained from a variety of experimental and computational techniques. It would appear that the mathematical models are less successful at higher pressures. A general power law correlation of unstretched burning velocities in terms of pressure and temperature is presented.

- The global activation energies for the mass burning rate were experimentally determined. Correlations of laminar burning velocities are established using these energies. Zeldovich numbers for methane-air mixtures are calculated from the activation energies. They are found to increase with pressure. There is a slight variation with ϕ, with a minimum value of β for near-stoichiometric mixtures.

- Two different stretched burning velocities have been recognized, one based on the disappearance of the unburned mixture, and another based on the appearance of the burned products. These have different values for a given flame stretch and

the difference increases with flame thickness as initial pressure decreases. They show different sensitivities to stretch rate and the associated Markstein numbers have been measured.

- Effects of flame stretch on laminar flame speeds are found to be substantial, with variations up to 35% in the stretched burning velocity for a variation in stretch between 400 and 100 (s^{-1}). This highlights the significance of flame stretch on laminar and, hence, by implication, turbulent burning velocities.

- Markstein numbers for methane-air mixtures are found to increase with equivalence ratio. They decrease with initial pressure, but only up to 0.5 MPa. They are less sensitive to initial temperature.

- Comparisons between the present methane-air data and those of iso-octane-air, presented elsewhere, show that flame stretch has opposite influences on both the burning rate and the stability of the two fuels.

- The predictions of chemical kinetic models are, in general, satisfactory for lean mixtures but less so for rich mixtures, particularly at high pressures. Flame instability, which can wrinkle the flame and also increase the burning velocity, is not predicted by these models.

- Flame instability, with associated flame acceleration, is observed for the methane-air flames at higher pressures, especially for the lean mixtures. Its intensity decreases with increase in equivalence ratio and Markstein number. A linear relationship is established between the critical Peclet number, Pe_{cl} for the onset of cellularity and Ma_{sr} for both methane-air and iso-octane-air mixtures.

- Flame speeds are found to be slower in the present study than predicted by the $t^{3/2}$ rule, which is more valid for large scale unconfined explosions. However, there is clear evidence that the flame spread law in the present work tends towards that in the large scale explosions.

- A variety of ways in which turbulent burning velocities might be defined has been scrutinized. In the analyses different masses and reference radii are considered in predictions of turbulent burning velocities. The reference radius, R_v, which satisfies the condition that the volume of unburned gas inside a circumference of this radius is equal to that of burned gas outside that circumference, is found to be most suitable radius to define the turbulent burning velocity. With this reference radius, all three definitions of turbulent burning velocities attain identical values.

- The study of flame curvature distributions show these to become more dispersed as the r.m.s. turbulent velocity increases. A decrease in Markstein number also increases this dispersion, in line with the flame stability studies.

The following observations are made with regard to future work:

- The present studies have covered laminar methane-air burning velocities and Markstein numbers for equivalence ratios between 0.8 and 1.2. Because of the increased tendency to burn lean in engines, further measurements should be made for leaner mixtures.

- Flame speeds have been measured as cellular instability begins to develop. Other workers have made measurements in large scale explosions. There is a need for measurements at intermediate scales.

- Measurements of turbulent burning velocities simultaneously with schlieren photography and laser sheet images would strengthen (or weaken) the correlations suggested in the present work.

- The influence of pressure, Karlovitz stretch factor and Markstein number on curvature pdfs of turbulent flames are not completely clear. Further experiments are required to separate the influences of these variables.

Appendix A

Estimation of Thermodynamic and Transport Properties

A.1 Introduction

For the processing of the experimental data from flames, an associated family of transport, thermodynamic and thermo-chemical parameters are required. Procedures to evaluate them are well established (Bird *et al.* 1960, Assael *et al.* 1996), and a brief overview of such techniques to estimate the properties required in the present study is reported in this appendix.

A.2 Thermodynamic Properties

For a real gas or mixture of gases, the value of any thermodynamic property, X, can be written as the sum of an ideal-gas term and a residual term (Assael *et al.* 1996):

$$X = X^{\text{ig}} + X^{\text{res}} \tag{A.1}$$

where, X^{res} is defined as the difference between the actual value of the thermodynamic property X and the value X^{ig} that would prevail in a hypothetical ideal gas at the same thermodynamic state. The residual term becomes insignificant for dilute gases or their mixture (Assael *et al.* 1996).

A.2.1 Compressibility factor

The compressibility factor, Z, is widely used to express the deviation of actual gas properties from the ideal gas law. For methane-air mixtures, Z is computed using the Lee-Kesler scheme (Lee and Kesler 1975) that expresses Z as a function of 3-parameters:

- reduced pressure, $P_r(= P/P_{cr})$, where P_{cr} is the critical pressure,
- reduced temperature, $T_r(= T/T_{cr})$, where T_{cr} is the critical temperature,
- acentric factor, ω, which represents the non-sphericity of a molecule.

In this scheme, Z of any fluid or fluid mixtures is related to the compressibility factor of a simple fluid, Z_o, and the compressibility factor of a reference fluid, Z_r, by:

$$Z = Z_o + (\omega/\omega_r)(Z_r - Z_o) \tag{A.2}$$

Here, $\omega_r = 0.3978$, and Z_o and Z_r have been represented by the same equation:

$$Z = \left[\frac{P_r v}{T_r}\right] = 1 + \frac{B}{v} + \frac{C}{v^2} + \frac{D}{v^5} + \frac{c_4}{T_r^3 v^2}\left[\beta + \frac{\gamma}{v^2}\right]\exp\left[-\frac{\gamma}{v^2}\right] \tag{A.3}$$

$$\text{for} \quad 0.3 \le T_r \le 4 \quad \& \quad 0.01 \le P_r \le 10$$

$$\text{where} \quad B = b_1 - b_2/T_r - b_3/T_r^2 - b_4/T_r^3$$

$$C = c_1 - c_2/T_r - c_3/T_r^3$$

$$D = d_1 + d_2/b_1$$

and,

Constant	Simple Fluid	Reference	Constant	Simple Fluid	Reference
b_1	0.1181193	0.2026579	c_3	0.0	0.016901
b_2	0.265728	0.331511	c_4	0.042724	0.041577
b_3	0.154790	0.027655	$d_1 * 10^4$	0.155488	0.48736
b_4	0.030323	0.203488	$d_2 * 10^4$	0.623689	0.0740336
c_1	0.0236744	0.0313385	β	0.65392	1.226
c_2	0.0186984	0.0503618	γ	0.060167	0.03754

Hence, to calculate the values of Z for both the simple and reference fluids, Eq. A.3 is solved for the dimensionless volume, v, and Z is calculated from the reduced pressure and temperature as $Z = (P_{\mathrm{r}}/T_{\mathrm{r}})v$. The mixture properties are defined as the mole-fraction-weighted averages of the pure-component values:

$$\omega = \sum_i x_i \omega_i \quad T_{\mathrm{cr}} = \sum_i x_i T_{\mathrm{c}i} \quad \text{and} \quad P_{\mathrm{cr}} = \sum_i x_i P_{\mathrm{c}i} \tag{A.4}$$

The physical constants required to compute Z, along with the Lennard-Jones potential parameters, required to estimate some transport properties, are presented in Table A.1.

The computed values of Z for methane-air mixtures with pressures between 0.1 and 1.0 MPa at 300 K, suggests that the ideal gas law approximates the real gas properties with error less than 0.4 % (At 300 K and 1.0 MPa, $Z = 0.9962$). Therefore, in methane-air property calculations only *ideal-gas* values are considered.

Table A.1.
Physical constants and Lennard-Jones potential parameters for reactant gases.

Compound name	$\frac{M}{\mathrm{kg/kmol}}$	$\frac{T_{\mathrm{cr}}}{\mathrm{K}}$	$\frac{P_{\mathrm{cr}}}{\mathrm{MPa}}$	ω	$\frac{\sigma}{\mathrm{nm}}$	$\frac{\epsilon/k_{\mathrm{B}}}{\mathrm{K}}$
Methane	16.0436	190.55	4.599	0.011	0.3758	148.6
Nitrogen	28.0130	126.20	3.390	0.039	0.3798	71.4
Oxygen	32.0000	154.60	5.040	0.025	0.3467	107.6

A.2.2 Heat capacities and Enthalpies

For each species i, polynomial curve fits of the type used by NASA are used to calculate the following standard molar thermodynamic properties as (Burcat and McBride 1997):

$$\frac{C_{\mathrm{p},i}}{R} = a_{i1} + a_{i2}T + a_{i3}T^2 + a_{i4}T^3 + a_{i5}T^4 \tag{A.5}$$

$$\frac{H_{\mathrm{T},i}}{RT} = a_{i1} + \frac{a_{i2}}{2}T + \frac{a_{i3}}{3}T^2 + \frac{a_{i4}}{4}T^3 + \frac{a_{i5}}{5}T^4 + \frac{a_{i6}}{T} \tag{A.6}$$

Hence, $C_{\mathrm{p},i}$ is the molar heat capacity at constant pressure, and $H_{\mathrm{T},i}$ is the absolute enthalpy of species i and is related to its standard heat of formation $\Delta_f H^o_{298,i}$ by (Burcat and McBride 1997):

$$H_{\mathrm{T},i} = \Delta_f H^o_{298,i} + \int_{298}^{T} C_{\mathrm{p},i}\, \mathrm{d}T. \tag{A.7}$$

For a gas mixture, properties are:

$$C_{\mathrm{p}} = \sum_{i=1}^{N} x_i C_{\mathrm{p},i} \qquad H = \sum_{i=1}^{N} x_i H_{\mathrm{T},i} \tag{A.8}$$

where, x_i is the mole fraction of species i.

Values of coefficients a_{ij} for CH_4, CO, CO_2, H, H_2, H_2O, O, O_2, OH, N_2 and NO are obtained from Burcat and McBride (1997), and are presented in Table. A.2. In this data base, the thermodynamic and thermo-chemical data are represented as two sets of polynomial coefficients for each species. The first set reproduces data at temperatures above 1000 K, the second set for those below 1000 K, and the same value is reproduced by both sets at 1000 K.

A.3 Equilibrium Composition and Flame Temperature

Adiabatic flame temperature is the maximum temperature generated from chemical reactions under equilibrium condition, and serves as the key factor to effect the density ratio, σ. Its value is computed with the assumptions of negligible work and friction, and no heat loss. With these assumptions, the combustion process at constant pressure reduced to an isoenthalpic ($\mathrm{d}H = 0$) one and thus simplified the computation. However, the equilibrium combustion product composition and temperature are interrelated, and an iteration process is employed to evaluated them.

A.3.1 Computation Method

A computer program, `prprty.for`, is developed to calculate the properties of equilibrium combustion products of methane-air combustion for a given equivalence ratio, ϕ,

Table A.2.
Coefficients for species thermodynamic properties from Burcat and McBride(1997).

Species	T range,K	a_{i1}	a_{i2}	a_{i3}	a_{i4}	a_{i5}	a_{i6}
CO	1000-5000	0.30484859E+01	0.13517281E-02	-0.48579405E-06	0.78853644E-10	-0.46980746E-14	-0.14266117E+05
	300-1000	0.35795335E+01	-0.61035369E-03	0.10168143E-05	0.90700586E-09	-0.90442449E-12	-0.14344086E+05
CO_2	1000-5000	0.46365111E+01	0.27414569E-02	-0.99589759E-06	0.16038666E-09	-0.91619857E-14	-0.49024904E+05
	300-1000	0.23568130E+01	0.89841299E-02	-0.71220632E-05	0.24573008E-08	-0.14288548E-12	-0.48371971E+05
H	1000-5000	0.25000000E+01	0.00000000E+00	0.00000000E+00	0.00000000E+00	0.00000000E+00	0.25473660E+05
	300-1000	0.25000000E+01	0.00000000E+00	0.00000000E+00	0.00000000E+00	0.00000000E+00	0.25473660E+05
H_2	1000-5000	0.29328305E+01	0.82659802E-03	-0.14640057E-06	0.15409851E-10	-0.68879615E-15	-0.81305582E+03
	300-1000	0.23443029E+01	0.79804248E-02	-0.19477917E-04	0.20156967E-07	-0.73760289E-11	-0.91792413E+03
H_2O	1000-5000	0.26770389E+01	0.29731816E-02	-0.77376889E-06	0.94433514E-10	-0.42689991E-14	-0.29885894E+05
	300-1000	0.41986352E+01	-0.20364017E-02	0.65203416E-05	-0.54879269E-08	0.17719680E-11	-0.30293726E+05
N_2	1000-5000	0.29525407E+01	0.13968838E-02	-0.49262577E-06	0.78600091E-10	-0.46074978E-14	-0.92393753E+03
	300-1000	0.35309628E+01	-0.12365950E-03	-0.50299339E-06	0.24352768E-08	-0.14087954E-11	-0.10469637E+04
NO	1000-5000	3.26071234E+00	1.19101135E-03	-4.29122646E-07	6.94481463E-11	-4.03295681E-15	9.92143132E+03
	300-1000	4.21859896E+00	-4.63988124E-03	1.10443049E-05	-9.34055507E-09	2.80554874E-12	9.84509964E+03
O	1000-5000	2.54363697E+00	-2.73162486E-05	-4.19029520E-09	4.95481845E-12	-4.79553694E-16	2.92260120E+04
	300-1000	3.16826710E+00	-3.27931884E-03	6.64306396E-06	-6.12806624E-09	2.11265971E-12	2.91222592E+04
O_2	1000-5000	3.66096083E+00	6.56365523E-04	-1.41149485E-07	2.05797658E-11	-1.29913248E-15	-1.21597725E+03
	300-1000	3.78245636E+00	-2.99673415E-03	9.84730200E-06	-9.68129508E-09	3.24372836E-12	-1.06394356E+03
OH	1000-5000	2.83864607E+00	1.10725586E-03	-2.93914978E-07	4.20524247E-11	-2.42169092E-15	3.94395852E+03
	300-1000	3.99201543E+00	-2.40131752E-03	4.61793841E-06	-3.88113333E-09	1.36411470E-12	3.61508056E+03

at any initial pressure and temperature. The species included in the product mixture are: CO, CO_2, H, H_2, H_2O, O, O_2, OH, N_2 and NO. Therefore the overall chemical equation can be expressed by:

$$\epsilon\phi CH_4 + (0.2095O_2 + 0.7905N_2) = \nu_1 N_2 + \nu_2 O_2 + \nu_3 CO + \nu_4 H_2 + \nu_5 CO_2 + \nu_6 H_2O + \nu_7 H + \nu_8 O + \nu_9 NO + \nu_{10} OH$$

where, ϵ is the molar fuel-air ratio, and ν_i is the stoichiometric coefficient for species i. Atom balancing yields the following four equations:

$$C: \quad \epsilon\phi \quad = (x_3 + x_5)N \tag{A.9}$$

$$H: \quad 4\ \epsilon\phi \quad = (2x_4 + 2x_6 + x_7 + x_{10})N \tag{A.10}$$

$$O: \quad 0.419 \quad = (2x_2 + x_3 + 2x_5 + x_6 + x_8 + x_9 + x_{10})N \tag{A.11}$$

$$N: \quad 1.581 \quad = (2x_1 + x_9)N \tag{A.12}$$

where $N(= \sum_{i=1}^{10} \nu_i)$ is the total number of moles and x_i are the mole fractions satisfying the condition:

$$\sum_{i=1}^{10} x_i = 1 \tag{A.13}$$

The introduction of six equilibrium constants for six non-redundant reactions provide the required equations, ten unknown mole fractions, x_i, and the total number of moles, N. The equations are:

$$\frac{1}{2}H_2 \rightleftharpoons H \qquad K_1 = \frac{x_7 . P^{1/2}}{x_4} \tag{A.14}$$

$$\frac{1}{2}O_2 \rightleftharpoons O \qquad K_2 = \frac{x_8 . P^{1/2}}{x_2^{1/2}} \tag{A.15}$$

$$\frac{1}{2}H_2 + \frac{1}{2}O_2 \rightleftharpoons OH \qquad K_3 = \frac{x_{10}}{x_2^{1/2} . x_4^{1/2}} \tag{A.16}$$

$$\frac{1}{2}N_2 + \frac{1}{2}O_2 \rightleftharpoons NO \qquad K_4 = \frac{x_9}{x_1^{1/2} . x_2^{1/2}} \tag{A.17}$$

$$H_2 + \frac{1}{2}O_2 \rightleftharpoons H_2O \qquad K_5 = \frac{x_6}{x_2^{1/2} . x_4 . P} \tag{A.18}$$

$$CO + \frac{1}{2}O_2 \rightleftharpoons CO_2 \qquad K_6 = \frac{x_5}{x_2^{1/2}.x_3.P^{1/2}} \tag{A.19}$$

Hence, the equilibrium constants, K, are expressed as a function of temperature by (Olikara and Bowman 1975):

$$\log K = A\ln(T/1000) + \frac{B}{T} + C + DT + ET^2 \tag{A.20}$$

and the constants A, B, C, D, E are generated from the curve fit to the equilibrium constants given JANAF tables and are presented in Table A.3.

Table A.3.
Constants to compute the equilibrium constants, K

	A	B	C	D	E
K_1	4.321680E-01	-1.124640E+04	2.672690E+00	-7.457440E-05	2.424840E-09
K_2	3.108050E-01	-1.295040E+04	3.217790E+00	-7.383360E-05	3.446450E-09
K_3	-1.417840E-01	-2.133080E+03	8.534610E-01	3.550150E-05	-3.102270E-09
K_4	1.508790E-02	-4.709590E+03	6.460960E-01	2.728050E-06	-1.544440E-09
K_5	-7.523640E-01	1.242100E+04	-2.602860E+00	2.595560E-04	-1.626870E-09
K_6	-4.153020E-03	1.486270E+04	-4.757460E+00	1.246990E-04	-9.002270E-09

A.3.2 Solution Procedure

To calculate the adiabatic flame temperature, an initial gauss for $T_{ad} = 2500K$ is made and the equilibrium product composition is computed by `prprty.for`, which solves Eqs. A.9 to A.19 by a modified Fortran routine `lnsrch.for` from Press *et al.* (1992) using the Newton-Raphson method. The initial estimate of mole fractions to start the iteration procedure is the non-dissociated composition as suggested by Heywood (1988). Once the mixture composition is determined, the difference between the product and the reactant enthalpies are calculated, and a modified estimate of T_{ad} is made. The iteration process is repeated until T_{ad} converged to the specified accuracy. The equilibrium product composition is then calculated for this T_{ad}. Product density

is calculated from the composition, assuming the ideal gas law, because the adiabatic flame temperature is much higher than the critical temperature of the mixture, and the ideal gas law is applicable.

A.3.3 Equilibrium Temperature and Product

Shown in Fig. A.1 are the adiabatic flame temperatures and the major species as a function of equivalence ratio. The solid lines represent the values obtained from the method outlined in § A.3.1, while the points represent values obtained using PREMIX code (Kee *et al.* 1985) with GRI-Mech (Frenklach *et al.* 1995) as outlined in § 3.4. The negligible discrepancy between these results suggests that equilibrium temperature and composition, required to calculate the density ratio, computed from a small number of equations are quite accurate. As shown in Fig. A.1, the major products of lean methane-air combustion are H_2O, CO_2, O_2 and N_2; while for rich combustion, they are H_2O, CO_2, CO, H_2, and N_2. Consequently, (shown in Fig. A.2 and Table. A.4), the maximum flame temperature occurs at a slightly rich equivalence ratio ($\phi = 1.05$), owing to lower mean specific heats of the richer products (Glassman 1996). As the pressure is increased in a combustion system, the adiabatic flame temperature increases and so does the amount of dissociation. This observation is expected from Le Chatelier's principle (Glassman 1996). The effect is greatest at the stoichiometric mixture where the amount of dissociation is greatest and dissociation increases with increase in temperature in the combustion system. Shown in Fig. A.3 is the density ratio, σ, as a function of equivalence ratio for different initial pressures and temperatures. For a given equivalence ratio, the density ratio decreases as temperature is increased while it is less sensitive to pressure variations.

A.4 Evaluation of Diffusive Transport Coefficients

A transport property X, where X may be the viscosity μ, the thermal conductivity k, the diffusion coefficient D or the thermal diffusivity α, is written most conveniently as

Table A.4.
Equilibrium Product Composition and temperature of Methane-Air Combustion.

ϕ	0.6	0.6	0.6	1.0	1.0	1.0	1.4	1.4	1.4
P_u (MPa)	0.1	0.1	1.0	0.1	0.1	1.0	0.1	0.1	1.0
T_u (K)	300	400	300	300	400	300	300	400	300
Species									
CO	0	0	0	.0088	.0108	.0052	.0750	.0762	.0751
CO_2	.0591	.0591	.0591	.0853	.0832	.0893	.0442	.0430	.0442
H	0	0	0	.0004	.0005	.0001	.0003	.0005	.0001
H_2	0	0	0	.0030	.0037	.0017	.0603	.0591	.0603
H_20	.1181	.1181	.1182	.1838	.1824	.1864	.1779	.1790	.1781
N_2	.7424	.7421	.7425	.7091	.7077	.7115	.6422	.6421	.6423
NO	.0016	.0021	.0016	.0020	.0024	.0017	0	0	0
O	0	0	0	.0002	.0003	.0001	0	0	0
O_2	.0785	.0782	.0785	.0047	.0056	.0027	0	0	0
OH	.0002	.0004	.0001	.0027	.0033	.0015	0	0	0
T_{ad}	1665	1741	1666	2225	2274	2267	1965	2038	1966

the sum of three contributions (Assael *et al.* 1996):

$$X(\rho_n, T) = X_o(T) + \Delta X(\rho_n, T) + \Delta_c X(\rho_n, T) \tag{A.21}$$

Here, $X_o(T)$ represents the *dilute-gas* value of the property, $\Delta X(\rho_n, T)$ the *excess* value of the property and $\Delta_c X(\rho_n, T)$ the *critical enhancement.* For dilute gas conditions, the contribution of the last two terms are zero and in the present study, only the dilute gas properties are evaluated based on the discussion in § A.2.1.

A.4.1 Dynamic Viscosity

The dynamic viscosity at an absolute temperature T of a pure gaseous species i of molecular weight M_i is given by the kinetic theory expression (cf. Bird *et al.* 1960) by:

$$\mu_i = \frac{5}{16} \frac{\sqrt{\pi M_i k_B T}}{\pi \sigma_i^2 \Omega^*_{(2,2)}} \tag{A.22}$$

where, σ_i denotes the Lennard-Jones collision diameter, $\Omega^*_{(2,2)}$, which is a collision integral normalized by its rigid sphere value and k_B is the Boltzmann constant. If a Lennard-Jones-6-12-potential is assumed, the reduced collision integral $\Omega^*_{(2,2)}$ is a unique function of the reduced temperature T^* which is the ratio of the absolute temperature T and the depth of the intermolecular potential, ϵ i.e., $T^* = k_B T/\epsilon$. Its value is approximated using the Nuffield-Janzen equation (Neufeld *et al.* 1972):

$$\Omega^*_{(2,2)} = \frac{1.16145}{(T^*)^{0.14874}} + \frac{0.52487}{\exp(0.7732T^*)} + \frac{2.16178}{\exp(2.43787T^*)} - 6.435 * 10^{-4}(T^*)^{0.14874} \sin\left[18.0323(T^*)^{-0.7683} - 7.2371\right] \quad \text{(A.23)}$$

The dynamic viscosity of the gas mixture is calculated using the semi-empirical formula of Wilke (1950) from the respective viscosity, μ_i, and the mole fractions, x_i, of the component species according to

$$\mu_{\text{mix}} = \sum_{i=1}^{N} \frac{\mu_i}{1 + \frac{1}{x_i} \sum_{\substack{j=1 \\ j \neq i}}^{N} x_j \Phi_{ij}} \quad \text{(A.24)}$$

where the correction factors Φ_{ij} are calculated from the molar weights and the dynamic viscosities by (Strehlow 1984):

$$\Phi_{ij} = \frac{1}{2\sqrt{2}} \left[1 + \frac{M_i}{M_j}\right]^{-\frac{1}{2}} \left[1 + \left(\frac{\mu_i}{\mu_j}\right)^{\frac{1}{2}} \left(\frac{M_j}{M_i}\right)^{\frac{1}{4}}\right]^2 \quad \text{(A.25)}$$

Mixture kinematic viscosity, ν, is obtained by dividing the mixture dynamic viscosity, μ_{mix}, by the mixture density, ρ_u. Shown in Fig. A.4 are the variations of ν as a function of ϕ for methane-air mixtures at 300 K and 0.1 MPa.

A.4.2 Thermal Conductivity and Diffusivity

Thermal conductivity k_i of a pure gaseous species, i, is related to its dynamic viscosity μ_i by the *modified Eucken* correlation (cf. Bird *et al.* 1960):

$$\frac{k_i M_i}{\mu_i C v_i} = 1.32 + \frac{1.77}{(Cp_i/R) - 1} \tag{A.26}$$

The thermal conductivity of the mixture is calculated from the respective conductivities k_i using a semi-empirical formula of Mason and Saxena (1958)

$$k_{\text{mix}} = \sum_{i=1}^{N} \frac{k_i}{1 + \frac{1.065}{x_i} \sum_{\substack{j=1 \\ j \neq i}}^{N} x_j \Phi_{ij}} \tag{A.27}$$

where Φ_{ij} is defined in Eq. A.25.

The thermal diffusivity, D_{T} of the mixture is given by:

$$D_{\text{T}} = \frac{k_{\text{mix}}}{\rho_{\text{u}} C_{\text{p}}} \tag{A.28}$$

Shown in Fig. A.4 are the variations of D_{T} as a function of ϕ for methane-air mixtures at 300 K and 0.1 MPa.

A.4.3 Mass Diffusivity

Multi-component diffusion coefficients are very difficult to compute and, in practice, they are approximated by the binary diffusion coefficients (Strehlow 1984). Hence, the binary diffusion coefficient is the mass diffusivity of the deficient reactant with respect to the abundant reactant (Clavin 1985). Its value is dependent on the properties of both species and can be calculated from the kinetic theory of gases (cf. Bird *et al.* 1960) by:

$$D_{ij} = 0.0018583 \frac{\sqrt{T^3 \left(\frac{1}{M_i} + \frac{1}{M_j} \right)}}{P \sigma_{ij}^2 \Omega^*_{(1,1)}} \tag{A.29}$$

Hence, the mean molecular parameters σ_{ij} and ϵ_{ij} are approximated from the parameters of the molecules using the combination rules (Assael *et al.* 1996):

$$\sigma_{ij} = \frac{\sigma_i + \sigma_j}{2} \qquad \text{and} \qquad \epsilon_{ij} = \sqrt{\epsilon_i . \epsilon_j}. \tag{A.30}$$

The reduced collision integral $\Omega^*_{(1,1)}$ appeared in Eq. A.29 is a function of reduced temperature $T^*_{ij} = k_B T/\epsilon_{ij}$ and is approximated by the Nuffield-Janzen equation (Neufeld *et al.* 1972):

$$\Omega^*_{(1,1)} = \frac{1.06036}{(T^*)^{0.15610}} + \frac{0.19300}{\exp(0.47635T^*)} + \frac{1.03587}{\exp(1.52996T^*)} + \frac{1.76474}{\exp(3.89411T^*)} \tag{A.31}$$

Shown in Fig. A.4 are the variations of binary diffusion coefficients as a function of ϕ for methane-air mixtures at 300 K and 0.1 MPa.

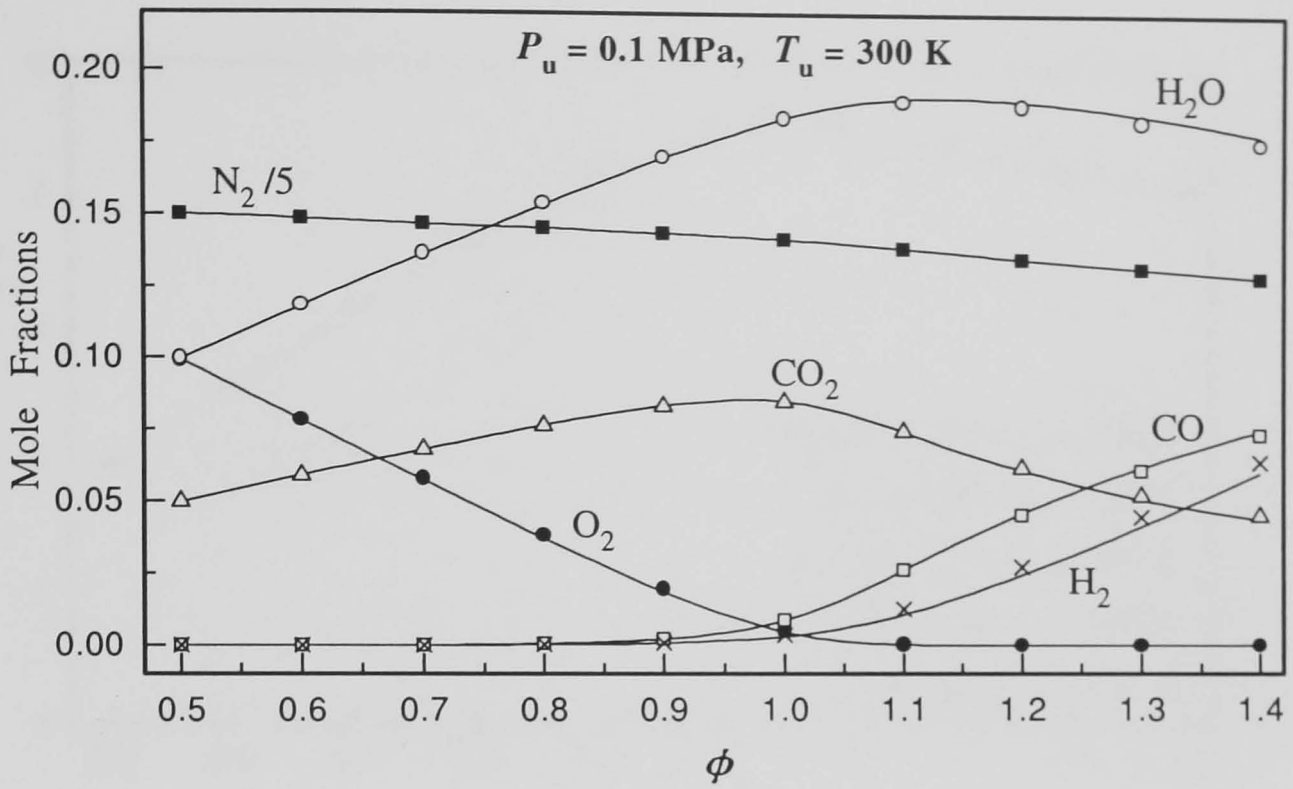

Fig. A.1. Mole fractions of equilibrium combustion products and adiabatic flame temperatures of methane-air mixtures as a function of equivalence ratios.

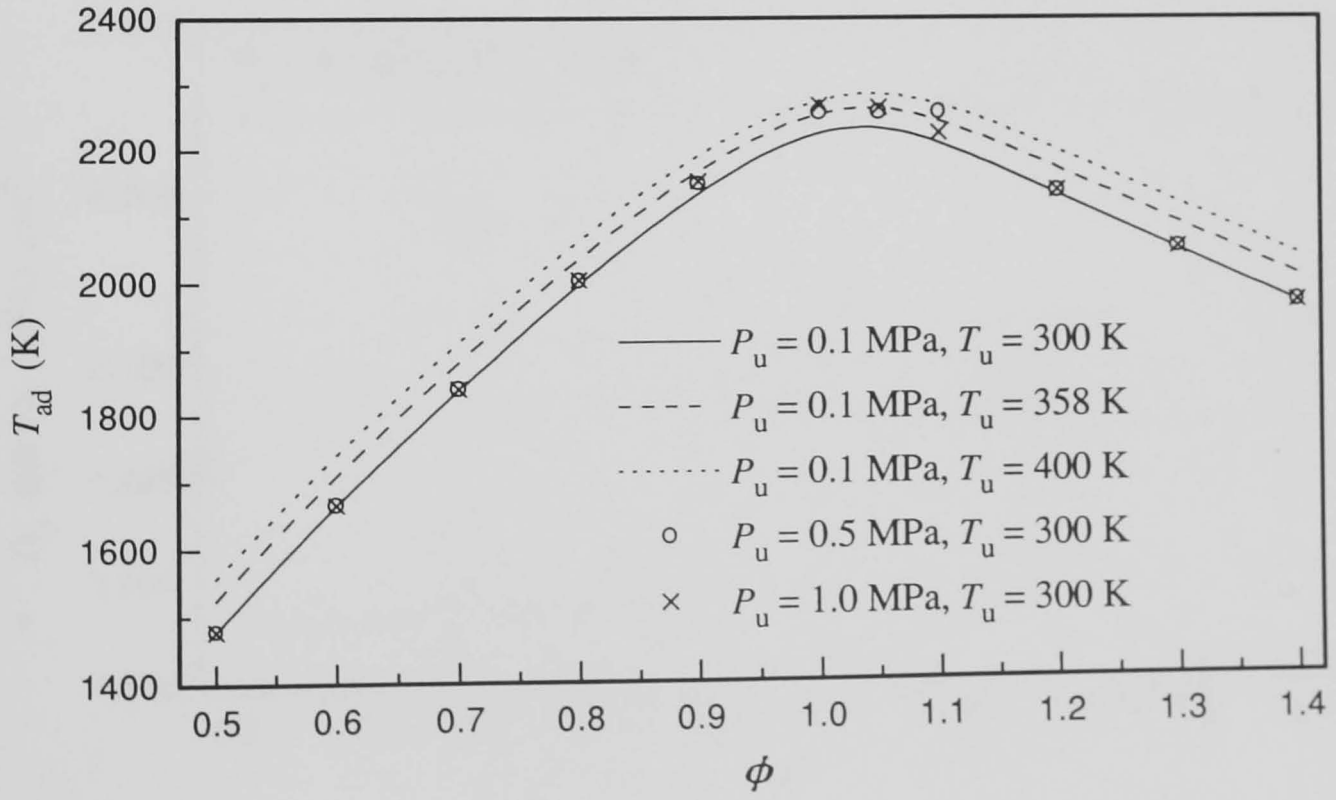

Fig. A.2. Adiabatic flame temperature as a function of equivalence ratio for different initial pressures and temperatures.

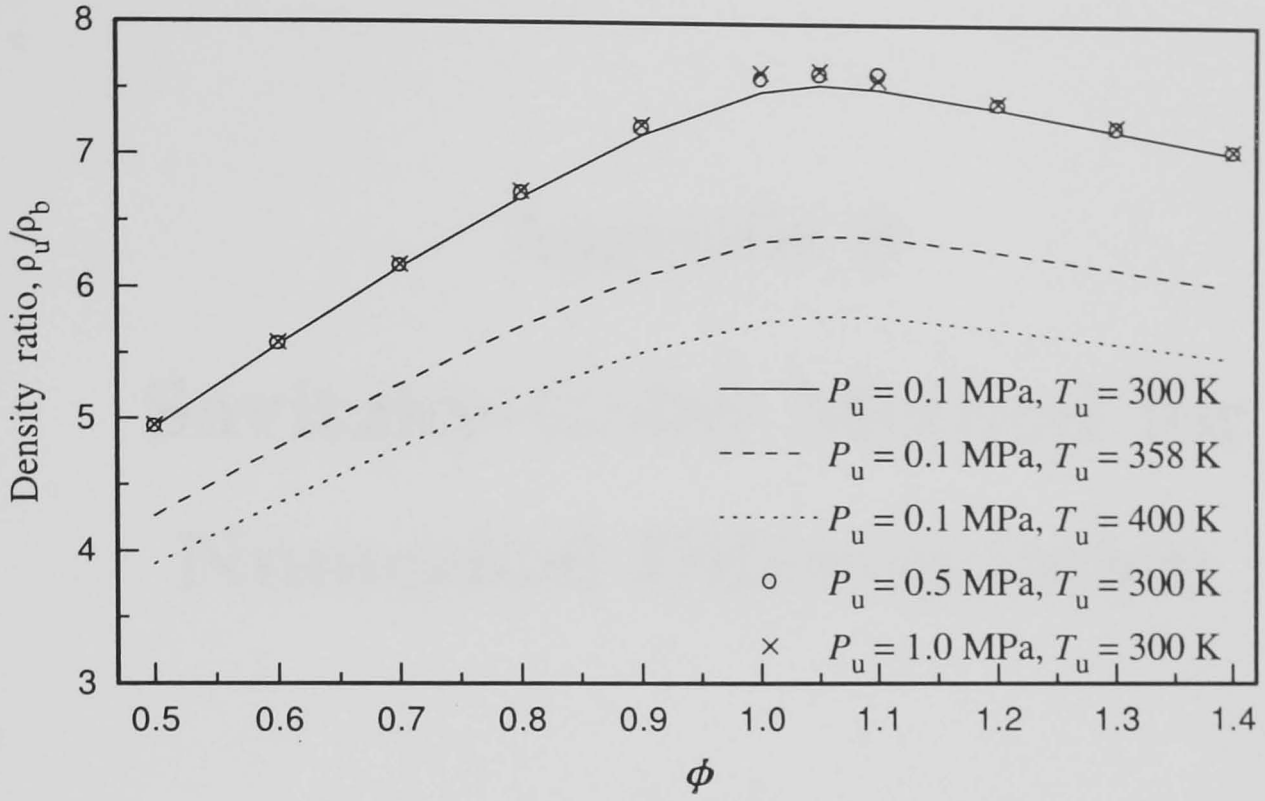

Fig. A.3. Density ratio for methane-air mixtures at different initial conditions.

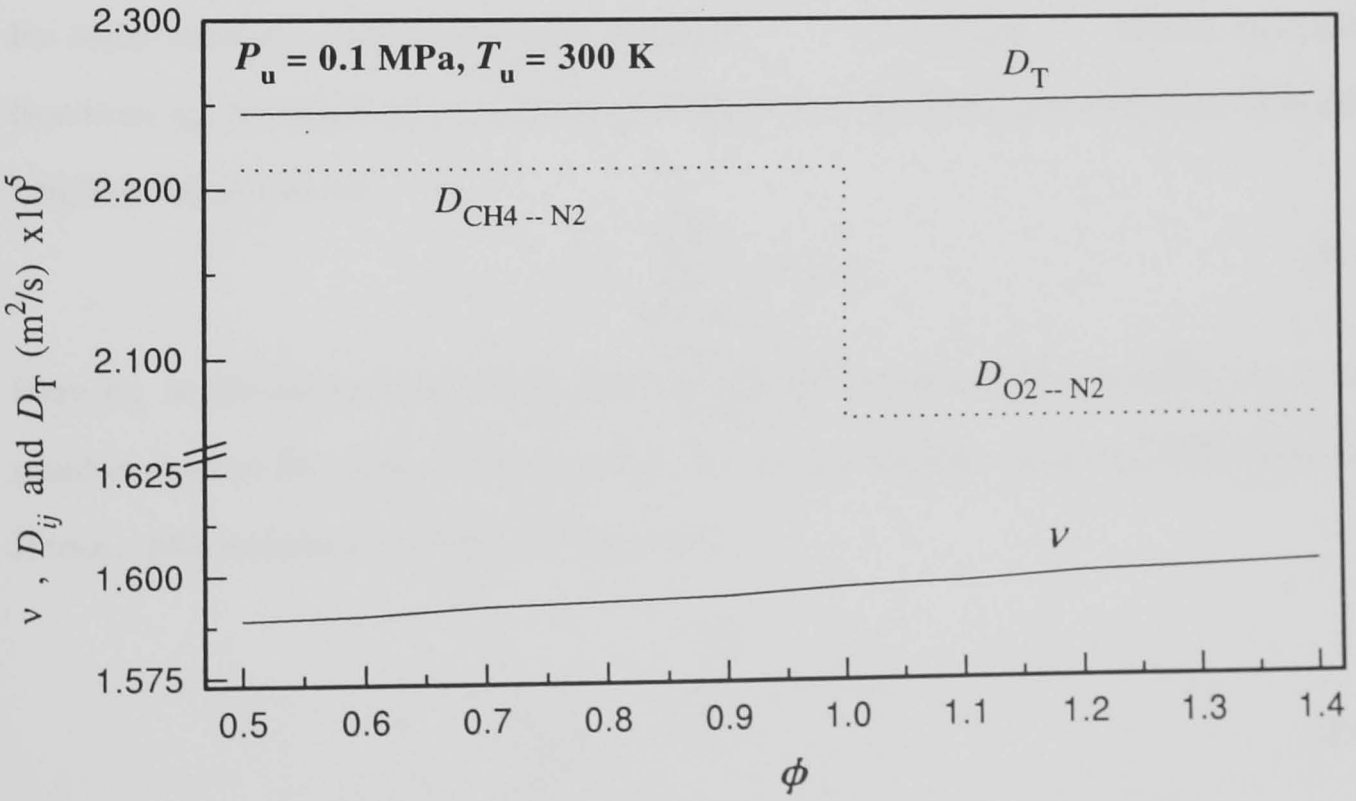

Fig. A.4. Transport properties for for methane-air mixtures at 0.1—MPa and 300 K.

Appendix B

Savitzky-Golay Method for Numerical Differentiation

In the present study, Savitzky-Golay algorithm (Savitzky and Golay 1964, Press *et al.* 1992) is used for data smoothing and differentiation. This is a low pass filter and is applied to a series of equally spaced data values $f_i \equiv f(x_i)$, where $x_i \equiv x_o + i\Delta$ for some constant sample spacing Δ and $i = \cdots -2, -1, 0, 1, 2, \cdots$. Hence, smoothed function, g_i, is computed by a linear combination of itself and some number of nearby neighboring points as:

$$g_i = \sum_{n=-n_L}^{n_R} c_n f_{i+n} \tag{B.1}$$

Here n_L is the number of points used "to the left" of data point i, while, n_R is the number used to the right. This algorithm can also be used for numerical differentiation. Hence, differentiation of order s is obtained as:

$$\frac{\mathrm{d}^s g_i}{\mathrm{d}x^s} = \frac{\sum_{n=-n_L}^{n_R} c_n f_{i+n}}{(s-1)!\ [\Delta]^{(s-1)}} \tag{B.2}$$

In Savitzky-Golay algorithm, the value of the coefficients c_n are obtained by using a least square fit a polynomial of degree m to all $(n_L + n_R + 1)$ points in a moving

window for each point f_i, and then set g_i to be the value of the polynomial at position i. This algorithm is reviewed by Press *et al.* (1992).

In the present study, data smoothing and numerical differentiation is carried out by a program `savit.for` written by the present author which uses a subroutine `savgol.for` from Press *et al.* (1992). Data smoothing and numerical differentiation using this algorithm is excellent and examples are shown in Figs. 7.1 and 7.2.

References

Abdel-Gayed, R. G., K. J. Al-Khishali, and D. Bradley (1984). Turbulent Burning Velocities and Flame Straining in Explosions. *Proc. R. Soc. Lond. A* **391**, 393–414.

Abdel-Gayed, R. G., D. Bradley, and M. Lawes (1987). Turbulent Burning Velocities: A General Correlation in terms of Straining Rates. *Proc. R. Soc. Lond. A* **414**, 389–413.

Abdel-Gayed, R. G., D. Bradley, M. Lawes, and F. K. Lung (1986). Premixed turbulent Burning During Explosions. In *Twenty-First Symposium (International) on Combustion*, pp. 497–504. The Combustion Institute.

Ali, Y. B. (1995, May). *Fundamentals of Turbulent Combustion Related to Gasoline Engines*. PhD dissertation, The University of Leeds, Department of Mechanical Engineering.

Andrews, G. E. and D. Bradley (1972). The Burning Velocity of Methane-Air Mixture. *Combust. Flame* **19**, 275–288.

Ashurst, W. T. (1997). Darrieus-Landau Instability, growing cycloids and expanding flame acceleration. *Combust. Theory Modelling* **1**, 405–428.

Assael, M. J., J. P. M. Trusler, and T. F. Tsolakis (1996). *Thermophysical Properties of Fluids: An Introduction to their Prediction*. London: Imperial College Press.

Aung, K. T., M. I. Hassan, and G. M. Faeth (1997). Flame Stretch Interactions of Laminar Premixed Hydrogen/Air Flames at Normal Temperature and Pressure. *Combst. Flame* **109**, 1–24.

Aung, K. T., L. K. Tseng, M. A. Ismail, and G. M. Faeth (1995). Response to Comment by S. C. Taylor and D. B. Smith on "Laminar Burning Velocities and Markstein Numbers of Hydrocarbon/Air Flames. *Combst. Flame* **109**, 526–530.

Baxes, G. A. (1994). *Digital Image Processing: Principles and Applications*. New York: John Wiley & Sons, Inc.

Bechtold, J. K. and M. Matalon (1987). Hydrodynamic and Diffusion Effects on the Stability of Spherically Expanding Flames. *Combst. Flame* **67**, 77–90.

Becker, H., M. Monkhouse, J. Wolfrun, R. S. Cant, K. N. C. Bray, R. Maly, W. Pfister, G. Stahl, and J. Warnatz (1990). Investigation of Extinction in Unsteady Flames in Turbulent Combustion by 2D-LIF OH Radicals and Flamelet Analysis. In *Twenty-Third Symposium (International) on Combustion*, pp. 817–823. The Combustion Institute, Pittsburgh.

Bird, R. B., W. E. Stewart, and E. N. Lightfoot (1960). *Transport Phenomena*. John Wiley & Sons.

Borghi, R. (1985). *Recent Advances in Aerospace Science*. Plenum Press, NY.

Borman, G. L. and K. W. Ragland (1998). *Combustion Engineering*. McGraw-Hill Book Company.

Bradley, D. (1990). Combustion in Gasoline Engines. In J. Wearing (Ed.), *Internal Combustion Engineering: Science and Technology*, pp. 287–331. Elsevier Applied Science.

Bradley, D. (1992). How Fast Can We Burn? In *Twenty-Fourth Symposium (International) on Combustion*, pp. 247–262. The Combustion Institute.

Bradley, D. (1998). Instabilities and Flame Speeds in Large Scale Premixed Gaseous Explosions. Submitted for publications.

Bradley, D., P. H. Gaskell, and X. J. Gu (1996). Burning Velocities, Markstein Lengths, and Flame Quenching for Spherical Methane-Air Flames: A Computational Study. *Combust. Flame* **104**, 176–198.

Bradley, D. and C. M. Harper (1994). The Development of Instabilities in Laminar Explosion Flames. *Combust. Flame* **99**, 562–572.

Bradley, D., R. A. Hicks, M. Lawes, and C. G. W. Sheppard (1996). Study of Turbulence and Combustion Interaction: Measurement and Prediction of the Rate of Turbulent Burning. Technical report, Department of Mechanical Engineering, The University of Leeds, Leeds, UK.

Bradley, D., R. A. Hicks, M. Lawes, C. G. W. Sheppard, and R. Woolley (1998). The Measurement of Laminar Burning Velocities and Markstein Numbers for Iso-octane-Air and Iso-octane-n-Heptane-Air Mixtures at Elevated Temperatures and Pressures in an Explosion Bomb. *Combust. Flame* **115**, 126–144.

Bradley, D., A. K. C. Lau, and M. Lawes (1992). Flame Stretch Rate as a Determinant of Turbulent Burning Velocity. *Phil. Trans. R. Soc. Lond. A* **338**, 359–387.

Bray, K. N. C. and R. S. Cant (1991). Some Applications of Kolmogorov's Turbulence Research in the Field of Combustion. *Proc. R. Soc. Lond. A* **434**, 217–240.

Brown, M. J., I. C. McLean, D. B. Smith, and S. C. Taylor (1996). Markstein Lengths of CO/H_2/Air Flames, Using Expanding Spherical Flames. In *Twenty-Sixth Symposium (International) on Combustion*, pp. 875–881. The Combustion Institute, Pittsburgh.

Bui-Pham, M. and J. A. Miller (1994). Rich Methane/air Flames: Burning Velocities, Extinction Limits, and Flammability Limit. In *Twenty-Fifth Symposium (International) on Combustion*, pp. 1309–1315. The Combustion Institute, Pittsburgh.

Burcat, A. and B. McBride (1997). 1997 Ideal Gas Thermodynamic Data for Combustion and Air-Pollusion Use. Technical Report TAE-804, Technion - Israel Institute of Technology.

Candel, S. M. and T. J. Poinsot (1990). Flame Stretch and the Balance Equation for the Flame Area. *Combust. Sci. and Tech.* **70**, 1–15.

Checkel, M. D. and D. S. Ting (1992). Measuring Turbulent Flame Growth by Visualization. *SAE Paper* **920184**.

Checkel, M. D. and D. S. Ting (1993). Turbulence Effects on Developing Turbulent Flames in a Constant Volume Combustion Chamber. *SAE Paper* **930867**.

Chung, S. H. and C. K. Law (1984). An Invariant Derivation of Flame Stretch. *Combst. Flame* **55**, 123–125.

Clarke, A., R. Stone, and P. Beckwith (1995). Measuring the Laminar Burning Velocity of Methane/diluent/air Mixtures within a Constant-Volume Combustion Bomb in a Micro-gravity Environment. *Journal of the Institute of Energy* **68**, 130–136.

Clavin, P. (1985). Dynamic Behavior of Premixed Flame Fronts in Laminar and Turbulent Flows. *Prog. Energy Combst. Sci.* **11**, 1–59.

Dixon-Lewis, G. (1990). Structure of Laminar Flames. In *Twenty-Third Symposium (International) on Combustion*, pp. 305–324. The Combustion Institute, Pittsburgh.

Dowdy, D. R., D. B. Smith, S. C. Taylor, and A. Williams (1990). The Use of Expanding Spherical Flames to Determine Burning Velocities and Stretch Effects in Hydrogen/Air Mixtures. In *Twenty-Third Symposium (International) on Combustion*, pp. 325–332. The Combustion Institute, Pittsburgh.

Durão, D. F. G. and M. V. Heitor (1990). Modern Diagnostic Techniques for Combusting Flows: An Overview. In D. F. G. D. M. V. Heitor, J. H. Whitelaw, and P. O. Witze (Eds.), *Combusting Flow Diagnostics*, pp. 1–45. Kluwer Academic Publishers.

Echekki, T. and J. H. Chen (1996). Brief Communication : Unsteady Strain Rate and Curvature Effects in Turbulent Premixed Methane-Air Flames. *Combst. Flame* **106**, 184–202.

Frenklach, M., H. Wang, M. Goldenberg, G. P. Smith, D. M. Golden, C. T. Bowman, R. K. Hanson, W. C. Gardiner, and V. Lissuanski (1995, November). GRI-MECH An Optimized Detailed Chemical Reaction Mechanism for Methane Combustion. Technical Report GRI-95/0058, Gas Research Institute.

Frenklach, M., H. Wang, and M. J. Rabinowitz (1992). Optimization and Analysis of Large Chemical Kinetic Mechanisms Using the Solution Mapping Method - Combustion of Methane. *Prog. Energy Combst. Sci.* **18**, 47–73.

Frisch, U. (1995). *Turbulence: The Legacy of A. N. Kolmogorov.* Cambridge: Cambridge University Press.

Glassman, I. (1996). *Combustion* (Third ed.). San Diego, California: Academic Press.

Gostintsev, Y. A., A. G. Istratov, and Y. V. Shulenin (1987). Self-similar Propagation of a Free Turbulent Flame in Mixed Gas Mixtures. *Combst. Explosion and Shock Waves* **24**, 563–569.

Göttgens, J., F. Mauss, and N. Peters (1992). Analytic Approximations of Burning Velocities and Flame Thicknesses of Lean Hydrogen, Methane, Ethylene, Ethane, Acetylene, and Propane Flames. In *Twenty-Fourth Symposium (International) on Combustion*, pp. 129–135. The Combustion Institute.

Groff, E. G. (1982). The Cellular Nature of Confined Spherical Propane-Air Flames. *Combst. Flame* **48**, 51–62.

Gu, X. J. (1998). Private Communication.

Hamamoto, Y., E. Tomita, and S. Yoshiyama (1996). Turbulent Premixed Flames in Closed Combustion Chambers. *JSME International Journal, Series B* **39**, 171–175.

Haniff, M. S., A. Melvin, D. B. Smith, and A. Williams (1989). The Burning Velocities of Methane and SNG Mixtures with Air. *Journal of the Institute of Energy*, 229–236.

Haworth, D. C. and T. J. Poinsot (1992). Numerical Simulations of Lewis Number Effects in Turbulent Premixed Flames. *J. Fluid Mech.* **224**, 405–436.

Heywood, J. B. (1988). *Internal Combustion Engine Fundamentals.* McGraw-Hill Book Company.

Istratov, A. G. and V. B. Librovich (1969). On the Stability of Gasdynamic Discontinuities Associated with Chemical Reaction. The Case of a Spherical Flame. *Astronautica Acta.* **14**, 453–467.

Kee, R. J., G. Dixon-Lewis, J. Warnatz, M. E. Coltrin, and J. A. Miller (1986). A FORTRAN Computer Code Package for the Evolution of Gas-Phase Multicomponent Transport Properties. Technical Report SAND86-8246, Sandia National Laboratorie, Livermore, CA.

Kee, R. J., J. F. Grcar, M. D. Smooke, and J. A. Miller (1985). A FORTRAN Program for Modeling Steady Laminar One-dimensional Premixed Flames. Technical Report SAND85-8240, Sandia National Laboratorie, Livermore, CA.

Kee, R. J., F. M. Rupley, and J. A. Miller (1989). A FORTRAN Chemical Kinetics Package for the Analysis of Gas-Phase Chemical Kinetics. Technical Report SAND89-8009, Sandia National Laboratorie, Livermore, CA.

Kobayashi, H., T. Nakashima, T. Tamura, K. Maruta, and T. Niioka (1997). Turbulence Measurements and Observations of Turbuelent Premixed Flames at Elevated Pressures up to 3.0 MPa. Private Communucation.

Kostiuk, L. W. and K. N. C. Bray (1994). Mean Effects of Stretch on Laminar Flamelets in a Premixed Turbulent Flame. *Combust. Sci. and Tech.* **95**, 193–212.

Kuo, K. K. (1986). *Principles of Combustion.* John Wiley & Sons.

Kuznetsov, E. A. and S. S. Minaev (1996). Formation and Propagation of Cracks on the Flame Surface. *Physics Letters A* **221**, 187–192.

Law, C. K. (1988). Dynamics of Stretched Flames. In *Twenty-Second Symposium (International) on Combustion*, pp. 1381–1402. The Combustion Institute.

Law, C. K., C. J. Sung, and C. J. Sun (1997). On The Aerodynamics of Flame Surfaces. *Ann. Rev. Heat Transfer* **8**, 93–151.

Lee, A. P. (1995). *The Effects of Bulk Air Motios and Turbulence on Combustion in SI Engines.* PhD dissertation, The University of Leeds, Department of Mechanical Engineering.

Lee, B. I. and M. G. Kesler (1975). A Generalized Thermodynamic Correlation Based on Three-Parameter Corresponding States. *AIChE J.* **21**, 510–527.

Lee, T. W., G. L. North, and D. A. Santavicca (1992). Curvature and Orientation Statistics of Turbulent Premixed Flame Fronts. *Combust. Sci. and Tech.* **84**, 121–132.

Lee, T. W., G. L. North, and D. A. Santavicca (1993). Surface Properties of Turbulent Premixed Propane/Air Flames at Various Lewis Numbers. *Combust. Flame* **93**, 275–288.

Lewis, B. and G. von Elbe (1987). *Combustion, Flames and Explosion of Gases* (Third ed.). San Diego, California: Academic Press.

Lind, C. D. and J. C. Whitson (1977). Explosion Hazards Associated with Spill of Large Quantities of Hazardous Materials Phase II. Technical Report CG-D-85-77, Department of Transportation, U.S. Coast Guard.

Makeev, V. I., Y. A. Gostintsev, V. V. Strogonov, Y. A. Bokhon, Y. N. Chernushkin, and V. N. Kulikov (1983). Combustion and Detonations of Hydrogen-Air Mixtures in Free Spaces. *Combst. Explosion and Shock Waves* **19**, 16–18.

Markstein, G. H. (1951). Experimental and Theoretical Studies of Flame-Front Stability. *J. Aero. Sci.* **18**, 199–209.

Mason, E. A. and S. C. Saxena (1958). Approximate Formula for the Thermal Conductivity of Gas Mixtures. *Phys. Fluids* **1**, 361–369.

Matalon, M. (1983). On Flame Stretch. *Combust. Sci. and Tech.* **31**, 169–181.

Matalon, M. and T. Erneux (1984). Expanding Flame May Delay the Transition to Cellular Structures. *SIAM J. Appl. Math.* **44**, 734–744.

Matalon, M. and B. J. Matkowsky (1982). Flames as Gasdynamic Discontinuities. *J. Fluid Mech.* **124**, 239–259.

Matthews, R. D., M. J. Hall, W. Dai, and G. C. Davis (1996). Combustion Modeling in SI Engines with a Peninsula-Fractral Combustion Model. *SAE Paper* **960072**.

Mauss, F. and N. Peters (1993). Reduced Kinetic Mechanisms for Premixed Methane-Air Flames. In N. Peters and B. Rogg (Eds.), *Reduced Kinetic Mechanisms for Application in Combustion Systems*, Number 15 in Lecture Notes in Physics, pp. 58–75. Berlin: Springer-Verlag.

McComb, W. D. (1990). *The Physics of Fluid Turbulence.* Oxford University Press.

Merdjani, S. and C. G. W. Sheppard (1993). Gasoline Engine Cylce Simulation Using the Leeds Burning Velocity Correlations. *SAE Paper* **932640**.

Metghalchi, M. and J. C. Keck (1980). Laminar Burning Velocity of Propane-Air Mixtures at High Temperature and Pressure. *Combst. Flame* **38**, 143–154.

Minaev, S. S., E. A. Pirogov, and O. V. Sharypov (1996). A Nonlinear Model for Hydrodynamic Instability of an Expanding Flame. *Combst. Explosion and Shock Waves* **32**, 481–488.

Mushi, E. M. J. (1992, February). *Fundamentals of Turbulent Gaseous Explosions.* PhD dissertation, The University of Leeds, Department of Mechanical Engineering.

Neufeld, P. D., A. R. Janzen, and R. A. Aziz (1972). Empirical Equations to Calculate 16 of the Transport Collision Integrals $\Omega^{l,s}$ for the Lennard-Jones (12-6) Potential. *J. Chem. Phys.* **57**, 1100–1103.

Olikara, C. and G. L. Bowman (1975). A Computer Program for Calculating Properties of Equilibrium Combustion Products with Some Applications to I. C. Engines. *SAE Paper* **750468**.

Peters, N. (1986). Laminar Flamelet Concepts in Turbulent Combustion. In *Twenty-First Symposium (International) on Combustion*, pp. 1231–1250. The Combustion Institute.

Peters, N. and F. A. Williams (1987). The Asymptotic Structure of Stoichiometric Methane-Air Flames. *Combust. Flame* **68**, 185–207.

Poinsot, T., D. Veynante, and S. Candel (1990). Diagrams of Premixed Turbulent Combustion Based on Direct Simulation. In *Twenty-Third Symposium (International) on Combustion*, pp. 613–619. The Combustion Institute, Pittsburgh.

Pontoppidan, M. (1995). Streamline Visualisation by Laser Sheet Imaging - A Useful Complementary Optimisation Tool for Intake Manifold Design. *SAE Paper* **950101**.

Press, W. H., S. A. Teukolsky, W. T. Vetterling, and B. P. Flannery (1992). *Numerical Recipies in Fortran 77 : The Art of Scientific Computing* (Second ed.). Cambridge: Cambridge University Press.

Rallis, C. J. and A. M. Garforth (1980). The Determination of Laminar Burning Velocity. *Prog. Energy Combst. Sci.* **6**, 303–329.

Rankin, D. D. and F. Weinberg (1997). Location of the Schlieren Image in Premixed Flames : Axially Symmetrical Refractive Index Fields. Accepted for publication in *Combust. and Flame.*

Rutland, C. J. and A. Trouvé (1993). Direct Simulation of Premixed Turbulent Flames with Nonunit Lewis Numbers. *Combust. Flame* **94**, 41–57.

Ryan, T. W. and S. S. Lestz (1980). The Laminar Burning Velocity of Isooctane, N-Heptane, Methanol, Methane, and Propane at Elevated Temperature and Pressures in the Presence of Diluent. *SAE Paper* **800103**.

Savitzky, A. and M. J. E. Golay (1964). *Analytical Chemistry* **36**, 1627–1639.

Scott, M. J. (1992, September). *Distributions of Strain Rate and Temperature in Turbulent Combustion.* PhD dissertation, The University of Leeds, Department of Mechanical Engineering.

Seshadri, K. (1996). Multistep Asymptotic Analyses of Flame Structures. In *Twenty-Sixth Symposium (International) on Combustion*, pp. 831–846. The Combustion Institute.

Seshadri, K. and F. A. Williams (1994). Reduced Chemical Systems and Their Application in Turbulent Combustion. In P. A. Libby and F. Williams (Eds.), *Turbulent Reacting Flows*, pp. 153–210. London: Academic Press.

Shen, H., P. C. Hinze, and J. B. Heywood (1996). A Study of Cycle-to-Cycle Variations in SI Engines Using a Modified Quasi-Dimensional Model. *SAE Paper* **961187**.

Shepherd, I. G. and W. T. Ashurst (1992). Flame Front Geometry in Premixed Turbulent Flames. In *Twenty-Fourth Symposium (International) on Combustion*, pp. 485–491. The Combustion Institute.

Sivashinsky, G. I. (1983). Instabilities, Pattern Formation, and Turbulence in Flames. *Ann. Rev. Fluid Mech.* **15**, 179–199.

Smith, F. A. and S. F. Pickering (1928). Bunsen Flames of Unusual Structure. *Ind. Engng. Chem.* **20**, 1012–1013.

Strehlow, R. A. (1984). *Combustion Fundamentals*. McGraw-Hill Book Company.

Taylor, S. C. (1991, September). *Burning Velocity and the Influence of Flame Stretch*. PhD dissertation, The University of Leeds, Department of Fuel and Energy.

Ting, D. S. and M. D. Checkel (1997). The Importance of Turbulence Intensity, Eddy Size and Flame Size in Spark Ignited, Premixed Flame Growth. *Proc. Instn. Mech. Engrs. Part D* **221**, 83–86.

Ting, D. S., M. D. Checkel, and B. Johnson (1995). The Importance of High-Frequency, Small-Eddy Turbulence in Spark Ignited, Premixed Engine Combustion. *SAE Paper* **952409**.

Turns, S. R. (1996). *An Introduction to Combustion: Concepts and Applications*. McGraw-Hill Book Company.

Vagelopoulos, C. M., F. N. Egolfopoulos, and C. K. Law (1994). Further Considerations on the Determination of Laminar Flame Speeds with the Counterflow Twin-flame Technique. In *Twenty-Fifth Symposium (International) on Combustion*, pp. 1341–1347. The Combustion Institute.

Van Maaren, A., D. S. Thung, and L. P. H. De Goey (1994). Measurement of Flame Temperature and Adiabatic Burning Velocity of Methane/Air Mixtures. *Combust. Sci. and Tech.* **96**, 327–344.

Warnatz, J., U. Maas, and R. W. Dibble (1996). *Combustion: Physical and Chemical Fundamentals, Modeling and Simulation, Experiments, Pollutant Formation.* Berlin: Springer-Verlag.

Weinberg, F. J. (1955). Location of the 'Schlieren Image' in a Flame. *Fuel* **34**, S84–87.

Wilke, C. R. (1950). A Viscosity Equation for Gas Mixtures. *J. Chem. Phys.* **18**, 517–519.

Williams, F. A. (1985). *Combustion Theory* (Second ed.). Menlo Park, California: Addison-Wesley Publishing Company.

Wirth, M., P. Keller, and N. Peters (1993). A Flamelet Model for Premixed Turbulent Combustion in SI-Engine. *SAE Paper* **932646**.

Yamaoka, I. and H. Tsuji (1984). Determination of Burning Velocity Using Counterflow Flames. In *Twentieth Symposium (International) on Combustion*, pp. 1883–1892. The Combustion Institute, Pittsburgh.

Zeldovich, Y. B., G. I. Barenblatt, V. B. Librovich, and G. M. Makhviladze (1985). *The Mathematical Theory of Combustion and Explosion* (First ed.). New York and London: Consultants Bureau.